

Numerical Simulation of Hydrogen Assisted Cracking in Supermartensitic Stainless Steel Welds

Vom Fachbereich Maschinenbau
der Helmut-Schmidt-Universität
– Universität der Bundeswehr Hamburg –
zur Erlangung des akademischen Grades
eines Doktor-Ingenieurs (Dr.-Ing.)
genehmigte

Dissertation

vorgelegt von:

Ekkarut Viyanit, M.Eng.

aus:

Ayutthaya, Thailand

Hamburg 2005

Die vorliegende Arbeit entstand an der Bundesanstalt für Materialforschung und -prüfung (BAM).

Gutachter: Prof. Dr.-Ing. Hans Hoffmeister
Assoc. Prof. Dr.-Ing. Gobboon Lothongkum
Dr.-Ing. Thomas Böllinghaus, VP u. Prof.

Tag der mündlichen Prüfung: 27. Januar 2005 in Hamburg

Impressum

**Numerical Simulation of Hydrogen Assisted Cracking
in Supermartensitic Stainless Steel Welds**

2005

Herausgeber:
Bundesanstalt für Materialforschung und -prüfung (BAM)
Unter den Eichen 87
12205 Berlin
Telefon: +49 30 8104-0
Telefax: +49 30 8112029
E-mail: info@bam.de
Internet: www.bam.de

Copyright © 2005 by Bundesanstalt für
Materialforschung und -prüfung (BAM)

Verlag und Vertrieb:
Wirtschaftsverlag NW
Verlag für neue Wissenschaft GmbH
27568 Bremerhaven
Telefon: +49 471 94544-0
Telefax: +49 471 94544-77/-88

Layout: BAM-Arbeitsgruppe Z.03

ISSN 1613-4249
ISBN 3-86509-270-5

ABSTRACT

Replacement of expensive duplex stainless steel and conventional carbon steel by a new generation of supermartensitic stainless steel has been taken into account since the last decade corresponding to the "Fitness for Purpose" concept in order to meet the technical-economical challenge for transportation flowlines of unprocessed oil and gas products in offshore technology, in particular. Supermartensitic stainless steels can provide appropriate material properties such as: improved strength-to-weight ratio, enhanced useful corrosion resistance as well as application at relatively low cost. With decreased carbon content and increased molybdenum content compared to traditional martensitic stainless steel, hydrogen assisted stress corrosion cracking (HASCC) problems have been found during service caused by hydrogen being taken up during from sour service environments by cathodic protection. Hydrogen assisted cold cracking in supermartensitic stainless steel can also occur during fabrication welding with hydrogen picked up during welding, since this steel is relatively crack-susceptible by hydrogen.

Therefore, effects of hydrogen assisted cracking (HAC), i.e. HASCC and HACC, on characteristic susceptibility of girth welds of supermartensitic stainless steel pipelines are studied in the present thesis by numerical modelling, which is developed using a available commercial finite element program. Firstly, numerical modelling for simulation of HASCC based on the NACE-TM 0177-96 approach is carried out for providing a basic understanding of the crack propagation behaviour. Secondly, a two dimensional finite element according to the gauge length cross-section of the orbitally welded pipeline is created for numerical modelling in order to calculate the time to failure of welded the component exposed to the NACE electrolyte solution with various H₂S saturation. Externally applied loads of a series of constant strain rates and of the load history of full scale testing are also taken into account. Finally, numerical modelling is carried out under three specific aspects, i.e. thermal analysis, structural analysis, and hydrogen diffusion analysis, in order to simulate HACC in supermartensitic stainless steel pipelines welded orbitally by four layers of matching filler wires with an interpass temperature of 40°C.

By indirect coupling of numerical diffusion and numerical structural modelling, all three stages of HASCC, i.e. crack initiation, stable crack growth and rapid rupture, are represented for the standard specimen when appropriate interaction between local hydrogen and local strain ahead of the crack tip takes place, so that the time to failure is controlled by Stage II: stable crack growth. In the case where the local strain rate is above $5.0E-05 \text{ s}^{-1}$, rapid rupture of the specimen occurs by mechanical overload rather than HASCC. As evidently represented by numerical modelling, the heat affected zone (HAZ) is the most susceptible region to HASCC due to its kinetics of crack propagation, which is affected by the metallurgical HAZ behaviour of HAZ and by relatively high hydrogen subsurface concentrations in the base metal (BM) diffusing into the susceptible HAZ region ahead of the crack tip. The life time of orbitally welded pipelines with HASCC is significantly dependent on the HAZ crack propagation characteristic, however, this phenomenon may be changed by the presence of a previous crack in the weld metal resulting from HACC, which can reduce the new crack length generated by HASCC during exposure to sour service environments. This HACC can be avoided by using a welding fabrication in which the local hydrogen concentration picked up during welding remains below $10 \text{ ml} \cdot (100\text{gFe})^{-1}$. In

Abstract

addition, the short-term approach of post weld heat treatment (PWHT) may be employed to reduce local hydrogen concentration from sensitive regions in order to minimise the risk of failure during the spooling/pipelaying process.

Keywords: numerical modelling, supermartensitic stainless steel, girth welds, pipeline, hydrogen assisted cracking (HAC), hydrogen assisted stress corrosion cracking (HASCC), hydrogen assisted cold cracking (HACC), hydrogen subsurface concentration, crack propagation, time to failure (TTF), hydrogen diffusion coefficient, post weld heat treatment (PWHT), full scale test

CONTENTS

	Page
ABSTRACT	III
CONTENTS.....	V
ACKNOWLEDGEMENT	IX
LIST OF SYMBOLS.....	XI
LIST OF TABLES	XVII
LIST OF FIGURES	XIX
1 INTRODUCTION.....	1
2 LITERATURE REVIEWS.....	5
2.1 Supermartensitic Stainless Steels	5
2.1.1 Base Material and Weld Microstructures	6
2.1.1.1 Martensite Formation.....	10
2.1.1.2 Second Phase Precipitation.....	12
2.1.1.3 Post Weld Heat Treatment.....	13
2.1.1.4 Filler Materials for Supermartensitic Stainless Steels	16
2.1.2 Mechanical Properties	17
2.1.3 Corrosion Resistance	19
2.2 Mechanisms of Hydrogen Assisted Cracking	20
2.2.1 Pressure Theory.....	21
2.2.2 Decohesion Theory.....	22
2.2.3 Adsorption Theory	23
2.2.4 Dislocation Interaction Theory	24
2.2.5 Hydride Theory	27
2.3 Effects of Crystal Structure of Steels on Hydrogen Transport	28
2.3.1 Hydrogen Evolution and Absorption	30
2.3.1.1 Hydrogen Absorption during Corrosion Processes.....	30
2.3.1.2 Modelling of Hydrogen Absorption during Welding.....	33
2.3.2 Determination of Hydrogen Diffusion Coefficients	35
2.3.3 The basic principle of diffusion	37
2.3.3.1 Trapping Effect	39

Contents

2.4	Crack Propagation Characteristics	43
2.4.1	Determination of Crack Propagation Kinetics	45
2.4.2	Mechanisms of Stress Corrosion Cracking	50
2.5	Failure and Fracture Mechanisms for Modelling Hydrogen Assisted Cracking	52
2.5.1	Fracture Theory	53
2.5.1.1	Definition of Local Strain Rate	54
2.6	Slow Strain Rate Test	57
2.6.1	NACE Standard TM 0177-96	59
2.6.1.1	Test specimen	60
2.6.1.2	Test Solution	60
2.6.1.3	Test Procedure	60
2.6.1.4	Failure Determination	61
2.7	Hydrogen Assisted Cold Cracking in Girth Welds	62
2.7.1	Overview of Hydrogen Assisted Cold Cracking of Welded Steels	64
2.7.2	Hydrogen Assisted Cold Cracking Test Methods	64
2.7.2.1	IRC-Test	64
2.7.2.2	Component Test	67
2.7.3	Model of Temperature Distribution in Welding Processes	70
2.7.3.1	Heat Generation in Arc Welding Processes	70
2.7.3.2	Heat Transfer in Metallic Materials	71
2.7.4	Modelling of Stress-Strain Distribution	73
2.7.5	Modelling of Hydrogen Distribution in Welded Joints	74
3	FINITE ELEMENT MODELLING DEVELOPMENT	77
3.1	Two-Dimensional Finite Element	77
3.2	Finite Element Models for Modelling HAC	77
3.2.1	Geometric Parameters	77
3.2.2	Modelling of Hydrogen Diffusion	82
3.2.3	Numerical Modelling Concept	87
3.2.4	Sequence of the Modelling Program	88
3.2.5	Specific Input Data for Modelling	90

3.2.6	Modelling of HASCC at Pipeline Welds	97
3.2.6.1	Description of the Test Procedure	97
3.2.6.2	Numerical Modelling Program Sequences.....	99
3.2.7	Modelling of HACC at Pipeline Welds.....	100
3.2.7.1	Definition of Boundary Conditions.....	101
3.2.7.2	Numerical Modelling Sequences	102
4	RESULTS AND DISCUSSION	107
4.1	Modelling of HASCC based on NACE Standard Test Method.....	107
4.1.1	Effects of Hydrogen Subsurface Concentration.....	109
4.1.2	Effects of Various Hydrogen Diffusion Coefficients	112
4.1.3	Global Strain Rates and Local Strain Factors.....	116
4.1.4	As-Quenched Supermartensitic Stainless Steel	118
4.1.5	Crack Tip Angle	122
4.2	Modelling of HASCC in Girth Welds of Pipelines.....	126
4.2.1	Series of Constant Strain Rate	126
4.2.2	Crack propagation in BM, HAZ and WM under the Realistic Test Condition	132
4.3	Modelling of HACC in Girth Welds of Supermartensitic Stainless Steel Pipelines.....	135
4.3.1	Thermal Analysis	136
4.3.2	Structural Analysis	138
4.3.3	Hydrogen Diffusion Analysis.....	143
4.3.3.1	Effects of Initial Hydrogen Concentration on Local Hydrogen Distribution	143
4.3.3.2	HACC Initiation and Propagation.....	149
4.3.4	Effects of PWHT on Local Hydrogen Concentration in the Welded Component.....	152
4.4	Modelling of HASCC in the Welded Component Having a Pre-Crack Caused by HACC	160
5	CONCLUSIONS AND PERSPECTIVES	165
5.1	Conclusions	165
5.2	Perspectives	168
	REFERENCES.....	171

ACKNOWLEDGEMENT

Since May 2000, the present thesis has been elaborated in the Division of Safety in Joining Technology, Department of Materials Engineering, Federal Institute for Materials Research and Testing (BAM), Berlin, within the framework of the Ph.D.-program.

Many people have assisted the author by giving advice, encouragement, discussion as well as great assistance. The author would like to take this opportunity to express sincere gratitude to all of them. First of all, sincere thanks are due to Dr.-Ing. Thomas Boellinghaus (Vice President and Professor at BAM), the author's major advisor, for his magnanimity in expending time and effort to guide and assist the author throughout this thesis and for opening the door on many professional opportunities along the way. The author has never forgotten to express his appreciation to Assoc. Prof. Dr.-Ing. Gobboon Lothongkum (Chulalongkorn University, Bangkok, Thailand) who provided many opportunities for the author. Additionally, the author's sincere acknowledgement must be reached to Prof. Dr.-Ing. Hans Hoffmeister (Institute for Failure Analysis and Failure Prevention, University of the Federal Armed Forces Hamburg) who is the thesis's major professor.

The author is very pleased to be grateful to Dr.-Ing. Thomas Kannengiesser, Acting Head of the Division, for his great assistance as well as to Mr. Andreas Hannemann and Mr. André Hofmann for their computer expertise.

Also, expressed appreciation is due to all doctoral candidates in the Division: Mr. Dirk Seeger for providing data of hydrogen diffusion behaviour, Mr. Mathias Neuhaus and Mr. Martin Wolf for valuable discussion on FEM-simulation and Mr. Peter Zimmer for useful discussion on hydrogen assisted cold cracking. The author is extraordinarily gratefully to Ms. Margit Bauer and Ms. Angelique Lasscigne (Colorado School of Mines) for their great assistance to review the manuscript of the present thesis.

Furthermore, the author must sincerely thank for the financial support of the present thesis by the Federal Institute for Materials Research and Testing (BAM).

Finally, the author would like to acknowledge to his parents and his near relatives as well as his girl friend for their support and understanding even though they are living on the other side of the world.

Ekkarut Viyanit

Berlin, October 2004

LIST OF SYMBOLS

a	Crack length
a_{H^+}	Activity reaction
a_{nor}	Activities of hydrogen on the normal site
a_{smb}	Crack distance advanced by movement of vacancies
a_{trap}	Activities of hydrogen on the trapping site
A_{sur}	Total surface exposed to ambient environments
A_{weld}	Arc voltage
α_{con}	Convection of film coefficient
α_{th}	Thermal coefficient expansion
γ_{HD}	Activity coefficient of hydrogen mass
$\gamma_{HD_{stress}}$	Activity coefficient of hydrogen mass affected by equivalent stress levels
$\gamma_{HD_{plm}}$	Activity coefficient of hydrogen mass affected by plastic strain levels and microstructure behaviours
c	Hardening index
C_p	Specific heat capacity
d	Membrane thickness
D_{awb}	Average diameter of the ring weld bead
D_{eff}	Effective hydrogen diffusion coefficient
D_{H_0}	Hydrogen diffusion coefficient in the normal state
D_{met}	Surface self-diffusion coefficient
D_{nor}	Hydrogen diffusion coefficient of the normal site
D_{th}	Thermal diffusivity
E	Young's modulus
E^0	Standard potential necessary for hydrogen evolution
E_B	Binding energy of hydrogen to dislocation (between 0.1- 0.5 eV)
$E_{H_{diff}}$	Activation energy required for hydrogen diffusion through solid materials
E_w	Potential of the specimen during polarisation
ϵ_{creep}	Creep strain

List of Symbols

ϵ_{crit}	Critical strain
$\epsilon_{elastic}$, $\dot{\epsilon}_{elastic}$	Elastic strain, Elastic strain rate
ϵ_{frac}	Fracture strain of the material
ϵ_{loc}	Local strain ahead of the crack tip
$\epsilon_{plastic}$, $\dot{\epsilon}_{plastic}$	Plastic strain, Plastic strain rate
ϵ_{th}	Thermal strain developed by temperature gradient effect
ϵ_{true}	True strain
ϵ_{ys}	Yield strain of material
ϵ_{total} , $\dot{\epsilon}_{total}$	Total strain, total strain rate
$\dot{\epsilon}_{ane}$	Annealing strain rate
$\dot{\epsilon}_{ct}$	Strain rate at the crack tip
$\dot{\epsilon}_{glob}$	Global strain rate
$\dot{\epsilon}_{loc}$	Local strain rate ahead of the crack tip
$\dot{\epsilon}_{ptr}$	Strain rate caused by phase transformation reaction
f_{H_2}	Fugacity of hydrogen gas
F	Faraday's constant (96,480 A·s·mol ⁻¹)
FF	Ferrite factor
F_{ad}	Force driving the dislocation
F_m	Maximum cohesive resistive force of iron atoms
F_y	Reaction force transverse to the welding direction
g	Average grain size of the given material
ΔG^0	Standard free energy change for the reaction ($\Delta H^0 - T\Delta S^0$)
h	Plate thickness
HD_{SS}	Hydrogen subsurface concentration
$[HD]$	Hydrogen concentration
$[HD]_{abs}$	Hydrogen concentration at the position with the absence of hydrostatic stress
$[HD]_{crit}$	Critical hydrogen concentration
$[HD]_{dis}$	Hydrogen concentration on a dislocation
$[HD]_{ini}$	Hydrogen concentration at the initial state

$[HD]_{nor}$	Hydrogen concentration of the normal site
$[HD]_{prs}$	Hydrogen concentration at the specific position with the presence of hydrostatic stress
$[HD]_{trap}$	Hydrogen concentration of the trapping site
$[HD]_{\infty}$	Equilibrium hydrogen concentration at the pick-up site
η	Arc efficiency dependent on welding process (for GTAW it is in the range of 0.45 – 0.75) ^[TDW 2]
θ_{nor}	Fraction of hydrogen concentration at the normal site with respect to the number of the normal sites per unit volume
θ_{trap}	Fraction of hydrogen concentration at the normal site with respect to the number of the trapping sites per unit volume
ϑ	Temperature
i	Applied current density for anodic reaction
$i_{inf lt}$	Current density at the inflection point
i_{∞}	Current density in steady state(Hydrogen permeation)
I_{weld}	Arc current
J_H	Hydrogen flux through the steel membrane
J_{∞}	Hydrogen flux through the steel membrane in steady state
j	Jump distance for crack propagation
k	Boltzmann's constant ($1.380E-23 \text{ J}\cdot\text{K}^{-1}$)
k_E	Equilibrium constant of the reaction
k_{GAPSI}	Spring constant of GAPSI 16 ($8.33E-05 \text{ N}\cdot\text{mm}^{-1}$)
k_{sp}	Spring constant of the test component
k_{trap}	Rate constant of trapping reaction
K	Thermal conductivity
K_I	Stress intensity factor of Mode I
K_{Ic}	Critical stress intensity factor of Mode I
K_{lid}	Lidbury's constant factor
l	Plate length
l_{mini}	Original length of miniature specimen
L_{smm}	Diffusion distance of vacancies
L_w	Total length of the weld bead

List of Symbols

m	Number of electrons passed in the reaction
m_H	Amount of hydrogen leaving the material
M	Mobility of the hydrogen cloud
M_{Fe}	Atomic weight of steels ($\approx 65 \text{ g}\cdot\text{mole}^{-1}$) [HAS 67]
M_H	Molecular weight of hydrogen ($1 \text{ g}\cdot\text{mole}^{-1}$)
M_x	Reaction moment around the axis in welding direction
M_z	Reaction moment around the vertical axis relative to the welding direction
μ	Chemical potential
$\mu_{H_{abs}}$	Chemical potential of dissolved hydrogen at the position with the absence of hydrostatic stress
$\mu_{H_{prs}}$	Chemical potential of dissolved hydrogen affected by hydrostatic stress
μ_0	Initial chemical potential
n	Number of metal atoms per unit area of the cracking plane
N	Number of cracks along the gauge length
ν	Poisson's ratio
pH_2	Partial pressure of molecular hydrogen
p^2H	Partial pressure of atomic hydrogen
P_{LM}	Laser-Miller parameter
ρ	Material density
ρ_{Fe}	Steel density
Q	Barrier energy for hydrogen diffusion
Q_f	Oxidation charge passed between rupture event
Q_g	Heat generation
Q_{loss}	Heat loss by surface convection
Q_{weld}	Effective power input during welding
r_{ct}	Radius of the crack tip
r_{dc}	Distance to centre of arc ($= \sqrt{w^2 + y^2 + z^2}$)
r_{pz}	Radius of the plastic zone ahead of the crack tip
R	Universal gas constant ($8.314 \text{ J mol}^{-1}\text{K}^{-1}$)

R_{F_y}	Restraint intensity
R_{M_x}	Bending restraint intensity around the axis in welding direction
R_{M_z}	Bending restraint intensity around the vertical axis relative to the welding direction
$R_{P_{0.2}}$	Offset yield strength
σ_{crit}	Critical tensile stress of Mode I required for crack propagation
σ_{ct}	Tensile stress at the crack tip
σ_{glob}	Global tensile stress
σ_{ii}	Spherical (hydrostatic) stress
σ'_{max}	Maximum local tensile stress ahead of the crack tip, MPa
σ_y	Stress distribution in butt joints transverse to the welding direction
σ_{ys}	Yield strength of the material
t	Time
$t_{1/2}$	Time required for the permeation flux to achieve a half of steady state
t_b	Time for the breakthrough method for hydrogen permeation
t_{lag}	Time at 63 per cent of the maximum quantity of permeation transient
t_{∞}	Permeation time in steady state
T	Absolute temperature
T_{amb}	Ambient temperature
T_0	Initial temperature of the specimen
T_{solid}	Instantaneous temperature of the solid material
\bar{v}_{DH}	Velocity of dislocation with hydrogen cloud
v_{weld}	Welding speed
v_x, v_y, v_z	Velocity vector for mass transport of the cartesian coordinate
V_{crack}	Crack propagation rate
\bar{V}_H	Partial molar volume of hydrogen in solution
w	Distance in the direction of moving co-ordinate ($= x - (v_{weld} \cdot t)$)
x^*	Value dependent on the movement of dislocation ahead of the crack tip
z	Valence electron of hydrogen ($z=1$)

List of Symbols

z_{Fe}	Valence electron of solute species (2 for iron)
$2\Delta y$	Transverse root gap displacement
$2\Delta\theta_x$	Deflection angles caused by the reaction moment in welding direction
$2\Delta\theta_z$	Deflection angles caused by the reaction moment vertical to the welding direction

LIST OF TABLES

Table 2-1:	Chemical composition of supermartensitic stainless steel pipeline and matching filler material.	7
Table 2-2:	Effects of alloying elements on material properties of supermartensitic stainless steel.	10
Table 2-3:	Typical transformation temperature of general categories of supermartensitic stainless steels ^[SPM 39]	11
Table 2-4:	Typical second-phase constituents observed in stainless steels ^[GEN 13]	12
Table 2-5:	Effects of two different kinds of filler materials on material properties of welded SMSS components ^[SPM 54]	16
Table 2-6:	Summary of possible electrochemical reactions in corrosion processes of the steels.....	32
Table 2-7:	Hydrogen diffusion parameter relating to the Arrhenius relationship for micro alloy steels ^[HPD 68]	38
Table 2-8:	Classification of the trapping sites based on the trapping energy for hydrogen-traps interaction.	42
Table 2-9:	Recommended appropriate strain rate for SSRT.....	58
Table 2-10:	Classification of cracking types occurring in welded components based on cracking characteristic and cracking causation ^[HAC 17]	63
Table 3-1:	Categories of applied loads for finite element modelling.....	78
Table 3-2:	Significant data of the as-delivered state and the as-quenched state of supermartensitic stainless steel for numerical modelling of HASCC.....	91
Table 3-3:	Hydrogen diffusion coefficients of supermartensitic stainless steel pipelines in the Arrhenius form for the base metal.....	96
Table 3-4:	Hydrogen diffusion coefficients of supermartensitic stainless steel pipelines in the Arrhenius form for the heat affected zone and the weld metal.....	96
Table 5-1:	Chemical composition of duplex stainless steels.....	169

LIST OF FIGURES

Figure 1-1:	The full scale test facility for performance of welding test and stress corrosion cracking test on girth welds of supermartensitic stainless steel pipelines.	2
Figure 2-1:	Effects of major alloying elements on microstructure formation of conventional stainless steel ^[GEN 24]	6
Figure 2-2:	WRC 92 constitution diagram for stainless steels influenced by alloying elements of austenite stabiliser and of ferrite stabiliser ^[GEN 13]	7
Figure 2-3:	Graphical illustration of the equilibrium constitution diagram showing microstructure formation of martensitic stainless steels in system 3:1 (Cr:Ni) ^[GEN 24]	8
Figure 2-4:	Region of γ -, δ - and α -phase in the iron-chromium constitution diagram ^[SPM 47]	9
Figure 2-5:	Effects of PWHT conditions on austenite reformation in two different systems of supermartensitic stainless steel ^[SPM 52]	14
Figure 2-6:	Average hardness levels of the weld metal dependent on PWHT parameters: a) Average values, b) Dependence on various carbon content ^[SPM 37]	14
Figure 2-7:	Mechanical properties of supermartensitic stainless steels: a) Comparison of proof stress and tensile strength of supermartensitics with lean martensitics and utility ferritics, b) Impact toughness value of supermartensitics ^[SPM 39]	17
Figure 2-8:	Influence of post heat treatment on mechanical properties of soft martensitic stainless steels: a) Impact toughness, b) Tensile strength ^{[GEN 24],[SPM 49]}	18
Figure 2-9:	Effects of GCI-index and temperature of the testing system on the general corrosion rate of martensitic stainless steel ^[SPM 48]	20
Figure 2-10:	Three main local factors influencing hydrogen assisted stress corrosion cracking behaviour ^[HAS 108]	20
Figure 2-11:	Schematic illustration of pressure theory for describing the hydrogen assisted cracking phenomenon ^[GEN 6]	21
Figure 2-12:	Variation of temperature at equilibrium pressure for molecular hydrogen precipitated within steels as a function of hydrogen concentration ^[HAS 40]	22
Figure 2-13:	Decohesion theory describing hydrogen assisted cracking phenomena: a) Model representation of decohesion of iron-iron bonds caused by dissolved hydrogen atoms, b) Schematic illustration of the equilibrium of hydrogen concentration at the position of maximum tensile stress at the specific value of hydrogen chemical potential, μ_{μ} ^[HAS 23]	23

List of Figures

Figure 2-14:	Schematic illustration of the mechanism of hydrogen assisted cracking based on the adsorption theory ^[HAS 109]	24
Figure 2-15:	Schematic demonstration of crack propagation in high strength steels based on Beachem's assumption: a) In the absence of hydrogen crack growth occurs by micro-void coalescence within a large plastic deformation ahead of the crack tip, b) In the presence of hydrogen deformation becomes easier and crack growth occurs as result of severely localised deformation at the crack tip ^{[HAS 25],[HAS 86]}	25
Figure 2-16:	Schematic illustration of hydrogen cloud on moving dislocation at left, which is stripped off at the particles of effective size D and spacing l. Diffusion along dislocation restores cloud uniformity as dislocation moves away, at right ^{[HAS 86],[HAS 110]}	26
Figure 2-17:	Schematic illustration of hydride theory showing crack propagation in the metallic hydride region ahead of the crack tip by stress induced hydride formation ^[HAS 105]	28
Figure 2-18:	Schematic illustration showing interstitial spacing for foreign atoms such as hydrogen in iron matrix lattice of bcc- and fcc-crystal structures ^{[GEN 28],[GEN 32]}	30
Figure 2-19:	Consequence of hydrogen discharge and recombination at the metal surface exposed to electrolytic solution with subsequent diffusion into the matrix material ^[HAC 21]	31
Figure 2-20:	Typical hydrogen concentration in the weld metal dependent on various arc welding processes ^[GEN 17]	34
Figure 2-21:	Graphical illustration of major hydrogen sources from which hydrogen is picked up by the weld metal during welding	34
Figure 2-22:	Schematic illustration of the hydrogen absorption procedure in the weld metal during welding	34
Figure 2-23:	Measurement of hydrogen concentration in the weld metal dependent on hydrogen fraction in Ar-CO ₂ shielding based on ISO 3690 ^[HAC 57]	36
Figure 2-24:	Schematic illustration of hydrogen permeation profile through steel membrane: a) Concentration profile of permeation, b) Permeation transient ^[HPD 21]	36
Figure 2-25:	Schematic illustration of the basic principle of diffusion theory based on Fick's second law ^[GEN 29]	38
Figure 2-26:	Graphical representation of general kinds of trapping sites interacting with dissolved hydrogen ^[GEN 19]	40
Figure 2-27:	Schematic illustration of interaction energy of atomic hydrogen and trapping sites ^[HPD 18]	41

Figure 2-28: Schematic illustration of various trapping sites in terms of trapping energies with influence of trapping diameter ^{[HAS 101],[HAS 104]}	41
Figure 2-29: Schematic illustration of binding energy between hydrogen and the trapping site influencing on cracking characteristic of α -iron ^[HAS 101]	41
Figure 2-30: Kinetics of the crack propagation as a function of stress intensity for hydrogen assisted cracking.	44
Figure 2-31: General relationship of crack length versus time for describing material properties under a condition of hydrogen assisted cracking.	44
Figure 2-32: Schematic illustration of the kinetics of crack propagation in Mode I.	46
Figure 2-33: Kinetics of crack propagation in Stage II of an AISI 4340 steel during exposure to hydrogen sulfide test solution ^[HAS 61]	47
Figure 2-34: Schematic illustration showing differentiation between anodic dissolution stress corrosion cracking and hydrogen assisted stress corrosion cracking at the cathodic reaction ^[GEN 15]	50
Figure 2-35: Schematic illustration of crack propagation by the surface mobility cracking mechanism during anodic reactions ^[HAS 111]	52
Figure 2-36: Macroscopic aspect of three main factors influencing hydrogen assisted stress corrosion cracking behaviour ^[HAS 112]	53
Figure 2-37: Graphical illustration of the three general modes of cracking ^[GEN 21]	53
Figure 2-38: Influence of externally applied strain rate on the local strain rate ahead of the crack tip taking account of the crack propagation and of the number of cracks along the gauge length ^[HAS 87]	55
Figure 2-39: Relationship between local and global strain rates as a function of global strain taking account of effects of notched forms ^[HAS 92]	57
Figure 2-40: Schematic illustration showing test facility and control connections for slow strain rate tests (SSRT) ^[HAS 94]	58
Figure 2-41: Dimension of the test specimen for the standard tensile test ^[GEN 35]	60
Figure 2-42: Failure of orbitally welded supermartensitic stainless steel pipeline during pipe laying in Tune oil and gas filed, North Sea: a) Overview of pipeline failure, b) Crack initiation adjacent to the 6-hour position.	62
Figure 2-43: Possible cracking types occurring in susceptible zones of welded steels for butt welds and fillet welds ^[HAC 17]	63
Figure 2-44: IRC–Test for verification of the susceptibility of welded components to hydrogen assisted cold cracking ^[HAC 49]	65
Figure 2-45: View of the full-scale test facility for evaluation of the susceptibility of welded components to hydrogen assisted cracking with simulation of the complete welding fabrication process and subsequent application of external loads.....	68

List of Figures

Figure 2-46: Basic principle of the measuring system of the full scale test facility for performing welding experiments with an addition function of externally applied loads on test components^[GEN 20] 69

Figure 2-47: Gaussian distribution of a heat source moving on the surface of a semi-finite plate, where the distribution parameter σ_{dp} is the standard distribution of the Gaussian function^{[TDW 2],[TDW 6]} 71

Figure 2-48: Schematic illustration of the simulation of temperature distribution during arc welding^[GEN 18] 71

Figure 2-49: Calculated equivalent strain and hydrogen distribution for identifying hydrogen assisted cold cracking^[HAC 33] 75

Figure 2-50: Calculation of transient hydrogen distribution for the Slit-Test at temperatures of 202°C and 100°C^[HAC 37] 75

Figure 3-1: Schematic illustration of the 2-D solid finite element of PLANE 55 for thermal analysis and PLANE 42 for structural analysis, four nodes with a single degree of freedom. 78

Figure 3-2: Two-dimensional finite element model according to the NACE standard test TM 0177–96. 79

Figure 3-3: Two-dimensional finite element model with a predefined cracking path in the gauge length of the test specimen in transverse direction to externally applied loads: a) Crack tip angle of 180°, b) Crack tip angle of 74° 80

Figure 3-4: Cross-section of the gauge length of the welded pipeline. 81

Figure 3-5: Two-dimensional finite element model with predefined cracking paths in three significant regions of the base metal, the heat affected zone, and the weld metal for modelling hydrogen assisted stress corrosion cracking in the orbitally welded pipeline. 81

Figure 3-6: Modified two-dimensional finite element model according to the gauge cross-section of the orbitally welded pipeline for simulation of hydrogen assisted cold cracking. 82

Figure 3-7: Simple finite element models and boundary conditions for confirming results of the advanced numerical modelling of hydrogen distribution in welded components. 83

Figure 3-8: Characteristic of hydrogen distribution obtained from finite element simulation and manual calculation in distances of 0.25 mm, 0.50 mm, 0.75 mm and 1.00 mm from the interface of a applied hydrogen source (Assumption: hydrogen diffusion coefficient = 2.0E-04 mm²·s⁻¹; M and S indicate the finite element simulation and manual calculation, respectively). 84

Figure 3-9:	Simple finite element model with assumption of an individual hydrogen diffusion coefficient for each finite element in order to confirm the modified advanced finite element modelling for calculating hydrogen diffusion during welding and subsequent cooling.....	85
Figure 3-10:	Characteristic of hydrogen distribution obtained from finite element simulation and manual calculation at the specific points with distances of 0.25 mm, 0.50 mm, 0.75 mm, and 1.00 mm from the interface of applied hydrogen: a) the first case, b) the second case. (M and S indicate the finite element simulation and manual calculation, respectively).....	86
Figure 3-11:	Schematic illustration of the concept of fictitious tensile specimens to simulate crack propagation with consideration of a local interaction for hydrogen assisted stress corrosion cracking ^[HAS 108]	88
Figure 3-12:	Flow chart for numerical modelling of hydrogen assisted cracking in a standard test specimen.....	89
Figure 3-13:	Subsurface concentration and diffusion coefficients of supermartensitic stainless steel in the as-delivered and the as-quenched with respect to various levels of the H ₂ S saturation in the NACE electrolytic solution at room temperature ^[HPD 21]	90
Figure 3-14:	Critical hydrogen concentration dependent on the true fracture strain of supermartensitic stainless steel: a) As-delivered state, b) As-quenched state ^[SPM 33]	92
Figure 3-15:	Significant material properties dependent on temperature for numerical modelling in temperature analysis: a) Specific density, b) Heat convection coefficient, c) Specific heat capacity, d) Thermal conductivity.....	93
Figure 3-16:	Stress-strain relationship of supermartensitic stainless steel as material property for numerical modelling in structural analysis: a) Experimental investigation at room temperature ^[GEN 19] , b) Modified values dependent on temperature for the base metal, c) Modified values dependent on temperature for the heat affected zone, d) Modified values dependent on temperature for the weld metal.....	94
Figure 3-17:	Material properties of supermartensitic stainless steel as a function of temperature: a) Thermal expansion coefficient, b) Poisson's ratio ^[GEN 31]	95
Figure 3-18:	Scatterband of hydrogen diffusion coefficients in steels having austenitic decomposition microstructure and in supermartensitic stainless steel as a function of temperature used for numerical modelling ^[HPD 69]	96
Figure 3-19:	Dimensions of supermartensitic stainless steel pipeline orbitally welded with four layers of matching filler wires materials.....	98

List of Figures

Figure 3-20:	Schematic illustration of boundary conditions for testing hydrogen assisted stress corrosion cracking in the orbitally welded pipeline.....	99
Figure 3-21:	Flow chart for modelling HASCC in the welded pipeline with three predefined cracking paths in the welded metal, the heat affected zone and the base metal.	100
Figure 3-22:	Overview of major effects on the behaviour of hydrogen assisted cold cracking in welded components.	101
Figure 3-23:	Schematic illustration of hydrogen diffusion and effusion reactions influencing the local hydrogen concentration in welded components.....	102
Figure 3-24:	Flow chart of numerical modelling of hydrogen assisted cold cracking in the orbitally welded supermartensitic stainless steel pipeline.	104
Figure 4-1:	Crack propagation and hydrogen distribution profile of hydrogen assisted stress corrosion cracking of supermartensitic stainless steel in the as-delivered state (Assumption: $\dot{\epsilon}'_{glob} = 1.0E-06 \text{ s}^{-1}$, $D = 3.7E-06 \text{ mm}^2 \cdot \text{s}^{-1}$, $HD_{ss} = 50.00 \text{ ml} \cdot (100\text{gFe})^{-1}$, K-factor = 5).	108
Figure 4-2:	Crack length versus time of the standard test specimen subjected to global constant strain rates in the range of $1.0E-04$ to $1.0E-07 \text{ s}^{-1}$ with respect to different levels of hydrogen subsurface concentration.	110
Figure 4-3:	Calculated time to failure of supermartensitic stainless steel dependent on the levels of H_2S saturation in the electrolytic NACE solution at various local strain rates.	112
Figure 4-4:	Calculated time to failure of supermartensitic stainless steel dependent on the local strain rates with respect to various levels of hydrogen subsurface concentrations based on the NACE standard test procedure.....	112
Figure 4-5:	Crack length versus time of as-delivered supermartensitic stainless steel with a assumption of higher and lower orders of magnitude for hydrogen diffusion coefficient from the average value (g: global, h: hydrogen subsurface concentration and d: hydrogen diffusion coefficient).	113
Figure 4-6:	Effects of various hydrogen diffusion coefficients with respect to local strain rates on the characteristics of crack propagation: a) $HD_{ss} = 20 \text{ ml} \cdot (100\text{gFe})^{-1}$, b) $HD_{ss} = 60 \text{ ml} \cdot (100\text{gFe})^{-1}$	114
Figure 4-7:	Crack length versus time of supermartensitic stainless steel in the as-delivered state taking account of the scatter effect of hydrogen diffusion coefficients at higher and lower orders of magnitude from the average value, $3.7E-06 \text{ mm}^2 \cdot \text{s}^{-1}$, (G: global, H: hydrogen subsurface concentration, D: hydrogen diffusion coefficient).	115
Figure 4-8:	Calculated time to failure of as-delivered supermartensitic stainless steel as a function of local strain rates with respect to effects of	

	hydrogen diffusion coefficients and hydrogen subsurface concentrations.....	116
Figure 4-9:	Calculated crack length versus time of supermartensitic stainless steel based on the NACE standard test method with various rates of the global strain rate, i.e. $1.0E-04 \text{ s}^{-1}$, $1.0E-05 \text{ s}^{-1}$, $1.0E-06 \text{ s}^{-1}$ and $1.0E-07 \text{ s}^{-1}$, (Assumption: $HD_{ss} = 50 \text{ ml} \cdot (100\text{gFe})^{-1}$, $D = 3.7E-06 \text{ mm}^2 \cdot \text{s}^{-1}$).....	117
Figure 4-10:	Calculated time to failure of as-delivered supermartensitic stainless steel taking account of the effects of K-factor (Assumption: $HD_{ss} = 50 \text{ ml} \cdot (100\text{gFe})^{-1}$, $\epsilon'_{glob} = 1.0E-06 \text{ s}^{-1}$, $D = 3.7E-06 \text{ mm}^2 \cdot \text{s}^{-1}$).....	118
Figure 4-11:	Crack propagation and hydrogen distribution profile of hydrogen assisted stress corrosion cracking of supermartensitic stainless steel in the quenched state (Assumption: $\epsilon'_{glob} = 1.0E-06 \text{ s}^{-1}$, $D = 1.8E-05 \text{ mm}^2 \cdot \text{s}^{-1}$, $HD_{ss} = 6.7 \text{ ml} \cdot (100\text{gFe})^{-1}$, K-factor = 5).....	119
Figure 4-12:	Calculated crack length versus time of supermartensitic stainless steel in the as-quenched state subjected to various global constant strain rates with respect to different levels of hydrogen subsurface concentration at a constant K-factor of 1.	121
Figure 4-13:	Calculated crack length versus time of supermartensitic stainless steel in the as-delivered state and the as-quenched state exposed to various levels of H_2S -saturation in the NACE electrolytic solution (Assumption: $\epsilon'_{glob} = 1.0E-06 \text{ s}^{-1}$, K-factor = 5).	121
Figure 4-14:	Influence of different states of supermartensitic stainless steel on the time to failure of the standard test specimen subjected to local strain rates and exposed to the NACE solution with H_2S saturations in the range of 1 to 100 %.....	122
Figure 4-15:	Crack propagation and hydrogen distribution profile for hydrogen assisted stress corrosion cracking of supermartensitic stainless steel in the delivered state (Assumption: $\epsilon'_{glob} = 1.0E-06 \text{ s}^{-1}$, $D = 3.7E-06 \text{ mm}^2 \cdot \text{s}^{-1}$, $HD_{ss} = 50 \text{ ml} \cdot (100\text{gFe})^{-1}$, K-factor = 5, crack angle = 74°).	123
Figure 4-16:	Crack length versus time of supermartensitic stainless steel in the as-delivered state subjected to global constant strain rates in the range of $1.0E-04$ to $1.0E-07 \text{ s}^{-1}$ with respect to different levels of hydrogen subsurface concentrations based on the NACE standard test method with assumption of a crack tip angle of 74°	124
Figure 4-17:	Crack length versus time of supermartensitic stainless steel in the delivered state in comparison between crack tip angles of 180° and 74° with respect to different levels of hydrogen subsurface concentration (Assumption: $\epsilon'_{glob} = 1.0E-06 \text{ s}^{-1}$, K-factor = 5).	125

List of Figures

Figure 4-18: Comparison between calculated time to failure dependent on local strain rates of the blunt crack tip (180°) and that of the sharp crack tip (74°) taking account of various levels of hydrogen subsurface concentrations.....	126
Figure 4-19: Calculated crack length versus time for three significant different zones in orbitally welded supermartensitic stainless steel pipelines exposed to NACE electrolytic solution with 1% H ₂ S saturation at a constant global strain rate of 1.0E-06 s ⁻¹	127
Figure 4-20: Simulated crack propagation in the base metal, heat affected zone and weld metal of orbitally welded pipelines during exposure to NACE standard solution with 1% H ₂ S saturation at a constant global strain rate of 1.0E-06 s ⁻¹	128
Figure 4-21: Local hydrogen concentration and local strain distribution at the crack tip in the base metal obtained from the simulated orbital component weld test.....	129
Figure 4-22: Local hydrogen concentration and local strain distribution at the crack tip in the affected zone obtained from the simulated orbital component weld test.....	129
Figure 4-23: Local hydrogen concentration and local strain distribution ahead of the crack tip in the weld metal obtained from the simulated orbital component weld test.....	129
Figure 4-24: Calculated time to failure dependent on the H ₂ S saturation of the orbitally welded supermartensitic stainless steel pipe exposed to NACE electrolytic solution.....	130
Figure 4-25: Calculated time to failure dependent on the local strain rate of the orbitally welded supermartensitic stainless steel pipe exposed to NACE electrolytic solution.....	130
Figure 4-26: Calculated time to failure of the orbitally welded pipe with respect to local strain rates and H ₂ S saturations in the NACE standard solution.	131
Figure 4-27: Circumferential stress distribution measured by strain gages in the near field at a restraint intensity of 0.45 kN·(mm·mm) ⁻¹ [SPM 56].....	132
Figure 4-28: Simulated crack propagation in the base metal, heat affected zone and weld metal of orbitally welded supermartensitic stainless steel pipeline exposed to 1% H ₂ S saturated NACE electrolytic solution at the load history applied to the component weld test.....	133
Figure 4-29: Crack length versus time of three significant different cracks in orbitally welded supermartensitic stainless steel pipeline at the load history of the component weld test.....	134
Figure 4-30: Cracked features taking place in the welded pipe during HASCC testing.....	134

Figure 4-31: Local hydrogen concentration and local strain distribution at the crack tip in the heat affected zone obtained from the numerical modelling with the adopted condition of load history.	135
Figure 4-32: Simulation of temperature distribution during orbital welding of supermartensitic stainless steel pipeline with four layers of matching filler material.....	137
Figure 4-33: Calculated temperature distribution at a distance of 25 mm from the weld bead centerline of supermartensitic stainless steel orbitally welded with four layers in comparison with the measured values.....	137
Figure 4-34: Calculated temperature distribution dependent on time captured from the middle point of each layer in the weld metal during welding and subsequent cooling.	139
Figure 4-35: Calculated temperature distribution captured at the specific points on the interface between the heat affected zone and base metal: a) Inside of the pipeline, b) Outside of the pipeline.	139
Figure 4-36: Simulation of equivalent strain distribution at the specific interpass temperature of each layer of the four-layer orbitally welded supermartensitic stainless steel pipeline.	141
Figure 4-37: Calculated equivalent strain distribution dependent on the running time of supermartensitic stainless steel orbitally joined by four layers of matching filler wires.	141
Figure 4-38: Simulation of equivalent stress distribution at the specific interpass temperature of each layer of the orbitally four-layer welded supermartensitic stainless steel pipeline.	142
Figure 4-39: Calculated equivalent stress distribution dependent on the running time of supermartensitic stainless steel pipelines orbitally joined by four layers of matching filler wires.	142
Figure 4-40: Hydrogen distribution in girth welds of supermartensitic stainless steel during welding and subsequent cooling with four layers of matching filler wires (Assumption: $HD = 10.00 \text{ ml} \cdot (100\text{gFe})^{-1}$ picked up during welding).	144
Figure 4-41: Calculated local hydrogen distribution dependent on time at the specific point in each welded layer during welding and subsequent cooling to conform to the specific thermal conditions for the pipeline girth welds (Assumption: $HD = 10.00 \text{ ml} \cdot (100\text{gFe})^{-1}$ picked up during welding).	147
Figure 4-42: Calculated local hydrogen concentration in the heat affected zone, 0.2 mm away from the fusion line, for each welding layer (Assumption: $HD = 10.00 \text{ ml} \cdot (100\text{gFe})^{-1}$ picked up during welding).	149

List of Figures

Figure 4-43: Reduction of the maximum hydrogen concentration, dependent on initial hydrogen concentration picked up during welding, in the upper third of the weld with increasing exposure time to ambient environments after completion of welding and cooling to room temperature of the last layer. 149

Figure 4-44: Simulation of hydrogen concentration profile and crack propagation for hydrogen assisted cold cracking in the weld metal of orbitally welded pipeline during cooling to room temperature (Assumption: $HD = 15.00 \text{ ml} \cdot (100\text{gFe})^{-1}$ picked up during welding). 150

Figure 4-45: Calculated hydrogen distribution, strain distribution and temperature distribution dependent on time at the specific points in the first layer and the third layer during the cooling process after orbital welding of the last layer of pipeline. 152

Figure 4-46: Schematic illustration of additionally applied heat on the surface of the orbitally welded supermartensitic stainless steel pipeline for post weld heat treatment. 153

Figure 4-47: Reduction of hydrogen concentration in the weld metal dependent on the tempering duration by long-term approach taking account of the effects of hydrogen concentration picked up during welding. 153

Figure 4-48: Effects of the tempering duration in the long-term approach on the reduction of weld metal hydrogen concentration with respect to various levels of hydrogen concentration picked up during welding. 154

Figure 4-49: Calculated local hydrogen concentration dependent on two major factors of post weld heat treatment by an assumption of different hydrogen concentration picked up by the weld metal during welding: a) $HD_{ini} = 5.00 \text{ ml} \cdot (100\text{gFe})^{-1}$, b) $HD_{ini} = 15.00 \text{ ml} \cdot (100\text{gFe})^{-1}$ 155

Figure 4-50: Calculated local hydrogen concentration as a function of the tempering duration for various temperature levels. 156

Figure 4-51: Calculation of normalised hydrogen concentrations as a function of tempering duration at various temperatures. 158

Figure 4-52: Calculated remaining hydrogen concentration at different temperature levels dependent on the tempering duration with respect to different levels of initial hydrogen concentration picked up by the weld metal during welding. 158

Figure 4-53: Effects of the tempering temperature for different tempering durations on the reduction of the local hydrogen concentration in the weld metal with respect to various levels of initial hydrogen concentration. 159

Figure 4-54: Calculation of local hydrogen concentration in the weld metal dependent on two major factors of short-term post weld heat treatment (Assumption: $HD = 15.00 \text{ ml} \cdot (100\text{gFe})^{-1}$ picked up during welding). 159

Figure 4-55: Effects of the long-term approach on the reduction of local hydrogen concentration in comparison with the short-term approach (Assumption: hydrogen concentration of $10 \text{ ml} \cdot (100\text{gFe})^{-1}$ picked up by the weld metal during welding).....	160
Figure 4-56: Simulation of hydrogen distribution in the orbitally welded supermartensitic stainless steel pipeline exposed to NACE electrolytic solution with 1% H_2S saturation after complete welding and subsequent cooling to room temperature with additionally extended time of 5 hours in ambient environments (Assumption: $\text{HD} = 10.00 \text{ ml} \cdot (100\text{gFe})^{-1}$ picked up during welding).....	161
Figure 4-57: Simulation of the influence of hydrogen assisted cold cracking on the lifetime of orbitally welded supermartensitic stainless steel pipeline during exposure to NACE standard solution with 100% H_2S saturation for hydrogen assisted stress corrosion cracking.	162
Figure 5-1: Development of a FE model for modelling hydrogen assisted cracking in a latest generation of duplex stainless steels.	169
Figure 5-2: Sequences of numerical modelling of hydrogen assisted cracking in duplex stainless steel compared with experimental investigation.	170

1 INTRODUCTION

Fitness for Purpose represents the key issue motivating the replacement of plain carbon steels and of duplex stainless steels by a new generation of supermartensitic stainless steels in offshore technology, particularly in the North Sea oil and gas fields. Supermartensitic stainless steels (SMSS) offer a number of advantages compared to conventional steels, such as a strength-to-weight ratio equal to that of high-strength low alloy steels at an enhanced corrosion resistance, good weldability as well as relatively low effective costs^[SPM 47].

This new generation of steels has been developed during the last two decades based on conventional martensitic stainless steels by modifying the chemical composition, i.e. keeping the carbon content below 0.02 wt.-% to improve weldability of the materials and increasing the nickel content up to 6.5 wt.-% and the molybdenum content up to 2.5 wt.-% to enhance corrosion resistance and mechanical properties. The matrix microstructure of soft martensite is obtained during complete steel production processes, including various heat treatment.

Until recently, supermartensitic stainless steels are predominantly applied to subsea flowlines. Through such flowlines, unprocessed oil and gas products are typically at sour service conditions, providing a potential risk of hydrogen and subsequent material degradation. To the extent that supermartensitic stainless steel might be used in such environments, it is a key question in offshore industrial research and development. The most important task to be investigated is the resistance of such materials against hydrogen assisted cracking (HAC).

In general, hydrogen assisted cracking can be categorised into hydrogen assisted stress corrosion cracking (HAC) and hydrogen assisted cold cracking (HACC), depending on the different hydrogen sources.

The resistance of supermartensitic stainless steel against hydrogen assisted stress corrosion cracking has extensively studied, usually using small scaled standard test specimens and exposing to standard test solutions.

Whereas the supermartensitic stainless steel pipelines are usually welded, special attention has recently been paid to microstructure transformations caused by thermal cycle effects in the weld metal and the heat affected zone (HAZ). Lifetime prediction of welded components is most significant for numerous applications in oil and gas industry, since serious problems, e.g. additional cost and environmental impact, might arise from in-service failure of flowlines.

Lifetime prediction of welded components is the most significant for numerous applications in oil and gas industry, since serious problems, e.g. additional cost and environmental impact, might arise from in-service failure of flowlines. It turned out that lifetime prediction of orbitally welded supermartensitic stainless pipelines taking account of real service of subsea flowlines can best be performed by adoption of conclusive test sequences and full scale test (Figure 1-1).

As a consequence of recent failure cases, hydrogen assisted cold cracking has to be regarded as a matter of prime concern in supermartensitic stainless steel flowline

1. Introduction

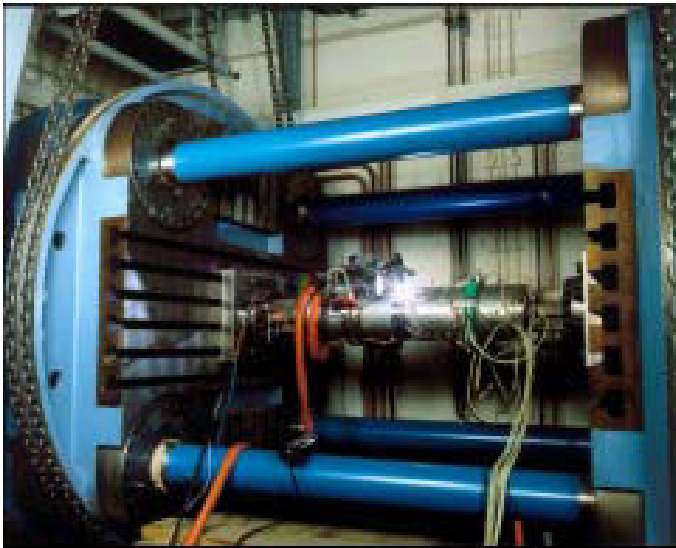


Figure 1-1: The full scale test facility for performance of welding test and stress corrosion cracking test on girth welds of supermartensitic stainless steel pipelines.

fabrication. Hydrogen might be provided by moisture or by non-hydrogen free base and filler materials and can be absorbed in the weld metal during arc welding. It can only be emphasised that it is impossible to avoid stress-strain build-up caused by thermal contraction resulting from welding thermal cycle as well as from the restraint intensity given by design of surrounding structure^[GEN 17]. Additionally, welded flowlines are largely strained during reeling and de-reeling as well as during pipeline laying operations.

Recently, post weld heat treatment procedures are under strong discussion to reduce the hydrogen levels in the welds. However, similar to hydrogen assisted stress corrosion cracking, also hydrogen assisted cold cracking has been tested up to the present predominantly by small scaled technological and particularly non-realistic procedures with respect to restraint and strong intensities, although specific procedures have been developed to transfer the real conditions to the laboratory and vice versa. To sum it up, both hydrogen assisted stress corrosion cracking and hydrogen assisted cold cracking have to be investigated by conclusive test sequences. Such test sequences have to be accompanied by numerical methods.

Since testing of real welded components is much more complicated and also requires a lot of resources, e.g. preparation time, operation cost, etc., such numerical modelling as a tool for the lifetime prediction is an alternative, which has been developed based on a commercial finite element programme. Additionally, various parameters can be studied by numerical modelling in order to gain a better understanding of the characteristics and mechanisms of hydrogen assisted stress corrosion cracking in welded pipelines with less consumption of time and resources in comparison with the realistic test.

Although the exact mechanism of hydrogen assisted cold cracking is still in question, it can simply be deduced that hydrogen assisted cold cracking will take place in sensitive regions of welded components if the following conditions are simultaneously encountered:

- I. Presence of a sufficiently high local concentration of hydrogen picked up during welding,
- II. Introduction of a local stress-strain distribution caused by unavoidable thermal contraction and global conditions of restraint intensity,
- III. Presence of susceptible microstructure with low ductility caused by subsequent rapid cooling, and
- IV. Inclination of the welded component's temperature to near room temperature during cooling.

The motivation for the present thesis is to further develop an existing model for simulation of hydrogen assisted cracking, so that the new model can be applied for simulation of both hydrogen assisted stress corrosion cracking and hydrogen assisted cold cracking at welded supermartensitic stainless steel pipelines. The purpose of this thesis is to provide the basics for numerical lifetime evaluations of such components.

2 LITERATURE REVIEWS

The supermartensitic stainless steels have also been taken as a reference material to study the characteristics of hydrogen assisted cracking, i.e. hydrogen assisted stress corrosion cracking and hydrogen assisted cold cracking, because they have a more or less homogeneous microstructure which allows easier using numerical finite element simulation. Nevertheless, these types of steels bear a number of additional characteristics to be modelled, and thus it is first necessary get a better understanding of the metallurgical behaviour of these steels.

There have been proposed numerous contrary mechanisms for hydrogen assisted cracking phenomena in literature. The common mechanisms are also reviewed in this chapter because particularly in the recent years new basic understandings of such phenomena have been gained. But still, hydrogen assisted cracking cannot be explained by reference to any of these mechanisms and there is more and more evidence coming up that the interactions between hydrogen and mechanical loads promote crack initiation and propagation^{[HAS 86],[HAS 99]}.

Numerical modelling of hydrogen assisted cracking is based on simulation of diffusion and thus, the basic diffusion theories are also reviewed in this section. Finally, the literature related to the two major groups of hydrogen-assisted cracking is summarised with a special emphasis on modelling such phenomena.

2.1 Supermartensitic Stainless Steels

The new generation of supermartensitic stainless steels has been developed in the last two decades based on so-called soft martensitic and on traditional martensitic stainless steels, for example AISI 410. As a result of improved steel production technology, carbon content can be decreased to the range of 0.01 to 0.02 wt.-%, whereas molybdenum content in the range of 2.0 to 4.0 wt.-% is used in order to improve corrosion resistance and mechanical properties of this steel^{[SPM 37],[SPM 47]}.

Since chromium with a content in the range of 11 to 14 wt.-% and nickel with a content in the range of 4 to 6 wt.-% are the major alloying elements of supermartensitic stainless steels, microstructure formation in equilibrium state can be described dependent on the major alloying element by binary iron-chromium equilibrium phase diagrams as represented in Figure 2-1a. This indicates that above a level of approximately 12 wt.-% Cr, binary alloys will not form austenite at any temperature, they cannot be hardened by heating and subsequent cooling. Increasing the chromium content can extend the α -region which will transform into the α' -phase if the steel temperature with a chromium content above 50 wt.-% falls below 600°C. It has to be mentioned, however, that due to the nickel content supermartensitic stainless steel still can be hardened. Figure 2-1a also clearly demonstrates that the σ -phase can be formed from a chromium content between 40 wt.-% and 50 wt.-% at temperatures in the range of 475°C to 820°C. For the second major alloying element, Figure 2-1b represents the binary iron-nickel equilibrium diagram indicating the effect of an austenite stabiliser. The γ -region is extended by increasing the nickel content even though the α -ferrite phase extends to about 6 wt.-% Ni.

2. Literature Reviews

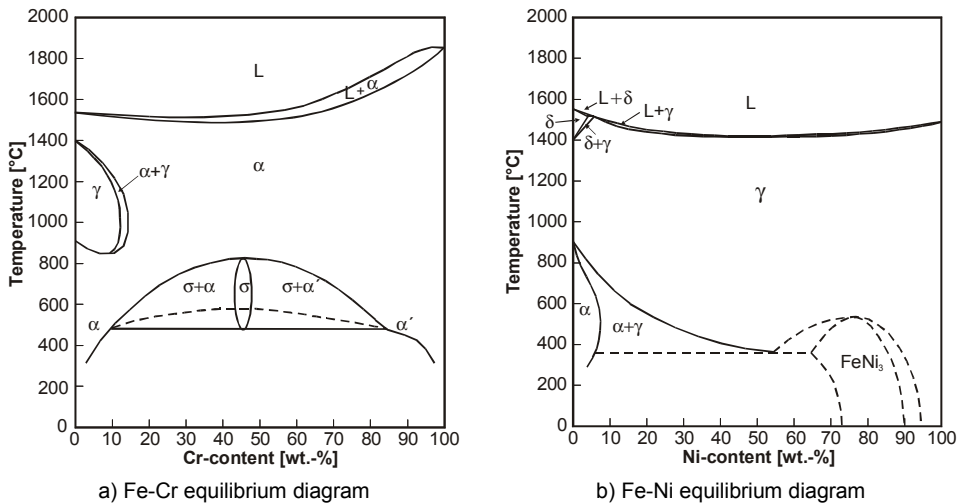


Figure 2-1: Effects of major alloying elements on microstructure formation of conventional stainless steel^[GEN 24].

Considering to these two diagrams, the prediction of microstructure formation of supermartensitic stainless steel experiencing arc welding operation for flowline fabrication in the offshore technology can be performed using constitution diagrams as represented by the corrected WRC-92 diagram in Figure 2-2.

Such diagrams propose a relationship between alloying elements that influentially promote the formation of ferrite, i.e. chromium equivalent, and elements that influentially promote the formation of austenite, i.e. nickel equivalent. Using such diagrams, calculation is carried out for both the chromium and the nickel equivalents from the chemical compositions of the weld metal and neighbouring zones. Subsequently, an estimation of microstructure can be illustrated by plotting the calculated chromium and nickel equivalents in the diagram.

A chromium equivalent in the range of 13.8 and a nickel equivalent in the range of 5.5 are typically obtained for supermartensitic stainless base materials (see Figure 2-2) and are located nearby the interface between the martensite and the ferrite region in the dual zone of martensite-ferrite (M+F). By using matching filler material, complete martensite occurs in the weld metal due to the chemical compositions provided by the chromium equivalent in the range of 14.6 and nickel equivalent in the range of 7.9.

2.1.1 Base Material and Weld Microstructures

Microstructure formation is dependent on constitutional alloying elements of supermartensitic stainless steel described as a main physical property in this paragraph. Table 2-1 lists main alloying elements of supermartensitic stainless steel pipeline and matching filler material employed as the reference materials for the present research.

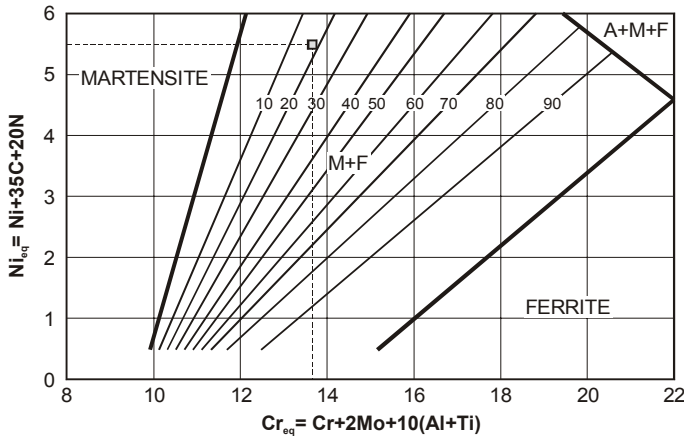


Figure 2-2: WRC 92 constitution diagram for stainless steels influenced by alloying elements of austenite stabiliser and of ferrite stabiliser ^[GEN 13].

Table 2-1: Chemical composition of supermartensitic stainless steel pipeline and matching filler material.

Materials	Composition [wt.-%]						
	C	Cr	Ni	Mo	Mn	S+P	N
Base metal	0.015	12.35	4.48	1.41	1.11	0.026	0.013
Filler wire	0.013	11.78	6.16	2.78	0.61	0.006	0.085

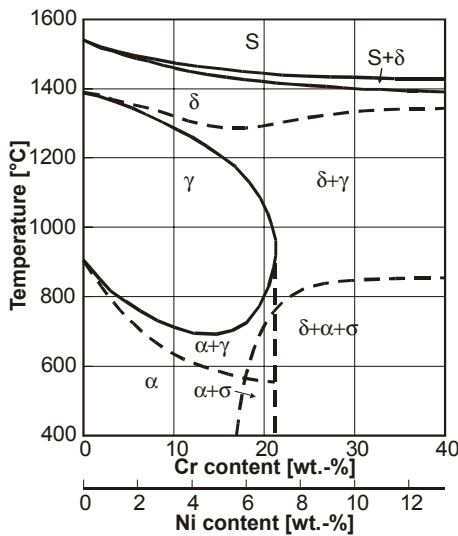
The vertical transverse section of the equilibrium microstructure dependent on temperature for the chromium-nickel system of 3:1 is represented in Figure 2-3a. Delta ferrite is always present as a primary phase in the solidification process by forming a dendrite core with the pure Fe-Cr phase.

As reported by Gooch^[SPM 47] based on the principle of austenite-martensite transformation of 12.0 wt.-% Cr and at least 3.0 wt.-% Ni with respect to low carbon (< 0.05 wt.-%), formation of lath-type soft martensite will be obtained at room temperature, which offers a combination of excellent toughness with high strength and good ductility. However, those material properties can drastically be decreased when some α -ferrite phases develop in the martensitic matrix. Thus, estimation of the amount of undesired α -ferrite formation at room temperature in supermartensitic stainless steel should be carried out based on chemical compositions by using the following equation known as Kaltenhauser ferrite factor^[SPM 47].

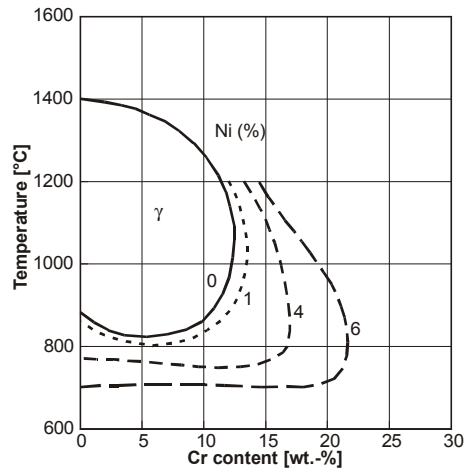
$$FF = Cr + 6Si + 8Ti + 4Mo + 2Al + 4Nb - 2Mn - 4Ni - 40(C + N) \quad (2-1)$$

This formula indicates the effects of alloying elements for promoting ferrite formation as well as for promoting martensite by forming austenite prior to phenomena of phase transformation. The ferrite factor can be decreased by increasing austenite stabilising elements such as manganese, nickel, carbon and nitrogen in order to enhance the austenite-martensite transformation. However, during TIG welding of supermartensitic stainless steel pipeline, a ferrite phase frequently appears at room temperature, in particular at the fusion line.

2. Literature Reviews



a) Equilibrium diagram of 3:1 system



b) Extent of γ -loop affected by increased Ni

Figure 2-3: Graphical illustration of the equilibrium constitution diagram showing microstructure formation of martensitic stainless steels in system 3:1 (Cr:Ni)^[GEN 24].

A duplex-microstructure region will appear in these diagrams if the chromium content exceeds approximately 21 wt.-%, which will subsequently transform into the dual phase, i.e. martensite + α -ferrite, during cooling to room temperature. From this diagram, it can be assumed that complete formation of martensite without the presence of ferrite might be required to avoid brittle microstructures by a decrease in the ductile transition temperature of the steel^[GEN 24].

However, at a chromium content of around 12 wt.-% formation of a duplex structure before directly transforming the microstructure into martensite under practical cooling conditions is not being anticipated from this diagram^[SPM 35]. Thus, as previously described, the formation of γ -region is significantly dependent on the austenite stabiliser nickel ranging between 4 and 6 wt.-%. Known to previously form austenite before cooling to room temperature, the effects of the nickel content on the γ -loop formation in the iron-chromium equilibrium system is presented in Figure 2-3b. The γ -region is extended by expanding its nose as well as by decreasing the temperature of austenite formation. It should be noted that increasing the nickel content up to 1.0 wt.-% will not significantly influence the extent of the γ -region compared to 4.0 wt.-% and 6.0 wt.-% Ni. Nickel represented a very effective alloying element for expanding the γ -loop rather than other austenite stabilisers, because it does not increase the hardness of the final martensitic microstructure^[GEN 24].

Also, the carbon and the nitrogen content have significant potential to decrease a tendency of the α -ferrite formation by expanding the γ -region, which subsequently transforms to martensite. The equilibrium phase diagram considering the effects of the carbon content is represented in Figure 2-4. Increasing the carbon content from 0.01 wt.-% to 0.05 wt.-% can enlarge the γ -region and also the duplex region, i.e. the δ -ferrite phase + γ -phase.

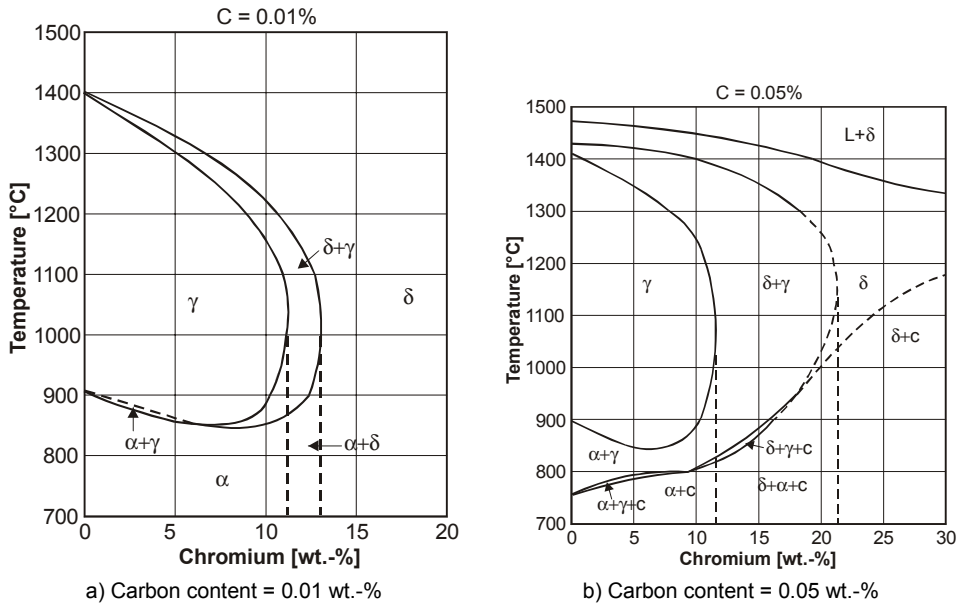


Figure 2-4: Region of γ , δ and α -phase in the iron-chromium constitution diagram^[SPM 47].

However, the carbon content in supermartensitic stainless steel, must strongly be limited to the range of 0.01 to 0.02 wt.-% in order to improve weldability and toughness properties while the γ -region should be large enough to form martensite during the subsequent cooling process^{[SPM 37],[SPM 46]}. Again, increasing the nickel content (to approximately 4.0 wt.-% to 6.0 wt.-%) represents a better procedure to achieve sufficient toughness of supermartensitic stainless steels at low carbon contents^[SPM 39]. In the estimation of the ferrite using Equation (2-1), a ferrite factor of close to zero is obtained for the supermartensitic stainless steel pipeline and the matching filler material with chemical compositions listed in Table 2-1. Due to the high nickel content, it has to be anticipated that also retained austenite will be present at room temperature. As an additional point, it has to be considered that during annealing treatment, as for instance during steel processing, but also during post weld heat treatment annealing, austenite may be formed^[SPM 39]. It has to be understood how these austenite fractions might contribute to the mechanical properties and to hydrogen diffusion.

Molybdenum with a content of up to 2.0 wt.-% or more has been taken into account as an additional alloying element for supermartensitic stainless steel in order to suppress a tendency of carbide precipitation during cooling after completed welding and to improve mechanical properties as well as corrosion resistance.

Depending on the amount of alloying elements, supermartensitic stainless steels are categorised into three major groups, i.e. lean supermartensitic stainless steels with 11%Cr-2%Ni, medium supermartensitic stainless steels with 12%Cr-4.5%Ni-1.5Mo, and high supermartensitic stainless steels with 12%Cr-6.5%Ni-2.5%Mo^{[SPM 39],[SPM 46],[SPM 47]}. The basic behaviour of significant alloying elements to be known for a better understanding of their effects on the material properties is listed in Table 2-2.

2. Literature Reviews

Table 2-2: Effects of alloying elements on material properties of supermartensitic stainless steel.

Element	Microstructure formation	Mechanical property	Corrosion resistance
Carbon (C)	<ul style="list-style-type: none"> - Decreasing δ-ferrite phase - No effects on A_{C1}-temperature - Depressing M_s-temperature (strongest) - Expanding γ-region - Increasing tendency of carbide formation - Strong austenite stabiliser 	<ul style="list-style-type: none"> - Increasing a tensile strength - Decreasing toughness - Increasing hardness 	<ul style="list-style-type: none"> - Decreasing HASCC-resistance - Decreasing general corrosion resistance
Chromium (Cr)	<ul style="list-style-type: none"> - Promoting δ-ferrite phase - Retarding ferrite and pearlite transformation - Depressing M_s-temperature - Strong ferrite stabiliser - Increasing α-ferrite 	<ul style="list-style-type: none"> - Increasing tensile properties - Increasing tempering resistance of martensite 	<ul style="list-style-type: none"> - Improving general corrosion resistance - Decreasing HASCC-resistance by forming carbide
Nickel (Ni)	<ul style="list-style-type: none"> - Decreasing δ-ferrite phase - Depressing A_{C1}-temperature - Depressing M_s-temperature - Assisting transformation to martensite - Expanding γ-region(austenite stabiliser) 	<ul style="list-style-type: none"> - Improving toughness - Increasing tempering resistance 	<ul style="list-style-type: none"> - Improving general corrosion resistance - Improving HASCC-resistance
Molybdenum (Mo)	<ul style="list-style-type: none"> - Promoting δ-ferrite phase - Increasing A_{C1}-temperature - Depressing M_s-temperature - Ferrite stabilise 	<ul style="list-style-type: none"> - Decreasing second phase formation - Increasing tensile strength - Improving toughness 	<ul style="list-style-type: none"> - Improving HASCC-resistance
Manganese (Mn)	<ul style="list-style-type: none"> - Decreasing δ-ferrite phase - Depressing A_{C1}-temperature - Depressing M_s-temperature - Expanding γ-region - Decreasing A_{C3}-temperature 	<ul style="list-style-type: none"> - Increasing tensile properties - Improving toughness - Increasing tempering resistance 	<ul style="list-style-type: none"> - Improving HASCC-resistance
Copper (Cu)	<ul style="list-style-type: none"> - Decreasing δ-ferrite phase - Austenite stabiliser 	<ul style="list-style-type: none"> - Improving toughness - Enhancing the secondary hardening reaction 	<ul style="list-style-type: none"> - Improving HASCC-resistance

2.1.1.1 Martensite Formation

As outlined above, extending the γ -region by increasing the nickel content in supermartensitic stainless steels is necessary for austenite-martensite transformation. Recently, matching filler wires are considered to be used for orbital welding of supermartensitic stainless steel pipeline in order to avoid triplex austenitic, ferritic and martensitic microstructure, in particular in the HAZ.

Estimation of martensite formation can simply be explained in terms of the M_s -temperature based on the chemical compositions, in particular for 13 wt.-% Cr stainless steels as follows^[SPM 27]:

$$M_s(^{\circ}C) = 300 - 474C - 33Mn - 17Ni - 17(Cr - 12) - 21Mo - 11W - 11Si \quad (2-2)$$

Table 2-3: Typical transformation temperature of general categories of supermartensitic stainless steels^[SPM 39].

Transformation temperature [°C]	Lean	Medium	High
M _s	360	250	150
M _f	220	120	30
A _{C1}	650	640	630

and for stainless steels with 10-18 wt.-%Cr and 0 – 7 wt.-% Ni is given by^[SPM 27]:

$$M_s(^{\circ}C) = 540 - 497C - 6.3Mn - 36.3Ni - 10.8Cr - 46.6Mo \quad (2-3)$$

The prediction of the M_s-temperature may be erroneously in the range of approximately ±30°C because of the simple order form of the equation^[SPM 27]. Additionally, it is possible that rapid cooling and higher peak temperature in the austenitic range can influence the depression of the M_s-temperature in supermartensitic stainless steels. By using Equation (2-2), M_s-temperatures of 145°C and 155°C are obtained for the supermartensitic stainless steel as base metal and matching filler material.

But, these M_s-temperatures will change if the estimation is carried out with Equation (2-3). In this case, M_s-temperatures of 164°C and 110°C are obtained, for instance, for supermartensitic stainless steel as base metal and matching filler material, respectively. A decrease of M_s-temperatures of supermartensitic stainless steel implies that the amount of retained austenite during cooling to room temperature in the welded component can be increased. These retained austenitic phases have been found to be inter-phase hydrogen trapping sites having relative low binding energy. Hence, hydrogen assisted cracking may take place in the most susceptible martensitic phases resulting from high hydrogen concentration in the retained austenitic phases diffusing into the neighbouring martensite under changing service conditions^[HAS 39]. It is well known that dual-phase (austenite+martensite) formation will result in a reduction of weld metal tensile strength.

In heat treatment technology, low M_s-temperature of supermartensitic stainless steels means that few auto-tempering phenomena might appear in the neighbouring zone of the weld metal during deposition of a single run. The hardness of the as-welded component can therefore be directly related to the carbon content of the material^[SPM 27]. Irvine et al.^[SPM 35] worked on 12 wt.-% Cr steels, where a reduction of the local chromium content resulted from the precipitation of chromium carbides at grain boundaries, which can increase the M_s-temperature and create plates of auto-tempered martensite adjacent to the boundary carbides. Irvine also explained that it is necessary to maintain the matrix microstructure of supermartensitic stainless steel with as few α-ferrite phase as possible in order to improve the mechanical properties. Furthermore, depression of the A_{C1}-temperature to below 700°C and of M_s-temperatures to below 200°C should be avoided. Low A_{C1}-temperature will influence the re-austenitisation temperature, which can suddenly increase the material's hardness if austenite is repeatedly reformed^[SPM 35].

M_r-temperature estimations reported by Haynes^[SPM 52] for a new generation of martensitic stainless steels approximately range between 80°C and 140°C below the M_s-temperature. It is also possible for some grades of martensitic stainless steel with high

2. Literature Reviews

Table 2-4: Typical second-phase constituents observed in stainless steels^[GEN 13].

Phase	Crystal structure	Lattice parameters, nm	Compositions	Comments
M ₂₃ C ₆	fcc	a ₀ =1.057-1.068	(Cr ₁₆ Fe ₅ Mo ₂)C ₆ (Cr ₁₇ Fe _{4.5} Mo _{1.5})C ₆ (Fe,Cr) ₂₃ C ₆	Observed carbide in austenitic stainless steels. Precipitates from 500-950°C, fastest 650-700°C
M ₆ C	fcc	a ₀ =1.085-1.111	(Cr,Co,Mo,Ni) ₆ C (Fe ₃ Mo ₃)C	Observed in austenitic grades containing substantial molybdenum or niobium after long time exposure
M ₇ C ₆	Hexagonal	a ₀ =1.398 c ₀ =0.4523	Cr ₇ C ₃	Observed in martensitic grades
MC	Cubic	a ₀ =0.430-0.470	TiC NbC	Observed in alloys with additions of titanium or niobium. Very stable carbide. Will usually contain some nitrogen
Sigma(σ)	Tetragonal	a ₀ =0.879-0.918 c ₀ =0.454-0.459	FeCr FeMo Fe(Cr,Mo) (Fe,Ni) _x (Cr,Mo) _y	Formation from δ-ferrite is much more rapid than from austenite. Potent embrittler below 595°C. Forms with long time exposure from 650-900°C
Chi(χ)	Bcc (α-Mn)	a ₀ =0.886-0.892	Fe ₃₆ Cr ₁₂ Mo ₁₀ (Fe,Ni) ₃₆ Cr ₁₈ Mo ₄ M ₁₈ C	Observed in alloys containing substantial molybdenum. Chi precipitates with exposure to 730-1100°C
Laves(η)	Hexagonal	a ₀ =0.470-0.474 c ₀ =0.772-0.7725	Fe ₂ Mo (Ti ₂₁ Mo ₉) (Fe ₃₀ Cr ₅ Si ₅)	Forms in austenitic alloys with substantial amounts of molybdenum, titanium, or niobium after long time exposure from 600-1100°C

carbon content and/or high content of alloying elements, that the M_f-temperature become close to ambient temperature, thus removing any retained austenite, which may conditionally form untempered martensite after multipass re-heating or single tempering.

However, Marshall et al.^[SPM 39] compiled general M_s-temperatures, M_f-temperatures, and A_{C1}-temperatures of general categories of supermartensitic stainless steels as listed in Table 2-3.

2.1.1.2 Second Phase Precipitation

The nature of high alloy steels, in particular of high chromium stainless steels is related to the complexity of microstructure formation such as second phase precipitation in the matrix microstructure under welding thermal cycles. Table 2-4 gives a compilation of possible second phases precipitated in stainless steels. In traditional 12 wt.-%Cr stainless steels, formation of chromium carbides may take place at grain boundaries involving reduced corrosion resistance. Control of chromium carbide precipitation has been enabled by advanced developments in steel production for fabricating extra low and/or low carbon supermartensitic stainless steels, e.g. C ≤ 0.02 wt.-%.

It is well known that titanium can also be taken into account as a carbide stabiliser forming very stable carbide phases and therefore decreasing the effective carbon

content^{[SPM 27],[SPM 35]}. This automatically enhances corrosion resistance and mechanical properties of supermartensitic stainless steels. However, using higher amounts of titanium added to the materials might adversely affect economic efficiency with respect to commercial production because this alloying element needs very high solution temperatures to dissolve carbides^[SPM 35].

During rapid cooling, the formation of austenite from ferrite is associated with the diffusion phenomenon of carbon and nitrogen rather than with that of substitutional elements and thus, a quenched martensitic microstructure will exhibit the former grain boundaries. Nevertheless, it has to be noted that carbides may develop in subcritically reheated areas during deposition of subsequent weld runs.

For 13 wt.-% Cr martensitic stainless steels, general precipitation of chromium carbide phases, i.e. M_7C_3 and $M_{23}C_6$, can easily occur at temperatures above 400°C. This means that precipitation of second phases throughout the martensitic structure will take place if the temperature of the component is in the range of 450°C to 500°C. Even high temperatures in the range of 600°C to 800°C might cause local chromium depletion^[SPM 27].

Folkhard^[GEN 24] reported that the precipitation phase, $M_{23}C_6$, can form in the matrix structure of soft martensitic stainless steels, in particular at grain boundaries. The formation of sigma phases and embrittlement might only occur if time is sufficiently long in the respective temperature range of around 475°C.

2.1.1.3 Post Weld Heat Treatment

In order to improve material properties, post weld heat treatment (PWHT) will conditionally be considered as the subsequent process after completed welding operation on components. In martensitic stainless steels, post weld heat treatment can primarily cause tempering and softening by carbide precipitation: maximum softening takes place with precipitation of $M_{23}C_6$ by heating at temperatures above 500°C^[SPM 27].

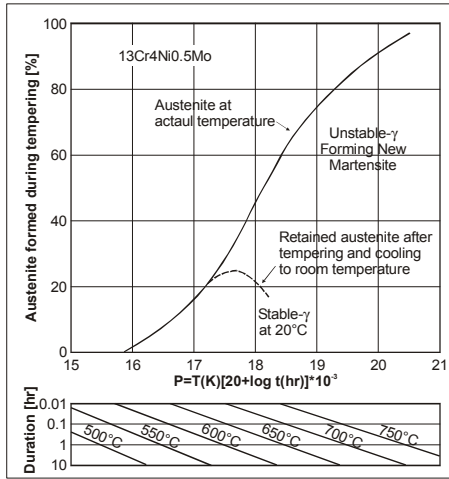
The temperature level of post weld heat treatment is usually dependent on the A_{C1} -temperature, for instance, conventional post weld heat treatment can be carried out at temperatures above 700°C for materials with low nickel and carbon content in order to receive the maximum softening effect. On the other hand, post weld heat treatment for materials with increased nickel content has to be carried out at temperatures lower than those for low-alloyed materials.

A_{C1} -temperature estimation of 13 wt.-% Cr martensitic stainless steels with a carbon content below 0.05 wt.-% as a function of alloying elements is given by^[SPM 27]:

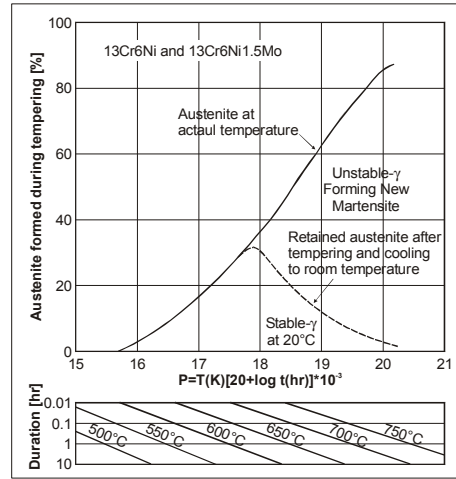
$$A_{C1} (^{\circ}C) = 850 - 1500(C + N) - 50Ni - 25Mn + 25Si + 25Mo + 20(Cr - 10) \quad (2-4)$$

Post weld heat treatment at 600°C is practically performed for 13Cr4Ni stainless steels because carbide formation may be decreased gradually at low temperatures, which inevitably promotes some reformations of austenite^[SPM 27]. This reformed austenite consists of different chemical compositions compared to the austenite retained after welding since the diffusion is a significant factor for controlling the reformation of austenite. Hence, an

2. Literature Reviews

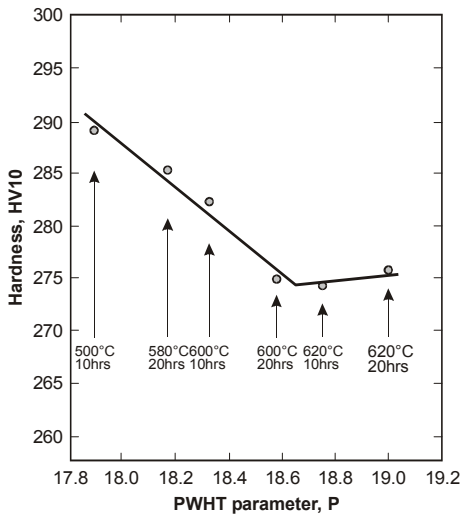


a) 13Cr4Ni0.5Mo system

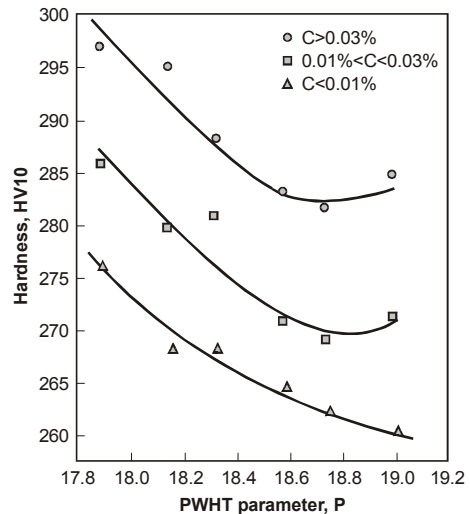


b) 13Cr6Ni and 13Cr6Ni1.5Mo system

Figure 2-5: Effects of PWHT conditions on austenite reformation in two different systems of supermartensitic stainless steel^[SPM 52].



a) Average values



b) Dependence on various carbon content

Figure 2-6: Average hardness levels of the weld metal dependent on PWHT parameters: a) Average values, b) Dependence on various carbon content^[SPM 37].

enrichment phase with nickel, carbon, and/or nitrogen in the reformed austenite can appear even though carbon content is fairly low for the modified supermartensitic stainless steels. In the case that PWHT is carried out at a temperature just slightly (say 40°C) above the A_{C1} -temperature, in this way the formation of enriched austenite will be stable during cooling to room temperature. On the other hand, at a further rise of temperature above the A_{C1} -temperature, equilibrium state of the austenite phase content can easily be obtained

with the reduction of enriched austenite and then the formation to virgin martensite can take place once again. Thus, softening effects intended for PWHT become more negative.

However, A_{C1} -temperatures of 640°C and 665°C are, respectively, obtained in the present research for supermartensitic stainless steel the base metal and matching filler material by estimation performed with Equation (2-4).

An estimation of the austenite content at room temperature with various PWHT conditions, in particular for the new generation of supermartensitic stainless steels can be obtained by using a Larsen-Miller parameter as expressed by^{[SPM 52],[SPM 37]}.

$$P_{LM} = T(^{\circ}K) \cdot [20 + \log t] \cdot 10^{-3} \quad (2-5)$$

where T and t are the tempering temperature ($^{\circ}K$) and the duration (hour), respectively.

Figure 2-5 represents effects of tempering conditions on the retained austenite in the new generation of supermartensitic stainless steels, i.e. 13Cr4Ni0.5Mo and 13Cr6Ni1.5Mo. The most reverted austenite forms at an P_{LM} -parameter in the range of 15.5 to 18, and it remains stable during cooling to room temperature. For P_{LM} -parameters above 18, the reverted austenite becomes unstable and then transforms to untempered martensite during cooling^[SPM 52].

As suggested by Gooch^[SPM 27], an extension of tempering duration for PWHT performed on 13 wt.-% Cr martensitic stainless steels is unacceptable for specific applications such as welded pipeline components. Therefore, short-term post weld heat treatment, i.e. 5 to 10 minutes at 650°C, has been recommended for the martensitic stainless steel family experiencing welding fabrication. The temperature at 650°C is proposed to promote required softening effects to a specific extent, but attention to the formation of partial re-austenite should be paid as well. Furthermore, possible side effects, i.e. stress corrosion cracking caused by a reduction of tensile strength, sensitisation, etc., after PWHT must be taken into account. At such short duration, the P_{LM} ranges between 15.5 to 18 and thus, has to be regarded as uncritical for the formation of annealing austenite.

In addition, Gooch^[SPM 37] who worked on heat treatment of welded 13Cr4Ni martensitic stainless steels, reported that the hardness level of the welded component decreases with increasing P_{LM} -parameter as shown in Figure 2-6a. The hardness of the welded component is inversely proportional to an increase of the P_{LM} -parameter until 18.8 which acts as a minimum, and then the hardness of the welded component increases, but only slightly. However, it must be recognised that for the reduction of the hardness by increasing the P_{LM} -parameter, heat treatment must be carried out for longer times instead of increasing the operation temperature.

This behaviour is observed at higher carbon levels. But, for extra low carbon steels, i.e. $C \leq 0.01\%$, increasing hardness values with the P_{LM} -parameter are achieved without a local minimum at $P_{LM} = 18.8$.

2. Literature Reviews

Table 2-5: Effects of two different kinds of filler materials on material properties of welded SMSS components^[SPM 54].

Conditions	Filler materials	
	Duplex and superduplex	Matching (12.5Cr6.5Ni2.5Mo)
General description	Having a track record of successful use in offshore projects.	Considering as a economical – technical challenge.
Strength value	- 22 Cr duplex : 603 MPa (0.2%PS at 20°C) 803 MPa (UTS at 20°C) 485 MPa (0.2%PS at 100°C) 672 MPa (UTS at 100°C) - 25 Cr superduplex : 755 MPa (0.2%PS at 20°C) 876 MPa (UTS at 20°C) 621 MPa (0.2%PS at 140°C) 769 MPa (UTS at 140°C)	Match or overmatch to the parent material.
Toughness value (for GMAW)	- 22 Cr duplex : 271 J at –30°C (weld metal) 292 J at –30°C (fusion line) - 25 Cr superduplex : > 185 J at –30°C	42J at –50°C
Corrosion resistance	Improving resistance against SCC and general corrosion in the weld metal and its neighbour zone for long term exposure to offshore oil and gas media.	No performance
Post weld heat treatment	Short-term heat treatment, e.g. 650°C/5min, has been applied to soften HAZ peak hardness without detrimental effects on weld metal microstructure.	Usually, a few minutes up to an half hour at temperature around 650°C can be carried out for PWHT, as a optimum temperature 650°C for holding time of 30 min is regarded.

2.1.1.4 Filler Materials for Supermartensitic Stainless Steels

Optimum arc welding consumable selection is based on the assumption that the weld metal and the base metal must have mechanical properties and corrosion resistance equal to or in excess of the specified requirements and also should have toughness and hardness values, which meet the demands of the relevant specification. Thus, the decision in selecting filler materials and welding processes for fabrication of subsea flowline components must be taken with the following factors in mind: I) Matching strength, II) Achieving adequate toughness value, III) Keeping hardness at an acceptable level, IV) Matching corrosion properties, and V) Minimising or avoiding PWHT^[SPM 55].

Until recently, supermartensitic stainless steel pipelines have been joined by using superduplex or duplex filler materials, but these filler materials often present a number of problems due to the so-called yield strength undermatch. Therefore, the development of matching filler materials for the consumable welding process is firmly focused on avoiding such problems. However, the elongation and toughness properties of the weld metal joined by the matching filler material still indicate the negative state, hence short-term heat treatment at 650°C for 5 to 30 minutes is additionally required to improve toughness^[SPM 53]. Such aspects have been investigated by Gough et al.^[SPM 54] and summarised in Table 2-5.

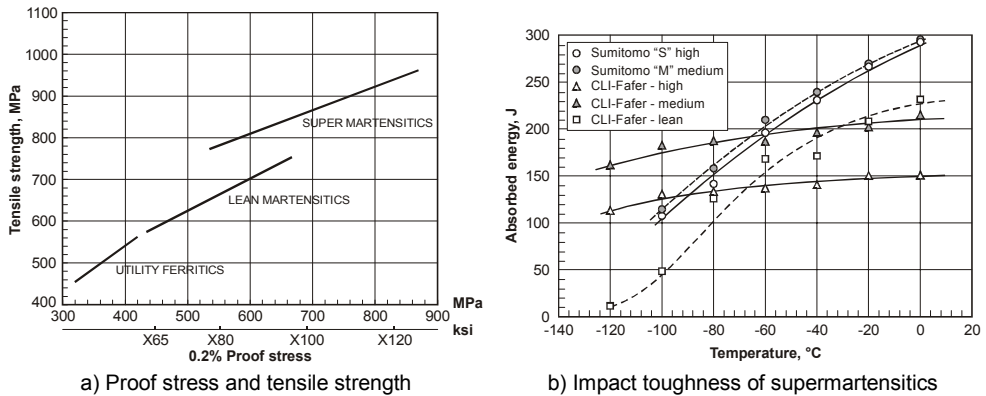


Figure 2-7: Mechanical properties of supermartensitic stainless steels: a) Comparison of proof stress and tensile strength of supermartensitics with lean martensitics and utility ferritics, b) Impact toughness value of supermartensitics^[SPM 39].

Investigation of microstructure formation during welding of supermartensitic stainless steel with matching material has been carried out by Karlsson^[SPM 55], who reported that arc welding of supermartensitic stainless flowlines using matching filler material is uncomplicated in comparison to using duplex or superduplex filler material. It is evidently shown that matching filler material with a molybdenum content above 1.5 wt.-% can improve the weld metal properties in order to avoid brittle behaviour compared to molybdenum-free filler materials. Furthermore, weld metal toughness values in the as-welded condition up to 141 J at -40°C were experimentally achieved in the TIG welding process due to the full martensite and low oxygen content in the weld metal. Further improvements of material properties can be achieved by decreasing the heat input and interpass temperature as well as by short-term post weld heat treatment.

2.1.2 Mechanical Properties

The basic mechanical properties of supermartensitic stainless steel are generally affected by the carbon content, the amount of alloying elements, and the types of matrix formation microstructure. Also, these mechanical properties are strongly influenced by manufacturing and heat treatment processes^[SPM 39].

Figure 2-7a represents the relationship between levels of proof stress and tensile strength of supermartensitic stainless steel in comparison with lean martensitic stainless steel and utility ferritic stainless steel. Both the proof stress and the tensile strength of supermartensitic stainless steels are higher those of lean supermartensitic and utility ferritic stainless steels. Proof stress ranging between 550 MPa and 900 MPa and tensile strength ranging between 800 MPa and 1000 MPa have been achieved for supermartensitic stainless steels, at ratios ranging between 0.75 and 0.90^[SPM 39].

Supermartensitic stainless steels with a proof stress of 550 MPa (X80) are commonly applied to flowline construction for transporting oil and gas products in offshore technology. For reasons of cost-efficiency and weight-saving, a number of flowline users and producers look for relatively high strength materials to replace lower strength ones. Therefore, supermartensitic stainless steels with a proof stress higher than 700 MPa (X100) are interestingly focused on by flowline manufacturers.

2. Literature Reviews

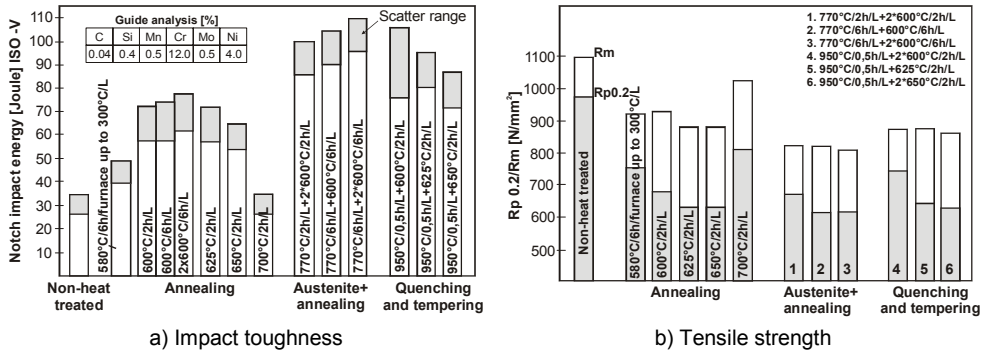


Figure 2-8: Influence of post heat treatment on mechanical properties of soft martensitic stainless steels: a) Impact toughness, b) Tensile strength^{[GEN 24],[SPM 49]}.

During service application at low temperatures, in particular, a reduction of the ductile to brittle transition temperature (DBTT) can play an important role in influencing component failure. Therefore, lean supermartensitic stainless steels can generally be considered to be appropriate for applications of at temperatures down to -20°C , whereas medium- and high-alloyed supermartensitic steels are designed for specific applications at temperatures down to -50°C ^[SPM 39].

As represented by the absorbed energy versus temperature curves in Figure 2-7b, medium alloys are slightly tougher than the high-alloyed steels. Lean supermartensitic stainless steels reach an energy range similar to that of medium and high martensitic stainless steels by increasing temperature close to zero, but they become more brittle at extremely low temperatures. However, at temperatures above -80°C , all types of supermartensitic stainless steels still have an absorbed energy value higher than 100 J ^[SPM 39].

In offshore applications, supermartensitic stainless steel pipelines transporting hot products may be exposed to high temperatures up to 100°C - 150°C ^[SPM 48]. During service performance at elevated temperatures, supermartensitic stainless steels exhibit good mechanical properties when compared with duplex stainless steels. For example, in the temperature range of 20°C to 250°C , high supermartensitic stainless steels have a reduced proof stress of around 15 percent, whereas a proof stress reduction of around 25 to 30 percent has been obtained for duplex and superduplex stainless steels ^[SPM 47].

Although the mechanical properties of the supermartensitic stainless steels are strongly dependent on their chemical compositions, heat treatment can also be taken into account as an additional process for improving the mechanical properties. The toughness values in terms of absorbed energy of supermartensitic stainless steels are dependent on different conditions of post weld heat treatment as represented in Figure 2-8a. The impact toughness of as-welded weld metal is somewhat lower than that of the weld metal after post weld heat treatment. It is obvious furthermore that the toughness value at room temperature becomes higher when the weld metal has been treated by an austenitising process with subsequent tempering or annealing. On the other hand, post weld heat treatment can affect the mechanical properties by decreasing the levels of proof stress and tensile strength of the weld metal as represented in Figure 2-8b.

A relatively simple way to assess the mechanical behaviour of such materials is represented by hardness measurements. This method seems to be more convenient particularly for welding engineers. For welded components of supermartensitic stainless steels, hardness values in the range of 250 to 350HV (10 Kgf) are dependent on the carbon content of the material, measuring positions, heat treatment processes, etc.^{[SPM 27],[SPM 31],[SPM 50]}

2.1.3 Corrosion Resistance

Because subsea flowlines in offshore technology are directly exposed to sour service environments and subjected to external mechanical loads concurrently, the corrosion resistance of the material must be taken into account as a significant factor in material selection. In this context, it should be noted that supermartensitic stainless steels have been designed for field application with exposure to slight or moderate sour electrolytic solutions. Hence, a description of the possible forms of corrosion in the specific environmental conditions is required in order to avoid misunderstanding on the selection of materials for offshore applications.

General corrosion is a simple form of corrosion, which is characterised by electrochemical reactions showing the loss of metal matrix over the entire environmentally exposed surface. A reduction of the carbon content can normally improve the general corrosion resistance of supermartensitic stainless steels. By avoidance of the formation of a chromium depleted zone caused by precipitation of chromium carbides. Moreover, beneficial additional alloying elements such as molybdenum and nickel can also improve the general corrosion resistance of supermartensitic stainless steels^[SPM 39]. The determination of general corrosion resistance of supermartensitic stainless steels regarding the effects of major alloying elements is given by the following equation of the general corrosion index (GCI)^[SPM 14]:

$$GCI = Cr - 12C + 0.77Ni + 10N \quad (2-6)$$

$$CCI = Cr - 10C + 2Ni \quad (2-7)$$

However, it still remains in question why the molybdenum content is not included in these equations, even though it can effectively improve the general corrosion resistance, as well. A GCI-value of 15.75 is obtained for the base metal of supermartensitic stainless steel pipeline calculated by Equation (2-6) and a GCI-value of 17.21 for the matching filler material.

In order to confirm this result, Hashizume^[SPM 48] examined effects of chemical compositions and tensile strength on general corrosion resistance of martensitic stainless steels in CO₂ and H₂S environments. He reported that the GCI-index is very useful for estimating the corrosion rate of martensitic stainless steels in the CO₂ and H₂S environments tested at elevated temperatures. The corrosion rate is decreased by increasing the GCI-index of the material as represented in Figure 2-9a. Moreover, increasing the temperature of the considered system can also enhance the general corrosion rate of the material as represented in Figure 2-9b.

2. Literature Reviews

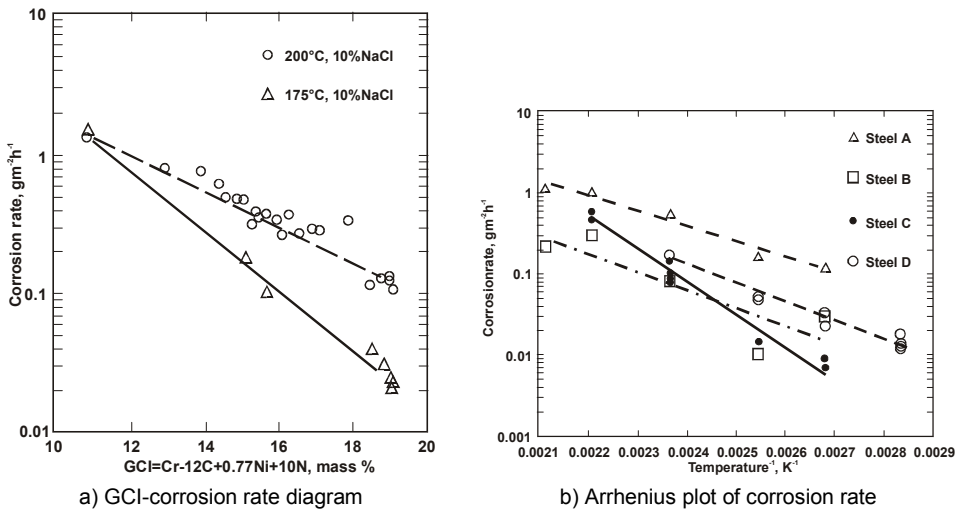


Figure 2-9: Effects of GCI-index and temperature of the testing system on the general corrosion rate of martensitic stainless steel^[SPM 48].

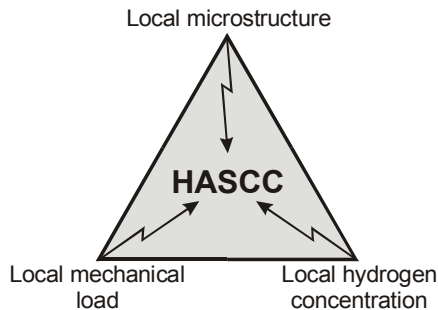


Figure 2-10: Three main local factors influencing hydrogen assisted stress corrosion cracking behaviour^[HAS 108].

2.2 Mechanisms of Hydrogen Assisted Cracking

Hydrogen assisted cracking can microscopically be regarded as the local interaction between the microstructures with the local mechanical load and the hydrogen concentration as represented in Figure 2-10.

Until recently, numerous contrary suggestions have been given on the mechanisms of hydrogen assisted cracking based on different points of view because critical events associated with interaction between local mechanical loads and local hydrogen concentration for hydrogen assisted cracking occur on atomic scale at the crack tip, thus, theories are not easily verified. There is general agreement in literature that the phenomenon cannot be described by a single mechanism. However, a basic understanding of the general mechanisms of hydrogen assisted cracking as well as of the hydrogen uptake and hydrogen diffusion processes, and a basic determination of mechanical loads may provide sufficient explanation of the phenomenon of hydrogen assisted cracking. For this reason, the different categories of mechanisms are described more in detail.

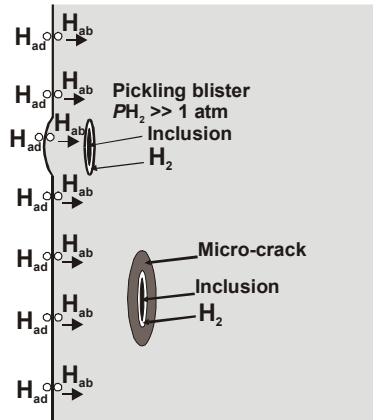


Figure 2-11: Schematic illustration of pressure theory for describing the hydrogen assisted cracking phenomenon^[GEN 6].

2.2.1 Pressure Theory

Pressure theory represents the oldest proposed mechanism for hydrogen assisted cracking. According to this theory, blisters and internal cracking are produced by charging unstressed specimens with hydrogen which precipitates and recombines to molecules at internal defects such as flakes, voids and non-metallic inclusions, and subsequently generates high internal pressure within the defects. As proposed by Zapffe et al.^[HAS 40], the principal portion of absorbed hydrogen in iron consists of partially ionised molecules occluded in internal defects such as micro-voids, non-metallic inclusions etc.

The pressure of hydrogen molecules from the recombination of adsorbed atoms in such defects increases according to the solubility law. However, if the precipitation of molecular hydrogen is sufficiently pronounced or the reinforcement of the lattice is weak, nucleation and growth of micro-cracks may occur in the absence of externally applied stress. Generally, the local pressure is by orders of magnitude higher than 1 atm, i.e. higher than the yielding pressure of the steel, which will dominate an extent of the micro cracks as shown in Figure 2-11, where micro-voids or micro-cracks eventually combine to form more macroscopic cracks^[HAS 14], which play a significant role for rupture of the material.

The fact that stresses in steel structures are of the triaxial type means that imposed stress, i.e. local stress combined with externally applied stress, may lead to the rupture of the materials^[HAS 41]. Hydrogen in micro voids can easily be removed by either baking the material at elevated temperatures or holding it at room temperature for a certain amount of time if it is not recombined to molecules^[HAS 86]. In any case, micro-voids with molecular hydrogen still remain as substructures of the material, which have a nature of triaxial stress and imposed stress.

In the description by Zapffe et al., it is stated that pickling and cathodic electrolysis can also cause great supersaturation, because these processes produce hydrogen concentrations on the steel surface that equal to or greater than the concentrations occurring in pure hydrogen at elevated temperatures. When hydrogen supersaturation exceeds a certain degree, hydrogen is recombined to molecules at the internal defects,

2. Literature Reviews

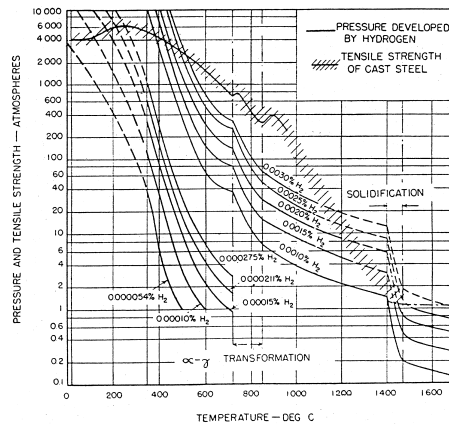


Figure 2-12: Variation of temperature at equilibrium pressure for molecular hydrogen precipitated within steels as a function of hydrogen concentration^[HAS 40]

hydrogen under pressure exceeding the elastic strength, thus to breaking off the lattice bonds at low temperatures rather than at high temperatures as represented in Figure 2-12.

As a special effect regarding welding it has to be considered that hydrogen molecules are usually formed at higher temperatures, and consequent pressure occurs during cooling.

2.2.2 Decohesion Theory

The effect of hydrogen on the cohesive strength of the iron lattice has first been mentioned by Troiano et al.^{[HAS 18],[HAS 106]}. This theory has been extended by Oriani^{[HAS 3],[HAS 23],[HAS 100]}, who proposed that dissolved hydrogen can reduce the average cohesion force between iron atoms as shown in Figure 2-13a. This assumption is supported by the fact that the fracture of steel in a hydrogen environment appears brittle, and that it is easier for the metal to respond to the applied stress by parting iron-iron atomic bonds rather than by plastic deformation.

Furthermore, the local concentration of hydrogen is increased by the positive component of elastic stress, since hydrogen must first diffuse into a severe elastically stressed region^[HAS 23] and accumulate in the regions with a specific hydrostatic stress up to equilibrium in short atomic distance from the crack tip. Under these assumptions, the main point of this mechanism is to describe how hydrogen affects crack propagation, not crack nucleation, although the two phenomena are most likely dependent on the same physical processes.

Based on the basic principle of this model, crack propagation can occur if the local maximum tensile stress σ'_{max} at the specific location ahead of the crack tip normal to the plane of the crack equals the maximum cohesive resistive force of the metal nF_m per unit area of the cracking plane. It can be formulated by^[HAS 23]:

$$\sigma'_{max} = n \cdot F_m \cdot [HD] \quad (2-8)$$

where n is the number of metal atoms per unit area of the cracking plane and F_m is the maximum cohesive resistive force of iron atoms.

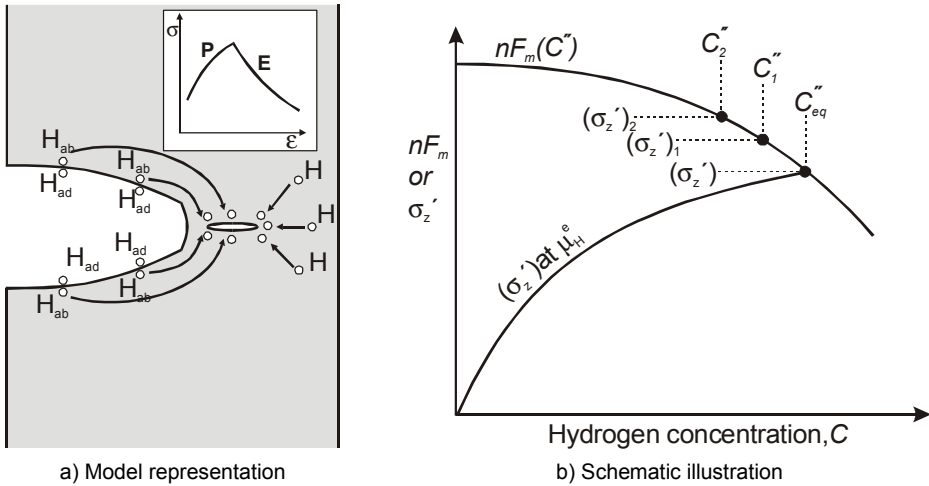


Figure 2-13: Decoherence theory describing hydrogen assisted cracking phenomena: a) Model representation of decohesion of iron-iron bonds caused by dissolved hydrogen atoms, b) Schematic illustration of the equilibrium of hydrogen concentration at the position of maximum tensile stress at the specific value of hydrogen chemical potential, $\mu_{\text{H}}^{\text{e}}$ [HAS 23].

However, with respect to the effect of hydrogen concentration on the crack propagation behaviour, larger hydrostatic and/or larger shear stresses will lead to a larger accumulation of dissolved hydrogen ahead of the crack tip up to equilibrium state while the maximum cohesive drag force will be decreased more than usual as represented in Figure 2-13a.

Moreover, Oriani also suggests that hydrogen assisted cracking occurs by distinct processes, i.e. decohesion facilitated by hydrogen and plastic tearing of ligaments unaffected by hydrogen between decoherent region. Thomson [HAS 29] proposed that plastic zones around the crack tip shields the crack tip from the full force of the externally applied stress. Cracking with brittle failure may occur if there is a large energy barrier for the emission of dislocations ahead of the crack tip.

As a particular advantage, the decohesion theory is based on the assumption that hydrogen diffusion is required to transport it into the critical strain region ahead of the crack tip, which explains delayed cracking.

2.2.3 Adsorption Theory

The adsorption theory proposed by Uhlig [HAS 62] is based on the Griffith criterion for fracture in ideally brittle solids. Atomic hydrogen has been thought to reduce the binding energy of the metal atoms, particularly at the specific location of the extreme root of notch, below a critical level of the shear stress which is required to create new fracture surfaces. This means that crack initiation and propagation takes place without the dissolution of the metal as as represented in Figure 2-14 [HAS 14], [HAS 109].

The application of the adsorption theory to hydrogen assisted cracking remains in questions because crack initiation and propagation have been assumed to take place by rupture of material in a limited distance ahead of the crack tip in the area of maximum stresses and strains normal to the crack plane [HAS 14]. Moreover, the energy that is required

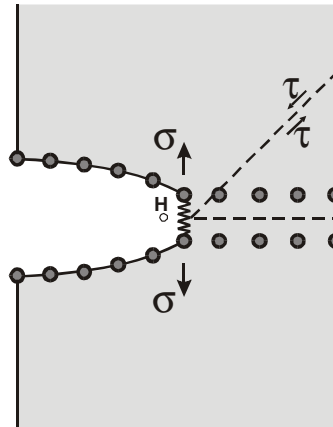


Figure 2-14: Schematic illustration of the mechanism of hydrogen assisted cracking based on the adsorption theory^[HAS 109].

for fracture in the material is associated almost entirely with plastic deformation, hence change in surface energy should not be significant^[HAS 41]. Other disagreements to this model have been reported by Hirth^[HAS 99], for instance, an underestimation of the required energy for creating new fracture surfaces and non-consideration of continuous crack propagation processes. Thus, the adsorption theory is not quite adequate to account for the dynamic stages of crack propagation.

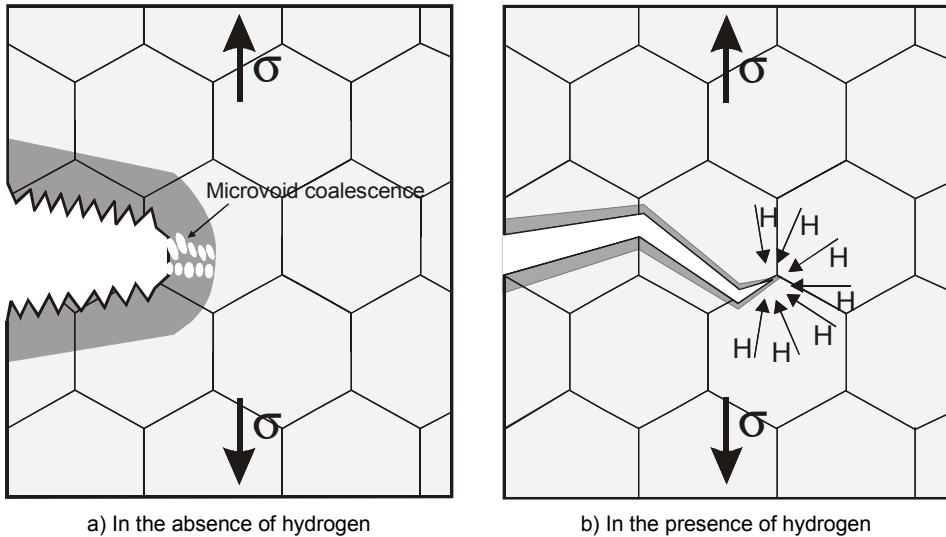
2.2.4 Dislocation Interaction Theory

The basic assumption for the hydrogen-dislocation interaction is that the presence of hydrogen around a dislocation can change the mobility of dislocation. This mobility can influence the fracture behaviour of materials by changing the extent and character of plasticity. Nelson^[HAS 86] observed that the influence of hydrogen on the dislocation mobility represents either a hardening effect or a softening effect dependent on the material and on the alloying composition.

Regarding the hardening effect, it is assumed that hydrogen will interact with the high tensile stress field adjacent to the dislocation to form a Cottrell-atmosphere^[GEN 22], i.e. a hydrogen cloud, that can strongly hinder the movement of a dislocation so that more dragging forces are required for the movement of dislocation.

The reduction in dislocation mobility and change in slip character makes deformation at the crack tip more difficult, hence the crack propagation takes place at low levels of external load applied to the component.

In contribution to such cracking phenomena, Louthan et al.^[HAS 46] reported that the association and movement of hydrogen with dislocations can cause degradation of metal properties because the hydrogen-dislocation interaction modifies plastic deformation processes by stabilising micro-cracks and by changing the work hardening rate. However, such a mechanism of embrittlement is more applicable to ductile materials than to brittle ones, since deformation of brittle materials is already limited^[HAS 86].



a) In the absence of hydrogen
 b) In the presence of hydrogen
 Figure 2-15: Schematic demonstration of crack propagation in high strength steels based on Beachem's assumption: a) In the absence of hydrogen crack growth occurs by micro-void coalescence within a large plastic deformation ahead of the crack tip, b) In the presence of hydrogen deformation becomes easier and crack growth occurs as result of severely localised deformation at the crack tip^{[HAS 25],[HAS 86]}

The idea behind the softening effect is the assumption that hydrogen may reduce the fracture strength of the materials. As experimentally observed by Beachem^[HAS 25], the reduction of microscopic plasticity and the change of fracture modes associated with hydrogen enhanced brittle fracture. Fractographical observations in high strength steels have been mentioned to support this idea. Such deformation is basically localised to the zone where the hydrogen concentration is saturated. Failure of the metal lattice will occur when the critical strain is reached within the specific local zone ahead of the crack tip as schematically represented in Figure 2-15. Lynch^[HAS 41] gave an extensive expression to support Beachem's observation that dissolved hydrogen on the crack tip surface facilitates the movement of the dislocation instead of restricting the moving dislocation. Since the chemisorption of a species like hydrogen increases the number of neighbours around the surface atoms, surface-lattice distortion will be reduced and dislocation nucleation will become easier.

The most comprehensive research dealing with these phenomena has been performed by Sofronis et al.^{[HAS 8],[HAS 9]} and Birnbaum^[HAS 39] by developing the theory of Hydrogen Enhanced Localised Plasticity (HELP) mechanism. The basic principle of their assumption is that the presence of hydrogen in solid solution reduces barriers to dislocation motion and increases the mobility of dislocations, thereby creating high capabilities of local deformation. The fracture process is a highly localised plastic failure process by decreasing the strength of the material rather than embrittlement, because the localised zone is softened by the presence of local hydrogen. Based on this mechanism, the crack propagation characteristic of relatively pure metals and alloyed metals can be different. For pure metals, fracture tended to be along slip planes and for alloys, fracture tended to be along the plane of maximum normal stress due to the action of multiple slip systems.

2. Literature Reviews

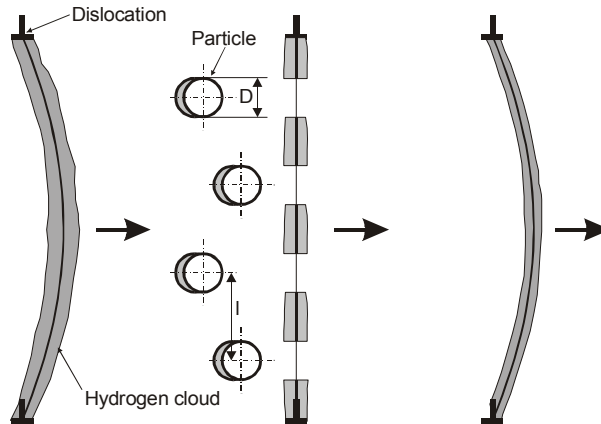


Figure 2-16: Schematic illustration of hydrogen cloud on moving dislocation at left, which is stripped off at the particles of effective size D and spacing l . Diffusion along dislocation restores cloud uniformity as dislocation moves away, at right^{[HAS 86],[HAS 110]}.

Considering the contribution of Tien et al^[HAS 110], who proposed a model for determining hydrogen transported by the dislocation as well as hydrogen enhancing the mobility of dislocation based on the assumption of the Cottrell-atmosphere model, the effect of hydrogen concentration on the dislocation can be described by the Boltzmann equation^[HAS 110] as:

$$[HD]_{dis} = [HD]_{\infty} \exp\left(-\frac{E_B}{kT}\right) \quad (2-9)$$

where E_B is the binding energy of hydrogen to the dislocation (0.1 – 0.5 eV), k is the typical Boltzmann's constant, T is the absolute temperature, $[HD]_{dis}$ is the hydrogen concentration on the dislocation, and $[HD]_{\infty}$ is the equilibrium hydrogen concentration at the pick-up site.

Figure 2-16 is the Cottrell-atmosphere model representing the dislocation with enrichment of hydrogen passing across inclusion particles by an applied external load. Hydrogen can be captured at the inclusion that results in an increase of drag forces for dislocation movement and in the reduction of the amount of hydrogen at the moving dislocation, and then the movement of the passed dislocation becomes more difficult. Thus, the crack propagation can occur in susceptible regions in which the formation a sharper and more brittle crack tip is found. The kinetics of crack growth will drastically increase if the global load is additionally applied. The reason is that the change of fracture behaviour is affected by a reduction of the dislocation mobility with changes in slip characteristics^[HAS 86]. However, the dislocation velocity with a hydrogen cloud \bar{v}_{DH} can generally be expressed by the Einstein-Stokes relation^[HAS 110]:

$$\bar{v}_{DH} = M \cdot F_{dd} \quad (2-10)$$

where M is the mobility of the cloud and F_{dd} is the force driving the dislocation.

A usual form of mobility is given by $M = D_{eff} / (k \cdot T)$, therefore the velocity of the dislocation with a hydrogen cloud is written by^[HAS 110].

$$\bar{v}_{DH} = \frac{D_{eff}}{k \cdot T} \cdot F_{dd} \quad (2-11)$$

where D_{eff} is the effective hydrogen diffusion coefficient.

However, to date the theories regarding the effect of hydrogen on dislocation and deformation capability of materials are quite different and still have not been quantified.

2.2.5 Hydride Theory

Embrittlement of the metallic material by the formation of a second phase known as metal hydride has been categorised into hydrogen assisted cracking. Nelson^[HAS 86] explained that the formation of hydrides in the material can be classified into four groups depending on the hydride potential which causes the different forms of metal-hydrogen bonds; I) ionic hydrides are salt-like in characteristic, II) transition hydrides, III) intermediate hydrides and IV) covalent hydrides. The transition hydrides are relatively important, in particular for structural alloys, but not all of the metals in the transition region, for instance Fe, Ni, Cu, Cr and Mo, can interact with hydrogen to form a metal-hydrogen bond. However, the transition metals in Group V, including Nb, V, Ta, Zr, Ti and Mg, can possibly interact with hydrogen to form metallic hydrides with participation of other mechanisms as described in the previous contribution^[HAS 105].

Extensive research on the topic relating to hydride formation particularly for the Group-V metals has been reported by Birnbaum^[HAS 105]. The systems that have precipitated brittle hydrides at relatively low values of hydrogen diffusivity, such as zirconium, exhibit cleavage of the hydride during stressing and ductile failure in the solid solution between the hydrides during tension tests at room temperature. The metal hydrides simply assists in decreasing the material strength and ductility, therefore, the brittle fracture mode can be observed on the crack surface at very low strain rates and temperatures, at which hydrogen can still be transported to the crack tip. However, for a number of systems, for instance β -bcc (Ti-phase), significant embrittlement has been caused by hydrogen, which cannot be visualised because of the high hydrogen solubility in the material. On the other hand, for α -hcp system (Nb-phase), for instance, where stable hydrides can be formed, fracture turns into the cleavage fracture mode showing little local deformation, and crack propagation takes place along the hydride cleavage plane. For the system where hydrogen mobility is sufficiently high, the kinetics of hydride formation is generally governed by hydrogen interstitial diffusion in the embrittlement temperature range.

Additionally, Birnbaum also determined the mechanism of hydride embrittlement as represented in Figure 2-17. The chemical potential of the local hydrogen solute at the crack tip with an extreme stress-strain distribution, can be reduced by application of a tensile stress that results in the transportation of hydrogen into the crack tip. The local hydrogen concentration ahead of the crack tip increases until it attains a value as given in Equation (2-12).

2. Literature Reviews

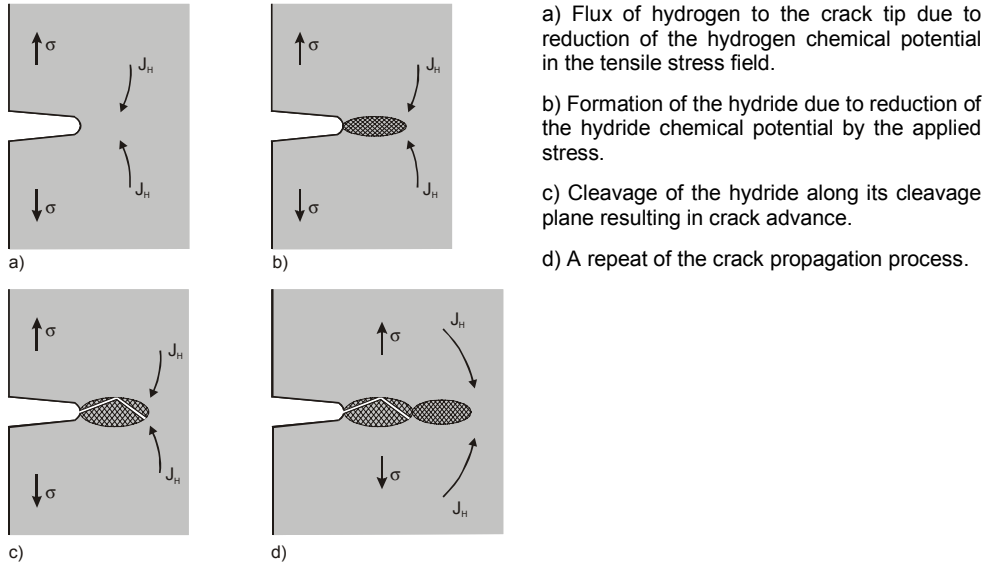


Figure 2-17: Schematic illustration of hydride theory showing crack propagation in the metallic hydride region ahead of the crack tip by stress induced hydride formation^[HAS 105].

$$[HD]_{prs} = [HD]_{abs} \exp \frac{\sigma_{ii} \cdot \bar{V}_H}{R \cdot T} \quad (2-12)$$

where $[HD]_{abs}$ is the hydrogen concentration in the absence of stress, R is the universal gas constant, σ_{ii} is the spherical stress, and \bar{V}_H is the partial molar volume of hydrogen in solution.

The stress also decreases the free energy hydride formation ($\Delta G_{\alpha-\beta}$) in the stress concentration areas, and hydride precipitation will occur if the free energy is equal to zero ($\Delta G_{\alpha-\beta} = 0$). In general, the embrittlement of alloys by the presence of metallic hydrides in the matrix lattice can take place. The kinetics of this process is controlled by hydrogen transportation to the hydrostatic stress field.

The embrittlement of material influenced by the presence of metallic hydrides in the matrix lattice can occur either because the local volume in the matrix lattice is increased by hydride formation, or because the material ductility is reduced by the presence of metallic hydrides, or both^[HAS 86].

However, there is no question that metallic hydride formation in the matrix lattice can be a main factor of embrittlement in alloys, but this mechanism cannot account for embrittlement of iron based alloys due to the reason described above.

2.3 Effects of Crystal Structure of Steels on Hydrogen Transport

In a quantitative lifetime assessment of components exposed to hydrogen environments, the calculation of hydrogen transportation is one of the major parts for modelling hydrogen assisted cracking with using finite element method. Transportation of

atomic hydrogen through metallic materials is significantly influenced by the crystal structure of the material. Thus, it is necessary to know the distinctive features of the basic crystal structures of an iron matrix lattice system, i.e. bcc-crystal structure and fcc-crystal structure, which provide interstitial sites with different behaviour for foreign atoms such as hydrogen. These crystal structures may be present in supermartensitic stainless steels as the matrix structure or the sub-structure dependent on the chemical compositions, on the history of heat treatment processes, etc.

When looking at a close-pack array of metal atoms, it becomes evident that interstitial sites can be categorised into two groups; I) a tetrahedral interstice with the co-ordination number six, and II) a octahedral interstice with the co-ordination number four.

The fcc-crystal system has two types of interstitial positions which may accommodate a smaller atom belonging to another element. The larger type of interstice is represented by the hole at the centre of the cube and centres on the cube edge. It is surrounded by six atoms in the fcc lattice at the corners of a regular octahedron, namely by octahedral interstices as represented in Figure 2-18a. The smaller type of interstice is represented in Figure 2-18b, which is the tetrahedral interstice surrounded by four atoms in the fcc lattice. The maximum radii of the spheres which can be inserted in the interstitial sites are equal to $0.41r$ and $0.225r$ for the octahedral interstice and the tetrahedral interstice, respectively, (r denotes the radius of metal atoms $\approx 1.26 \text{ \AA}$).

The bcc-crystal system is less close packed than the fcc-crystal system, and also contains two types of interstice. The larger type is the tetrahedral interstice represented at the respective position on the cubic faces. It is surrounded by four atoms of the bcc lattice at the corners of a regular tetrahedron as illustrated in Figure 2-18d. The octahedral interstice is represented in Figure 2-18c. It is smaller than the tetrahedral interstice and surrounded by six atoms arranged at the corners of an irregular octahedron. The atom is located at the centre of the cubic edge and at the face centre. The tetrahedral space can accommodate a sphere with a maximum radius equal to $0.291r$, whereas the octahedral space can accommodate a sphere with a radius of only $0.154r$.

Consequently, hydrogen solubility diffusion is affected by the characteristic of interstices. For example, the hydrogen solubility with an fcc-crystal structure is higher than that with the bcc-crystal structure.

Smailowski^[GEN 28] reported that the solubility of hydrogen in the matrix structure of steel is directly proportional to the amount of the austenite (fcc-crystal structure). The tetrahedral interstice is a stable sorption site for hydrogen in the fcc-crystal structure. In the bcc-crystal structure the tetrahedral interstice is more stable for atomic hydrogen than the octahedral one. Although no explanation of absorption phenomenology for hydrogen in the interstices has been found yet, it is clear that hydrogen can be solved in the γ -iron system rather than in the α -iron system due to different interstitial spacings.

2. Literature Reviews

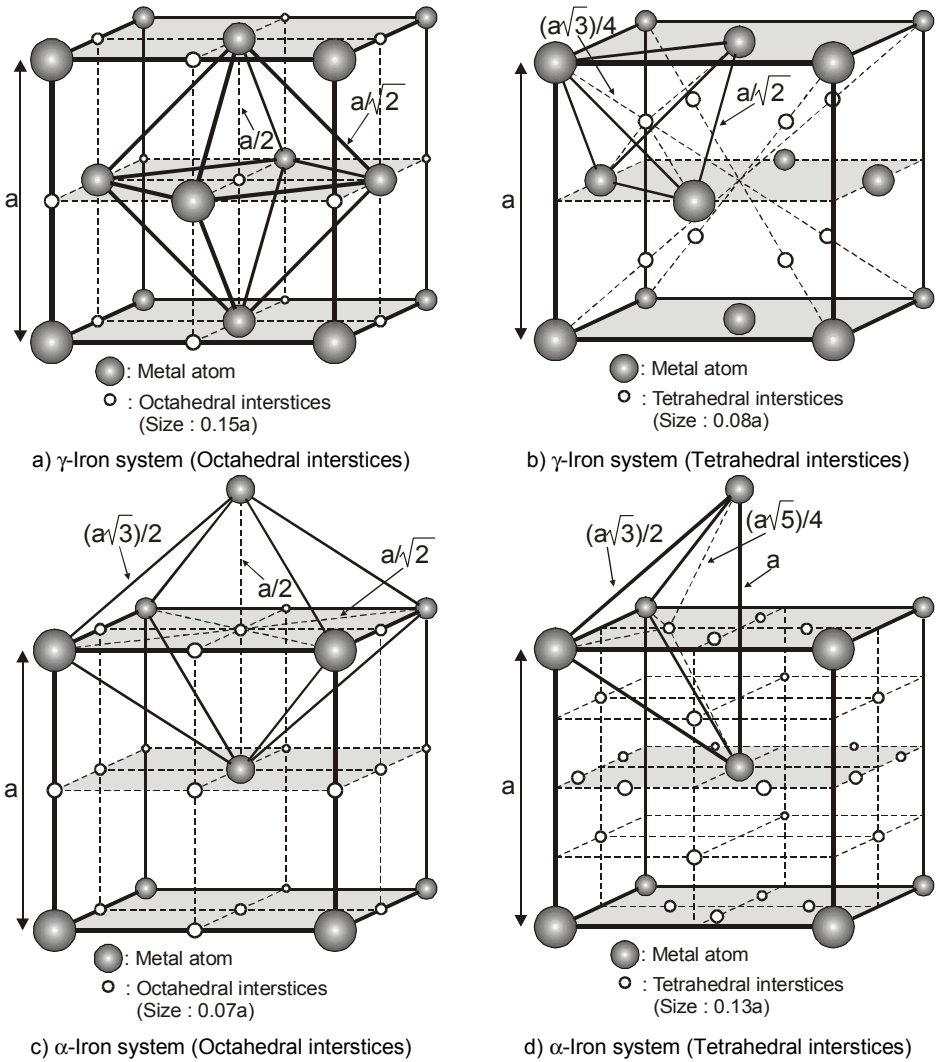


Figure 2-18: Schematic illustration showing interstitial spacing for foreign atoms such as hydrogen in iron matrix lattice of bcc- and fcc-crystal structures^{[GEN 28],[GEN 32]}.

2.3.1 Hydrogen Evolution and Absorption

Hydrogen diffusion requires generally chemical gradients of hydrogen concentration. Such gradients are generated by the different types of hydrogen sources. For welding applications, Two ways of hydrogen uptake are relevant: I) Hydrogen uptake in the weld metal during the welding process, II) Hydrogen uptake by cathodic reactions in electrolytic solutions during corrosion processes^[GEN 6].

2.3.1.1 Hydrogen Absorption during Corrosion Processes

In corrosion processes, atomic hydrogen can be assumed to be generated from aqueous environments during cathodic electrochemical reaction in the way described in Table 2-6 and as illustrated in Figure 2-19.

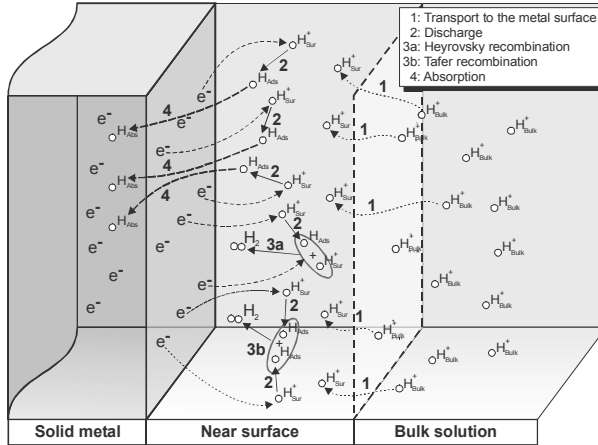
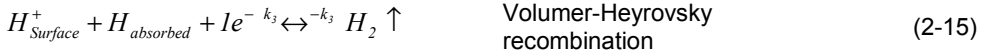
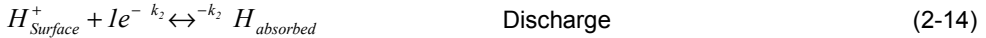
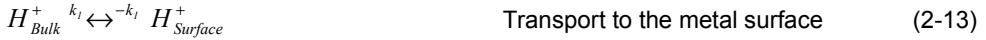


Figure 2-19: Consequence of hydrogen discharge and recombination at the metal surface exposed to electrolytic solution with subsequent diffusion into the matrix material^[HAC 21].



Evolution of hydrogen from sour service environments is most significant for the present research because it is directly related to many serious problems of flowline failure in oil and gas industry as reported elsewhere^{[HAS 108],[HPD 52]}. Hydrogen uptake processes at steel surfaces exposed to electrolytic solutions are usually subdivided into four partial reactions as represented in Figure 2-19^{[HAC 21],[HPD 47]}.

The initial reaction is the mass transportation of hydrogen ions from the bulk electrolytic solution to the near surface area of the steel, which is a reversible reaction with a specific rate constant of k_f as formulated in Equation (2-13). Subsequently, reduction of positive hydrogen ions takes place in the discharge reaction by consuming an electron from the anodic reaction to generate adsorbed atomic hydrogen in a neutral situation (Equation (2-14)). This adsorbed hydrogen can also interact with another one to form molecular hydrogen in the Tafel-recombination reaction as described in Equation (2-16). Moreover, the Heyrovsky-recombination is also assumed to generate molecular hydrogen as represented in Equation (2-15). Finally, the most significant reaction for hydrogen assisted stress corrosion cracking is the absorption reaction because it represents the rate control of the hydrogen uptake process by the slowest rate constant of the reaction as shown in Equation (2-17).

2. Literature Reviews

Table 2-6: Summary of possible electrochemical reactions in corrosion processes of the steels.

Reaction	Remarks	Reference
<p>- Anodic reactions $3\text{Fe} + 4\text{H}_2\text{O} \rightarrow \text{Fe}_3\text{O}_4 + 8\text{H}^+ + 8\text{e}^-$, $\text{Ni} + \text{H}_2\text{O} \rightarrow \text{NiO} + 2\text{H}^+ + 2\text{e}^-$, $2\text{Cr} + 3\text{H}_2\text{O} \rightarrow \text{Cr}_2\text{O}_3 + 6\text{H}^+ + 6\text{e}^-$,</p> <p>- Hydrolysis reaction $\text{Ni} \rightarrow \text{Ni}^{2+} + 2\text{e}^-$, $\text{Ni}^{2+} + \text{H}_2\text{O} \leftrightarrow \text{NiOH}^+ + \text{H}^+$, $\text{Ni}^{2+} + 2\text{OH}^- \rightarrow \text{NiO} + \text{H}_2\text{O}$,</p> <p>- Cathodic reaction $\text{H}_2\text{O} + \text{e}^- \rightarrow \text{OH}^- + \text{H}$, $\text{H}^+ + \text{e}^- \rightarrow \text{H}$,</p> <p>- Ionisation of water in the crack $\text{H}_2\text{O} \leftrightarrow \text{H}^+ + \text{OH}^-$,</p>	<p>- The solubility of metal cations is so low at temperatures of BWR application, that the anodic reaction process can be considered as a source of hydrogen ions.</p> <p>- There is no evidence of oxidation of hydrogen atoms on the metal surfaces within the crack. Oxidation of hydrogen produced initially from cathodic reaction in a crack represents as a relevant factor in low temperature application.</p> <p>- The reduction of oxygen is neglected because the oxygen concentration in the crack is low. Material: sensitised 304ss</p>	[HAS 11]
<p>- Anodic reaction $\text{Fe} \rightarrow \text{Fe}^{2+} + 2\text{e}^-$, $\text{Fe}^{2+} + \text{H}_2\text{O} \leftrightarrow \text{FeOH}^+ + \text{H}^+$, $\text{Cr} \rightarrow \text{Cr}^{3+} + 3\text{e}^-$, $\text{Cr}^{3+} + \text{H}_2\text{O} \leftrightarrow \text{Cr}(\text{OH})^{2+} + \text{H}^+$,</p> <p>- Ionisation of water $\text{H}_2\text{O} \leftrightarrow \text{H}^+ + \text{OH}^-$,</p> <p>- Cathodic reaction $\text{H}_2\text{O} + \text{e}^- \rightarrow \text{H} + \text{OH}^-$, $\text{H}^+ + \text{e}^- \rightarrow \text{H}$,</p>	<p>- The reactions occur in the crack at steady state in aqueous solution. Material: High strength 4130</p>	[HAS 10]
<p>- Cathodic reaction $\text{H}^+ + \text{e}^- \rightarrow \text{H}$</p> <p>- Ionisation of water $\text{H}_2\text{O} \leftrightarrow \text{H}^+ + \text{OH}^-$</p>	<p>- In aqueous solutions hydrogen atoms are electrochemically generated on the metal surface as a partial reaction in the corrosion process or as the primary reaction during cathodic polarisation. The reduction of water provides the dominant source of hydrogen atoms at pH greater than neutral (pH>7).</p>	[HAS 21]
<p>- The enhancement of hydrogen adsorption by iron due to H_2S: $\text{HS}^- \leftrightarrow (\text{HS}^-)_{\text{ads}}$, $(\text{HS}^-)_{\text{ads}} + \text{H}_3\text{O}^+ \leftrightarrow (\text{H}-\text{S}-\text{H})_{\text{ads}} + \text{H}_2\text{O}$, $(\text{H}-\text{S}-\text{H})_{\text{ads}} + \text{e}^- \rightarrow (\text{HS}^-)_{\text{ads}} + \text{H}_{\text{ads}}$,</p> <p>- Reaction involves H_2S compared to HS^- in acid solution. $\text{H}_2\text{S}_{\text{ads}} + \text{e}^- \rightarrow \text{H}_2\text{S}_{\text{ads}}^-$, $\text{H}_2\text{S}_{\text{ads}}^- + \text{H}_{\text{ads}}^+ \rightarrow \text{H}_2\text{S} \dots \text{H}_{\text{ads}}$, $\text{H}_2\text{S} \dots \text{H}_{\text{ads}} \rightarrow \text{H}_2\text{S}_{\text{ads}} + \text{H}_{\text{ads}}$,</p>	<p>- Hydrogen occurs in the presence of hydrogen sulfide during cathodic charging of iron. The presence of H_2S in service solutions can sharply increase hydrogen concentration in the materials.</p> <p>- The first group of reaction does not correspond with the fact that in acid solution the H_2S concentration is higher than HS^-.</p>	[HPD 52]

Because crack propagation behaviour of hydrogen assisted stress corrosion cracking is partially controlled by hydrogen diffusion behaviour through the metallic material, i.e. hydrogen subsurface concentration and hydrogen diffusion coefficient, methods to determine hydrogen diffusion behaviour for the specific material system have to be used, which are explained in Section 2.3.2.

2.3.1.2 Modelling of Hydrogen Absorption during Welding

The susceptibility of welded components to cold cracking can be reduced if the local hydrogen concentration in sensitive regions is constrained to be lower than the critical value, because it is impossible to avoid a build-up of stress-strain distribution in fabrication welding, particularly in offshore construction. In order to improve the understanding of how to control hydrogen absorption levels in the weld metal, the hydrogen sources possible in arc welding should be discussed first in the following section.

In general, the amount of hydrogen absorption in the weld metal during welding is dependent on the hydrogen potential level. For example, a submerged-arc welding process will provide a higher hydrogen concentration in the weld metal than a gas-shielded arc welding processes. The reason may be attributed to hydrogen concentration from surrounding environments and to hydrogen dissociation from atmospheric moisture. As a rough approach, the moisture can be converted to a potential hydrogen content by assuming that all H₂O is completely converted to H₂ (1g H₂O = 1245 ml H₂)^[GEN 17].

Most known Figure 2-20 represents the normal distribution of the hydrogen concentration in the weld metal dependent on the welding processes, determined by the mercury measurement technique. It clearly indicates that relatively low hydrogen concentrations in the weld metal will be obtained by welding with high quality welding processes associated with corresponding filler material and shielding media conditions. For example, the TIG welding process should be designed for fabricating high-quality welded components, which may assist to decrease the risk of hydrogen-assisted cold cracking because the lowest weld metal hydrogen concentration in comparison with other welding processes has been obtained.

In fabrication welding using TIG welding, the weld metal hydrogen distribution can be derived from three possible providers of hydrogen potential: I) shielding gas and ambient environments, II) initial conditions of parent materials, and III) filler material properties as represented in Figure 2-21.

During the TIG welding process, the local hydrogen concentration in welded components is influenced by the procedure of hydrogen dissociation and subsequent hydrogen absorption, which can briefly be described as follows (see Figure 2-22):

1. Dissociation and ionisation of molecular hydrogen in the arc column.
2. Transformation of ionised hydrogen along the arc column into the atomic hydrogen with subsequent absorption by the weld pool, particularly in the hot spot region.
3. Adsorption and desorption reaction of molecular hydrogen at the interface between the arc column and the shielding gas column above the surface of the weld pool.

2. Literature Reviews

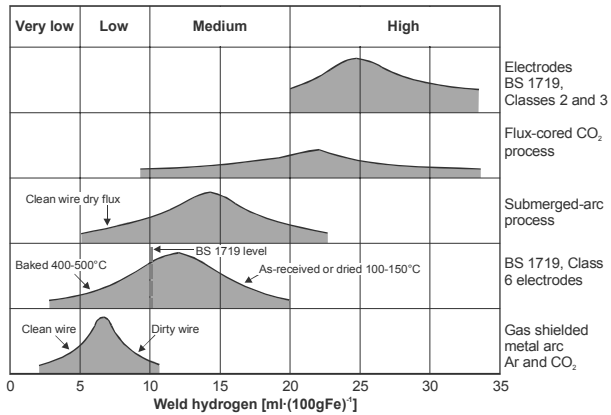


Figure 2-20: Typical hydrogen concentration in the weld metal dependent on various arc welding processes^(GEN 17).

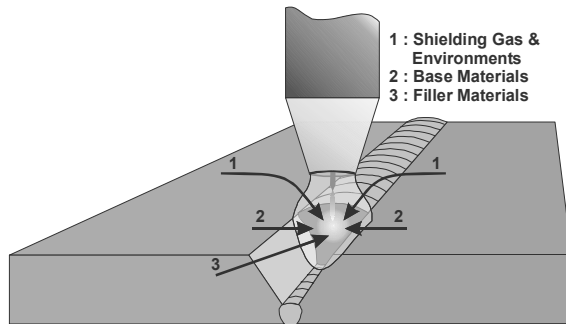


Figure 2-21: Graphical illustration of major hydrogen sources from which hydrogen is picked up by the weld metal during welding.

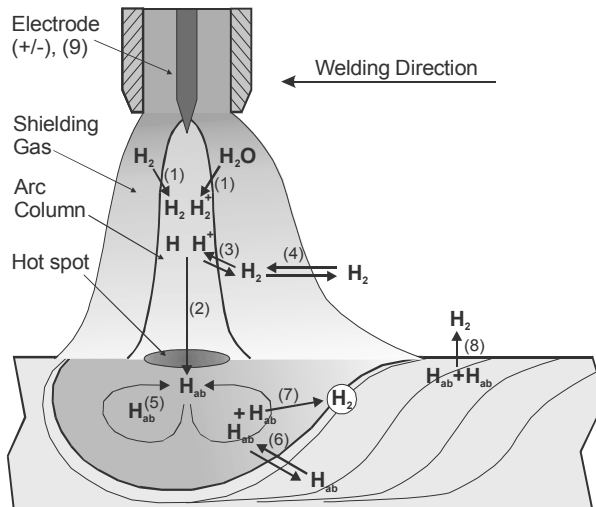


Figure 2-22: Schematic illustration of the hydrogen absorption procedure in the weld metal during welding.

4. Reversible transfer of molecular hydrogen between the shielding gas and ambient environments.
5. Distribution of the absorbed hydrogen in the weld pool by fluid movement affected by Marangoni effects, Lorentz forces, etc.
6. Movement of the absorbed hydrogen from the weld pool into the freshly solidified weld metal by high pressure of the molten metal and of the arc column.
7. Combination of the absorbed hydrogen atoms to form bubbles if hydrogen concentration in the molten metal exceeds the solubility limit in the solid state at the melting point for $p_{H_2} = 1 \text{ atm}$.
8. Equilibrium desorption of the hydrogen atoms absorbed from the solidified weld metal during cooling.
9. Influence of the electrical pole during arc welding on the behaviour of hydrogen distribution in the weld pool.

Figure 2-23 shows the total hydrogen concentration in the weld metal determined by carrier hot gas extraction dependent on hydrogen fraction in Ar-CO₂ shielding gas with using a MAG welding process. The measurement has been carried based on ISO 3690-2000^[GEN 39]. Since a convenient way to calculate hydrogen concentration in the weld metal is generally required by relevant industries, two different methods of the hydrogen content calculation, i.e A method (hydrogen content with respect to the entirely fused metal) and B method (hydrogen content with respect only to the excess of fused metal), have been compared. It clearly shows that the hydrogen concentrations in the weld metal increase by increasing the hydrogen fraction in shielding gas. For example, the hydrogen concentration can be increased up to nearly $6 \text{ ml} \cdot (100\text{gFe})^{-1}$ when the shielding gas mixture with 2% H₂ is used (see A method).

Draugelates et al.^[HAC 18] performed an experimental investigation of hydrogen absorption in the weld pool during welding using TIG welding with argon-hydrogen mixed shielding gas. The results indicate that an increase of the arc voltage and application of pulse technique lead to an increase of the hydrogen concentration in the weld metal. Additionally, the hydrogen concentration in the weld metal was clearly shown to be directly proportional to the hydrogen content in the shielding gas, which can also be affected by various chemical compositions of filler materials.

Thus, homogeneous weld metal hydrogen concentrations of variously typical levels during TIG welding can reasonably be assumed to study the characteristic of hydrogen distribution in welded components by numerical modelling.

2.3.2 Determination of Hydrogen Diffusion Coefficients

The hydrogen diffusion coefficient is a significant material property dependent on the specific system, which can experimentally be determined by electrochemical techniques. Iyer et al.^[HPD 45] reported that hydrogen diffusion through the material is the slowest reaction and acts as a process control for the crack propagation behaviour.

Based on the assumption that the entry of hydrogen into the steel surface is an intermediate adsorption-absorption reaction within local equilibrium reaction, the permeation

2. Literature Reviews

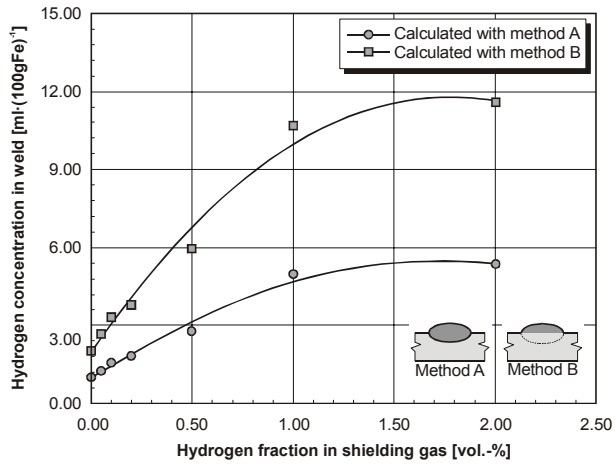


Figure 2-23: Measurement of hydrogen concentration in the weld metal dependent on hydrogen fraction in Ar-CO₂ shielding based on ISO 3690^[HAC 57].

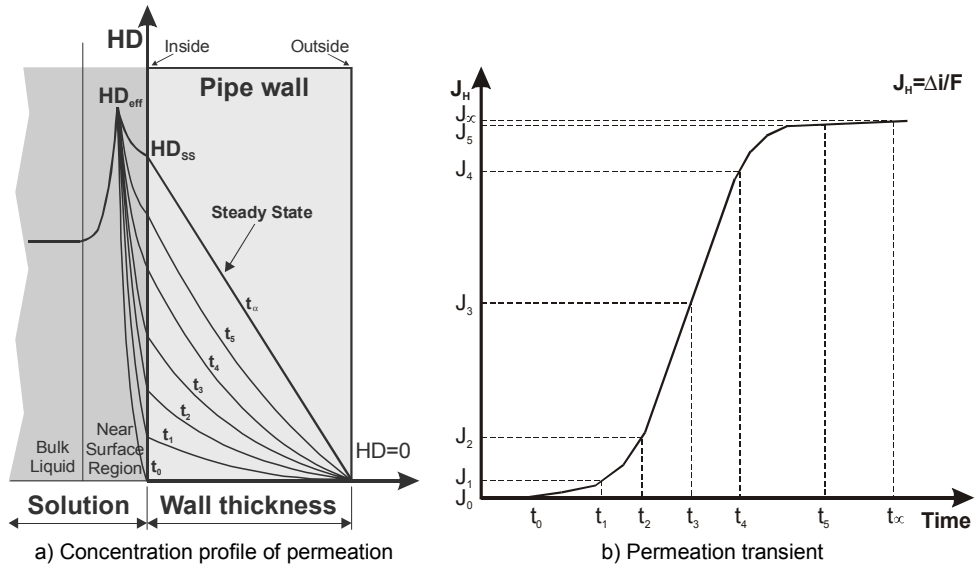


Figure 2-24: Schematic illustration of hydrogen permeation profile through steel membrane: a) Concentration profile of permeation, b) Permeation transient^[HPD 21].

of flux i_{∞} can simply be described as diffusion of hydrogen through the membrane (see Figure 2-24).

For this boundary condition it is assumed that the hydrogen concentration in the membrane increases as a function of time producing a respective increase in the permeation current density measured at the exit surface, where zero concentration of hydrogen is defined because hydrogen is completely oxidised at the exit side^{[HPD 21],[HPD 44]}.

At steady state, the concentration profile of hydrogen permeation is quite flat linear and does not change with permeation time, and the permeation transient reaches its maximum. Therefore, at the final state, hydrogen permeation or current density is given by^{[HPD 21],[HPD 44],[HPD 45]}.

$$\Delta i_{\infty} = \frac{F \cdot D_{eff} \cdot HD_{SS}}{d}, \quad (2-18)$$

where D_{eff} is the effective hydrogen diffusion coefficient, HD_{SS} is the hydrogen subsurface concentration, and d is the membrane thickness.

Due to a difference of hydrogen concentration between the entry surface and the exit surface of the membrane, the hydrogen flux or permeation rate is directly related to the hydrogen subsurface concentration at the cathodic side that has experimentally been determined in previous contributions^{[HPD 21],[HPD 43]} by using the following equations:

$$\frac{J_{\infty}}{z \cdot F} = \frac{D_{eff} \cdot HD_{SS}}{d} \quad (2-19)$$

$$J_H = \frac{\Delta i_{\infty}}{F} = \frac{D_{eff} \cdot HD_{SS}}{d}, \quad (2-20)$$

where J_H is the hydrogen flux through the steel membrane.

After obtaining results of the hydrogen transient curve dependent on time from permeation experiments, hydrogen diffusion coefficients can be evaluated using quantitative analyses as follows^{[HPD 21],[HPD 66],[HPD 67]}.

1. The time lag method
2. The breakthrough time method
3. The inflection point method

2.3.3 The basic principle of diffusion

Diffusion represents the basic mechanism for the modelling in the present work so that an understanding of atomic movement phenomena in materials is necessary. A number of authors^{[HPD 33]-[HPD 50]} proposed that the diffusion of hydrogen through metallic materials can generally be explained based on a basic theory of Fick's law in which the influence of the chemical potential of hydrogen is considered. Therefore, the flux of hydrogen passing through the specific plane can be expressed in terms of a hydrogen concentration gradient based on Fick's first law under the assumption of a constant hydrogen diffusion coefficient by the equation^{[GEN 23],[GEN 29]}.

$$J_H = -D_{eff} \left(\frac{d[HD]}{dx} \right), \quad (2-21)$$

where J_H is the hydrogen flux passing through the specific plane.

2. Literature Reviews

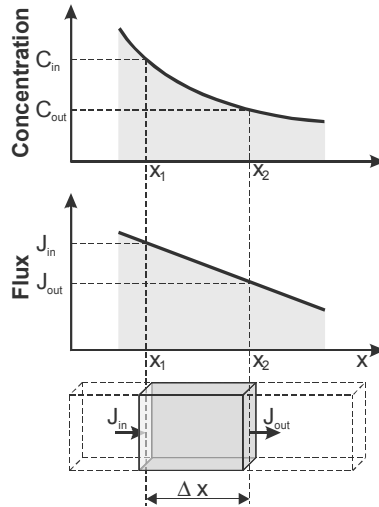


Figure 2-25: Schematic illustration of the basic principle of diffusion theory based on Fick's second law^[GEN 29].

Table 2-7: Hydrogen diffusion parameter relating to the Arrhenius relationship for micro alloy steels^[HPD 68].

Temperature [°C]	D_{H_0} (mm ² ·s ⁻¹)	Q (kJ·mole ⁻¹)
RT-740 (α -range)	1.07E-01	11.14
740-1400 (γ -range)	2.84E-01	31.59
1400-1540 (δ -range)	17.05E-01	42.71
>1540 (Liquid state)	8.49E-01	31.57

In real conditions, hydrogen diffusion coefficients are dependent on position, time, and temperature, but they can be deduced by an Arrhenius relationship to obtain a common form of diffusion coefficient as follows^{[GEN 23],[GEN 29]}:

$$D_{eff} = D_{H_0} \exp\left(-\frac{Q}{R \cdot T}\right), \quad (2-22)$$

where D_{H_0} is the hydrogen diffusion coefficient in the normal state, and Q is the barrier energy for hydrogen diffusion.

A transient diffusion process involves a variation of hydrogen concentration at any position as a function of time, so that the flux of hydrogen has to be modified by integrating second differential into Fick's first law. According to an assumption in Figure 2-25, the gradient of hydrogen entering through the entry surface and subsequently escaping at the exit surface can simply be described by^[GEN 29]:

$$\frac{\partial J_{H_{diff}}}{\partial x} dx = J_{H_{out}} - J_{H_{in}}. \quad (2-23)$$

Under an assumption that the hydrogen diffusion coefficient is constant, the change of hydrogen concentration in the considered element with respect to time is characterised by the following relationship^{[GEN 23],[GEN 29]}:

$$\frac{\partial [HD]}{\partial t} = D_{eff} \left(\frac{\partial^2 [HD]}{\partial x^2} \right). \quad (2-24)$$

This is a principle equation to represent the relationship of hydrogen diffusion in metallic materials based on an assumption of Fick's second law.

2.3.3.1 Trapping Effect

A derivation of effective hydrogen diffusion coefficients in metallic materials from the Arrhenius relationship was generally postulated that the interaction between the dissolved hydrogen atoms and trapping sites such as impurity atoms and structural imperfections is the main reason for changing diffusion behaviour from the ideal situation. Usually, metallic materials consists of a number of heterogeneous structures, for instance grain boundaries, second phases, etc. These heterogeneous structures might represent as traps, which can strongly affect the reduction of hydrogen diffusivity through solid materials.

Figure 2-26 shows trapping sites that can be categorised into five groups; I) grain boundaries, II) pores or micro voids, III) dislocations, IV) precipitates or second phase particles, and V) internal defects such as substituted atoms and stacking faults of the crystal structure^[GEN 19]. The different kinds of trapping sites can be classified based on the active energy or binding energy between hydrogen and the traps as reported elsewhere^{[HAS 101],[HAS 102],[HAS 104],[HPD 39]}.

Referring to the contribution of Oriani^[HPD 18], the interaction between dissolved hydrogen and trapping sites can be determined under equilibrium conditions. In a general state, dissolution of atomic hydrogen in metallic materials is characterised by the enthalpy of solution ΔH^0 with respect to an atmosphere of gaseous hydrogen. In the case where there are trapping sites in the lattice structure of the steels, the interaction between the trapping sites and dissolved hydrogen can commonly be expressed by:



This equation represents a reversible reaction of hydrogen from a normal site to a trapping site with the differential of free energy ΔE_{trap} , and the equilibrium state, which can simply be described as:

$$k_{trap} = \frac{a_{trap}}{a_{nor}}, \text{ or } k_{trap} = \exp\left(-\frac{\Delta E_{trap}}{R \cdot T}\right), \quad (2-26)$$

2. Literature Reviews

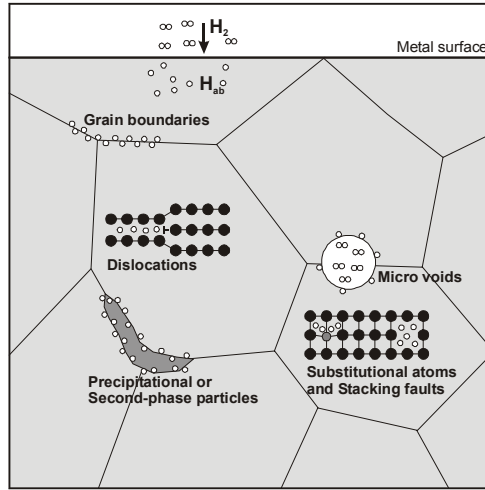


Figure 2-26: Graphical representation of general kinds of trapping sites interacting with dissolved hydrogen^[GEN 19].

where k_{trap} is the rate constant of trapping reaction and a_{trap} and a_{nor} are the hydrogen activities on the trapping site and the normal site, respectively.

Considering a system that consists of a number of normal sites per unit volume N_{nor} and of a number of trapping sites per unit volume N_{trap} , the hydrogen concentration of the two states in such system can be written as $[HD]_{nor} = N_{nor} \cdot \theta_{nor}$ and $[HD]_{trap} = N_{trap} \cdot \theta_{trap}$ for the normal site and the trapping site, respectively. The total hydrogen concentration in the considered system is expressed by:

$$[HD] = [HD]_{nor} + [HD]_{trap}, \quad (2-27)$$

where $[HD]_{nor}$ and $[HD]_{trap}$ are hydrogen concentration in the normal site and trapping site, respectively.

The effective hydrogen diffusion coefficient in the system containing both the normal site and the trapping site can be formulated by the following equation^{[HPD 16],[HPD 18]}:

$$D_{eff} = D_{nor} \frac{d[HD]_{nor}}{d[HD]} = D_{nor} \frac{d[HD]_{nor}}{d[HD]_{nor} + d[HD]_{trap}}, \quad (2-28)$$

where D_{nor} is the hydrogen diffusion coefficient of the normal site.

Thus, the flux of hydrogen given with a combination of normal sites and trapping sites may be expressed based on Fick's first law as^[HPD 18]:

$$J_H = -D_{eff} \frac{d[HD]}{dx} = -D_{eff} \frac{d[HD]_{nor} + d[HD]_{trap}}{dx}, \quad (2-29)$$

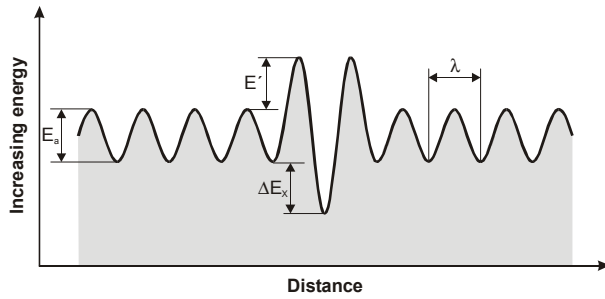


Figure 2-27: Schematic illustration of interaction energy of atomic hydrogen and trapping sites^[HPD 18].

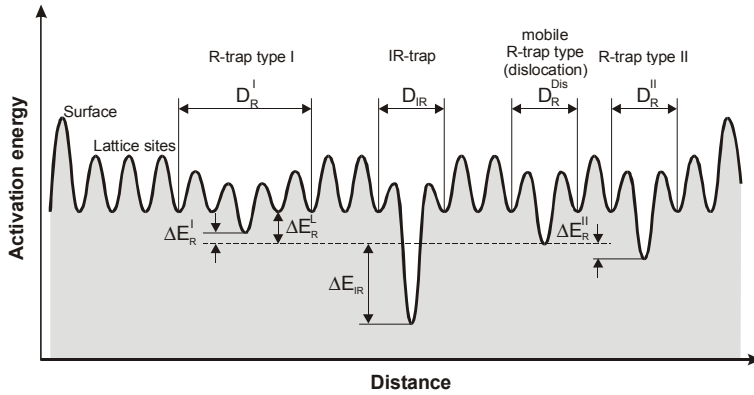


Figure 2-28: Schematic illustration of various trapping sites in terms of trapping energies with influence of trapping diameter^{[HAS 101],[HAS 104]}.

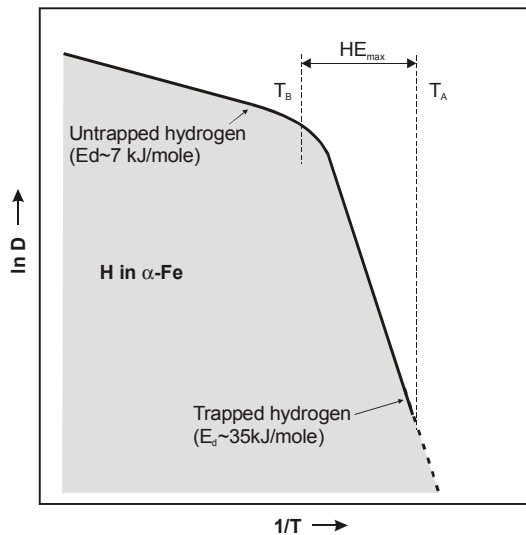


Figure 2-29: Schematic illustration of binding energy between hydrogen and the trapping site influencing on cracking characteristic of α -iron^[HAS 101].

2. Literature Reviews

Table 2-8: Classification of the trapping sites based on the trapping energy for hydrogen-traps interaction.

Trapping sites	ΔE_{trap} (kJ·mole ⁻¹)	Remark	Reference
Dislocation-elastic stress filed	20	α -Iron system	[HAS 101]
Screw dislocation	20-30	α -Iron system	[HAS 101]
Mixed dislocation	59	α -Iron system	[HAS 101]
Grain boundary	~59	α -Iron system	[HAS 101]
Free surface	70-95	α -Iron system	[HAS 101]
Fe ₃ C interface	84	α -Iron system	[HAS 101]
TiC interface	96	α -Iron system	[HAS 101]
TiC	51-63	Irreversible /Fe-Ti alloy	[HPD 39]
Grain boundary	53-58	Reversible/Fe-Ti alloy	[HPD 39]
Dislocation	24	Reversible/Fe-Ti alloy	[HPD 39]
Lattice site	8	Very reversible/Fe-Ti alloy	[HPD 39]
Ti-Substitutional atom	26	Reversible/Fe-Ti alloy	[HPD 39]

Jumping of atomic hydrogen into the favourite trapping sites is controlled by free energy of the considered system^{[HAS 101],[HPD 18]}. Figure 2-27 schematically represents the sinusoidal curve of free energy levels of the trapping site, which is lower than that of the normal site by a quantity of ΔE_x and is bounded by a high energy barrier, which is the sum of the amplitude energy in the normal site E_a and the additional energy E' . This means that hydrogen requires energy equal to E_a+E' in order to overcome the barrier energy before arriving at the trapping site, and it requires much more energy to escape from the trapping site. From these insights, one reason is given to explain the phenomenology of the accumulation of dissolved hydrogen at the trapping sites^[HPD 18].

However, Bernstein et al.^[HAS 105] stated that the trapping sites can be classified into two major groups: I) the reversible trapping site and II) the irreversible trapping site based on the potential energy or binding energy between hydrogen and trapping sites without consideration of barrier energies as represented in Figure 2-28.

Additionally, Gibara et al.^[HAS 101] confirmed that hydrogen-trap interactions may well be characterised if the density of trapping sites, the binding energy of traps, and the fraction of hydrogen at the trapping sites are known. Four major groups of trapping sites were approximately determined with respect to the required heat for hydrogen dissolution in iron ΔE^0 (~29 kJ·mole⁻¹) as follows: I) point defects have been characterised as the weak traps by ΔE_{trap} lower than 15 kJ·mole⁻¹, II) point defects with moderate to strong interaction have been characterised as the moderate traps by $\Delta E_{trap} \geq 20$ kJ·mole⁻¹, III) dislocations with moderate to strong interaction have been characterised as strong traps by $20 \text{ kJ}\cdot\text{mole}^{-1} \leq \Delta E_{trap} \leq 60 \text{ kJ}\cdot\text{mole}^{-1}$, and IV) grain boundaries or interface surfaces with strong interaction have been characterised by $\Delta E_{trap} \sim 50\text{-}100 \text{ kJ}\cdot\text{mole}^{-1}$.

Table 2-8 lists required activation energies for hydrogen-trap interactions with respect to different kinds of traps and material systems.

Hydrogen assisted cracking caused by trapping effects can take place in the material if the binding energy of the hydrogen-traps interaction becomes stronger and the atomic hydrogen cannot escape from the trapping sites^[HAS 101]. As represented in Figure 2-29, hydrogen assisted cracking in α -iron mostly occurs at room temperature if the binding energy is in the range of 7 to 35 kJ·mole⁻¹. At elevated temperatures, the binding energy becomes lower than at room temperature, and hydrogen can then overcome attractive forces from the trapping sites, which is defined as the untrapped hydrogen.

2.4 Crack Propagation Characteristics

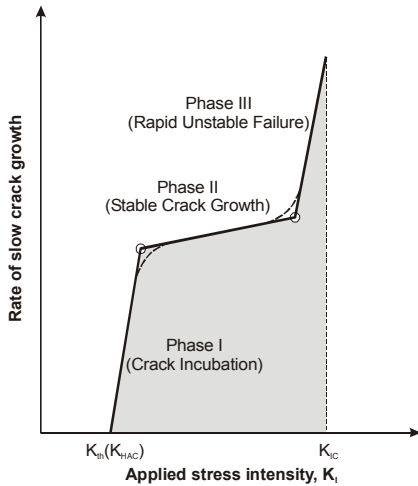
Crack propagation of metallic materials is usually characterised by three distinct phases:

I) Crack incubation, Phase I, is the first cracking period where the degradation of the materials requires significant dislocation movement or plasticity, particularly for the local scale. Nucleation and the subsequent formation of a micro-crack takes place. The crack will continue to propagate if the local stress-strain reaches the critical value. Hirth^[HAS 99] reported that hydrogen lowers the yield stress and the initial flow stress of pure iron at temperatures higher than 200 K and that a sufficient local hydrogen concentration is able to facilitate the mobility of screw dislocation by enhancing double-kink nucleation with promotion of slip planarity. For edge dislocations, dissolved hydrogen hinders the kink motion.

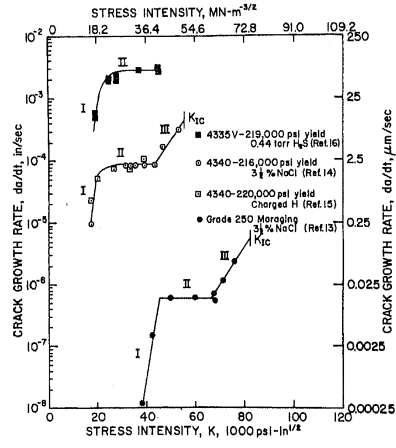
In alloyed steels, local hydrogen concentration may reduce the yield stress with subsequent occurrence of rupture of the alloyed steels by either enhanced dislocation formation or void formation at grain boundaries and of the interface of second-phase particles^[HAS 99]. However, a competition between softening effects associated with an enhanced mobility of screw dislocations in the case of dislocation injection and hardening effects associated with multiple slip caused by plastic incompatibility may take place in this cracking stage^[HAS 99]. Nevertheless, the crack propagation characteristic in this stage is generally described in terms of the crack propagation rate as a function of stress intensity levels (see Figure 2-30). The nucleation of the crack appears if the local stress intensity reaches the threshold stress intensity, K_{th} , affected by hydrogen assisted cracking. The crack propagation rate during the incubation period is relatively high compared to that during stable crack growth. Fractographic analyses of the crack incubation stage might reveal intergranular (IG) or quasi-cleavage (QC)^{[HAS 13],[HAS 99]}.

II) Stable crack growth, Phase II, is stable propagation of a macroscopic crack at stress intensity levels higher than the threshold value, but lower than the critical value K_{IC} (see Figure 2-30). In the presence of local hydrogen taken up from aqueous environments, the hydrogen-iron interaction ahead of the crack tip can significantly influence the behaviour of the crack propagation by degrading the material properties. The interesting phenomenon of this stage is the compatibility between local hydrogen concentration and stress intensity at the specific point ahead of the crack tip. This means that a sufficient local hydrogen concentration must be available at the specific point ahead of the crack tip for a specific stress intensity level.

2. Literature Reviews

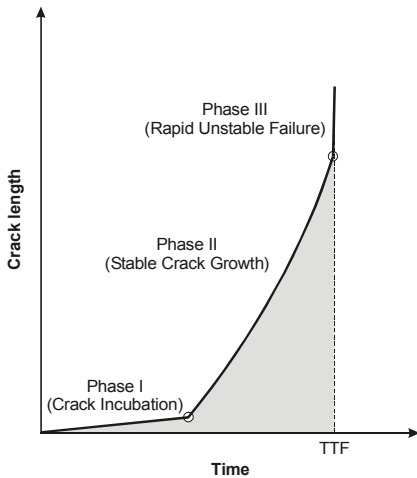


a) Schematic illustration

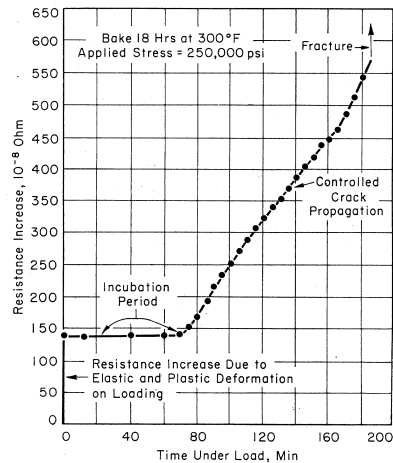


b) Experimental determination^[HAS 13]

Figure 2-30: Kinetics of the crack propagation as a function of stress intensity for hydrogen assisted cracking.



a) Schematic illustration



b) Experimental determination^[HAS 18]

Figure 2-31: General relationship of crack length versus time for describing material properties under a condition of hydrogen assisted cracking.

Crack propagation in this stage can shift to the region of unstable crack propagation if the required local hydrogen concentration is not available while local stress continuously increases. Therefore, the kinetics of stable crack growth can be said to be strongly dependent on the transportation of hydrogen from the environment exposed newly cracked surface into the specific zone ahead of the crack tip because a sufficient hydrogen concentration must be provided for crack growth in this stage^[HAS 86].

Due to the fact that fracture in this stage occurs at the lowest rate of crack propagation rate, this stage can dominate the lifetime of components. The fractograph of the stable

crack growth is characterised by transgranular (TG) or mixed mode tearing and quasi-cleavage (QC)^[HAS 99].

III) Unstable crack growth, Phase III, occurs when the stress intensity ahead of the crack tip is greater than the critical stress intensity K_{IC} , which can be decreased by the presence of a sufficient local hydrogen concentration. The last stage of fracture is controlled by high stress intensity levels due to increased crack length or local stress-strain in front of the crack tip, and this portion of the fractograph is less susceptible to hydrogen degradation than that of the previous stage of stable crack propagation^[HAS 86]. Hence, the fractograph of unstable crack growth is characterised by micro-void coalescence (MVC)^[HAS 86] or transgranular ductile rupture by hole growth^[HAS 99].

Although the degradation of material properties affected by hydrogen assisted cracking is usually described in terms of the crack propagation rate dependent on stress intensity levels as represented in Figure 2-30, a relationship of crack length as a function of time can also be used to describe the crack propagation behaviour of materials as represented in Figure 2-31.

For lifetime prediction, the crack length versus time diagrams are more useful and applicable than the conventional diagram of crack growth rate versus stress intensity because the crack length versus time diagram directly represents the time to failure of components under the specific test condition. Troiano^[HAS 18], who investigated the effects of hydrogen on the mechanical properties of high strength steels, has shown that an incubation period for crack initiation and a period of stable crack growth control the total lifetime of such steels. The kinetics of crack initiation and propagation can be illustrated by the electrical resistance changes method as represented in Figure 2-31B.

In fact, failure of high-strength steel components has evidently been found that the loss in ductility has played as a significant role in controlling lifetime of such components. Therefore, the characteristics of crack growth caused by hydrogen assisted cracking can explicitly be explained in terms of strain versus hydrogen and crack length. Additionally, in comparison with stress and/or stress intensity, strain is more conveniently used to make a direct correlation with the material ductility.

2.4.1 Determination of Crack Propagation Kinetics

The relationship between crack propagation and time describes the kinetics of crack growth. It is very useful for studying the properties of materials subjected to mechanical loads, interacting mechanical loads, environmental impacts and particularly hydrogen in the case of this study. Therefore, the crack propagation under the influence of interacting mechanical loads and hydrogen attacks is the main focus of attention in this section. Generally, crack propagation kinetics can be expressed by^[HAS 108].

$$V_{crack} = \frac{a}{t} = \frac{\sum \Delta a}{\sum \Delta t}, \quad (2-30)$$

where V_{crack} is the crack propagation rate, a is the total crack length, and t is the total time for the crack propagation.

2. Literature Reviews

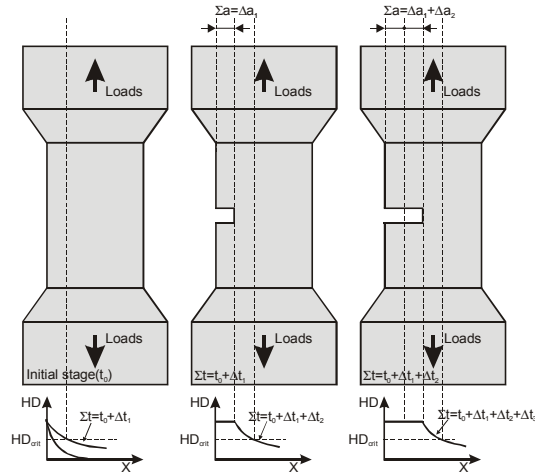


Figure 2-32: Schematic illustration of the kinetics of crack propagation in Mode I.

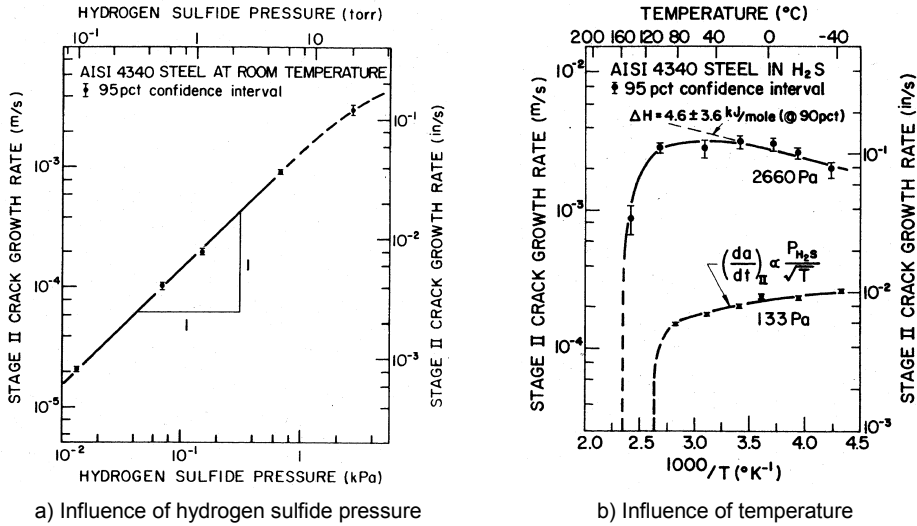
Figure 2-32 schematically illustrates the crack propagation rate of hydrogen assisted stress corrosion cracking in standard test specimens according to Equation (2-30): The interaction between the local hydrogen concentration and the local stress-strain distribution is taken into account for defining the crack propagation rate.

The kinetics of crack propagation is influenced by hydrogen supplying processes, which are related either to the rate of hydrogen production at the newly cracked surface depending on the rate of hydrogen transportation from the bulk solution to the crack tip and on a subsequent adsorption process, or to the rate of hydrogen diffusion into the specific zone ahead of the crack tip.

Considering the contribution of Wei et al.^[HAS 103], models for studying the effects of environmental factors such as pressure and temperature assisting crack propagation under sustained loads have been developed in order to obtain a better explanation of the kinetics of crack propagation, particularly in Stage II for 18Ni maraging steels. In this case of very high rates of surface reaction, the newly cracked surfaces act as an effective sink and can significantly reduce the hydrogen pressure at the crack tip. The transportation rate of hydrogen may control the reaction net rate when the external hydrogen pressure is sufficiently low. According to the authors, the kinetics of crack propagation can simply be found by keeping balance between the transportation rate and the consumption rate by surface reaction, which is directly proportional to the external hydrogen pressure and inversely proportional to the square-root of the absolute temperature as^[HAS 103]:

$$\left(\frac{da}{dt}\right)_{II} \propto \frac{P_{H_2}}{\sqrt{T}}. \quad (2-31)$$

As more general approach just to emphasize this, the model developed by Wei et al.^[HAS 103] represents definitively an analytical model which considers the effects of crack propagation and hydrogen uptake. Lu et al.^[HAS 61] carried out an experimental investigation to determine the crack growth rate control process in hydrogen sulfide environments for an AISI 4340 steel, and proposed that the mean crack propagation rate of Stage II is directly



a) Influence of hydrogen sulfide pressure
 b) Influence of temperature
 Figure 2-33: Kinetics of crack propagation in Stage II of an AISI 4340 steel during exposure to hydrogen sulfide test solution^[HAS 61].

proportional to the partial pressure of hydrogen sulfide in the test solution in accordance with the following equation^[HAS 61]:

$$\left(\frac{da}{dt}\right)_{II} \propto (p_{H_2S})^b, \tag{2-32}$$

where p_{H_2S} is the partial pressure of hydrogen sulfide environments and b is the constant value equal to 1 at low partial pressure, which decreases with increasing the partial pressure of hydrogen sulfide in the test solution as represented in Figure 2-33a. The effects of crack propagation and hydrogen redistribution are not considered appropriately.

The kinetics of crack propagation in Stage II can be affected by the environment temperature (see Figure 2-33b). For example, at a hydrogen sulfide partial pressure of 133 Pa, the crack propagation rate is inversely proportional to the square root of temperature for the determination in the low temperature range (analogous to Equation (2-31)). In the case that the hydrogen sulfide pressure reaches to 2660 Pa, the crack propagation rate seems to be different from that at the lower hydrogen sulfide partial pressure. The Arrhenius relationship is more suitable to describe the crack propagation rate in the low temperature range than in the elevated temperature range. Similar to Lu et al.^[HAS 61] and as to the model from the diagram (Figure 2-33b), it should be noted that increasing partial pressures of hydrogen sulfide in environments will increase the crack propagation rate, because a sufficient local hydrogen concentration ahead of the crack tip can be provided by high hydrogen sulfide partial pressures within shorter time than by the low partial pressure of hydrogen sulfide.

With increasing hydrogen pressure, the kinetics of crack propagation for hydrogen assisted stress corrosion cracking is controlled by the diffusion process of atomic hydrogen into the susceptible zone ahead of the crack tip rather than by the transport process in the

2. Literature Reviews

bulk solution and surface reaction. As anticipated by the authors, the kinetics of crack propagation is directly proportional to the square root of the hydrogen diffusion coefficient and of the hydrogen pressure as expressed by the following equation^[HAS 103]:

$$\left(\frac{da}{dt}\right)_{II} \propto \sqrt{p_{H_2} \cdot D_{eff}} = \sqrt{p_{H_2} \cdot D_{H_0}} \exp\left(-\frac{E_{H_{diff}}}{2RT}\right), \quad (2-33)$$

where $E_{H_{diff}}$ is the activation energy required for hydrogen diffusion through solid materials.

In the case that the pressure of hydrogen at the crack tip is equal to the external pressure since hydrogen adsorption processes or surface reactions are relatively slow, the crack propagation rate is directly proportional to the partial pressure of hydrogen at the crack tip and the reaction rate constant of adsorption processes can be formulated by the following equation^[HAS 103]:

$$\left(\frac{da}{dt}\right)_{II} \propto p_{H_2} \cdot k_{ads} \propto p_{H_2} \exp\left(-\frac{E_{ads}}{RT}\right), \quad (2-34)$$

where k_{ads} is the rate constant of the adsorption process and E_{ads} is the energy required for the adsorption process.

The study of hydrogen assisted stress corrosion cracking in high-strength and martensitic steels by Gerberich^[HAS 13] presents fractographs of Stage I of the crack propagation process with relatively low stress intensities corresponding to the small plastic zone which show either an intergranular (IG) fracture topography or a quasi-cleavage (QC) fracture topography. Based on the assumption that crack propagation takes place when the local hydrogen concentration reaches the critical value, the kinetics of the crack propagation of Stage I can simply be described as the average incremental crack jump divided by the average time between jumps by the relationship^[HAS 13]:

$$\left(\frac{da}{dt}\right)_I = \frac{2 \cdot (1 + \nu) \cdot [HD]_{ini} \cdot D_{eff} \cdot \bar{V}_H \cdot K_I}{3 \cdot g^{1.5} \cdot ([HD]_{crit} - [HD]_{ini}) \cdot R \cdot T}, \quad (2-35)$$

where $[HD]_{ini}$ and $[HD]_{crit}$ are the hydrogen concentration at the initial state and the critical state, respectively.

The main difference between Stage I and Stage II is that the hydrostatic stress gradient at the susceptible zone ahead of the crack tip increases with increasing stress intensity level for the crack propagation in Stage I, but it is independent of stress intensity levels for the crack propagation of Stage II. Therefore, the approximation of the crack propagation rate in Stage II will take account of the yield stress of the material instead of the hydrostatic stress as given by^[HAS 13]:

$$\left(\frac{da}{dt}\right)_{II} = \frac{9 \cdot [HD]_{ini} \cdot D_{eff} \cdot \bar{V}_H \cdot \sigma_{ys}}{2 \cdot g \cdot R \cdot T \cdot ([HD]_{crit} - [HD]_{ini})}, \quad (2-36)$$

where g is the average grain size of the material and σ_{ys} is the yield strength of the material.

Prior to an occurrence of material rupture, the stress intensity level ahead of the crack tip becomes high enough to produce ductile rupture. Typical fractographs of Stage III would reveal partially intergranular (IG) and mostly ductile rupture. The rupture stress intensity of Mode I is thus taken into account for calculating the kinetics of the crack propagation in Stage III as formulated in the following equation^[HAS 13]:

$$\left(\frac{da}{dt}\right)_{III} = \frac{9 \cdot [HD]_{ini} \cdot D_H \cdot \bar{V}_H \cdot K_I^2}{2 \cdot \sigma_{ys} \cdot E \cdot g^2 \cdot R \cdot T \cdot ([HD]_{crit} - [HD]_{ini})}, \quad (2-37)$$

where E and K_I are material properties as the Young's modulus and the stress intensity of Mode I, respectively.

Summarising the approach by Gerberich^[HAS 13], it represents at least an analytical model considering the diffusion process ahead of the crack tip. It also represents a more simple approach than a numerical model^[HAS 108]. However, the presumed effects of an increased grain size g in the approach by Gerberich on decreasing the crack propagation rate shows some inconsistency. Normally, the opposite influence of the grain size has to be presumed. Gerberich does not mention in his publication why he uses such an approach for the effects of the grain size^[GEN 40]. The consistency of the model has thus at least to be verified by respective experiments. As proposed by Toribio et al.^[HAS 28], the kinetics of the crack propagation for hydrogen assisted cracking in metallic materials can be expressed as function of stress intensity factors, which are dependent on the total time of hydrogen assisted cracking. Thus, the relationship is simply written by:

$$\frac{\partial a}{\partial t} = f(K_I, t_{crack}), \quad (2-38)$$

where t_{crack} is the total time of hydrogen assisted cracking.

However, it should be noted that the critical stress intensity factor is always dependent on the changing parameters involved with hydrogen assisted stress corrosion cracking and also varies drastically with increasing crack length and the redistributed hydrogen concentrations^[HAS 28].

Chu et al.^[HAS 35] examined the stress corrosion crack growth behaviour of high-strength steels (4130 and 4340) in aqueous solution. The results showed that the Stage II crack growth rate is exponentially thermal-dependent. This means that the crack growth rates increase with temperature at a constant activation energy of 34 ± 3 kJ/mole. Furthermore, the rate of electrochemical reaction plays as a significant role in controlling the kinetics of crack propagation in high-strength steels in aqueous environments. The general mathematical form that can be used to describe the kinetics of crack propagation according to the above description is simply given by^[HAS 35].

2. Literature Reviews

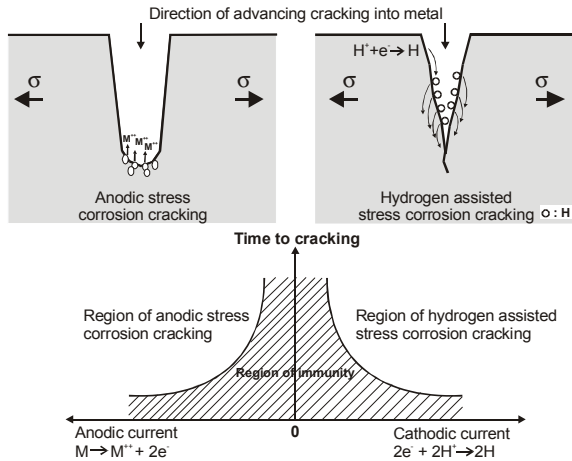


Figure 2-34: Schematic illustration showing differentiation between anodic dissolution stress corrosion cracking and hydrogen assisted stress corrosion cracking at the cathodic reaction^[GEN 15].

$$\left(\frac{\partial a}{\partial t}\right)_{II} = C_{xx} \exp\left(-\frac{E_{xx}}{R \cdot T}\right), \quad (2-39)$$

where C_{xx} and E_{xx} are the pre-exponent terms and the corresponding activation energy, respectively, that individually depend on the hydrogen uptake process including the transport process, the surface reaction process, and the diffusion process.

2.4.2 Mechanisms of Stress Corrosion Cracking

The phenomenon of hydrogen assisted stress corrosion cracking has been distinguished from that of the stress corrosion cracking by the interaction with applied currents for many years. However, recent conferences showed that both failure types of structural metallic materials are related more with each other than generally anticipated. Thus, the distinct mechanisms of stress corrosion cracking should be described for a better understanding of the crack behaviour of metallic materials. Stress corrosion cracking in the fashioned style is considered if a component becomes more locally anodic and if accelerated cracking occurs during this process. Hydrogen assisted stress corrosion cracking is frequently only associated, if the crack initiation site is more cathodic. Figure 2-34 represents the crack propagation of metallic materials taking account of the cracking mode and of applied currents for hydrogen assisted stress corrosion cracking and anodic stress corrosion cracking.

The anodic reaction of stress corrosion cracking involves the movement of metallic ions from the matrix into the environmental solution, namely anodic dissolution. The anodic dissolution process is assumed to contribute to crack propagation with the generation of electrons from metal atoms to form metal ions during the anodic reaction. Therefore, the kinetics of crack propagation in the anodic dissolution mode is sometimes related to Faraday's law.

Results from experimental examinations of environment-induced deformation localisation during transgranular stress corrosion cracking of steels by Lian et al.^[HAS 67]

showed that the crack nucleation and subsequent propagation in steels dealing with the anodic dissolution mode can be calculated with Faraday's relationship as given in the following equation^[HAS 67]:

$$\frac{\partial a}{\partial t} = i \frac{M_{Fe}}{z_{Fe} \cdot F \cdot \rho_{Fe}}, \quad (2-40)$$

where i is the applied current density, M_{Fe} is the atomic weight of steels, z_{Fe} is the valence electron of dissolved species, and ρ_{Fe} is the density of steels.

Turnbull^[HAS 21] summarised the mechanisms of environment assisted cracking focused as anodic dissolution (slip-dissolution), anodic reaction-induced cleavage, and surface mobility.

The Slip dissolution model of cracking is a simple model for describing the crack advance with respect to the interaction between environments and mechanical loads. The basic principle of this model is that crack propagation may occur by a loss of localised metals, which results from the damage of oxidation surfaces by sufficient localised straining. Thus, the rate of crack propagation is dependent on the extent of mass loss during rupture of the oxide surface, which can be described by using the modified equation based on Faraday's relationship as expressed by^[HAS 21]:

$$\frac{da}{dt} = \frac{M_{Fe} \cdot Q_f}{z_{Fe} \cdot F \cdot \rho_{Fe} \cdot \varepsilon_{frac}} (\dot{\varepsilon}_{ct}), \quad (2-41)$$

where Q_f is the oxidation charge passed the rupture event, ε_{frac} is the fracture strain of the material and $\dot{\varepsilon}_{ct}$ is the strain rate at the crack tip.

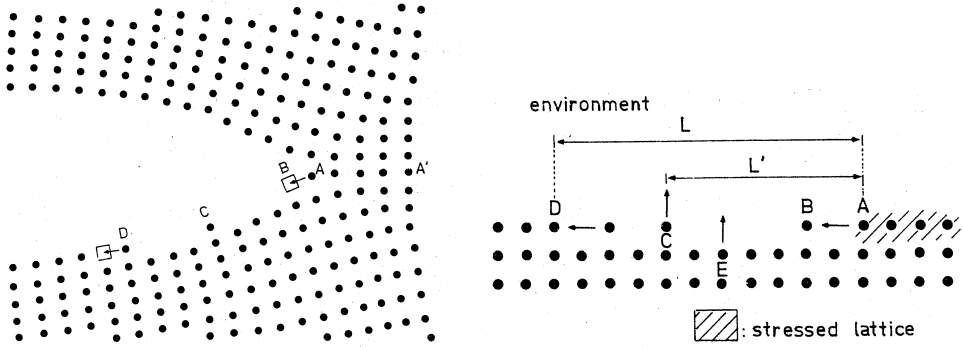
The re-filming reaction can result in the decay of the metal dissolution. Both the dissolution rate and the re-filming rate will be dependent on the interaction of the metal with the local environments at the crack tip.

Anodic reaction-induced cleavage is a mechanism proposed to be responsible for high rates of transgranular crack propagation in comparison with the normal reaction of metal dissolution. The basic premise of this model is that crack initiation takes place in ductile thin films induced by anodic reaction at the crack tip, and crack propagation subsequently takes place in ductile metal substrates in a cleavage mode. However, the extent of crack propagation is dependent on the rate of dislocation emission from the crack tip and on the dislocation density that would be greater for high-strength steels. Cracking in the metal substrates can completely be induced by mechanical loads. Since the crack propagation of this mode involves film rupture induced cleavage, the average crack propagation rate is simply expressed by^[HAS 21]:

$$\frac{da}{dt} = \left(\frac{M_{Fe}}{z_{Fe} \cdot F \cdot \rho_{Fe}} Q_f + j \right) \frac{\dot{\varepsilon}_{ct}}{\varepsilon_{frac}}, \quad (2-42)$$

where j is the jump distance for crack propagation.

2. Literature Reviews



a) Travelling of atoms along the crack surface b) Atoms travel to the kink site on crack the surface
 Figure 2-35: Schematic illustration of crack propagation by the surface mobility cracking mechanism during anodic reactions^[HAS 111].

The surface mobility model was proposed for characterising the crack propagation of non-hydride forming metals based on anodic reaction processes and is applicable to both liquid metal embrittlement and hydrogen embrittlement as demonstrated by Galvele^[HAS 111]. The basic hypothesis of this model is that the capture of vacancies by the stressed lattice at the crack tip may result in crack propagation. An increase of the stresses at the crack tip will enhance the escape of metal atoms from the crack tip to the crack opening by coming along the crack surface (see Figure 2-35a). Consequently, vacancies are created at the crack tip, which induce the extent of crack propagation with one atomic distance as represented in Figure 2-35 b.

The crack propagation rate according to the surface mobility model can be determined using the following equation^[HAS 111]:

$$\frac{\partial a}{\partial t} = \frac{D_{met}}{L_{smm}} \left[\exp \left(\frac{\sigma_{ct} \cdot a_{smm}^3}{kT} \right) - 1 \right], \quad (2-43)$$

where D_{met} is the surface self-diffusion coefficient, L_{smm} is the diffusion distance of vacancies, σ_{ct} is the tensile stress at the crack tip and a_{smm} is the crack distance advanced by movement of vacancies.

2.5 Failure and Fracture Mechanisms for Modelling Hydrogen Assisted Cracking

Hydrogen assisted stress corrosion cracking is a subordinate form of hydrogen assisted cracking, which involves the interaction of material properties, environments, and mechanical loads (see Figure 2-36) leading to crack initiation and subsequent crack propagation until rupture of the component.

The mechanical load is partially a significant factor for hydrogen assisted stress corrosion cracking. For modelling hydrogen assisted stress corrosion cracking, it is necessary to provide the mechanisms for the mechanical fracture failure of materials.

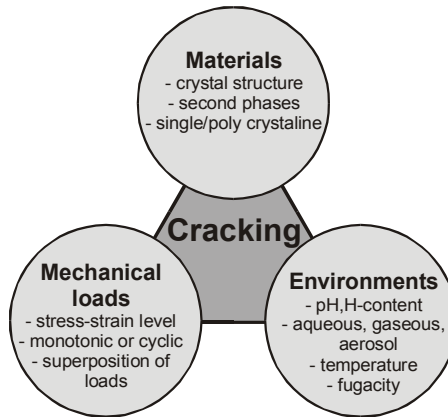


Figure 2-36: Macroscopic aspect of three main factors influencing hydrogen assisted stress corrosion cracking behaviour^[HAS 112].

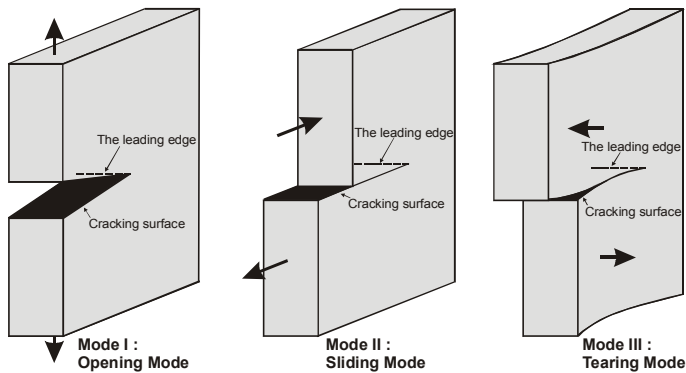


Figure 2-37: Graphical illustration of the three general modes of cracking^[GEN 21].

2.5.1 Fracture Theory

Typical cracking in the solid materials can be subdivided into three modes as demonstrated in Figure 2-37. The opening mode, Mode I, relates to applied external stress normal to the faces of the crack which results in the displacement of the crack surface in the perpendicular direction to the leading edge of the crack. Mode II, sliding mode, refers to external stresses applied normal to the leading edge of the crack. The displacement of the crack surface appears in the plane of the crack and perpendicular to the leading edge of the crack. Mode III, the tearing, is caused by external shear stresses applied parallel to the leading edge of the crack. The crack surface displacement is in the plane of the crack and parallel to the leading edge of the crack.

Since Mode I is the most important cracking mode for technical applications^{[GEN 14],[GEN 21]}, all calculations of crack propagation generally focus more on Mode I than the others. The stress intensity factor for Mode I, K_I , is likely to determine the stress-strain field around the crack tip. The critical value of stress intensity generated by the stress-strain distribution ahead of the crack tip, K_{Ic} , is a material property and generally given by^[GEN 21]:

2. Literature Reviews

$$K_{Ic} = \sigma_{crit} \sqrt{\pi \cdot a}, \quad (2-44)$$

where σ_{crit} is the critical tensile stress of Mode I required for the crack propagation, and a is the actual crack length.

In the general case, the stress intensity as a function of the specimen's geometry can be expressed by^[GEN 14]:

$$K_I = \sigma \sqrt{\pi \cdot a} \cdot f(a, W). \quad (2-45)$$

Rupture of the material will take place when the stress intensity factor K_I reaches the critical value of stress intensity. However, the critical value can be decreased with a degradation of material properties by environment-material-load interactions, as for example.

2.5.1.1 Definition of Local Strain Rate

Since hydrogen assisted cracking is a time-dependent phenomenon which depends on the diffusion process on one side and on the mechanical load on the other, strain rates with respect to a unit of time are much more applicable for lifetime prediction of components. As proposed by Ford^[HAS 31], the local strain rate at the crack tip can differently be calculated dependent on the test methods containing constant strain rate test, slow strain rate test, and cyclic loads test, which are described as follows:

$$\dot{\epsilon}_{loc} = A \dot{\epsilon}_{creep} + B \left[\frac{V_{crack}}{x^*} \right] : \text{for constant load} \quad (2-46)$$

$$\dot{\epsilon}_{loc} = C \dot{\epsilon}_{glob} + D \left[\frac{V_{crack}}{x^*} \right] : \text{for slow strain rate} \quad (2-47)$$

$$\dot{\epsilon}_{loc} = \left[\frac{\delta \epsilon}{\delta K} \right] \dot{K} + \left[\frac{\delta \epsilon}{\delta a} \right] V_{crack} : \text{for cyclic load}, \quad (2-48)$$

where $\dot{\epsilon}_{loc}$ is the local strain rate ahead of the crack tip, $\dot{\epsilon}_{glob}$ is the global strain rate, V_{crack} is the average value of the crack propagation rate, x^* is the value dependent on the movement of dislocation, and A , B , C , and D are constant values dependent on the test method.

Considering these equations, it should be noted that the local strain rate is a function not only of the externally applied stress of stress intensity, but also of the crack propagation rate.

The study on the effect of strain rate on the behaviour of stress corrosion cracking in alloyed metals performed by Parkins^[HAS 87] indicated that the local strain rate ahead of the crack tip is a function not only of externally applied strain and of the crack propagation rate, but also of a number of cracks along the gauge length. The equation for calculating the

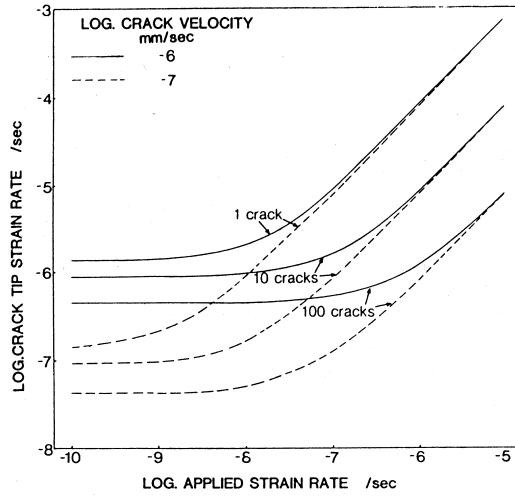


Figure 2-38: Influence of externally applied strain rate on the local strain rate ahead of the crack tip taking account of the crack propagation and of the number of cracks along the gauge length^[HAS 87].

local strain rate taking account of the number of cracks existing on the gauge length is written by:

$$\dot{\epsilon}_{loc} = \left(\frac{75}{N}\right) \dot{\epsilon}_{glob} + \left(\frac{V_{crack}}{5}\right) \log\left(\frac{1000}{N}\right), \quad (2-49)$$

where N is the number of cracks along the gauge length.

This equation indicates that the local strain rates decrease with increasing number of cracks along the gauge length at any applied global strain rates as represented in Figure 2-38. This equation represents one of the seldom approaches to consider the run of concurrent cracks.

From the article, it can be proposed that a single crack appearing on the gauge length of a test component exerts more influence on control the life time than many cracks because at the specific global strain rate the single crack can generate higher local strain rates than a greater number of cracks along the gauge length.

As another point, the local and global strain rates have to be distinguished. Toribio^[HAS 92] experimentally examined local parameter effects on the behaviour of stress corrosion cracking and hydrogen assisted stress corrosion cracking of alloyed steels by using four different types of pre-cracked and notched tensile specimens. He proposed that the local strain rate and the global strain rate can simply be expressed by the differential of the displacement within a specific time as given in the following equations:

$$\dot{\epsilon}_{loc} = \frac{u_{loc}^{i+1} - u_{loc}^i}{B \cdot \Delta t} \quad (2-50)$$

2. Literature Reviews

$$\dot{\epsilon}_{glob} = \frac{u_{glob}^{i+1} - u_{glob}^i}{D \cdot \Delta t}, \quad (2-51)$$

where B and D denote the specimen parameters of thickness and of diameter, respectively.

Furthermore, Toribio also formulated a simple relationship in order to describe the ratio of the local strain rate and the global strain rate as a function of various dimensionless variables referring to material properties, crack geometry, and levels of global loading as:

$$\frac{\dot{\epsilon}_{loc}}{\dot{\epsilon}_{glob}} = f(\nu, c, P/E; r_{ct}/D, a/D, L_{glob}/D; \epsilon_{glob}), \quad (2-52)$$

where ν is Poisson's ratio, c is the hardening index, P/E is the plastic-elastic ratio, r_{ct}/D is the ratio between the radius of the crack tip and the specimen diameter, a/D is the ratio of crack length with respect to the specimen diameter, and L_{glob}/D is the ratio of the global reference length with respect to the specimen diameter.

Finally, Toribio has published a most useful work by determining the relation between global and local strain rates by respective finite element analyses for different crack and notch geometries. Figure 2-39 indicates the relation of the local strain rate with respect to the global strain rate as a function of global strain. The notched specimens exert a great influence on the fraction behaviour when the global strain levels become higher. However, it should be noted that the factor ratio between the local strain rate and the global strain rate will be up to 20 for the specimen with the longest notch.

Until recently, an exact calculating the local strain rate has not been found. However, Lidbury^[HAS 113] proposed an applicable equation for determining the local strain rate as a function of the global strain rate, which plays a significant role in dominating the crack propagation behaviour. The equation is given by:

$$\dot{\epsilon}_{loc} \approx \frac{\pi}{2(1-c)\epsilon_{ys}} \cdot \left(\frac{\bar{a}}{a_{1C}} \right) \cdot \left(\frac{\sigma_{ys}}{\sigma_{max}} \right)^2 \cdot \dot{\epsilon}_{glob}. \quad (2-53)$$

From this equation, Lidbury deduced that the ratio between local and global strain rate in the range 10 to 20 ($10 \leq \dot{\epsilon}_{loc}/\dot{\epsilon}_{glob} \leq 20$) could be valid for alloyed steels, which are generally used as main construction materials for pressure vessels, and using this ratio, Lidbury also takes account of the actual crack length. The simple form for calculating the local strain rate dependent on the global strain rate is:

$$\dot{\epsilon}_{loc} = K_{lid} \cdot \dot{\epsilon}_{glob}. \quad (2-54)$$

However, in order to reduce the number of complicated variables for estimating the local strain rate as a function of the global strain rate, it is possible to use the K-factor ($\dot{\epsilon}_{loc}/\dot{\epsilon}_{glob}$) as a simple variable instead of all complicated variables, particularly for performing numerical finite element simulations of hydrogen assisted stress corrosion cracking,

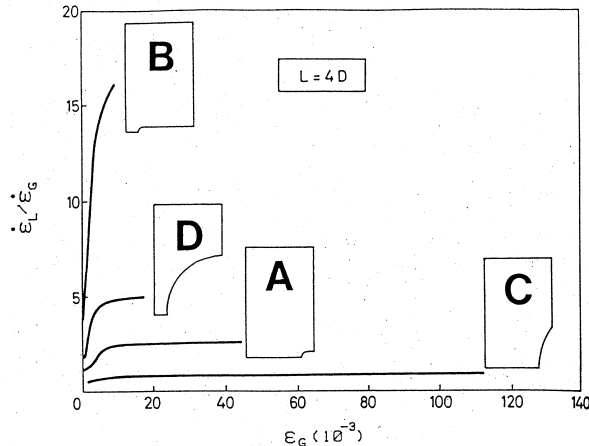


Figure 2-39: Relationship between local and global strain rates as a function of global strain taking account of effects of notched forms^[HAS 92]

because, based on the various points of view of the authors there is currently a variety of equations variable for determining the local and the global strain rate.

2.6 Slow Strain Rate Test

As a first approach to modelling of hydrogen assisted cracking, the simulation of respective test procedure is very appropriate, because this allows a direct comparison between modelling and experiment. As the most relevant test procedures for this contribution, the slow strain rate test (SSRT) is described here.

In order to improve the testing technology for determining the susceptibility of alloyed materials to stress corrosion cracking (SCC) taking account of the interaction between mechanical loads and corrosive environments, the slow strain rate test was performed first in the 1960s. One of the most notable features is the testing speed, at which the test results can be achieved within the specific test duration^[HAS 114]. The SSRT consumes less financial resources than fracture mechanics crack propagation tests, because its specimen geometry and test procedure are more simple^[HAS 88]. For these reasons, the SSRT has recently been accepted for screening materials which will be exposed to service conditions with stress corrosion cracking reaction.

The basic principle of this method is that the test specimen is continuously displaced by a constant deformation rate until total fracture: The test method is very attractive because it gives a definitive answer within a relatively short time to the question of whether or not a given alloy-environment system shows susceptibility to SCC^[HAS 87]. The time to failure of the material is normally used to draw conclusions about the material properties under the specific test conditions because it can be obtained immediately after the failure of the specimen has taken place. Additionally, ductility parameters of the tested specimen, such as reduction in area or elongation can easily be measured after completion of the test.

Since this test method is most sensitive to the strain rate which plays a significant role in controlling the time to failure of the material, the appropriate strain rate must previously be

2. Literature Reviews

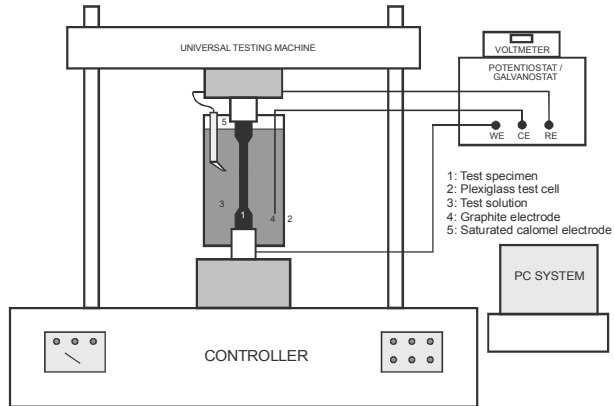


Figure 2-40: Schematic illustration showing test facility and control connections for slow strain rate tests (SSRT)^[HAS 94].

Table 2-9: Recommended appropriate strain rate for SSRT.

Materials	Suggested strain rate (s^{-1})	Reference
steels, nickel, aluminium based alloys	1.0E-7 – 1.0E-05	[HAS 87]
Magnesium based alloys, titanium based alloys	1.0E-06 – 1.0E-04	[HAS 87]
Stainless steels (AISI 316)	1.0E-07 – 1.0E-06	[HAS 88]
Nickel based alloys	1.0E-06 – 3.0E-08	[HAS 88]
Copper alloys	<1.0E-04	[HAS 88]
Aluminium alloys in chloride solution	1.0E-06	[HAS 89]
Copper alloys in ammoniacal solution	1.0E-06	[HAS 89]
Ferrite steels in carbonate, hydroxide, or nitrate solution	1.0E-06	[HAS 89]
Magnesium alloys in chromate/ chloride solution	1.0E-05	[HAS 89]
Nickel based alloys in high temperature water	1.0E-07	[HAS 89]
Stainless steel in chloride solution	1.0E-06	[HAS 89]
Stainless in pure water	1.0E-06	[HAS 89]
Titanium alloys in chloride solution	1.0E-05	[HAS 89]

determined to ensure that the failure of the specimen is completely caused by the interaction between mechanical loads and environmental attack, and not by individual mechanical loads or by individual environmental degradation mechanisms. For example, when the test is carried out at relatively high strain rates, the material degradation is not dominated by environmental effects which act as a main reason for SCC phenomena because a sufficient period of time is required for the interaction between materials and environments. Therefore, the appearance of micro-void coalescence on the fracture surface is typically found and used to identify the specimen failure by rapid rupture. The failure of the specimen by SCC can occur when the appropriate strain rate has been used because sufficient time for the environment-material-mechanical load interaction has to be provided.

Nevertheless, it should be noted that the strain rate should not be much slower because it will consume a lot of testing time without useful results.

Depending on the specific test conditions and material systems, constant strain rates for the SSRT- technique in the range of $1.0\text{E-}05$ to $1.0\text{E-}08$ s^{-1} are generally recommended for evaluating the cracking susceptibility of materials caused by mechanical-environmental interaction as listed in Table 2-9.

SSRT tensile test specimens can be fabricated in different forms dependent on the standard tests and given materials. In the present research, the standard test based on NACE TM 0177-96 "Laboratory Testing of Metals for Resistance to Sulfide Stress Cracking and Stress Corrosion Cracking in H_2S Environments" is highlighted in the present research for determining the susceptibility of supermartensitic stainless steel to hydrogen assisted stress corrosion cracking.

2.6.1 NACE Standard TM 0177-96

This standard was established by The National Association of Corrosion Engineering (NACE) for evaluating the susceptibility of metallic materials to sulfide stress corrosion cracking in H_2S environments. A brief account of this standard is given as follows:

1. Anisotropy of the material with respect to the mechanical properties and to the environment-related cracking susceptibility can be an important parameter. The fracture path in the test specimen should match that anticipated in the actual component.
2. Galvanic effects between dissimilar metals can either accelerate or suppress the cracking susceptibility: For instance, an acceleration of the cracking susceptibility may take place in some nickel-based alloys when they are coupled to electrochemically less noble materials, e.g. plain steel, whereas the cracking susceptibility of duplex stainless steels coupled to the electrochemically less noble material may be suppressed.
3. The testing temperature can affect the cracking susceptibility. Testing at temperatures above 23°C reduces the cracking susceptibility of the test materials (steels), whereas the cracking susceptibility can be severely increased when the test is performed at temperatures below 23°C .
4. Different test methods may not necessarily provide the same ranking of like materials.
5. Inhomogeneous structure of test materials, e.g. weld metal, segregation, etc., can deviate test results.
6. Maximum no-failure stresses for a specified exposure period should be considered as apparent threshold stress. Longer exposure times or larger numbers of specimens may result in lower threshold values.
7. Sulfide stress corrosion cracking can show statistical variability. The replicate tests are required to obtain representative values applicable for characterising the susceptibility of the material to cracking.

2. Literature Reviews

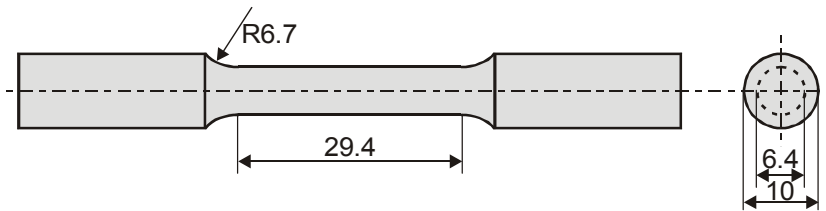


Figure 2-41: Dimension of the test specimen for the standard tensile test^[GEN 35].

8. For measuring the cracking resistance of the material, the results can be better obtained from some test specimens.
9. The period of time for the test varies dependent on different types of the SSC test.

Among the four existing methods, i.e. the standard tensile test (Method A), the standard bent beam test (Method B), the standard C-ring test (Method C), and the standard double-cantilever-beam (DCB) test (method D), the standard tensile test has been chosen as the most interesting test to conduct this research.

2.6.1.1 Test specimen

In standard test specimen specification, the following points should be considered:

- a. Influence of specimen size and shape.
- b. The gauge section of the test specimen has a diameter of 6.4 mm and a length of 25.4 mm as represented in Figure 2-41.
- c. The radius of curvature at both ends of the gauge section should be at least 6.4 mm in order to avoid high stress concentration and fillet failure.
- d. Both ends of the specimen must be sufficiently long to accommodate seals for the test container and to be firmly held by the fixture.
- e. Machining of the test specimen must be done carefully to avoid overheating and cold working. From the final two passes of the specimen, no more than 0.05 mm should be removed. Grinding is also acceptable. The surface roughness of the specimen should be lower than 0.81 μm .
- f. The specimen should be degreased before installing it in the test cell. The gauge section should not be handled or contaminated after cleaning.

2.6.1.2 Test Solution

The electrolytic solution for the tensile test of the NACE standard should consist of 5.0 wt.-% NaCl and 0.5 wt.-% glacial acetic acid in distilled or deionised water.

2.6.1.3 Test Procedure

In order to obtain precise results from the test, the test procedure should be carried out step by step as follows:

1. Measuring the gauge diameter of the test specimen in order to calculate the specimen load according to a desired stress level.

2. Installing the specimen in the test cell and then sealing the test cell in order to prevent contamination from ambient environments in the test cell during the test.
3. The external tension load is applied on the test specimen with a slight increase of monotonic displacement, but care should be exercised not to exceed the desired stress level.
4. The test cell is immediately filled with deaerated solution. This solution should be purged with inert gas for at least 20 minutes in order to ensure that the test solution is oxygen-free prior to the introduction of H₂S.
5. The test solution is then saturated at a rate of 100 to 200 ml·min⁻¹. for 20 minutes per litre of the test solution.
6. The termination of the test should be at the point in time when specimen failure appears or after 720 hours.

2.6.1.4 Failure Determination

Occurrence of completed test specimen separation within the specific testing period is defined as failure. After 720 hours of testing, visual inspection should be performed on the gauge section for examining evidence of cracking.

The time-to-failure seems to be very useful and much more applicable for evaluating the cracking susceptibility of the materials caused by an interaction of mechanical loads and specific environments, and should therefore be recorded using timing recorder systems.

As described above, the advantages and disadvantages of this test method can be summarised as follows:

Advantages:

1. Decreasing test duration by controlling strain rates.
2. Receiving quantitatively useful data for characterising material degradation.
3. Variability of test conditions according to sour service applications.
4. Convenience for monitoring test reactions and for operating test machines.

Disadvantages:

1. Consumption of more resources for providing the test chamber and specimens.
2. Specification of test specimen dimensions and geometries.
3. Occupation of a tensile test machine for longer time by testing.
4. Requirement of more attention to test procedures for avoiding the deviation of tested results.

2. Literature Reviews

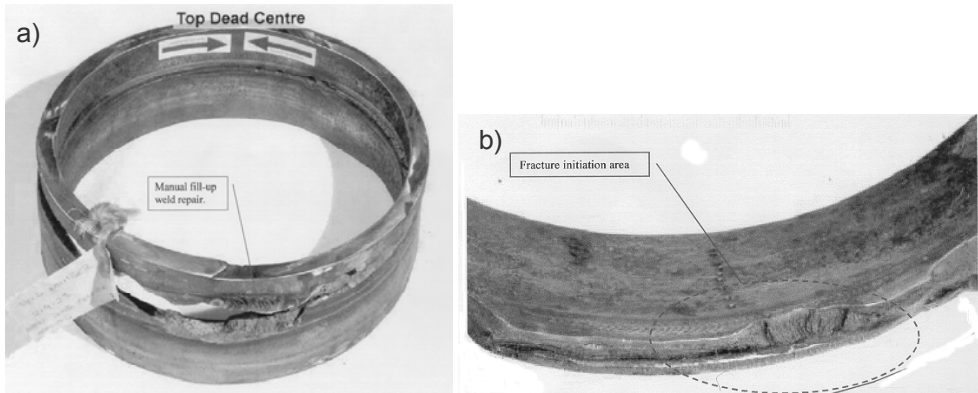


Figure 2-42: Failure of orbitally welded supermartensitic stainless steel pipeline during pipe laying in Tune oil and gas field, North Sea: a) Overview of pipeline failure, b) Crack initiation adjacent to the 6-hour position.

2.7 Hydrogen Assisted Cold Cracking in Girth Welds

High-strength steels are increasingly employed in many industries since they can provide optimum conditions to meet the technical-economical challenge in structural component engineering. However, serious problems of hydrogen assisted cold cracking must be taken into account when such steel components are fabricated by arc welding with relative high hydrogen concentration picked up by the weld metal during welding.

As failure of Tune supermartensitic stainless steel pipelines orbitally welded by a TIG process with matching filler material during pipe laying in North Sea oil and gas production, hydrogen assisted cold cracking has been mentioned to be a potential reason for such a failure case^[HAC 55].

The failure occurred during pipeline laying operations in the Tune field in Summer 2001 during straightening at pipeline laying after 2 % straining during reeling and de-reeling, respectively. An inter-run lack of fusion has been identified as the primary origin of the failure. The fracture spread from both sides of the lack of fusion towards the top and root side of the weld^[HAC 56]. In the first part of the fracture surface the crack propagated into the weld metal and then shifted more towards the heat affected zone (HAZ). However, at the crack initiation site the fracture surface appeared brittle in a transgranular cleavage or cleavage-like mode^[HAC 56]. The rest and the major part of the fracture surface in the weld metal and in the heat affected zone, respectively, was identified as ductile microvoid coalescence. Figure 2-42a shows an overview of the failed supermartensitic stainless steel weld of Tune pipeline taking place during pipe laying operations. Crack initiation has occurred in a susceptible region adjacent to the 6-hour position as shown in Figure 2-42b.

Thus, the main mechanism of hydrogen assisted cold cracking should be described for deepening the basic knowledge and for avoiding serious impairment of welded components.

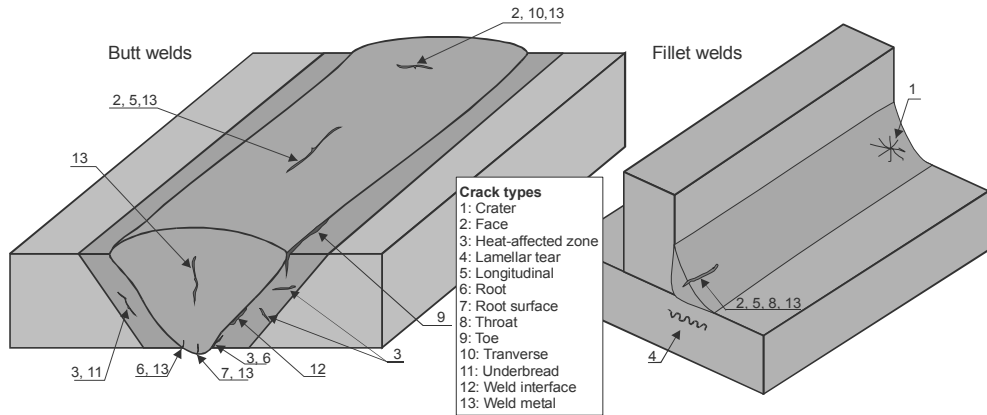


Figure 2-43: Possible cracking types occurring in susceptible zones of welded steels for butt welds and fillet welds^[HAC 17].

Table 2-10: Classification of cracking types occurring in welded components based on cracking characteristic and cracking causation^[HAC 17].

Cracking type	Characteristic	Causes
Throat cracking	Crack propagation parallel or longitudinal to the weld bead. It appears in the weld metal and extends towards the root. It typically counts among hot cracking.	High cooling rate and high restraint simultaneously appear in the weld metal.
Root cracking	Crack initiates in the root of the weld metal and then propagates longitudinal to the weld bead.	High stress intensity in an area of uncompleted fusion of the root pass.
Longitudinal cracking	Cracking appears in the weld metal longitudinal to the weld bead.	Interaction between high cooling rate and high restraint of the welded component.
Transverse cracking	Crack propagation across the weld bead transverse to the welding direction. It may just appear in the weld metal or progress into the heat affected zone or the base metal.	High shrinkage stresses from low weld metal ductility and/or hydrogen concentration in the weld metal higher than solubility limit.
Crater cracking	Star-like cracking in the weld metal at the terminal position.	Depression of the molten metal at the termination of the arc. This can be avoided by backstepping into the weld pool before breaking off the arc.
Toe cracking	Cracking occurs at the toe of the weld metal.	racking results form high shrinkage stresses in a low ductility zone such as the heat affected zone.
Underbead cracking	Cracking often occurs in the heat affected zone under the weld bead and does not propagate to the external surface of the component.	Low ductility of the heat affected zone interacting with hydrogen results in underbead cracking.

2. Literature Reviews

2.7.1 Overview of Hydrogen Assisted Cold Cracking of Welded Steels

General location of cracking that may occur in susceptible zones of welded steels are represented in Figure 2-43. Table 2-10 lists all cracking types and briefly gives a description of cracking characteristic and main causation for each cracking type.

Hydrogen assisted cold cracking is classified as a partial phenomenon of hydrogen assisted cracking, which is known as delayed cracking occurring either during manufacturing processes or later service applications. The exact mechanism of hydrogen assisted cold cracking is hitherto unclear, but similar to hydrogen assisted stress corrosion cracking. This has evidently been confirmed by the SEM observation showing the identical fracture topography, i.e. cleavage-like cracking. The local interaction between hydrogen and stress-strain distribution in susceptible regions affected by welding can be assumed to influence the behaviour of hydrogen assisted cold cracking.

In order to assess the susceptibility of metallic materials to hydrogen assisted cold cracking, appropriate test methods should be performed using realistic boundary conditions for fabrication welding, which are described in the next Section.

2.7.2 Hydrogen Assisted Cold Cracking Test Methods

The purpose of this Section is to give an overview of the basic principles of test procedures, which are widely recommended to be used for assessing the susceptibility of materials welded with the filler materials and of parent materials to hydrogen assisted cold cracking during welding fabrication and subsequent cooling.

2.7.2.1 IRC-Test

For quantitative assessment of the susceptibility of metallic materials to hydrogen assisted cold cracking, the Instrumented Restraint Cracking (IRC)-Test has been developed by Hoffmeister^{[HAC 47],[HAC 49],[HAC 51],[HAC 53]} drawing upon the basic principle of the self-restraint test method. Further advantages of the IRC-Test in comparison with other test methods are to be seen in the time-dependent parameters involving the reaction force transverse to the welding direction F_y and a moment around the axis in welding direction M_x as well as a moment around the vertical axis of the welding direction M_z which can continuously be monitored during welding and subsequent cooling^{[HAC 47],[SDW 9]}. Hence, the IRC-Test is practically performed to provide useful information for explaining cold cracking phenomena in welded components, particularly in those made of high-strength steels for offshore applications^[HAC 47]. Furthermore, global effects in realistic fabrication welding, e.g. shrinkage situations influenced by restraint intensity conditions, heat treatment processes, hydrogen diffusion behaviour etc. can be simulated with the IRC-Test in order to verify the reliability the welded component with regard to hydrogen assisted cold cracking.

For a quantitative analysis of hydrogen assisted cold cracking, mechanical effects of the crack relevant parameters, i.e. reaction forces caused by restrained transverse shrinkage and reaction moments caused by restrained angular distortion, should continuously be monitored after the completed welding thermal cycle until any the possible start of cracking through to the end of cracking^[HAC 47].

The reaction force transverse to the welding direction is predominantly dependent on the shrinkage characteristic caused by the restraint boundary conditions and by the thermal

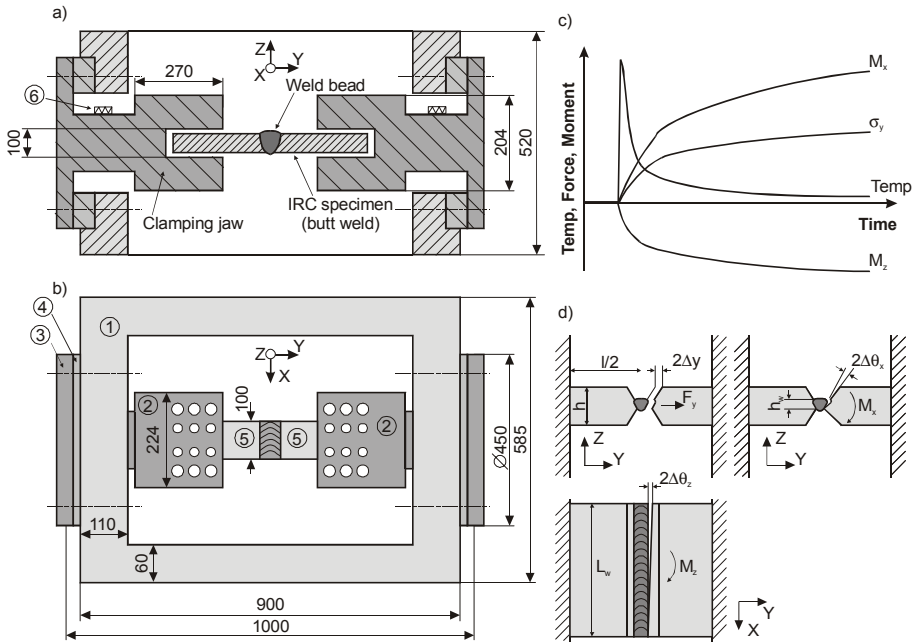


Figure 2-44: IRC-Test for verification of the susceptibility of welded components to hydrogen assisted cold cracking^[HAC 49].

history of the welding process. Thus, the shrinkage restraint of the welded component is simply evaluated in terms of the restraint intensity R_{F_y} , which is given by^{[HAC 47],[SDW 9]}.

$$R_{F_y} = \frac{F_y}{2\Delta y \cdot L_w} = \frac{E \cdot h}{l}, \quad (2-55)$$

where F_y is the reaction force transverse to the welding direction, L_w is the total length of the weld bead, $2\Delta y$ is the transverse root gap displacement, h is the plate thickness, and l is the plate length.

Based on a similar definition to the transverse restraint intensity, the reaction moments around the axis in the welding direction M_x and the around the vertical axis of the welding direction M_z influenced by the restrained distortion angle, respectively, are used to express the shrinkage restraint of the welded component in terms of the bending restraint intensities which are described in the following equations^[HAC 47]:

$$R_{M_x} = \frac{M_x}{2\Delta\theta_x \cdot L_w} \quad (2-56)$$

$$R_{M_z} = \frac{M_z}{2\Delta\theta_z \cdot L_w}, \quad (2-57)$$

2. Literature Reviews

where R_{M_x} and R_{M_z} are the bending restraint intensities around the axis in the welding direction and in the direction vertical to the welding direction, and $2\Delta\theta_x$ and $2\Delta\theta_z$ are the deflection angles caused by M_x and M_z , respectively.

As previously described by Hoffmeister^[HAC 47], the transverse reaction stress σ_{F_y} in butt welds caused by the shrinkage reaction during cooling can usually be defined as the nominal transverse reaction force acting on the unit area of the weld bead along the welding direction as given by:

$$\sigma_{F_y} = \frac{F_y}{L_w \cdot h_w} \quad (2-58)$$

Additionally, Boellinghaus et al.^[SDW 9] introduced an equation for calculating the transverse reaction stress taking account of effects of the shrinkage displacement $2\Delta y$ and of the transverse restraint intensity, which is written by:

$$\sigma_{F_y} = \frac{2\Delta y}{h_w} \cdot R_{F_y} \quad (2-59)$$

The stress distribution in linear butt welds transverse to the welding direction after completed cooling down to ambient temperature can be calculated by inserting the combination of transverse reaction stresses and bending reaction stresses. The equation is given by^[HAC 47]:

$$\sigma_y = \sigma_{F_y} + \sigma_{M_x} + \sigma_{M_z} \quad (2-60)$$

where σ_y is the stress distribution in butt welds transverse to the welding direction,

$$\sigma_{M_x} = \frac{12 \cdot M_x \cdot z}{L_w \cdot h_w}, \text{ and } \sigma_{M_z} = \frac{12 \cdot M_z \cdot x}{L_w^3 \cdot h_w}.$$

In orbital welding, an appearance of the respective moment of inertia for a thin ring as the circumferential weld bead may be incorporated into Equation (2-60) by introduction of the average diameter of the ring weld bead ring. Accordingly, the transverse stress distribution in the orbital welds can be calculated by the formula^[SDW 9]:

$$\sigma_y = \left(\frac{F_y}{h_w \cdot \pi \cdot D_{awb}} \right) + \left(\frac{8 \cdot M_x \cdot z}{\pi \cdot D_{awb}^3 \cdot h_w} \right) + \left(\frac{8 \cdot M_z \cdot x}{\pi \cdot D_{awb}^3 \cdot h_w} \right), \quad (2-61)$$

where D_{awb} is the average diameter of the ring weld bead.

However, this equation can also be used to calculate the reaction stresses at any position over the circumference by inserting the respective cantilever in x and z direction. For multi-run welding, such reaction stresses should be calculated for the different passes by assumption of an average weld metal thickness, which is calculated from the total weld metal thickness with respect to the number of weld layers^[SDW 9].

The assembly of the IRC-Test set-up is vital importance prior to testing. This arrangement consists of a rigid box-shape steel frame (1) to which two symmetric restraining beams (2) are tightly connected as schematically illustrated in Figure 2-44a-b. The parent material specimens (5) are installed on each side of the symmetric restraining beams between the clamping jaw and then fastened by screw bolts.

Monitoring the reaction force, F_y , and the reaction moments, M_x and M_z , is realised by continuous registration of the electrical signals of strain gauges (6) positioned on one side of the restraining beams. The registration of the reaction force and of both reaction moments during the test is translated by transferring the electrical signals from the strain gauges into a commercial data receiver program working on a PC platform via amplifiers and A/D converter^[SDW 9].

In order to calibrate the transverse reaction force, a gradual increase of the external force in y-direction is stepwise affected at the weld edges for registration of strain gauge signals. At the same time, measurement of weld edge displacement, Δy , is performed in order to calculate the restraint intensity, R_{F_y} , using Equation (2-55). Additionally, calibration of the reaction moment around the axis in the welding direction, M_x , and around the axis vertical to the welding direction, M_z , can be performed adopting the same procedure as for transverse reaction force calibration. With the application of bending forces around the welding direction, F_x , and around the axis vertical to the welding direction, F_z , the angular deflections $\Delta\theta_x$ and $\Delta\theta_z$ can be generated, respectively. The bending restraint intensity around the axis in the welding direction is then obtained using Equation (2-55), and around the axis vertical to the welding direction using Equation (2-56).

Although the IRC-Test can simulate phenomena of hydrogen assisted cold cracking in welded components under various restraint conditions, of the hydrogen concentration picked up by the weld metal during welding, and of the heat treatment process corresponding to realistic welding fabrication, this test method needs further development to enable more precise elucidation of those phenomena. Hence, a universal large-scale test facility has been developed following the basic principle of the IRC-Test, in which additional and modified working functions have been implemented permitting complete welding fabrication simulation as well as testing of welded components with the boundary conditions experienced in field service.

2.7.2.2 Component Test

In order to improve the test capability of the IRC-Test, the full-scale test has been developed for conducting complete welding fabrication test with the greater sizes of test components. Additionally, the welded component can immediately be subjected to the external load test reproducing field service conditions in order to verify applicable properties of the welded components.

The large-scale test facility, named „GAPSI 16“ (**G**roß **A**nlage zur **P**rüfung und **S**imulation von Bauteilschweißungen, Prüfkraft 16 MN), is actually employed for testing welded components with the three-dimensional modified monitoring and applying load system. It has been designed for operation with quasi-static loads and taking account of all

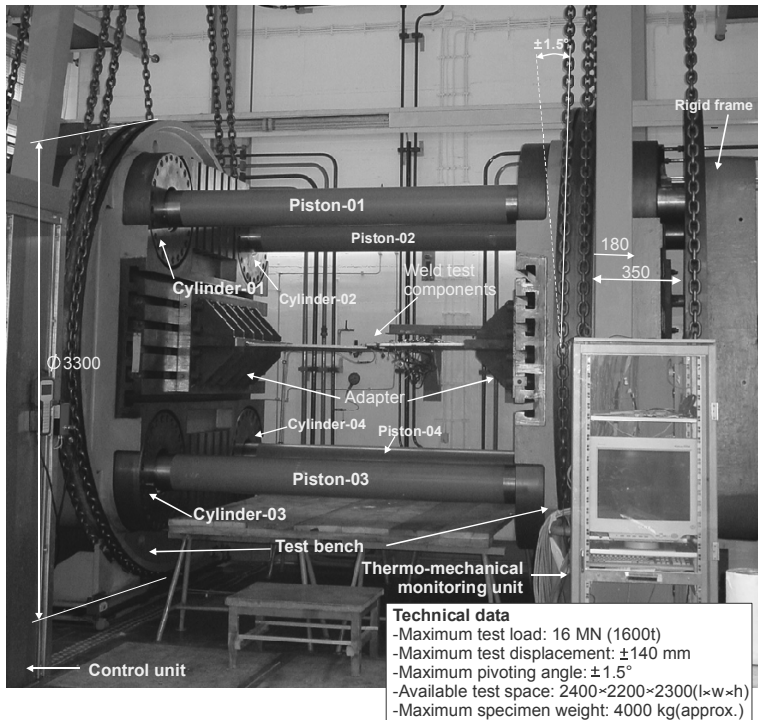


Figure 2-45: View of the full-scale test facility for evaluation of the susceptibility of welded components to hydrogen assisted cracking with simulation of the complete welding fabrication process and subsequent application of external loads.

factors of the complicated component phenomena which are normally induced by the occurrence of many reactions in the welding and subsequent cooling processes.

The construction of the test system basically consist of two main test tables, at which four bore holes each are symmetrically drilled through the thickness for provide a housing for a cylinder unit compassed of a reaction load measuring system and of a load application system. Four long displacement pistons are then assembled through four cylinders mounted to each test table to realise a servo-hydraulic controlling test machine. (see Figure 2-45). A maximum distance of approximately 2400 mm of the test components from the test tables is then available. Finally, two fixed cross-heads are tightly clamped on both ends of all displacement pistons for constructing a rigid frame similar to that of the IRC-Test set-up. The test tables can be moved independently of each other which offers further advantages over the IRC-Test with regard to measuring coefficients for complicated reactions during welding and subsequent cooling.

The test system has been designed as the four-pillar machine with servohydraulic system. In the GAPS1 16 measuring system, both distance control and force control are available. During the test, all displacement pistons experience an elastic-linear change due to affected reaction forces exerted on the specimen, which can be both of tensile and compressive type dependent on the reaction force characteristic. Changes of the distance between the test table and the rigid frame are detected by eight sensors located at each cylinder unit along the displacement piston in the form of digital and/or analogical signals.

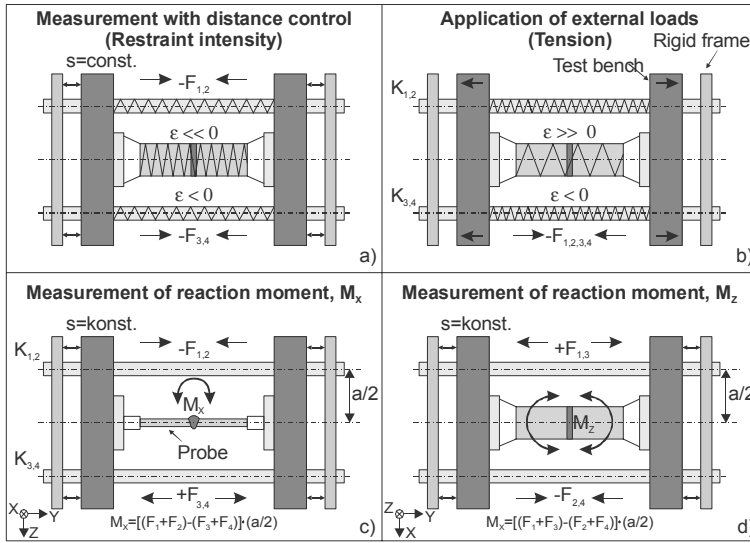


Figure 2-46: Basic principle of the measuring system of the full scale test facility for performing welding experiments with an addition function of externally applied loads on test components^[GEN 20].

These signals are immediately converted into comparable data for reaction forces as well as reaction moments. This procedure is defined as the distance control method. Additionally, oil pressure in each cylinder unit can be used to determine the reaction force during the test and also to impose external loads, in particular for tensile tests. On the other hand, the force control method involves the reaction force measurements including individual linear-elastic reactions from the internal sensor of each displacement piston.

As schematically represented in Figure 2-46a, the distance control method is carried out based on the assumption that the distance between the test table and the rigid table is completely constant. The shrinkage reaction of the welded component during cooling can produce shrinkage reaction on the rigid body of GAPS16. Therefore, the difference in distance of the displacement piston is usually used for the reaction force and moment determinations. In the other case, in order to keep a constant distance between the test tables on both sides, the test tables must be moved counter to the shrinkage reaction by applying additional pressure on the hydraulic system, which is schematically represented in Figure 2-46b. The restraint intensity of the welded component provided by GAPS16 can be calculated by using the following equation^[GEN 20]:

$$R_{F_y} = \frac{k_{GAPS16}}{k_{sp} + k_{GAPS16}} \left(\frac{E \cdot h}{l} \right), \quad (2-62)$$

where k_{GAPS16} is the spring constant value of GAPS16 from experimental determination ($8.33E-05 \text{ N mm}^{-1}$), and k_{sp} is the spring constant value of the test component.

Since GAPS16 has been developed in compliance with the basic principle of the IRC-Test, the reaction moment around the axis in welding direction and the reaction moment around the axis vertical to the welding direction are calculated as represented in Figure

2. Literature Reviews

2-46c and Figure 2-46d, respectively. These reaction moments are subsequently used to calculate the bending restraint intensities around the axis in welding direction and around the axis vertical to the welding direction (see Equation(2-56) and Equation (2-57)).

2.7.3 Model of Temperature Distribution in Welding Processes

In fabrication welding, the temperature history of welded components is the main factor for an increased susceptibility of materials to failure. Therefore, a through understanding of the behaviour of transient temperature distribution influenced by effects of temperature gradient during welding and subsequent cooling is necessary. Additionally, temperature distribution during welding strongly dominates hydrogen diffusion behaviour in components because diffusion coefficients of hydrogen increase with temperature levels.

2.7.3.1 Heat Generation in Arc Welding Processes

Heat input is required to sufficiently melt the metallic material with avoidance of undesirable side effects, e.g. grain growth, precipitation of the second phase at grain boundaries, residual stress-strain distribution etc., which is generally described by^[GEN 16]:

$$Q_{weld} = \eta \cdot I_{weld} \cdot A_{weld} , \quad (2-63)$$

where Q_{weld} is the effective heat input during welding, η is the arc efficiency dependent on the welding process (for GTAW, it is in the range of 0.45 to 0.75^[TDW 2]), I_{weld} and A_{weld} are the arc current and the arc voltage, respectively.

As proposed by Rykalin et al.^[TDW 2], arc welding heat generates a heat flux on the specimen surface with a ring zone around the electrically active spot. This ring zone is heated by convection and radiant heat exchange between the plasma of the arc column and the spot of the welding electrode. For this reason, the heat flux drops more slowly than the electric current density with the radial distance from the hot spot, and the heat spot is usually larger than the electrically active arc spot.

The Gaussian relationship can be used to describe the temperature distribution induced by a steady state point heat source moving on the surface of a semi-finite plate as shown in Figure 2-47. The temperature distribution is given by^[TDW 6]:

$$T - T_0 = \frac{Q_{weld}}{2 \cdot \pi \cdot K \cdot r_{dc}} e^{-\frac{v_{weld}(w+R)}{2D_{th}}} , \quad (2-64)$$

where T_0 is the initial temperature of the specimen, k is thermal conductivity, r_{dc} is the distance from the arc centre ($= \sqrt{w^2 + y^2 + z^2}$), w is the distance in the direction of the moving co-ordinate ($= x - (v_{weld} \cdot t)$), D_{th} is the thermal diffusivity, and v_{weld} is the welding speed.

Until recently, prediction of the weld pool geometry, however, has still been carried out due to the complicated phenomena resulting from effects of the heat flux distribution during arc welding as previously described, and from other effects such as surface tensile (Marangoni) effects, electromagnetic (Lorentz) forces, etc.

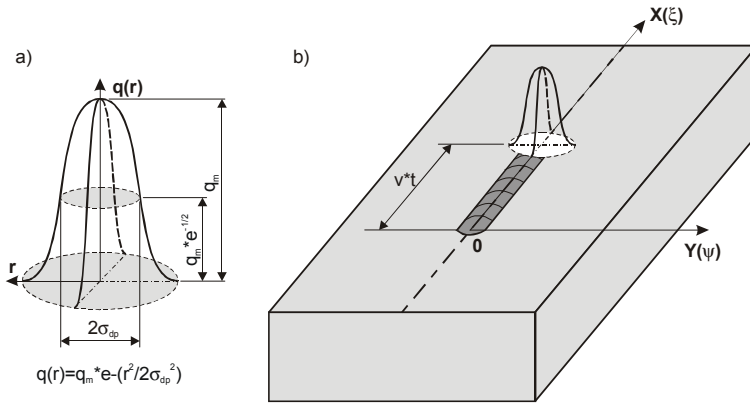


Figure 2-47: Gaussian distribution of a heat source moving on the surface of a semi-finite plate, where the distribution parameter σ_{dp} is the standard distribution of the Gaussian function^{[TDW 2],[TDW 6]}.

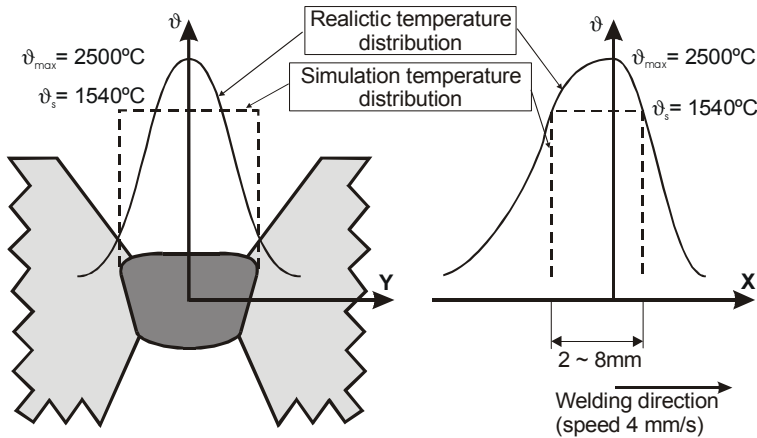


Figure 2-48: Schematic illustration of the simulation of temperature distribution during arc welding^[GEN 18].

Therefore, the assumption of homogeneous temperature distribution for the weld pool above melting point, i.e. 1540 °C, in the specific co-ordinate system may be suitable for simulating the temperature distribution during arc welding^[GEN 18], which is much more applicable to numerical modelling for avoiding overheat effects induced by application of heat input to specific nodes of the finite element.

2.7.3.2 Heat Transfer in Metallic Materials

Due to the generation of temperature gradients between the arc welding heat source and neighbouring zones in solid materials, the first law of thermodynamic state, i.e. conservation of thermal energy, is generally used to describe the temperature distribution in the solid material by using the following equation^[GEN 26]:

$$(\rho \cdot C_p) \cdot \left[\left(\frac{\partial \vartheta}{\partial t} \right) + v_x \left(\frac{\partial \vartheta}{\partial x} \right) + v_y \left(\frac{\partial \vartheta}{\partial y} \right) + v_z \left(\frac{\partial \vartheta}{\partial z} \right) \right] = \quad (2-65)$$

2. Literature Reviews

$$Q_g + \frac{\partial}{\partial x} \left(K_x \frac{\partial \vartheta}{\partial x} \right) + \frac{\partial}{\partial y} \left(K_y \frac{\partial \vartheta}{\partial y} \right) + \frac{\partial}{\partial z} \left(K_z \frac{\partial \vartheta}{\partial z} \right),$$

where ρ is the material density, C_p is the specific heat capacity, ϑ is the temperature, t is the time, Q_g is the heat generation, and v_x , v_y , and v_z are the velocity vectors for mass transport of the cartesian co-ordinate.

From the fact that the velocity vector for mass transport of heat in the global cartesian system (v_x , v_y and v_z) can be ignored for normal calculation of heat conduction in solid materials, the simple formulation by reduction of Equation (2-65) is given^[TDW 7]:

$$(\rho \cdot C_p) \cdot \left(\frac{\partial \vartheta}{\partial t} \right) = Q_g + \frac{\partial}{\partial x} \left(K_x \frac{\partial \vartheta}{\partial x} \right) + \frac{\partial}{\partial y} \left(K_y \frac{\partial \vartheta}{\partial y} \right) + \frac{\partial}{\partial z} \left(K_z \frac{\partial \vartheta}{\partial z} \right), \quad (2-66)$$

where $(\rho \cdot C_p)$ is the volumetric specific heat, K is thermal conductivity with subscription of the cartesian system(x, y, and z) and Q_g is the heat generation rate per unit volume.

It should be recognised that all material properties as a function of temperature are usually taken in account for calculating the temperature distribution in the welding process. Additionally, Cao et al.^[SDW 16] proposed that in arc welding processes with constant welding speed, the heat transfer equation can also be formulated taking account of effects of the welding speed as given by:

$$(\rho \cdot C_p) \left(\frac{\partial \vartheta}{\partial t} \right) = \frac{\partial}{\partial x} \left(K_x \frac{\partial \vartheta}{\partial x} \right) + \frac{\partial}{\partial y} \left(K_y \frac{\partial \vartheta}{\partial y} \right) + \frac{\partial}{\partial z} \left(K_z \frac{\partial \vartheta}{\partial z} \right) - \left(\rho \cdot C_p \cdot v_{weld} \left(\frac{\partial \vartheta}{\partial x} \right) \right). \quad (2-67)$$

For isotropic materials, the thermal conductivity can be defined to be a similar value in all directions. The reduction of Equation (2-66) leads to:

$$\frac{\partial \vartheta}{\partial t} = D_{th} \left[\left(\frac{\partial^2 \vartheta}{\partial x^2} \right) + \left(\frac{\partial^2 \vartheta}{\partial y^2} \right) + \left(\frac{\partial^2 \vartheta}{\partial z^2} \right) \right]. \quad (2-68)$$

In the case where the heat loss resulting from the drop of the material surface temperature down to the ambient environment temperature may affect the temperature distribution in solid materials, it can be considered as the additional effect on the temperature distribution characteristic in solid materials as given by^[TDW 10]:

$$\frac{\partial \vartheta}{\partial t} = D_{th} \left[\left(\frac{\partial^2 \vartheta}{\partial x^2} \right) + \left(\frac{\partial^2 \vartheta}{\partial y^2} \right) + \left(\frac{\partial^2 \vartheta}{\partial z^2} \right) \right] - Q_{loss}, \quad (2-69)$$

and the heat loss equation, Q_{loss} , is written by:

$$Q_{loss} = \alpha_{con} \cdot A_{sur} \cdot (\vartheta_{solid} - \vartheta_{amb}), \quad (2-70)$$

where α_{con} is the convection or film coefficient of the considered system, A_{sur} is the total surface exposed to ambient environments, ϑ_{solid} and ϑ_{amb} are the instantaneous temperatures of the solid material and of the ambient environment, respectively.

However, the consideration of the heat loss by the radiation effect can be ignored for solid materials, but it will be a significant factor for fluid systems as described by Carslaw and Jaeger^[GEN 26].

2.7.4 Modelling of Stress-Strain Distribution

Instantaneous temperature gradients during welding and subsequent cooling are widely submitted as major effects on the introduction of stress-strain distributions in welded components due to the thermo-mechanic properties of the materials. Moreover, change of volumetric thermal strain and possible phase transformed strain are a main reason for plastic deformation of in the welded component which will lead to a decrease of the load carrying capability during service and to cracks in sensitive zones. Therefore, calculation of the instantaneous stress-strain distribution is necessary taking account of the thermo-mechanic continuum of the given material subjected to thermal contraction during welding.

A fundamental approach to address the introduction of thermal strain, ε_{th} , due to the effects of temperature gradients is simply expressed by^[GEN 34].

$$\varepsilon_{th} = \int_{T=T_0}^{T=T} \alpha_{th}(T) \cdot dT \quad (2-71)$$

where α_{th} is the thermal expansion coefficient.

Due to the nonlinear stress-strain relationship of alloyed materials, a path-dependent behaviour of the flow curve of the material has to be taken into account instead of Hooke's law, if the material is deformed in the plastic region. In finite element calculation, the total strain is basically employed to establish further relationships in the structural analysis, which is given by^[GEN 34].

$$\varepsilon_{total} = \varepsilon_{elastic} + \varepsilon_{plastics} + \varepsilon_{th} + \varepsilon_{creep} , \quad (2-72)$$

where ε_{total} , $\varepsilon_{elastic}$, $\varepsilon_{plastic}$, ε_{th} , and ε_{creep} are the total, elastic, plastic, thermal, and creep strain, respectively.

Based on Equation (2-72), Dong^[SDW 17] proposed an equation for determining the stress-strain distribution in welded components using finite element simulation. The equation takes account of a strain rate instead of normal strain due to the continuum of stress-strain distribution during welding and subsequent cooling. Additionally, the strain rates induced by annealing reaction and phase transformation reaction have also been included in the modelling, in particular for welding fabrication of components. The equation is written by:

$$\dot{\varepsilon}_{total} = \dot{\varepsilon}_{elastic} + \dot{\varepsilon}_{plastic} + \dot{\varepsilon}_{th} + \dot{\varepsilon}_{ane} + \dot{\varepsilon}_{ptr} , \quad (2-73)$$

2. Literature Reviews

where $\dot{\epsilon}_{elastic}$, $\dot{\epsilon}_{plastic}$, $\dot{\epsilon}_{ane}$ and $\dot{\epsilon}_{ptr}$ are the elastic, plastic, annealing and phase transformation strain rate, respectively.

However, it must be recognised that both the hardening effect and the Bauschinger effect should be considered as side effects for a change of the behaviour of stress-strain distribution in welded components, in particular for multi-run welding with high restraint intensities.

2.7.5 Modelling of Hydrogen Distribution in Welded Joints

Considering the contribution of Yurioka et al.^[HAC 33], an analysis of hydrogen assisted cracking in welded joints has been carried out by using the finite difference method. The hydrogen distribution behaviour can be calculated using the basic equation for computing the hydrogen flux as a function of the chemical potential, which is expressed by:

$$J_H = -\frac{D_{eff} \cdot [HD]}{R \cdot T} \nabla \mu, \quad (2-74)$$

where μ is the chemical potential.

The chemical potential is usually affected by the hydrogen concentration formulated as:

$$\mu = \mu_0 + RT \ln(\gamma_{HD} \cdot [HD]), \quad (2-75)$$

where μ_0 is the initial chemical potential and γ_{HD} is the activity coefficient of hydrogen mass.

Additionally, Yurioka et al. developed a model for determining the hydrogen distribution in welded components based on Fick's second law taking account of effects of the chemical hydrogen potential and of the instantaneous temperature distribution, which is given by:

$$\frac{\partial [HD]}{\partial t} = \frac{\partial}{\partial x} \left(\left(\frac{D_{eff}}{\gamma_{HD}} \frac{\partial}{\partial x} (\gamma_{HD} \cdot [HD]) \right) + \left(\frac{D_{eff} \cdot [HD]}{T} \ln(\gamma_{HD} \cdot [HD]) \frac{\partial}{\partial x} T \right) \right). \quad (2-76)$$

The hydrogen distribution in the weld metal and in neighbouring zones may also be affected by stress-strain distributions in terms of the chemical hydrogen potential. Thus, the calculation of the chemical hydrogen potential can be performed by substitution of the activity coefficient of hydrogen mass influenced by the equivalent stress distribution as well as the equivalent strain and the microstructure behaviour into Equation (2-75), which is given by:

$$\mu = \mu_0 + RT \ln(\gamma_{HD_{stress}} \cdot \gamma_{HD_{plm}} \cdot [HD]) \quad (2-77)$$

where $\gamma_{HD_{stress}}$ and $\gamma_{HD_{plm}}$ are the activity coefficients of hydrogen mass affected by equivalent stress levels as well as by plastic strain levels and microstructure behaviours.

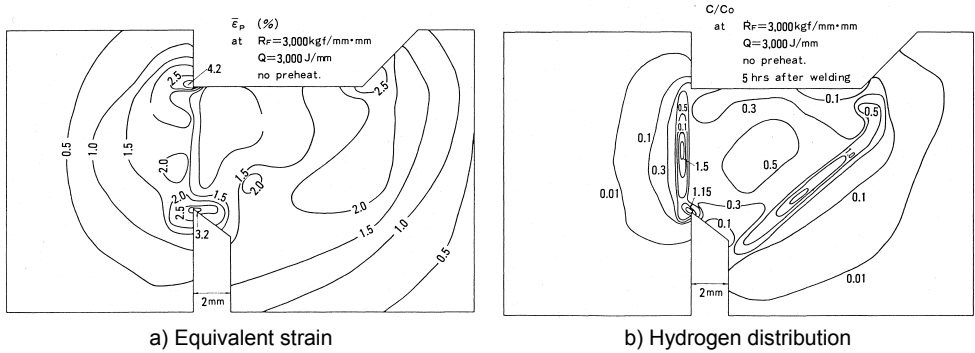


Figure 2-49: Calculated equivalent strain and hydrogen distribution for identifying hydrogen assisted cold cracking^[HAC 33].

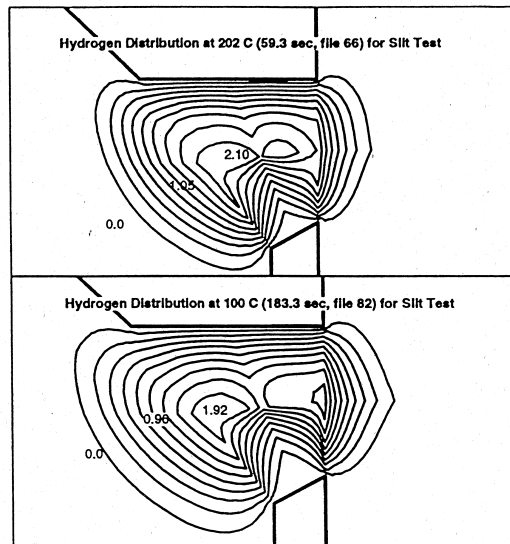


Figure 2-50: Calculation of transient hydrogen distribution for the Slit-Test at temperatures of 202°C and 100°C^[HAC 37].

Based on the above assumption, calculation of the transient hydrogen distribution has been carried out. For a period of 5 hours after completion of welding with a restraint intensity of 30 kN·mm⁻² and without preheat, the presence of a relatively high local hydrogen concentration associated with a relatively high stress-strain distribution at the weld root and the heat affected zone will influence the susceptibility of the welded component to hydrogen assisted cold cracking as represented in Figure 2-49. However, the most significant hydrogen accumulation at the weld root and the heat affected zone is due to microstructural transformation affected by the thermal history of welding and subsequent cooling.

Focusing on the topic of the susceptibility of metallic materials to hydrogen assisted cold cracking during fabrication welding, particularly girth welding of pipeline, Goldak et al.^[HAC 37] developed finite element modelling for simultaneous calculation of the hydrogen and stress-

2. Literature Reviews

strain distribution taking account of effects of the microstructural behaviour in the Slit-Test. The mass conservation of hydrogen has been proposed for determining the hydrogen distribution, which is written by:

$$\frac{\partial[HD]}{\partial t} = D_{eff} \frac{\partial^2[HD]}{\partial x^2} - \frac{\partial S}{\partial t}; \quad \frac{\partial S}{\partial t} = a \cdot [HD] - bS, \quad (2-78)$$

where a and b are the rate constants of forward and backward reactions, respectively, and S is the immobilised hydrogen concentration.

In the modelling, effects of stress-strain distribution in the Slit-Test specimen have been taken into account as a significant factor for the hydrogen distribution behaviour. Thus, hydrogen flux affected by stress-strain distribution is calculated by the following equation:

$$J_H = \frac{D_{eff} \cdot [HD]}{R \cdot T} \nabla \psi; \quad \psi = \bar{V}_H \left(\frac{\sigma_{ii}}{3} + \frac{\sigma \cdot \epsilon}{2} \right). \quad (2-79)$$

Moreover, hydrogen diffusion coefficients as a function of temperature for matrix microstructure of ferrite and austenite have also been taken into account in the finite element modelling of Goldak et al. The simulation of hydrogen distribution in the Slit-Test is represented in Figure 2-50. The appearance of two peaks of hydrogen concentration near the centre of the weld bead has been attributed to relatively high levels of local equivalent stress which play a significant role in dominating this phenomenon, whereas compressive stresses will lead to a decrease of the local hydrogen concentration.

However, the calculation of hydrogen diffusion based on Fick's second law is adequately applicable because a significant increase in hydrogen concentration with increasing stress-strain levels is not observed when the complicated equation with an additional term of stress-strain effects is employed for the calculation. For example, hydrogen concentrations in the weld metal have increased less than five percent by increasing stress-strain levels during cooling (see Figure 2-50). Therefore, effects of stress-strain assisted hydrogen diffusion can reasonably be ignored. In order to exploit the capability of Fick's second law taking account of all enhanced and hindered effects, hydrogen diffusion coefficients ranging in the scatterbands can more accurately be used to calculate hydrogen diffusion in components.

3 FINITE ELEMENT MODELLING DEVELOPMENT

Application of the finite element method (FEM) is presently necessary for a number of industries who need to decrease the cost for new product development and to increase product reliability, simultaneously. Based on a commercial finite element program with the code name "ANSYS", the development of numerical finite element simulation is the main purpose of this research focusing on the phenomenon of hydrogen assisted cracking in supermartensitic stainless steels. Hence, the principle procedure of the finite element method is subsequently described in order to advance the finite element method for calculating hydrogen assisted cracking in terms of hydrogen assisted stress corrosion cracking and hydrogen assisted cold cracking.

3.1 Two-Dimensional Finite Element

In order to reduce the operating time of the simulations, a 2-D finite element model was established the first choice for creating finite element models with further advantages as described in the previous contributions^{[HAC 21],[HAC 23]}. Selection of an appropriate finite element must first be taken into account, dependent on boundary conditions, in order to obtain more precise results. Figure 3-1 represents a two-dimensional finite element with its co-ordinate system and its condition for load application. It should be recognised that the ratio dimension of the finite element should be nearly a unity, particularly in the interesting area of the finite element model for minimising erroneous simulation, which may be caused by an irregular shape of finite elements.

Elements with the code numbers of PLANE 55 and PLANE 42 are employed to create the finite element model for thermal analysis, i.e. temperature distribution and hydrogen diffusion, and for mechanical analysis, respectively. In general, the two-dimensional finite element model must be defined in an x-y plane, but the co-ordination can be adapted dependent on the specific boundary condition as well as on the model geometry. Six categories of applied loads for finite element analysis are available in the commercial finite element program as compiled in Table 3-1.

Following the selection of the finite element, the subsequent step of the numerical modelling simulation is the creation of a finite element model from such finite element.

3.2 Finite Element Models for Modelling HAC

3.2.1 Geometric Parameters

The numerical modelling of hydrogen assisted stress corrosion cracking based on the NACE standard test TM 0177-96 (see Section 2.6.1) constitutes the first part of the present thesis, the creation of the finite element model according to the dimension of the standard specimen is then necessary for the simulation as represented in Figure 3-2 (see dimension of the standard specimen in Figure 2-41). The finite element model will be created either from the solid model, or from the predefined nodes as described below:

- 1) The solid model offers a convenient way to create the finite element model. The initial step is to generate the solid model by defining the position of each keypoint, after that the solid model is generated from these keypoints. Finally, the finite

3. Finite Element Modelling Development

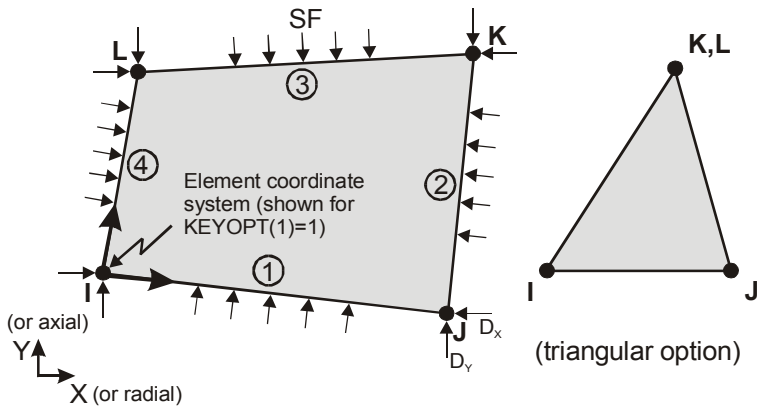


Figure 3-1: Schematic illustration of the 2-D solid finite element of PLANE 55 for thermal analysis and PLANE 42 for structural analysis, four nodes with a single degree of freedom.

Table 3-1: Categories of applied loads for finite element modelling.

Load category	PLANE 55 (Thermal analysis)	PLANE 42 (Structural analysis)
DOF constraint Fixing a value at a node	Temperature(Temp)	Displacement and symmetry boundary conditions
Force Applying a concentration load at a node	Heat flow rate	Forces and moments
Surface load Applying a distributed load over a surface	Convection and heat flux	Pressure
Body load Applying a volumetric load	Heat generation	Temperature and influence
Inertia load Mass matrix of a body	-	Gravitational acceleration, angular velocity and angular acceleration
Coupled-field load	Taking results from one analysis as loads in another analysis	Taking results from one analysis as loads in another analysis

element model is created from the given solid model. The relative advantages and disadvantages of this approach are summarised below:

- Advantages:

- 1) It is generally more appropriate for large and complex models, in particular for three dimensional models of solid volumes.
- 2) Geometric operation, such as dragging and rotation, can be performed.
- 3) The use of primitive areas and volumes as well as Boolean operation for top down construction is available.
- 4) The modification of the finite element model, e.g. adaptive meshing, etc., is readily allowed.

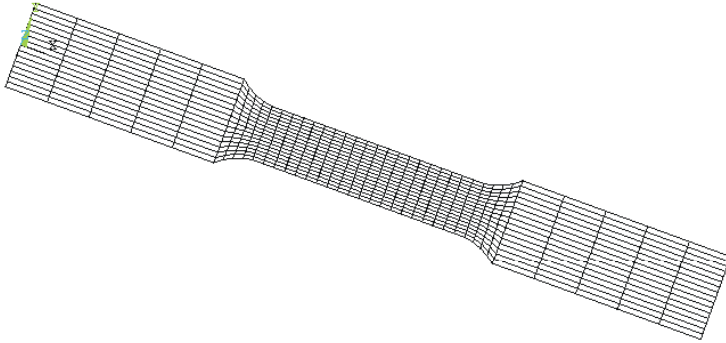


Figure 3-2: Two-dimensional finite element model according to the NACE standard test TM 0177–96.

- Disadvantages:

- 1) Large amounts of CPU time are usually required.
- 2) It sometimes needs more data entries than the other approach.
- 3) The program will not be able to generate the finite element mesh under certain circumstances.

II) Direct generation of the finite element from the defined nodes is more useful if an uncomplicated geometry of the finite element model is going to be used for the simulation. The relative advantages and disadvantages of this approach are summarised as:

- Advantages:

- 1) It is more convenient for small or uncomplicated models.
- 2) Complete control over the geometry and numbering of every node and of every element can be provided by the user.

- Disadvantages:

- 1) Generation of finite element models will consume a lot of time and also need more attention for every detail of meshing finite elements.
- 2) Adaptive meshing is not available.
- 3) Design optimisation is less convenient.
- 4) Modification of meshing elements is quite difficult.

In order to reduce the time required for simulation of hydrogen assisted stress corrosion cracking with the standard specimen, the finite element model focuses on the particularly sensitive area, i.e. the gauge length. Respective fine elements in this specific area are generated for obtaining precise results. The finite element model with a predefined cracking path in the middle of the gauge length transverse to externally applied load direction is shown in Figure 3-3a for a crack tip angle of 180° and in Figure 3-3b for a crack tip angle of 74° .

3. Finite Element Modelling Development

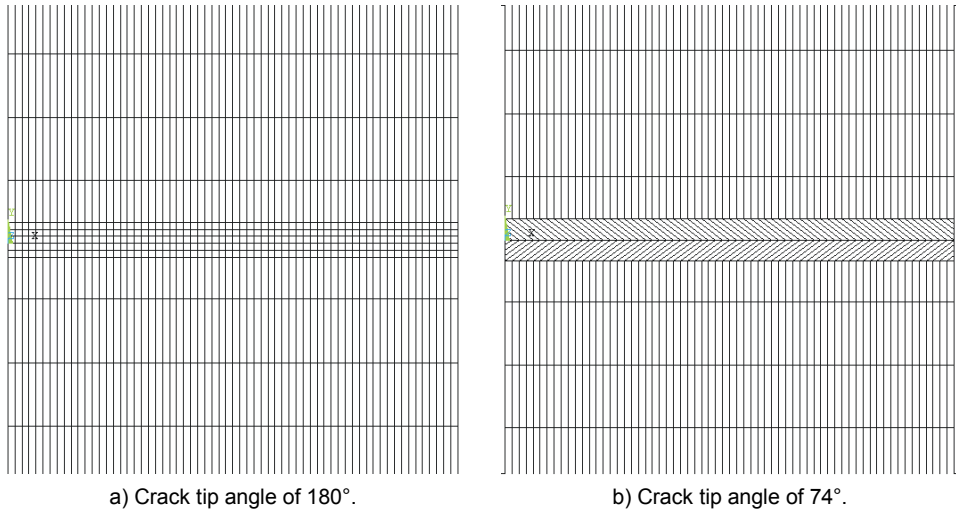


Figure 3-3: Two-dimensional finite element model with a predefined cracking path in the gauge length of the test specimen in transverse direction to externally applied loads: a) Crack tip angle of 180°, b) Crack tip angle of 74°.

Reflecting on the CTOD concept^{[GEN 14],[GEN 30]}, a finite element with 0.1 mm in width is reasonable for simulating crack propagation associated with the phenomenon of hydrogen assisted stress corrosion cracking. Also, reliable results from the numerical analysis can be obtained without too much elongation of CPU-time. Thus, a series of 64 finite elements located through the specimen's diameter of 6.4 mm is generated. A width of the predefined crack is 0.5 mm has been selected as a constant parameter of the crack geometry.

In numerical modelling of hydrogen assisted stress corrosion cracking of supermartensitic stainless steel pipes, the finite element model is created in accordance to the cross-section area along the gauge length of such welded pipes as shown in Figure 3-4. This cross-section is used as the dimensional reference for generating the two-dimensional finite element model.

As previously described, the cracking during the test may take place in the base metal, the heat affected zone and the weld metal dependent on their individual susceptibility to hydrogen assisted stress corrosion cracking. Therefore, the finite element model created for calculating the anticipated lifetime of the pipeline under the aspect of hydrogen assisted stress corrosion cracking has three predefined cracking paths in the respective significant areas, i.e. the base metal, the heat affected zone and the weld metal, as represented in Figure 3-5.

It should be noted that the relatively dense finite elements in the interesting zone, i.e. the cracking path, are created in order to receive precise results from the finite element simulation. The width of the finite element in crack propagation direction is approximately 0.1 mm and can be applied for calculation of hydrogen assisted stress corrosion cracking as a compromise with respect to precise results and CPU-time.

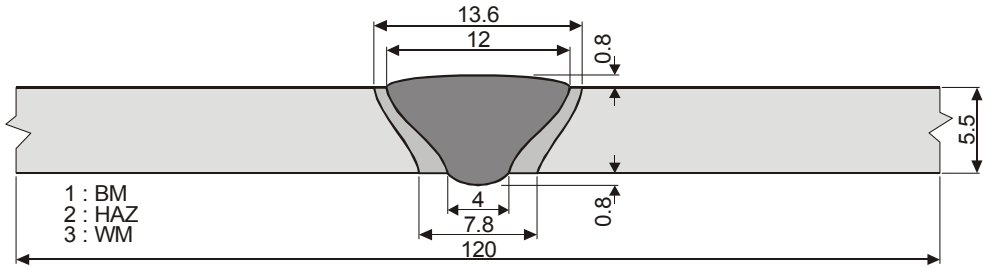


Figure 3-4: Cross-section of the gauge length of the welded pipeline.

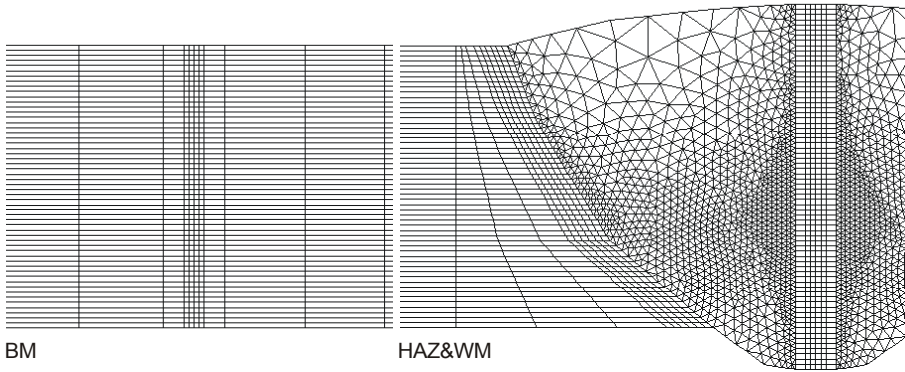


Figure 3-5: Two-dimensional finite element model with predefined cracking paths in three significant regions of the base metal, the heat affected zone, and the weld metal for modelling hydrogen assisted stress corrosion cracking in the orbitally welded pipeline.

Experimental simulation is subsequently required to describe how the full-scale testing of hydrogen-assisted stress corrosion cracking can be performed on pipelines usually installed as subsea flowlines transporting oil and gas products in offshore technology.

Since much longer CPU-time is required for simulating hydrogen assisted cold cracking by three fields of calculation when compared with the traditional finite element simulation, a modified finite element model has to be created, containing particularly less elements. The finite element model represented in Figure 3-6, which shows relatively small sizes of finite element in the weld metal and the heat effected zone where extreme effects from temperature distribution, stress-strain strain distribution and hydrogen distribution inevitably arise during welding and subsequent cooling. By widening the transverse length, coarse finite elements in remote zones from the extreme interaction zone can reasonably be generated in order to reduce the required CPU-time. Additionally, the predefined cracking paths are introduced into the susceptible zones to hydrogen assisted cold cracking, i.e. the weld metal and the heat affected zone, to allow comparisons and see which zone dominates the failure of a welded component due to hydrogen assisted cold cracking. However, it must be recognised that the aspect ratio of the finite element should not be higher more than twenty in order to avoid erroneous results from the simulation.

3. Finite Element Modelling Development

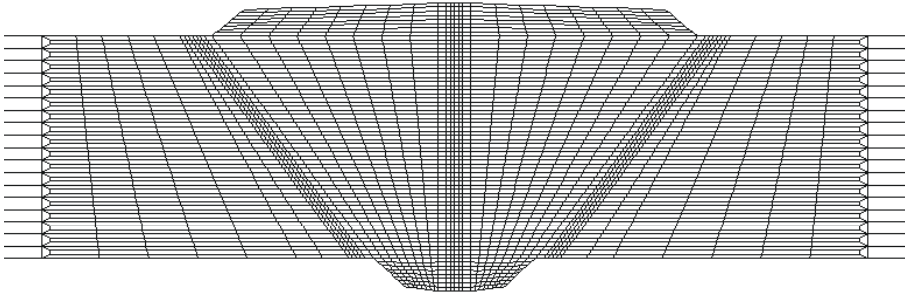


Figure 3-6: Modified two-dimensional finite element model according to the gauge cross-section of the orbitally welded pipeline for simulation of hydrogen assisted cold cracking.

The finite element type PLANE 55 is employed for temperature and hydrogen distribution analysis and the finite element type PLANE 42 is employed for stress-strain distribution analysis. These finite elements can directly be changed in the given finite element model according to the analysis purpose.

3.2.2 Modelling of Hydrogen Diffusion

Finite element calculations of hydrogen diffusion represent the case for modelling hydrogen assisted stress corrosion cracking and hydrogen assisted cold cracking, and are thus described here in detail.

The exponential equations are very helpful in the numerical finite element simulation of hydrogen distribution because they can directly be used to generate the material properties in terms of the hydrogen diffusion coefficient dependent on temperature with connection to the previous temperature analysis.

Due to an advanced numerical finite element program for hydrogen diffusion analysis in welding technology based on the commercial finite element program, the basic simple model finite elements was created for performing the trial analysis of hydrogen distribution with different boundary conditions as represented in Figure 3-7 in order to confirm that the modified advanced finite element modelling is in agreement with the basic principle. With model A, assuming an initial state with a constant hydrogen concentration of $20.00 \text{ ml} \cdot (100\text{gFe})^{-1}$ at every node of the finite elements located at $x \leq 0$ for a short period of time (1 second), and a hydrogen-free condition at the nodes on the opposite side are, a constant hydrogen diffusion coefficient of $2.0\text{E-}04 \text{ mm}^2 \cdot \text{s}^{-1}$ was used for the simulation. Subsequently, the amount of local hydrogen concentration in distances of 0.25 mm, 0.50 mm, 0.75 mm, and 1.00 mm was determined for any time of diffusion. The obtained hydrogen concentrations must be compared with the values calculated by the following equation^{[GEN 23],[GEN 29]}:

$$[HD]_{(x,t)} = \frac{[HD]_{mi}}{2} \left[1 + \operatorname{erf} \left(\frac{x}{2\sqrt{D_{eff} \cdot t}} \right) \right] \quad (3-1)$$

where x is the distance from the ordinary system and $[HD]_{mi}$ is the initial hydrogen concentration.

3. Finite Element Modelling Development

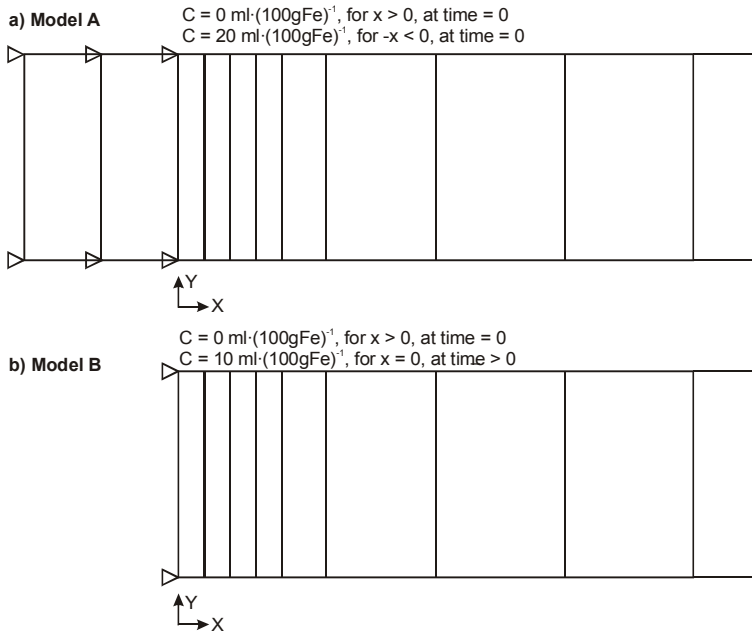


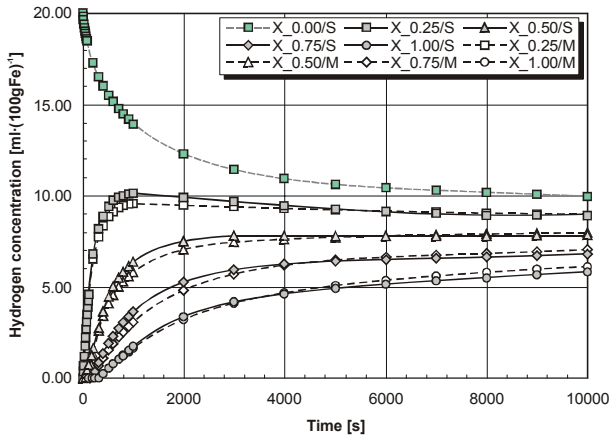
Figure 3-7: Simple finite element models and boundary conditions for confirming results of the advanced numerical modelling of hydrogen distribution in welded components.

With model B, in which a constant hydrogen diffusion coefficient of $2.0\text{E}-04 \text{ mm}^2 \cdot \text{s}^{-1}$ was specified to the finite element model, a constant hydrogen concentration of $10.00 \text{ ml} \cdot (100\text{gFe})^{-1}$ is continuously applied at the nodes located at $x = 0$ through the calculation according to the assumption of a pair of semi-infinite solids (see Figure 3-7b). The hydrogen concentration levels determined in distances of 0.25 mm, 0.50 mm, 0.75 mm and 1.00 mm are compared with the values calculated by Equation (3-1).

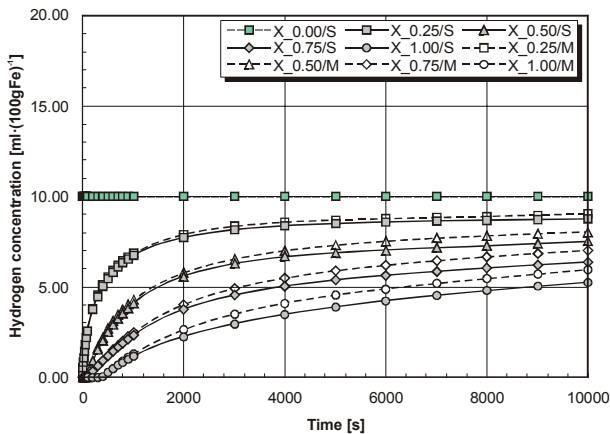
The results from the model A are shown in Figure 3-8a. The hydrogen concentration at the interface line decreases continuously with increasing time of simulation, whereas the increase of hydrogen concentration at the points in the specific distance from the interface line is individually represented. It should be noted for the nearest point to the interface line that after a simulation time of 2,000 seconds there is a tendency towards reduced hydrogen concentration. The reason is that the initial source cannot provide sufficient amounts of hydrogen for a concurrent action of hydrogen loss. Since manual calculation with Equation (3-1) relies on the assumption of a pair of semi-infinite solids, the calculation of hydrogen concentration in terms of time and location must take account of the actual hydrogen concentration at the interface of the applied hydrogen source because this actual hydrogen concentration does not immediately drop to half the amount of the full initial hydrogen concentration as in the assumption of a pair of semi-infinite solids. This phenomenon might be influenced by hydrogen diffusion coefficient. However, the results from the manual calculation indicate a good agreement with the simulated results.

In the other case, the finite element simulation has been carried out exactly according to the assumption of a pair of semi-infinite solids, Figure 3-8b represents the results from the finite element simulation and the manual calculation with constant application of half the

3. Finite Element Modelling Development



a) Simulation and calculation with model A



b) Simulation and calculation with model B

Figure 3-8: Characteristic of hydrogen distribution obtained from finite element simulation and manual calculation in distances of 0.25 mm, 0.50 mm, 0.75 mm and 1.00 mm from the interface of a applied hydrogen source (Assumption: hydrogen diffusion coefficient = $2.0E-04 \text{ mm}^2 \cdot \text{s}^{-1}$; M and S indicate the finite element simulation and manual calculation, respectively).

hydrogen concentration, $10.00 \text{ ml} \cdot (100\text{gFe})^{-1}$, of the initial hydrogen source at the nodes on the interface line of the semi-infinite solids.

The hydrogen concentration at the given points with the specific distance from the interface line increases with the diffusion time, and the point with the shortest distance always indicates highest hydrogen concentration. Again, the results of hydrogen distribution from the finite element simulation are in good agreement with those from the manual calculation. More interestingly, the hydrogen distribution curves at the given point nearest to the interface line from model A and the model B obviously indicate the difference in their characteristics due to the actual hydrogen concentration at the interface line.

The advanced finite element modelling approach for simulating hydrogen distribution in arc welding processes taking account of the hydrogen diffusion coefficient dependent on temperature, has been assessed on a trial and error basis. The finite element trial modelling was performed only with the model B because of the assumption of a pair of semi-infinite solids.

3. Finite Element Modelling Development

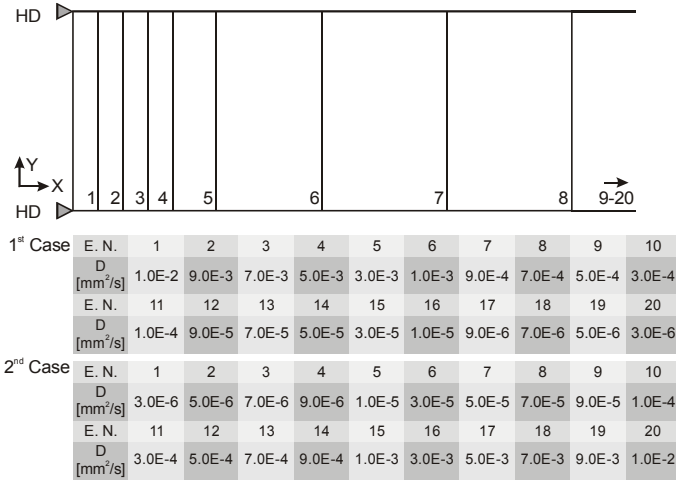


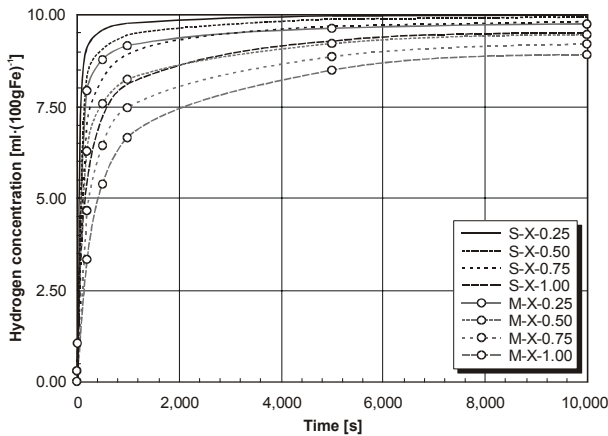
Figure 3-9: Simple finite element model with assumption of an individual hydrogen diffusion coefficient for each finite element in order to confirm the modified advanced finite element modelling for calculating hydrogen diffusion during welding and subsequent cooling.

The finite element model contains 20 finite elements. An individual hydrogen diffusion coefficient has been applied as the material property for each finite element. As represented in Figure 3-9, in the first case, a series of hydrogen diffusion coefficients has been applied to the finite element model in which each finite element has an individual value for the hydrogen diffusion coefficient (see the first case in Figure 3-9). The hydrogen diffusion coefficient of $1.0E-02 \text{ mm}^2 \cdot \text{s}^{-1}$ has been applied as the material property to the first finite element adjacent to the interface of the applied hydrogen source, and the gradual decrease of the hydrogen diffusion coefficient has subsequently been applied to the next finite element and so on. In the second case, the hydrogen diffusion coefficient of $3.0E-06 \text{ mm}^2 \cdot \text{s}^{-1}$ has been applied to the first finite element adjacent to the interface of the applied hydrogen source, and the gradual increase of the hydrogen diffusion coefficient has been applied to the next finite element and so on (see the second case in Figure 3-9).

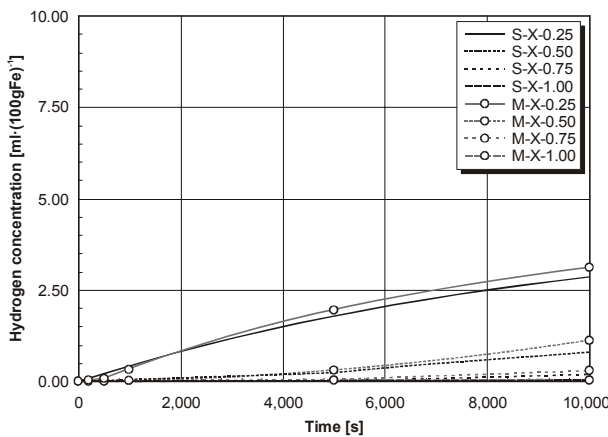
The hydrogen concentrations dependent on the diffusion time at the specific points with distances of 0.25 mm, 0.50 mm, 0.75 mm and 1.00 mm from the interface of the applied hydrogen source are determined in order to compare the results with those obtained from the manual calculation. The manual calculation of the hydrogen distribution is carried out with Equation (3-1), but the average hydrogen diffusion coefficients have to be substituted into the equation for the effective value. This average value has been determined by the sum of the hydrogen diffusion coefficients of all elements between the point of the applied load and the capture point, with the next finite element to the capture point, with respect to the number of finite elements.

The hydrogen distribution result of the first case obtained by both the finite element simulation and the manual calculation is represented in Figure 3-10a showing a deviation of less than 5 percent between both methods. The hydrogen concentration at the specific points with increasing diffusion can nearly reach the applied level of constant hydrogen concentration, i.e. $10.00 \text{ ml} \cdot (100\text{gFe})^{-1}$, without the requirement of longer diffusion time due to a higher hydrogen diffusion coefficient in the zone adjacent to the surface of the applied

3. Finite Element Modelling Development



a) First case



b) Second case

Figure 3-10: Characteristic of hydrogen distribution obtained from finite element simulation and manual calculation at the specific points with distances of 0.25 mm, 0.50 mm, 0.75 mm, and 1.00 mm from the interface of applied hydrogen: a) the first case, b) the second case. (M and S indicate the finite element simulation and manual calculation, respectively).

constant hydrogen source as compared to the remote zone, which can also result in drastic rise of hydrogen concentration at the specific distances in a short time period (2000 seconds) for the diffusion of hydrogen.

In the second case, there is an indication of good agreement between finite element simulation and manual calculation for determining the hydrogen distribution based on the assumption of the semi-infinite solids represented in Figure 3-10b. The hydrogen concentration at the specific points slowly increases even though the diffusion time continuously increases due to low values of the hydrogen diffusion coefficient specified for the finite elements adjacent to the surface of the applied constant hydrogen source.

Therefore, the advanced finite element model can be accepted to be used to simulate hydrogen distribution taking account of the hydrogen diffusion coefficient dependent on temperature, in particular, for finite element modelling of welding processes with high reliability.

Hydrogen diffusion coefficients are very significant as material property for numerical simulation of hydrogen diffusion and can be determined by electrochemical techniques as previously described in Section 2.3.2. Additionally, due to the fact that the hydrogen subsurface concentration is a result of hydrogen uptake at the specimen surface during exposure to sour service environments, a hydrogen source for diffusion through solid materials can be influenced by the degree of H₂S saturation in the standard test solution and by the material's conditions, i.e. the as-quenched state and the as-delivered state. Thus, significant input data containing hydrogen diffusion coefficients, hydrogen subsurface concentrations and the failure criterion for numerical modelling of hydrogen assisted stress corrosion cracking are described in Section 3.2.5.

3.2.3 Numerical Modelling Concept

Following the CTOD concept, fracture can be regarded as a fracture sequence of a number of fictitious tensile specimens which are positioned along the crack path. Minimum crack propagation in the global tensile specimen is represented by failure in the specific fictitious tensile specimen just ahead of the crack tip. The fictitious tensile specimen will be fractured when the hydrogen concentration profile across the whole specimen reaches the critical value. This critical value is dependent on the respective mechanical load. Assuming a homogeneous microstructure, the critical hydrogen concentration is reduced by increasing the true fracture strain, furthermore, a definition of the crack growth behaviour can also be taken into account. For example, unstable crack propagation occurs when the failure of the first specimen adjacent to the crack tip immediately causes the failure of the next specimen, and so on, whereas, if the failure of the first specimen adjacent to the crack tip does not induce immediate rupture of all the subsequent specimen, stable crack propagation of the global tensile specimen can be defined.

Therefore, the numerical modelling concept for simulating hydrogen assisted stress corrosion cracking can be established by assuming a sufficiently small size of the finite element representing a fictitious tensile specimen as schematically illustrated in Figure 3-11. A calculation of the local strain of the finite element ahead of the crack tip can be carried out as a function of the global strain based on the Lidbury's equation (2-54). This equation is used in the calculation because no analytical approach is up to now ascertained for calculating continuous crack propagation. The hydrogen distribution profile is calculated based on the Fick's second law. Hydrogen subsurface concentration is constantly assumed to be applied to all nodes of the surface exposed to the electrolytic standard test solution with the specific level of H₂S saturation, even though the stagnant solution in the cracked path and the freshly cracked surface may also influence the behaviour of hydrogen uptake by the material surface.

Consequently, the interaction between local hydrogen concentration and local strain distribution in the finite element adjacent to the crack front is regarded by using the criterion equations (Equation (3-2) or Equation (3-3)). Comparison between the local hydrogen concentration and the critical value at the specific point in time is carried out. When the local hydrogen distribution profile across the whole first element at the crack tip reaches the critical value, the specific finite element, in which the crack propagation of the global specimen occurs, is deleted.

3. Finite Element Modelling Development

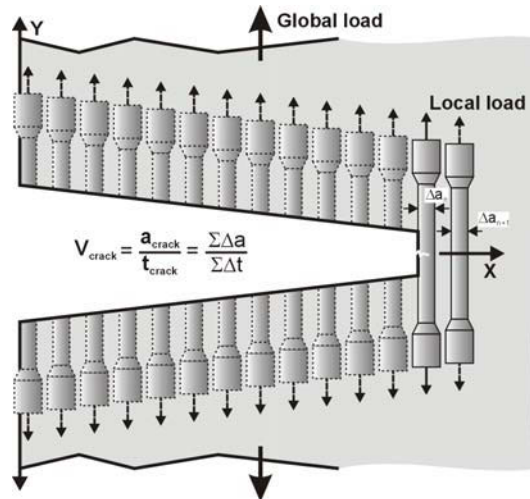


Figure 3-11: Schematic illustration of the concept of fictitious tensile specimens to simulate crack propagation with consideration of a local interaction for hydrogen assisted stress corrosion cracking^[HAS 108]

Since the modelling of continuous crack propagation concerns a number of finite elements as fictitious tensile specimens, a sequence in the numerical modelling program must be determined in order to clarify the complicated phenomenon of continuous crack propagation.

3.2.4 Sequence of the Modelling Program

Following the creation of the finite element model, an operation command for specifying the boundary conditions on the finite element model is required which can be generated by using either a graphical user interface (GUI), or a Macro-file. However, in the present work, the generation of only a Macro-file is highlighted because it offers a more convenient way to completely generate a numerical program for complicated calculation, and it enables the user to edit the program much quicker.

Since the commercial finite element program, ANSYS, has been developed based on the FORTRAN programming language, the program structure for the Macro-file can be constructed in a similar approach as APDL (ANSYS Parametric Design Language). In general, a sequence of the numerical program. The flow chart showed in Figure 3-12 outlines the route of the programme after the decision about the modelling concept has been taken.

The program begins with a test specimen initially assumed to be in a hydrogen-free state, meaning that a very low hydrogen concentration (say 10^{-6} Nml $(100\text{gFe})^{-1}$) is applied to every node of the finite element model. Subsequently, the specific hydrogen subsurface concentration dependent on the H_2S saturation is continuously applied to every node on the external surface of the specimen exposed to the electrolytic test solution at constant incremental time until the incubation time is reached at which the first series of finite elements in the crack path is deleted.

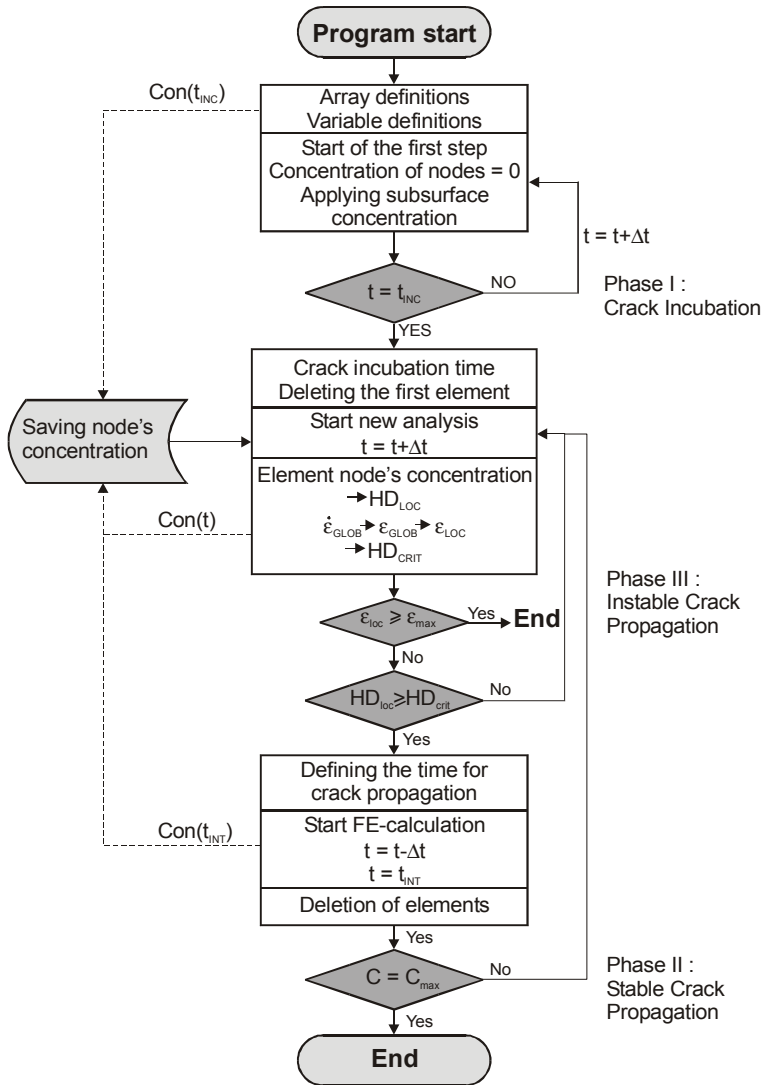


Figure 3-12: Flow chart for numerical modelling of hydrogen assisted cracking in a standard test specimen.

The new analysis begins with the same conditions, i.e. hydrogen concentration, point in time, and local strain level, as those at the end of the previous step. At the same time, hydrogen subsurface concentration is initiated at every node on the newly cracked surface. The local hydrogen concentration and the local strain level at the node opposite to the crack tip in the first element is evaluated and compared to the critical hydrogen concentration in order to define the characteristic of crack propagation. Unstable crack propagation, i.e. Stage III, takes place when the local strain reaches the mechanical rupture strain of the material (overload) that will finish the running program by already described failure of the rest of the specimens. On the other hand, a comparison between the local hydrogen

3. Finite Element Modelling Development

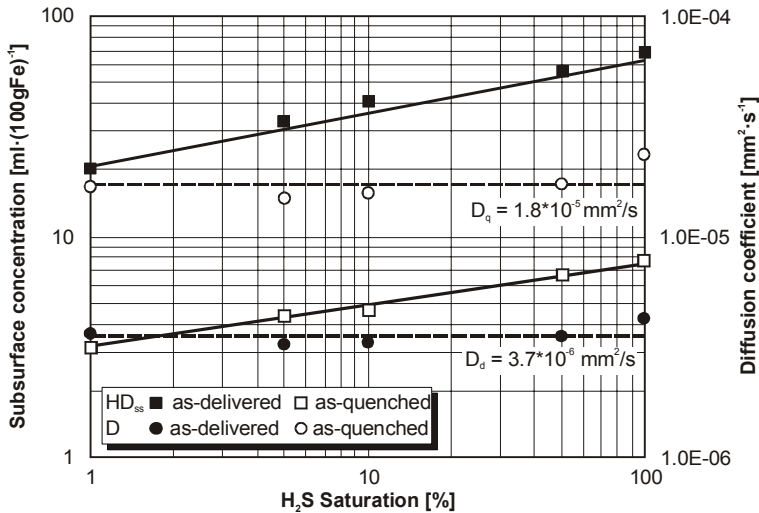


Figure 3-13: Subsurface concentration and diffusion coefficients of supermartensitic stainless steel in the as-delivered and the as-quenched with respect to various levels of the H₂S saturation in the NACE electrolytic solution at room temperature^[HPD 21].

concentration and the critical hydrogen concentration is carried out if the specimen does not fail by overload, and the exact time for crack propagation is defined by an interpolation technique if the local hydrogen concentration reaches the critical value. Crack propagation will take place with deleting the first series of the elements ahead of the crack tip. In turn, if the hydrogen concentration at the detected point is still lower than the critical value, the program will continuously run for the next load step at the specific incremental time until the hydrogen concentration at the specific point reaches the critical value. Finally, the program ends when the crack length is equal to the diameter of the global specimen.

3.2.5 Specific Input Data for Modelling

In the following passages the basic input data for modelling hydrogen assisted cracking in supermartensitic stainless steel are represented.

Boellinghaus et al.^[HPD 21] experimentally determined hydrogen permeation and diffusion in supermartensitic stainless steel in the as-quenched state and the as-delivered state, which were examined in the NACE standard test solution with various levels of H₂S saturation. The results clearly indicate that hydrogen diffusion coefficients in both the as-delivered state and the as-quenched state are nearby independent of the degree of H₂S saturation in the electrolytic standard test solution, but are dependent on their condition. Levels of hydrogen subsurface concentrations are directly proportional to the H₂S saturation for both states of supermartensitic stainless steel as represented in Figure 3-13. Hydrogen diffusion coefficients of 3.7E-06 mm²·s⁻¹ and of 1.8E-05 mm²·s⁻¹, respectively, are defined in the finite element model as the material property for the as-delivered state and the as-quenched state. Additionally, the effects of various H₂S saturations in the NACE standard test solution on the hydrogen subsurface concentration are also taken into account in the numerical modelling as variable boundary conditions.

Table 3-2: Significant data of the as-delivered state and the as-quenched state of supermartensitic stainless steel for numerical modelling of HASCC.

H ₂ S Saturation [%]	Delivered state		Quenched state	
	HDss [ml·(100gFe) ⁻¹]	D [mm ² ·s ⁻¹]	HDss [ml·(100gFe) ⁻¹]	D [mm ² ·s ⁻¹]
1	20	3.70E-06	3.20	1.8E-05
10	35	3.70E-06	5.00	1.8E-05
30	45	3.70E-06	6.00	1.8E-05
50	50	3.70E-06	6.70	1.8E-05
100	60	3.70E-06	7.40	1.8E-05

Table 3-2 lists some significant data according to Figure 3-13, which are directly used for numerical modelling of hydrogen assisted stress corrosion cracking in supermartensitic stainless steel with respect to both the as-delivered state and the as-quenched state.

Since as-quenched supermartensitic stainless steel weld metal and heat affected zone have experimentally been found after completed arc welding, the hydrogen diffusion behaviour, i.e. the hydrogen diffusion coefficient and the hydrogen subsurface concentration, of the weld metal and the heat affected zone are obviously different from those of the base metal (see Section 3.2.5). For instance, the NACE standard test solution with 1% H₂S saturation leads to a hydrogen subsurface concentration of 3.20 ml·(100gFe)⁻¹ corresponding to a hydrogen diffusion coefficient of 1.80E-05 mm²·s⁻¹ for the weld metal and the heat affected zone, whereas a hydrogen subsurface concentration of 20.00 ml·(100gFe)⁻¹ corresponding to a hydrogen diffusion coefficient of 3.70E-06 mm²·s⁻¹ is found for the base metal. Therefore, the different hydrogen diffusion behaviour in each zone has to be defined as a material property (diffusion coefficient) and as a boundary condition (subsurface concentration) for the numerical modelling.

Since the propagation of hydrogen assisted stress corrosion cracking is a time-dependent phenomenon involving local interaction of hydrogen concentration and strain distribution, a failure criterion of the specific material is needed for integrating into the numerical program as the logical function for characterising the crack propagation. There are two important failure criteria for supermartensitic stainless steel that are employed for the present research: I) the first is the criterion for the as-delivered state as represented in Figure 3-14a and II) the second is the criterion for the as-quenched state as represented in Figure 3-14b. These criteria indicate that the critical hydrogen concentration is decreased by increasing the true fracture strain. The critical hydrogen concentration in the as-quenched state is lower than that in the as-delivered state at the same level of true fracture strain. The reason for this is that the supermartensitic stainless steel in the as-quenched state is more susceptible to hydrogen assisted cracking and fails by greater loss in ductility. However, it should be recognised that both the hydrogen diffusion coefficient and the hydrogen subsurface concentration can be the chief factor characterising crack propagation.

Based on the experimental determination performed by Boellinghaus et al.^[SPM 33], the mathematical models corresponding to Figure 3-14 for calculating the critical hydrogen concentration as a function of the true fracture strain derived by linear regression can be expressed as follows:

3. Finite Element Modelling Development

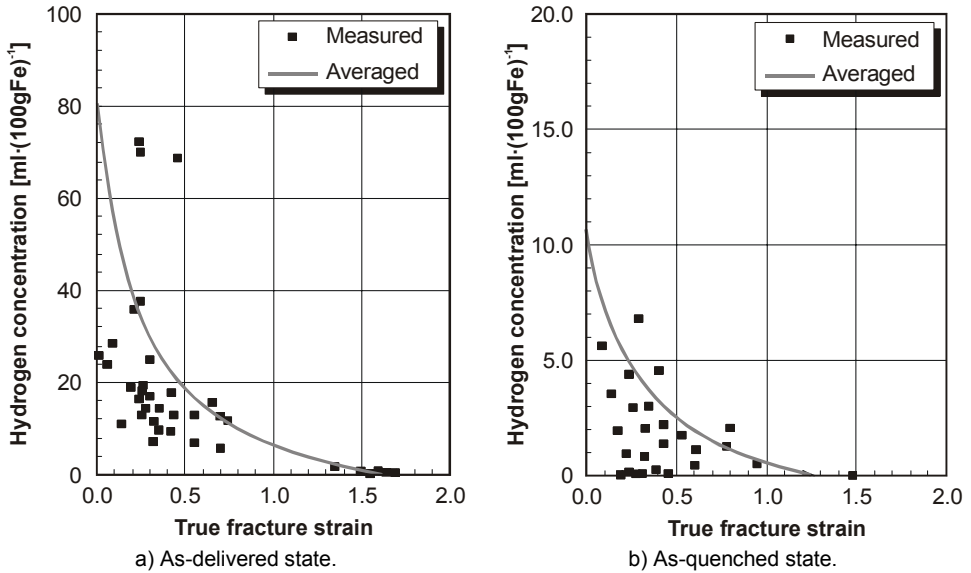


Figure 3-14: Critical hydrogen concentration dependent on the true fracture strain of supermartensitic stainless steel: a) As-delivered state, b) As-quenched state^[SPM 33].

$$[HD]_{crit} = 64.2490 \exp(-4.5 \cdot \epsilon_{true}) - (9.9447 \cdot \epsilon_{true}) + 16.3060 \quad (3-2)$$

given for supermartensitic stainless steel in the as-delivered state. And

$$[HD]_{crit} = 6.3410 \exp(-5.2 \cdot \epsilon_{true}) - (3.5953 \cdot \epsilon_{true}) + 4.5320 \quad (3-3)$$

given for supermartensitic stainless steel in the as-quenched state, where $[HD]_{crit}$ is the critical hydrogen concentration and ϵ_{true} is the true fracture strain.

In general, the finite element simulation needs adequate material properties for obtaining exact results. Still, there is a lack of exact data, and thus, efforts to modify material properties based on the general knowledge of material behaviour have been made in order to further develop the finite element modelling for supermartensitic stainless steels. Significant material properties as a function of the temperature of supermartensitic stainless steel, i.e. specific density, heat convection coefficient, specific heat capacity, and thermal conductivity for the temperature analysis are represented in Figure 3-15. These have been obtained from Richter^[GEN 31] giving the values for similar steels having a high carbon content.

These basic material properties are employed in the modelling program for calculating the temperature distribution resulting from the temperature gradient. Additionally, the structural analysis requires mechanical material properties dependent on temperature, since the stress-strain distribution during welding and subsequent cooling is partly of the main causes of the phenomenon of hydrogen assisted cold cracking due to consequent effects of thermal contraction.

3. Finite Element Modelling Development

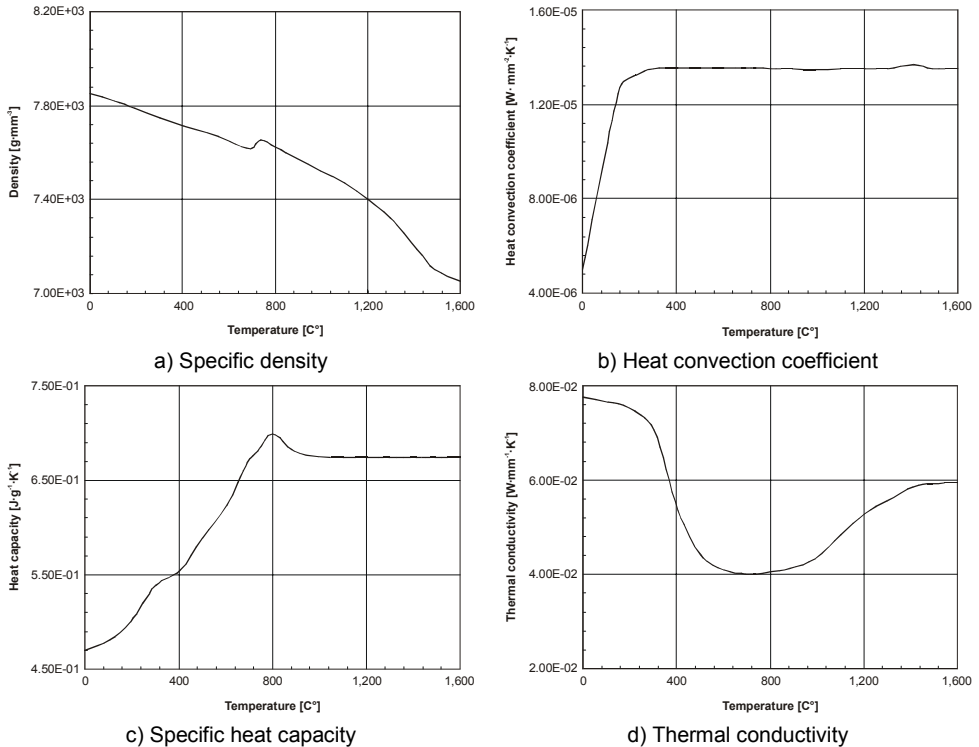


Figure 3-15: Significant material properties dependent on temperature for numerical modelling in temperature analysis: a) Specific density, b) Heat convection coefficient, c) Specific heat capacity, d) Thermal conductivity.

True stress-strain relationship of supermartensitic stainless steel at room temperature is represented in Figure 3-16a. The engineering stress-strain flow curve with a tensile proof stress of 770 MPa and an ultimate tensile stress of 870 MPa has been converted into both a multi-linear flow curve and a bilinear flow curve for the numerical finite element simulation. Since the determination of the multi-linear flow curve is more complicated than that of the bilinear flow curve, bilinear flow curves dependent on temperature based on actual stress-strain relationship of supermartensitic stainless steel for the base metal have been modified as shown in Figure 3-16b. Due to the fact that the weld metal and the heat affected zone have higher levels of elastic-plastic transformation stress as well as higher work hardening effects, in particular at ambient temperature than those of the base metal, the stress-strain relationships of the heat affected zone and the weld metal dependent on temperature have been modified as represented in Figure 3-16c and Figure 3-16d, respectively. It has to be mentioned that such curves represent a simplification of the true stress-strain behaviour of the materials as shown in Figure 3-16a by the bilinear flow curve.

The calculation of stress-strain distribution due to thermal contraction caused by the temperature gradient needs further material properties including thermal expansion coefficient and Poisson's ratio. Figure 3-17a represents the thermal expansion coefficient of supermartensitic stainless steel as a function of temperature for the base metal. But, for the

3. Finite Element Modelling Development

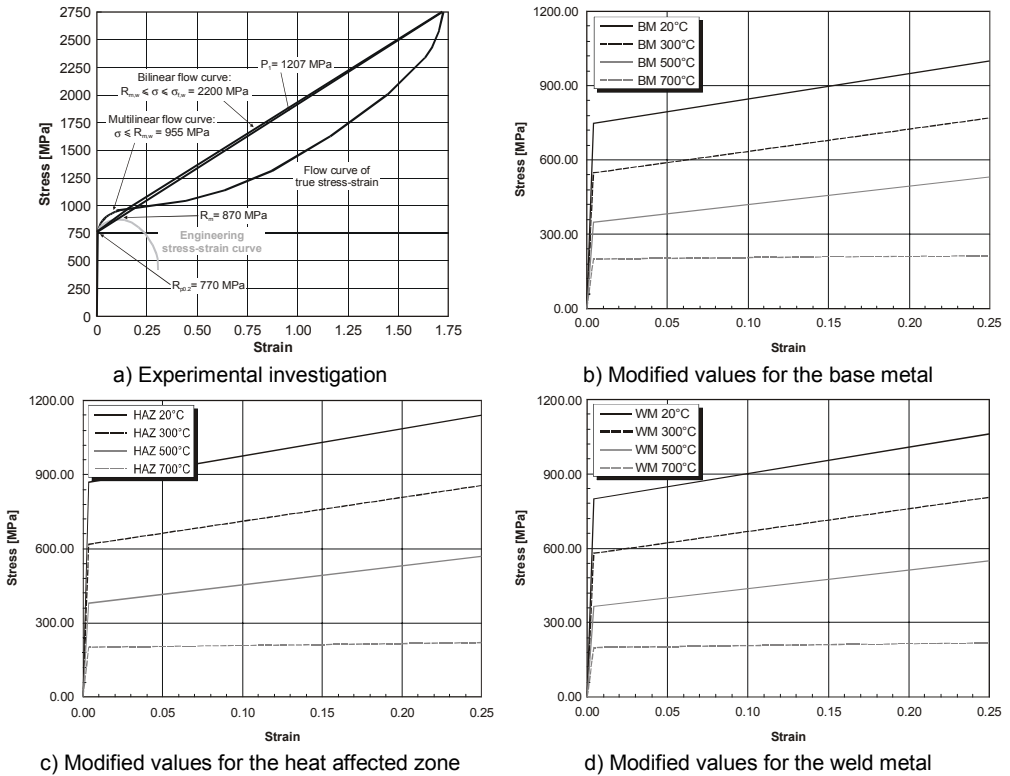


Figure 3-16: Stress-strain relationship of supermartensitic stainless steel as material property for numerical modelling in structural analysis: a) Experimental investigation at room temperature^[GEN 19], b) Modified values dependent on temperature for the base metal, c) Modified values dependent on temperature for the heat affected zone, d) Modified values dependent on temperature for the weld metal.

heat affected zone and the weld metal, there is great difference in the thermal expansion coefficient as compared with the base metal, because these values are strongly dependent on the type of microstructure formation, e.g. austenitic structure, martensitic structure, etc. This reason is also valid for the Poisson's ratio value which is represented in Figure 3-17b for the base metal. The effect of austenite-martensite transformation on a rise of thermal expansion coefficients during of components to room temperature has not been taken into account in the modelling because this effect is not remarkable for supermartensitic stainless steel.

Although the significant material properties for both the temperature analysis and the structure analysis have completely been described above, the calculation of hydrogen assisted cold cracking cannot be complete if the important analysis of hydrogen distribution in the welded component is not simultaneously performed. Therefore, significant material properties for hydrogen diffusion analysis should particularly be described because up to date the commercial finite element program offers no option for taking account of the material properties with a view to the diffusion coefficient as a function of temperature.

3. Finite Element Modelling Development

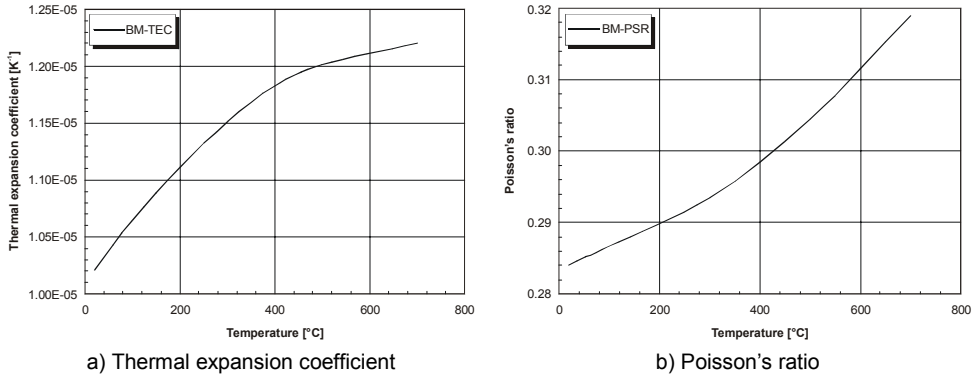


Figure 3-17: Material properties of supermartensitic stainless steel as a function of temperature: a) Thermal expansion coefficient, b) Poisson's ratio^[GEN 31].

Two quantitative influences of stress and trapping effects on the hydrogen diffusion behaviour are still contrary to each other, but there is clearly a number of evidences showing that the hydrogen diffusion behaviour is drastically governed by temperature, in particular as concerns hydrogen distribution during the welding process^[HAC 21]. In contrast, the temperature effect on the hydrogen diffusion behaviour can better be evaluated and will be highlighted in the following passages.

As previously described, thermal analysis is normally employed for the diffusion analysis based on Fourier's equation (see Equation (2-67)) so that the transformation of the thermal conductivity, K_{xx} , into the mass diffusion coefficient, D_{xx} , is needed. This can simply be carried out by defining the material density and the specific heat capacity to be a unity. The relation between the mass diffusion coefficient and the thermal conductivity is generally described by:

$$D_{xx} = \frac{K_{xx}}{\rho \cdot C_p} \quad (3-4)$$

Figure 3-18 represents the scatterband of the hydrogen diffusion coefficient in steels having austenitic decomposition microstructure and in supermartensitic stainless steel as a function of temperature. It clearly shows that at high temperature the hydrogen diffusion coefficient becomes higher than at room temperature by several orders of magnitude and the hydrogen diffusion coefficient of steels is lowered by the presence of some austenitic decomposition microstructure in the matrix material.

For analysing the hydrogen distribution in girth welds of supermartensitic stainless steel pipelines, the flow curve of the hydrogen diffusion coefficient of supermartensitic stainless steel can be applied to the modelling program as the material property. The Arrhenius exponential forms of the hydrogen diffusion coefficient of as-delivered supermartensitic stainless steel are listed in Table 3-3. In the heating up process, the hydrogen diffusion coefficient of the as-delivered steel with martensitic microstructure exponentially increases with increasing temperature until about 700°C, becomes lower due to the presence of austenitic microstructure and increases again when the austenite completely transforms to delta-ferrite.

3. Finite Element Modelling Development

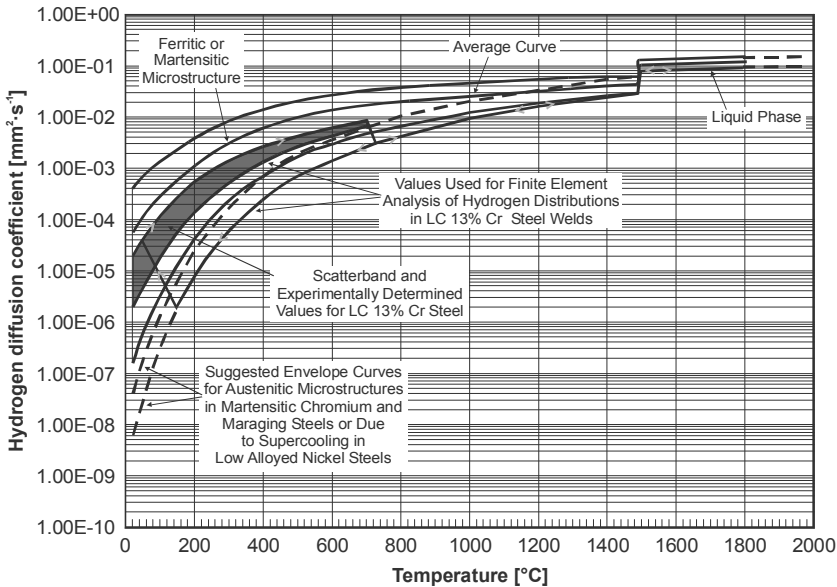


Figure 3-18: Scatterband of hydrogen diffusion coefficients in steels having austenitic decomposition microstructure and in supermartensitic stainless steel as a function of temperature used for numerical modelling^[HPD 69].

Table 3-3: Hydrogen diffusion coefficients of supermartensitic stainless steel pipelines in the Arrhenius form for the base metal.

Heating up		Cooling down	
Temperature [°C]	Diffusion coefficient [mm ² ·s ⁻¹]	Temperature [°C]	Diffusion coefficient [mm ² ·s ⁻¹]
20-700 (Martensite)	0.15exp(-3100/T)	>1470 (Liquid)	0.348exp(-1975/T)
700-1200 (Austenite)	0.895exp(-5205/T)	1470-1200 (δ-ferrite)	0.253exp(-3001/T)
1200-1470 (δ-ferrite)	0.253exp(-3001/T)	1200-150 (Austenite)	0.895exp(-5205/T)
>1470 (Liquid)	0.348exp(-1975/T)	150-100 (Phase trans.)	((-4.5423E-07)·T)+1.9622E-04
		100-20 (Martensite)	0.15exp(-3100/T)

Table 3-4: Hydrogen diffusion coefficients of supermartensitic stainless steel pipelines in the Arrhenius form for the heat affected zone and the weld metal.

Heating up		Cooling down	
Temperature [°C]	Diffusion coefficient [mm ² ·s ⁻¹]	Temperature [°C]	Diffusion coefficient [mm ² ·s ⁻¹]
20-700 (Martensite)	0.535exp(-3000/T)	>1470 (Liquid)	0.348exp(-1975/T)
700-1200 (Austenite)	0.895exp(-5205/T)	1470-1200 (δ-ferrite)	0.253exp(-3001/T)
1200-1470 (δ-ferrite)	0.253exp(-3001/T)	1200-150 (Austenite)	0.895exp(-5205/T)
>1470 (Liquid)	0.348exp(-1975/T)	150-50 (Phase trans.)	((-4.5423E-07)·T)+1.9622E-04
		50-20 (Martensite)	0.535exp(-3000/T)

In the cooling process, the hydrogen diffusion coefficient is similar to that in the heating up process for the liquid state, delta-ferrite and austenitic range, but the important point is that austenitic microstructure still remains until the martensite-start temperature (say 150°C) is reached, and it completely transforms to martensite at 100°C.

Because of the higher cooling rate in the weld metal and its neighbouring zones compared to that in the remote zones of girth welded supermartensitic stainless steel pipelines, the as-quenched state of the weld metal and the heat affected zone is normally obtained. Table 3-4 represents the Arrhenius exponential forms of the hydrogen diffusion coefficient of the quenched state which has a hydrogen diffusion coefficient five times higher than the delivered state and the martensite finish temperature is also lower (approximately 50°C)^{[HPD 21], [HPD 22]}.

3.2.6 Modelling of HASCC at Pipeline Welds

Joining of larger dimensioned pipes will produce respectively high transverse reaction forces depending on the transverse shrinkage restraint. Therefore, a large scale test facility with the capacity of carrying or introducing loads up to 16 MN in the horizontal direction is intentionally used to investigate and simulate failure behaviour of such pipes caused by thermo-mechanical effects during welding and cooling. In orbital fabrication welding of supermartensitic stainless pipes, the welds were performed by orbital pulsed TIG welding of four layers. The slightly various values of average heat input ranging at about $E_1 = 0.8 \text{ kJ}\cdot\text{mm}^{-1}$, $E_2 = 1.1 \text{ kJ}\cdot\text{mm}^{-1}$, $E_3 = 1.1 \text{ kJ}\cdot\text{mm}^{-1}$ and $E_4 = 1.1 \text{ kJ}\cdot\text{mm}^{-1}$ were performed for each layer. Welding parameters such as base current, travel speed and electrode weaving were varied during welding in order to optimise the weld pool shape in down and up hill position. An interlayer temperature was about 40°C in order to ensure that the microstructure of the weld metal and neighbouring zones fully transforms into martensitic microstructure which can facilitate component strength improvement.

A graphic sketch with the dimensions of the assembled pipeline is represented in Figure 3-19a. The original pipeline has an external diameter of 323 mm, a wall thickness of 6 mm and a length of 700 mm. This pipe was machined at each end to form the test gauge with a length of 60 mm and to reduce the wall thickness to 0.5 mm as well as to provide a U-joint preparation. In order to arrange for the test volume to be available for the NACE standard test solution, a backing plate with upper limit diameter of 311 mm is fabricated from supermartensitic stainless steel and assembled by anchor welds in a distance of 250 mm from the end of the component where the machined part begins. The other component is fabricated in the same procedure as described above. The two component parts are finally joined to each other by TIG welding process giving a test volume of around 40 litre.

The purpose of the gauge section is to ensure that the crack will occur only in the area of the welded joint which is highly useful for comparing the actual characteristic of the susceptibility to hydrogen assisted stress corrosion cracking in the base metal, the heat affected zone and the weld metal.

3.2.6.1 Description of the Test Procedure

The interaction between local hydrogen concentration and stress-strain distribution in a specific material will lead to component failure, which must be taken into account in finite element simulation of hydrogen assisted stress corrosion cracking in assembled pipelines.

3. Finite Element Modelling Development

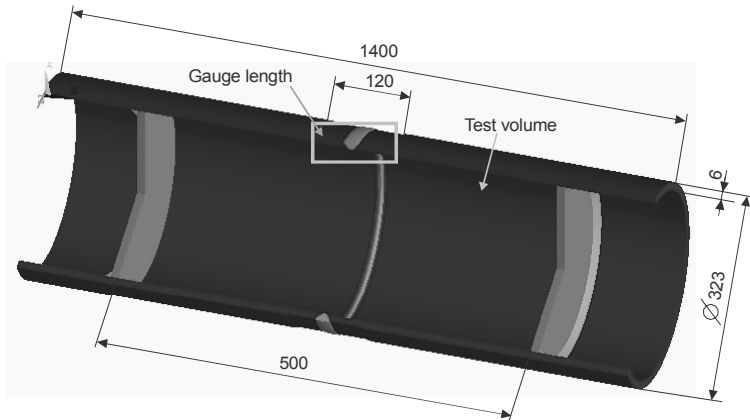


Figure 3-19: Dimensions of supermartensitic stainless steel pipeline orbitally welded with four layers of matching filler wires materials.

After assembly of the pipeline by TIG welding with four layers of matching material, which is practically accomplished on the GAPS1 16 (see Section 2.7.2.2), the test volume is filled up with the NACE standard test solution in order to simulate hydrogen uptake on the inside surface of the pipeline. External application of mechanical loads can be performed by using the loading system of the GAPS1 16 as schematically represented in Figure 3-20. H₂S saturation is usually added to the test solution to adjust the hydrogen uptake capability of the component surface.

In order to gain a basic knowledge of the modelling procedure and its respective results in comparison to respective slow strain rate test, it was first assumed that the component is subjected to constant strain rates ranging between $1.0\text{E-}07$ to $1.0\text{E-}05 \text{ s}^{-1}$ and is exposed to the electrolytic NACE solution at 1, 10, 30, 50 and 100% H₂S saturations. The respective hydrogen diffusion coefficients were $3.70\text{E-}06 \text{ mm}^2\cdot\text{s}^{-1}$ and $1.80\text{E-}05 \text{ mm}^2\cdot\text{s}^{-1}$ for the as-delivered and as-quenched materials, respectively. The respective hydrogen subsurface concentrations can be taken from Table 3-2. In addition to this, the modelling was adjusted to the real component test.

With these basic considerations in mind, the first attempts have been undertaken to model the performance of supermartensitic stainless steel pipelines more realistically, in particular with respect to the load history of the large-scale test. Consistent with the component test, constant global straining of the pipe at $\epsilon = 0.1\%$ has been assumed, corresponding to a stress distribution of around 250 MPa introduced during welding and cooling of the pipe at realistic low shrinkage restraints. For three weeks, the pipe has internally been exposed to this stress-strain level and to a realistic sour service condition. After that period, the welded component was stepwise strained each day at rates of around $1.0\text{E-}05 \text{ s}^{-1}$ to 70% and 100% of the weld metal yield strength, corresponding to simulated global strains of $\epsilon = 0.3\%$ and $\epsilon = 0.5\%$, respectively.

Subsequently, straining of the weld metal up to $\epsilon = 3\%$ and finally to $\epsilon = 5\%$ has been performed in the experiments and has been numerically modelled, respectively. Hydrogen subsurface concentration corresponding to exposure of the welded pipeline to the NACE standard test solution with 1% H₂S saturation is applied to all nodes of the internal pipeline

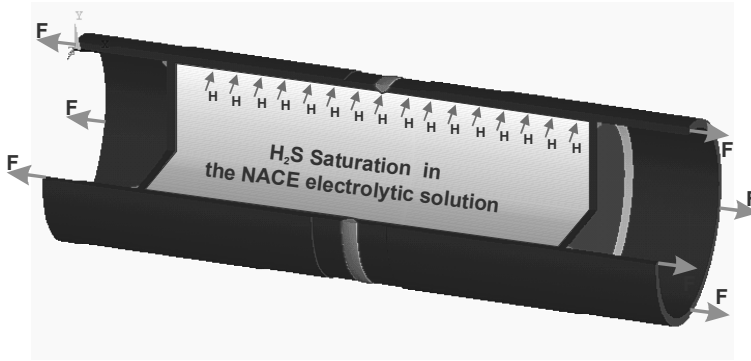


Figure 3-20: Schematic illustration of boundary conditions for testing hydrogen assisted stress corrosion cracking in the orbitally welded pipeline.

surface. However, it should be noted that constant H_2S saturation in the standard solution can cause in different levels of hydrogen subsurface concentration between the as-delivered state, i.e. the base metal, and the as-quenched state, i.e. the weld metal and the heat affected zone.

3.2.6.2 Numerical Modelling Program Sequences

The basic principle of modelling of hydrogen assisted stress corrosion cracking under the NACE standard test approach can successfully be modified for such a phenomenon in welded pipelines. The flow chart for modelling hydrogen assisted stress corrosion cracking in the supermartensitic stainless steel pipeline with three predefined cracking paths is represented in Figure 3-21.

The beginning of the modelling program for pipeline girth welds is in principle similar to that of the modelling program for the NACE standard test, but a number of definitions for variables and array parameters are required. The first series of finite elements is deleted when the total running time of the program reaches the specific incubation time. This is the point at which the new running of the program begins with constant incremental time. The purpose of the first check in the program is to detect the actual local strain in the first element ahead of the crack tip in each predefined cracking path. If the local strain of any specific element exceeds the true fracture strain of the material, the program is over, and the failure of the component is influenced by a mechanical overload.

On the other hand, the check for detecting the hydrogen concentration level at the first specific point beneath the crack front in each predefined cracking path with the aim of generating an analogue signal is carried out when the component does not fail by mechanical overload. If the local hydrogen concentration at the specific point reaches the critical value, the analogue signal is at a switch-on position. Subsequently, the analogue signals from each predefined cracking path are combined to form a signal, i.e. “Comcrack”, in a evaluation unit. If the signal combination gives a result equal to zero, i.e. there is no occurrence of cracks, the program is repeated with the constant incremental time. In turn, if the result from the signal combination is not equal to zero, the interpolation technique is employed to determine the exact time for crack propagation. The crack propagation is characterised by deleting the first series of finite elements ahead of the crack tip in each predefined cracking path representing the switch-on situation.

3. Finite Element Modelling Development

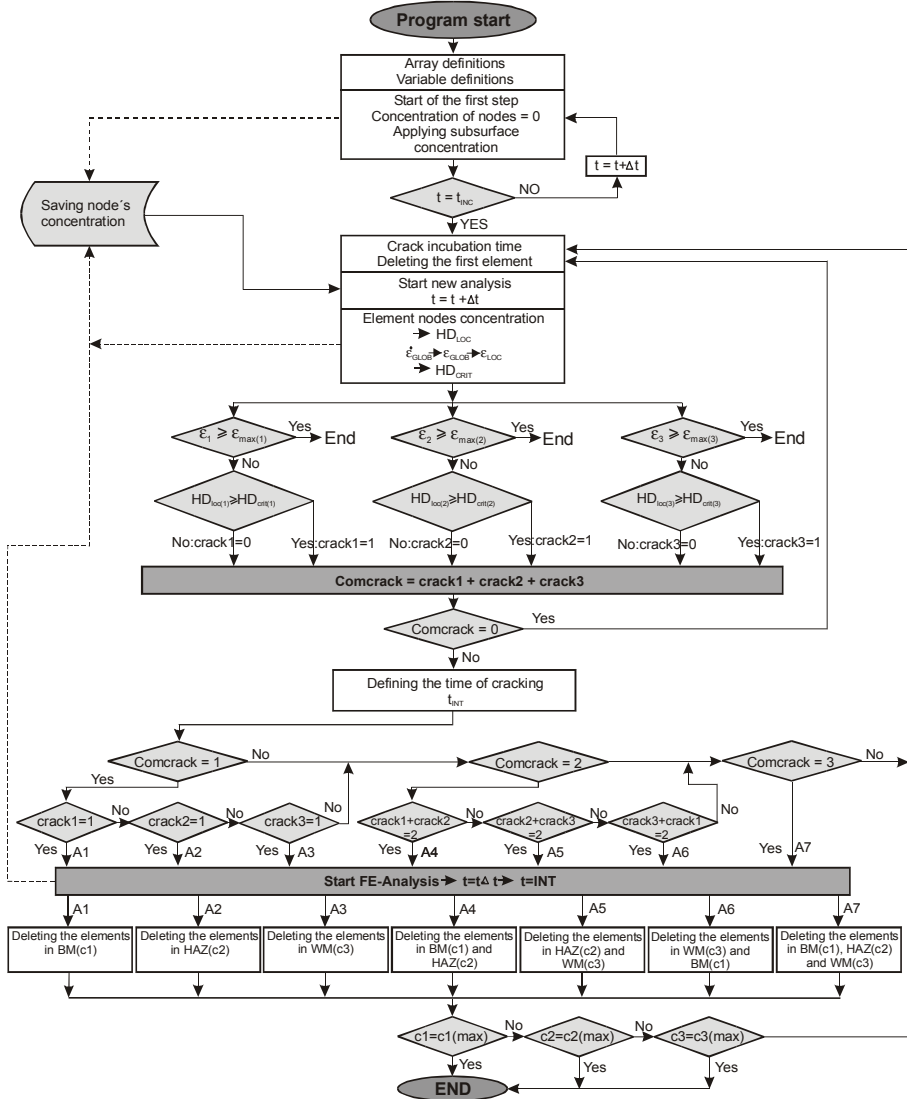


Figure 3-21: Flow chart for modelling HASCC in the welded pipeline with three predefined cracking paths in the welded metal, the heat affected zone and the base metal.

The last main step of the modelling program is to individually compare the actual crack length with the total crack length. If the actual crack length is equal to the total crack length, the running program is over. In turn, the program is continuously repeated at constant incremental time if the actual crack length is still lower than the total crack length.

3.2.7 Modelling of HACC at Pipeline Welds

Hydrogen assisted cold cracking in girth welds of supermartensitic stainless steel pipeline is one of the main topics in the present research. This type of cracking occurs when the assembled component experiences fabrication welding which has been deduced to be a main cause for building up sufficient stress-strain levels and increasing local hydrogen

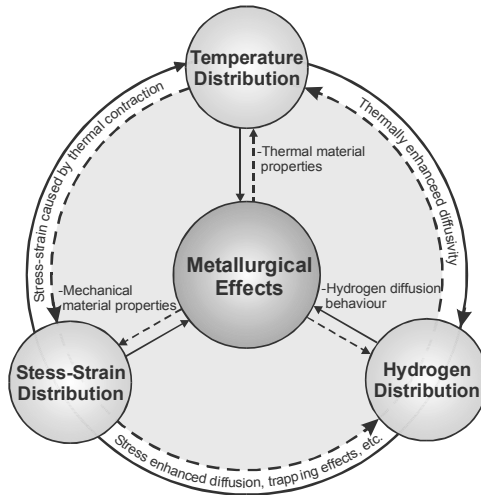


Figure 3-22: Overview of major effects on the behaviour of hydrogen assisted cold cracking in welded components.

concentration as well as generating some susceptible microstructures. In finite element modelling of hydrogen assisted cold cracking, three calculable fields have to be considered concurrently, i.e. thermal analysis, structural analysis and hydrogen diffusion analysis. However, it should be remarked that these analyses can be influenced by metallurgical effects in terms of material properties dependent on temperature and on specific microstructures as represented in Figure 3-22.

The correlation between temperature distribution, stress-strain distribution and hydrogen distribution must be established in numerical modelling. However, the most important parameter to dominate the cracking characteristic is metallurgical behaviour with respect to material properties dependent on the hydrogen concentration. Furthermore, the effects of temperature on stress-strain distribution and on hydrogen diffusion are also taken into account for modelling hydrogen assisted cold cracking in welded components. Due to the lack of the certain mechanism of local interaction between hydrogen and mechanical effects, hydrogen distribution directly coupled with the effects of stress-strain distribution in component cannot clearly be simulated using numerical modelling up to date. But, the new scatterbands of hydrogen diffusion coefficients can effectively be applied to such numerical modelling for analysing hydrogen diffusion with taking account of all mechanical effects which act as enhanced and/or hindered factors for hydrogen diffusion behaviour^[HPD 68].

3.2.7.1 Definition of Boundary Conditions

Because the purpose of hydrogen distribution simulation during girth welding with subsequent cooling of supermartensitic stainless steel pipeline is to assess the hydrogen assisted cold cracking susceptibility, the boundary conditions which can affect the remaining local hydrogen concentration should first be defined.

In general, local hydrogen concentration and hydrogen distribution are directly governed by two main phenomena, i.e. hydrogen diffusion and hydrogen effusion^[HAC 21]. Hydrogen diffusion describes changing levels of hydrogen concentration due to its chemical potential in solid materials, but the hydrogen concentration in the solid materials may also be quickly

3. Finite Element Modelling Development

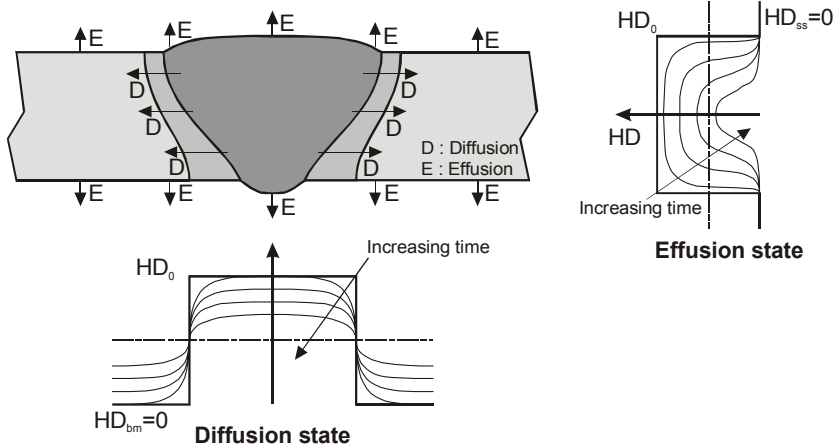


Figure 3-23: Schematic illustration of hydrogen diffusion and effusion reactions influencing the local hydrogen concentration in welded components.

lowered when hydrogen effusion takes place. Usually, hydrogen effusion is the loss of hydrogen at the surface by complete oxidation and desorption so that a hydrogen concentration of zero can be assumed for finite element modelling.

As schematically illustrated in Figure 3-23, the amount of hydrogen uptake in the weld metal during welding can subsequently be reduced by the hydrogen diffusion and effusion reaction with increasing cooling time. It should be noted that the hydrogen concentration in the heat affected zone and its neighbourhood is increased by hydrogen diffusion from the weld metal, and that the hydrogen concentration in every zone is decreased by the effusion phenomenon, which will influence the total hydrogen concentration of welded components with relatively small thickness.

Additionally, in which multi-run arc welding experiencing a greater loss of hydrogen in the early welded layer, the high hydrogen diffusion coefficient due to the high temperature of fabrication welding plays a significant role for the diffusion and effusion phenomena.

Thus, both diffusion and effusion must be taken into account for the finite element modelling of hydrogen distribution in order to precisely determine the actual remaining hydrogen concentration which strongly affects the characteristic of cold cracking in welded components.

3.2.7.2 Numerical Modelling Sequences

Since arc welding fabrication impacts the hydrogen assisted cold cracking susceptibility of components, it is of vital importance for finite element structure and diffusion analyses to perform preliminary temperature analyses during welding and subsequent cooling for quantitative temperature distribution assessment as a function of time.

In the initial state of temperature distribution analysis during welding, homogeneous temperature is applied to every node in the weld metal rising from room temperature to above the melting point of the given material, i.e. to 1550°C for supermartensitic stainless steel, within 1 second and holding time of 2 seconds. Subsequently, the temperature drops involving a heat loss due to the convection action on the surface of the finite element model

exposed to ambient temperature, and due to the thermal gradient effect. The temperature analysis is performed until cooling the temperature of the finite element model reaches the specific interpass temperature, i.e. 40°C, which was used in the investigation experiment.

Based on practical girth welding of supermartensitic stainless steel with four layers of matching filler material, further temperature analysis must be performed for the additional welding operation by finite element simulation under the same conditions defined for the first temperature analysis. For the last layer, the temperature distribution in the finite element model, after application of temperature to the nodes in the weld metal, is calculated until the temperature of the finite element reaches ambient temperature ($\approx 20^\circ\text{C}$).

Since traditional finite element simulation cannot be applied directly to welding technology due to disappearance of the finite elements in the weld metal before the welding operation starts, the option of active-deactive finite element technique, namely the Birth and Death elements, is required as a special tool for finite element simulation in welding.

Because of the direct connection in structural analysis and hydrogen distribution analysis with the thermal analysis, the calculated results from the temperature distribution analysis must be saved for two subsequent further simulations.

Following the temperature analysis, parallel simulations of structural analysis and hydrogen distribution analysis are performed by re-calling the saved results of the temperature analysis as shown in Figure 3-24. In the structural analysis, the finite element type "PLANE 55" in the model for the temperature distribution calculation must be changed to the element type "PLANE 42" for the stress-strain distribution analysis, whereas the original finite element type in the previous simulation of the thermal analysis is still used for the hydrogen distribution analysis.

In the structural analysis, both ends of the finite element model are firmly constrained without any movement in both the X- and Y-direction throughout the simulation. In the thermal analysis the actual temperature level at the specific time is read from every node and directly applied to the same node in the finite element model for the structural analysis as the body load (see Table 3-1). However, it must be recognised that the specific time for reading temperature from the thermal analysis must exactly be the same for the respective node in the structural analysis. This means that the simulation sequence, i.e. the specific incremental time, of the thermal analysis must correlate with that of the structural analysis.

The hydrogen diffusion analysis appears different from the structural analysis because the temperature level from the thermal analysis cannot directly be applied to the hydrogen distribution analysis as any kind of load at the nodes of the finite element model. Hence further modification is required in the finite element method for hydrogen distribution simulation taking account of a specific material property, i.e. the hydrogen diffusion coefficients, dependent on temperatures based on the principle of the thermal analysis. In the thermal analysis, the average temperature at the specific time of every finite element is read from every finite element in the temperature analysis, and is which is then used as the reference temperature for changing the hydrogen diffusion coefficients calculated with the Arrhenius equation (see Table 3-3 and Table 3-4). Therefore, the finite element model consists of a number of hydrogen diffusion coefficients at the specific point in time due to the generation of a temperature gradient.

3. Finite Element Modelling Development

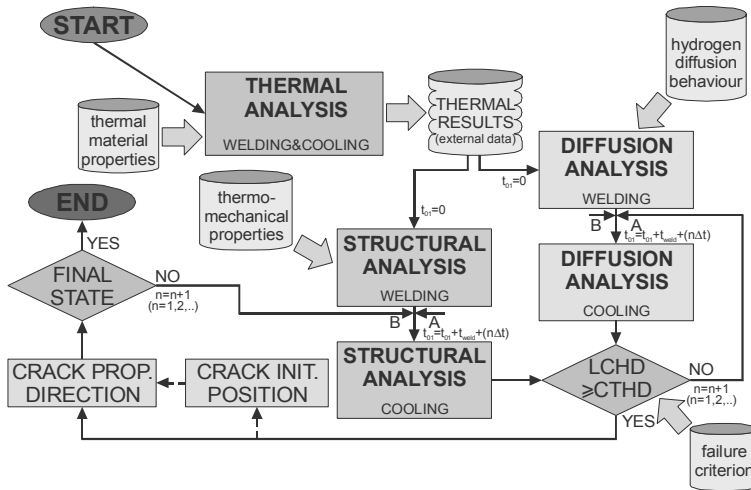


Figure 3-24: Flow chart of numerical modelling of hydrogen assisted cold cracking in the orbitally welded supermartensitic stainless steel pipeline.

In order to examine effects of initial hydrogen concentration on the local hydrogen distribution and on hydrogen assisted cold cracking susceptibility of the welded component, various amounts of hydrogen uptake, i.e. 2.50, 5.00, 7.50, 10.00, 15.00 and 20.00 $\text{ml} \cdot (100\text{gFe})^{-1}$ in the weld metal during welding are assumed and applied to every finite element node existing in the weld metal. During the subsequent cooling process, a hydrogen concentration of zero ($0 \text{ ml} \cdot (100\text{gFe})^{-1}$) is applied to the nodes on the surface exposed to ambient environments because either total oxidation or total hydrogen desorption has been assumed. Until the temperature of the component arrives of the specific interpass temperature, i.e. 40°C , the generation of finite elements for the new layer with the same level of hydrogen concentration as in the first layer is begun within the specific welding time, followed by the cooling process with the loss of hydrogen at the surface exposed to ambient environments until the specific interpass temperature is reached. For the next layer, the same procedure as previously described is performed, but the extent of the cooling time to room temperature for the last layer is simulated for hydrogen diffusion and effusion.

Due to the fact that hydrogen assisted cold cracking of supermartensitic stainless steel usually appears at temperatures below the M_f -temperature, the numerical finite element simulation of such phenomenon can be carried out at near ambient temperature. The local hydrogen concentration from the hydrogen diffusion analysis and the local strain distribution from the structural analysis are evaluated together at the central unit in order to state the susceptibility of the welded component to hydrogen assisted cold cracking. A risk of cold cracking can be excluded if the local hydrogen concentration is lower than the critical value decreased by increasing the local strain level. In the case that the local hydrogen concentration at any node in the predefined cracking path both in the weld metal and the heat affected zone reaches the critical level, the location of crack initiation can be defined by deleting the element arranged in the vicinity to the highest local hydrogen concentration.

In order to define the direction of crack propagation, a comparison between hydrogen concentration at the first node opposite to the crack front on the upper side and lower side

3. Finite Element Modelling Development

has to be carried out with increased specific time intervals. If both nodes have hydrogen concentrations at least equal to the critical value, crack propagation may take place in both downward and upward direction. On the other hand, crack propagation will appear in that preferential direction where the local hydrogen concentration at the specific node in that direction reaches the critical value. The crack propagation is continuously simulated with increased specific time interval and will be ceased if the local hydrogen concentration at the specific node cannot reach the critical value.

4 RESULTS AND DISCUSSION

The results of numerical finite element simulation of hydrogen assisted cracking in supermartensitic stainless steel are represented and discussed in this Chapter. First of all, the simulation of hydrogen assisted stress corrosion cracking in supermartensitic stainless steel based on the slow strain rate test has been modelled taking account of various test parameters such as hydrogen subsurface concentration, global strain rate, local strain factor, etc. Furthermore, the effects of the crack tip angle and the specimen condition, i.e. of the as-quenched state, has been simulated in order to evaluate the susceptibility of the material to hydrogen assisted stress corrosion in terms of the time to failure.

In the second part, the numerical simulation of hydrogen assisted stress corrosion cracking in girth welds of supermartensitic stainless steel pipelines is demonstrated. Such analyses have been carried out in order to calculate the lifetime of the pipeline exposed to the NACE test solution with different levels of H₂S saturation. The mechanical effects, i.e. global strain rate and the local strain factor, have also been taken into account for lifetime assessment of pipelines. Additionally, realistic pipeline test conditions have been transferred to the numerical finite element simulation in order to correlate the simulation results with the experimental determination.

Since hydrogen assisted cold cracking phenomena can influence the lifetime of welded pipelines joined by arc welding processes, the numerical finite element simulation of hydrogen assisted cold cracking in girth welds of supermartensitic stainless pipelines is performed with the aim of evaluating the effect of local hydrogen concentration resulting from hydrogen uptake in the weld metal during welding on the susceptibility of the welded pipelines to hydrogen assisted cold cracking. All results from the simulation of cold cracking are represented and discussed in the last part of this Chapter.

4.1 Modelling of HASCC based on NACE Standard Test Method

In order to study the effects of test parameters on the susceptibility of supermartensitic stainless steel to hydrogen assisted stress corrosion cracking, the numerical finite element simulation is employed to calculate the lifetime of the material based on the NACE standard test method.

As previously described, the two-dimensional finite element model is appropriate for characterising the crack propagation behaviour better than the three-dimensional finite element model as shown by obvious illustrations of the crack propagation direction^[HAS 108].

The simulation of hydrogen assisted stress corrosion cracking in supermartensitic stainless steel with a hydrogen diffusion coefficient of $3.7\text{E-}06 \text{ mm}^2\cdot\text{s}^{-1}$ has been carried out at a local strain factor of 5 with using the test conditions of $50.00 \text{ ml}\cdot 100\text{gFe}^{-1}$ in the hydrogen subsurface concentration and of $1.0\text{E-}06 \text{ s}^{-1}$ in the global strain rate as indicated in Figure 4-1.

A specific time of 5,000 seconds has been assumed as crack incubation time for initiating a crack with a length of 0.1 mm by deleting the first finite element series. Subsequently, the hydrogen subsurface concentration has been applied to the newly

4. Results and Discussion

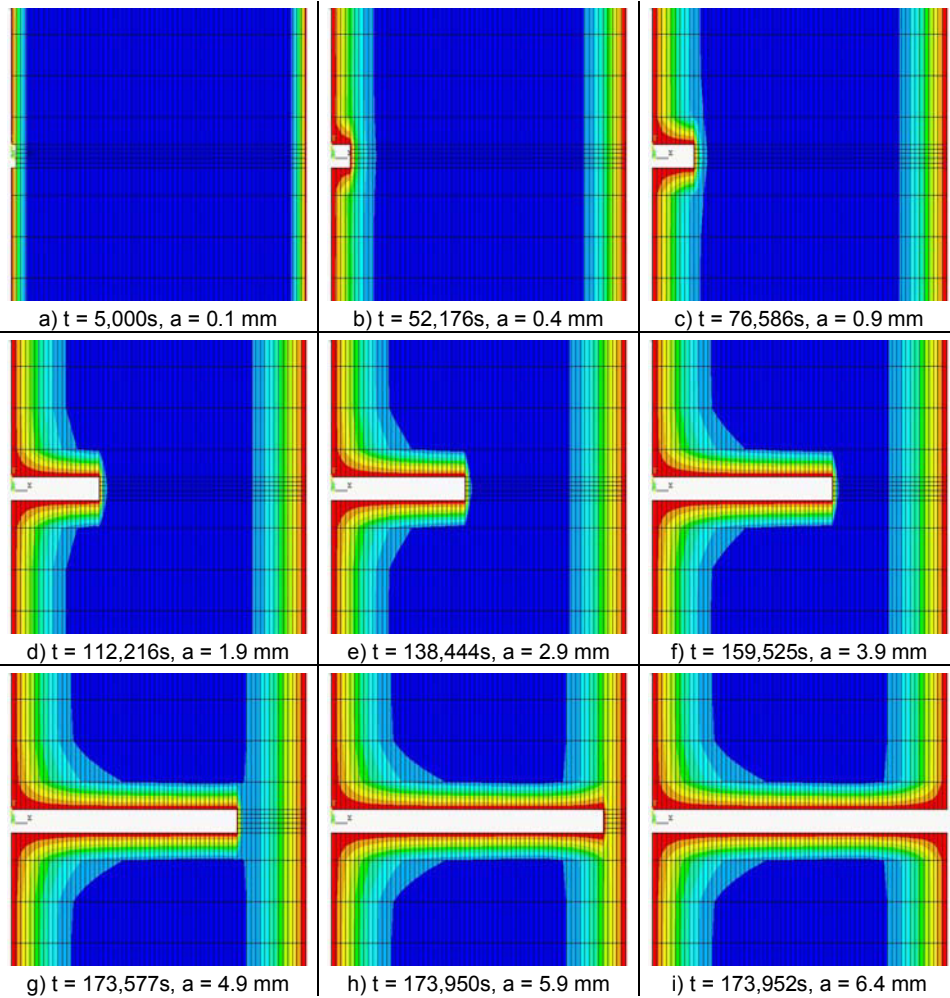


Figure 4-1: Crack propagation and hydrogen distribution profile of hydrogen assisted stress corrosion cracking of supermartensitic stainless steel in the as-delivered state (Assumption: $\dot{\epsilon}'_{glob} = 1.0E-06 \text{ s}^{-1}$, $D = 3.7E-06 \text{ mm}^2 \cdot \text{s}^{-1}$, $HD_{ss} = 50.00 \text{ ml} \cdot (100\text{gFe})^{-1}$, $K\text{-factor} = 5$).

cracked surface which is directly exposed to the electrolytic solution. During the test with application of global monotonic tensile load at the specific constant strain rate, the test specimen has continuously been pulled in transverse direction to the crack propagation, i.e. in Mode I, with increasing time. In this procedure, hydrogen subsurface concentration has sufficient time to augment the local hydrogen concentration ahead of the crack tip.

Crack propagation takes place when the local hydrogen concentration reaches the critical value by deleting a series of finite elements adjacent to the crack front. In the first stage, crack propagation proceeds very slowly because the critical hydrogen concentration affected by the local strain remains at a high level, whereas the local hydrogen concentration is also not sufficient for crack propagation due to the short diffusion time. For

example, a crack length of 0.9 mm (14% of the total crack length) has consumed a time of 76,586 seconds (about 44% of the time to specimen failure).

Standard test specimen failure can be in terms of rapid ductile rupture as the case where a crack propagates through the diameter of the gauge section. As shown in Figure 4-1, the time to specimen failure is 173,952 seconds at a crack length of 6.4 mm.

However, the material properties against hydrogen assisted stress corrosion cracking can obviously be evaluated by plotting crack length versus time diagrams which exhibit also very useful crack propagation characteristics, i.e. crack initiation, stable crack propagation and unstable crack propagation as well as time to specimen failure under different boundary test conditions.

4.1.1 Effects of Hydrogen Subsurface Concentration

During testing, the specimen is exposed to the NACE electrolytic solution with various levels of H₂S saturation providing different levels of hydrogen uptake at the global surface and at the newly cracked surface. As previously represented in Figure 3-13 (Section 3.2.5), the hydrogen subsurface concentration has been affected by the H₂S saturation level in the electrolytic solution.

For the as-delivered supermartensitic stainless steel, the effect of H₂S saturations of 1%, 10%, 50%, and 100% provided the hydrogen subsurface concentration of 20.00 ml·(100gFe)⁻¹, 35.00 ml·(100gFe)⁻¹, 50.00 ml·(100gFe)⁻¹ and 60.00 ml·(100gFe)⁻¹ (see Table 3-2), respectively, on the crack propagation characteristics and on the time to specimen failure has been studied in this section by numerical finite element simulation. Furthermore, the effect of the global constant strain rate on the cracking behaviour with respect to different hydrogen subsurface concentration has also been studied at the specific constant local strain factor of 1.

Figure 4-2a represents the crack length versus time simulation diagram obtained at a global constant strain rate of 1.0E-04 s⁻¹. The crack propagation behaviour and the time to specimen failure are influenced by the mechanical load rather than by the various hydrogen subsurface concentrations because the specimen fails within a short period, i.e. 15,300 seconds after the external application of tensile load. This means that the mechanical load increases very rapidly and hydrogen has no time to diffuse to the tip of the propagating crack.

Figure 4-2b shows the simulation results from the test specimen subjected to a constant global strain rate of 1.0E-05 s⁻¹. The crack propagation behaviour, e.g. the stable crack growth and the time to failure, are dependent on various levels of hydrogen subsurface concentration. For example, the time to failure of 134,940 seconds simulated with a hydrogen subsurface concentration of 20.00 ml·(100gFe)⁻¹ is decreased to 89,960 seconds when a hydrogen subsurface concentration of 60 ml·(100gFe)⁻¹ has been applied to the test specimen. This shows that hydrogen diffusion takes place and respective critical concentrations are reached earlier with increased subsurface concentrations.

In the case where global tensile strain is used to pull the specimen at a constant rate of 1.0E-06 s⁻¹, hydrogen has sufficient time to diffuse from the subsurface into regions further below, in particular into the region ahead of the crack tip, so that the local hydrogen

4. Results and Discussion

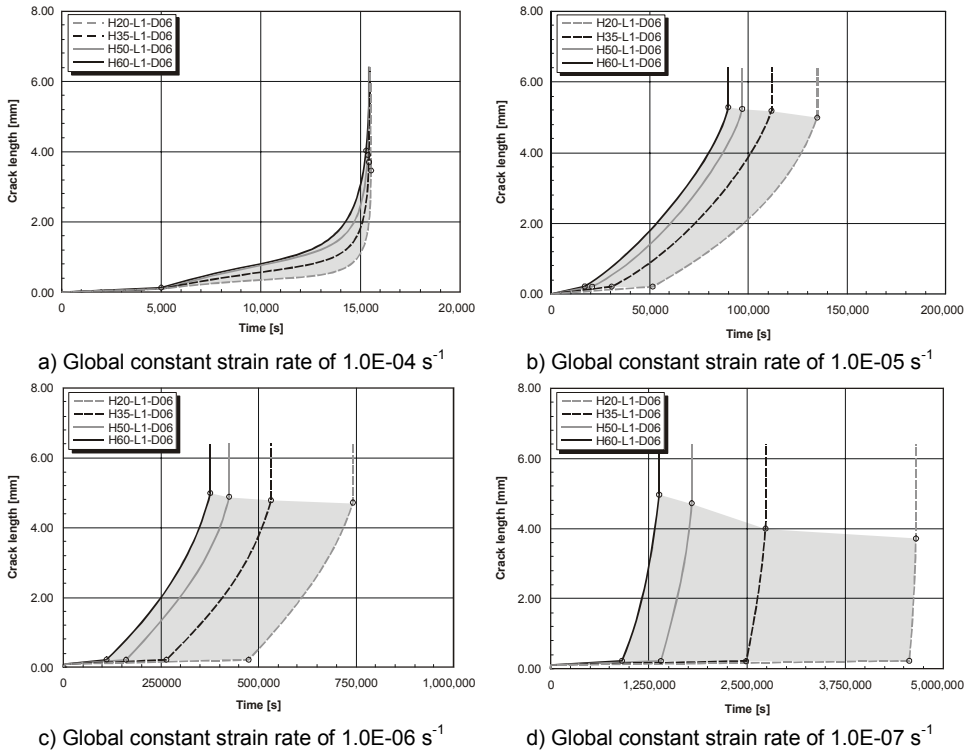


Figure 4-2: Crack length versus time of the standard test specimen subjected to global constant strain rates in the range of $1.0E-04$ to $1.0E-07 \text{ s}^{-1}$ with respect to different levels of hydrogen subsurface concentration.

concentration is continuously increased. The calculated results are represented in Figure 4-2c. Similar to the strain rate of $1.0E-05 \text{ s}^{-1}$, there is no evidence that the real mechanical load can rupture the specimen by overload. The interaction between local hydrogen concentration and the local strain ahead of the crack tip plays a significant role in controlling the crack propagation behaviour and the time to failure by increasing the local hydrogen concentration through prolonged diffusion time. Therefore, both an increased time to specimen failure and an extended stable crack growth range result from a reduction of the hydrogen subsurface concentration. A change in hydrogen subsurface concentration from $20.00 \text{ ml} \cdot (100\text{gFe})^{-1}$ to $60.00 \text{ ml} \cdot (100\text{gFe})^{-1}$ can reduce the time to specimen failure from 741,555 seconds to 376,432 seconds.

Due to the fact that increasing the time to failure is connected with decreased constant global strain rate, it is very interesting to study the crack propagation behaviour in terms of the cracking mode, i.e. cleavage, micro-void coalescence, etc., since prolonged diffusion time may involve much deeper hydrogen diffusion from the subsurface into the matrix material. Therefore, the numerical finite element simulation has been carried out at a constant strain rate of $1.0E-07 \text{ s}^{-1}$ with respect to the various hydrogen subsurface concentrations. The results from the simulation are represented in Figure 4-2d. Focusing on the crack propagation behaviour is a matter of special interest because the first crack propagation after crack initiation requires much more time, say 96%, of the total time to

failure (4,644,650 seconds) simulated with a hydrogen subsurface concentration of 20.00 ml·(100gFe)⁻¹, and 65% of the total time to failure (1,381,800 seconds) simulated with a hydrogen subsurface concentration of 60.00 ml·(100gFe)⁻¹. This means that the crack propagation is caused by saturated local hydrogen concentration due to an increase in the diffusion time influenced by the relatively low global strain rate. The first crack propagation in the first finite element series can cause rupture in the next finite element series without requiring more diffusion time because there is already sufficient local hydrogen concentration for crack propagation. Additionally, cleavage crack morphology caused by higher hydrogen concentrations may be identified for assessing the cracking characteristic of the test specimen.

Although the study on hydrogen assisted stress corrosion cracking in metallic materials needs an appropriate level of global strain rate without mechanical overload during the test, a global strain rate lower than 1.0E-07 s⁻¹ is not recommended for investigating the susceptibility of the material to hydrogen assisted stress corrosion cracking, since it would require a long period of time for testing without yielding valuable results^{[HAS 87],[HAS 90]}.

Figure 4-3 shows the time to failure of the specimen dependent on H₂S saturations in the NACE standard solution at various levels of local strain rates.

As represented in Figure 4-4, the time to failure of the as-delivered supermartensitic stainless steel has been calculated as a function of the local strain rate with respect to different hydrogen subsurface concentrations.

A high local strain rate, e.g. 1.0E-04 s⁻¹, produces no effects of the various hydrogen subsurface concentrations on the time to failure, whereas a gradually reduced local strain rate shows differences in the time to failure between high and low hydrogen subsurface concentrations. Hydrogen subsurface concentrations can drastically influence the time to failure. For example, comparing between hydrogen subsurface concentrations of 20.00 ml·(100gFe)⁻¹ and 60.00 ml·(100gFe)⁻¹, a difference in calculated time to failure of 3,262,815 seconds (≈ 38 days) has been obtained for a local strain rate of 1.0E-07 s⁻¹, and of 44,982 seconds (≈ 12.5 hours) for a local strain rate of 1.0E-05 s⁻¹.

Additionally, the individual curves of hydrogen subsurface concentration indicate that there is greater difference in the time to failure as a function of the local strain rate for low hydrogen subsurface concentration than for high hydrogen subsurface concentration. The difference in the time to failure for a high hydrogen subsurface concentration, 60.00 ml·(100gFe)⁻¹ between the local strain rates of 1.0E-07 s⁻¹ and 1.0E-04 s⁻¹ is 1,366,395 seconds (≈16 days) and for a low hydrogen subsurface concentration, 20.00 ml·(100gFe)⁻¹, 4,629,181 seconds (≈ 54 days).

From the above description, it can be concluded that specimen testing at global strain rates lower than 1.0E-07 s⁻¹ is not recommended for evaluating hydrogen assisted stress corrosion cracking on the specific material because it consumes a lot of operation time with invaluable results. An appropriate local strain rates for studying the effect of hydrogen assisted stress corrosion cracking should be lower than 1.0E-05 s⁻¹ in order to avoid specimen failure by mechanical overload. The hydrogen subsurface concentration plays a significant role in controlling the crack propagation behaviour if hydrogen has sufficient time to diffuse into the region ahead of the crack tip due to low levels of local strain rate.

4. Results and Discussion

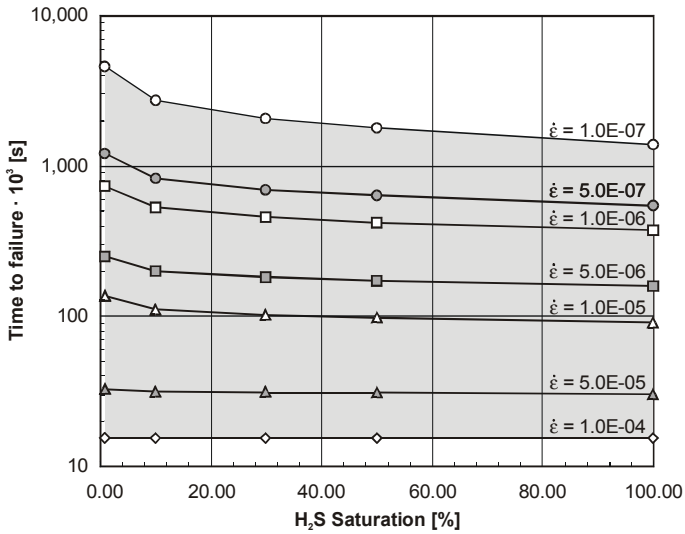


Figure 4-3: Calculated time to failure of supermartensitic stainless steel dependent on the levels of H₂S saturation in the electrolytic NACE solution at various local strain rates.

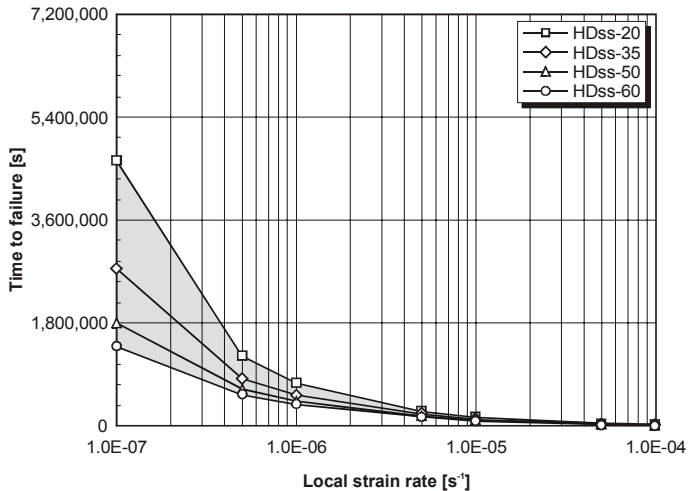


Figure 4-4: Calculated time to failure of supermartensitic stainless steel dependent on the local strain rates with respect to various levels of hydrogen subsurface concentrations based on the NACE standard test procedure.

4.1.2 Effects of Various Hydrogen Diffusion Coefficients

The hydrogen diffusion coefficient at room temperature may vary in the specific range as described by the scatterband in Figure 3-18. Therefore, hydrogen diffusion coefficients in the range of \pm one order of magnitude from the average value of $3.7E-06 \text{ mm}^2 \cdot \text{s}^{-1}$, i.e. $3.7E-05 \text{ mm}^2 \cdot \text{s}^{-1}$, and $3.7E-07 \text{ mm}^2 \cdot \text{s}^{-1}$, for the as-delivered supermartensitic stainless steel have been applied to the finite element modelling as varied material properties in order to study their effects on the crack propagation behaviour and on the time to specimen failure.

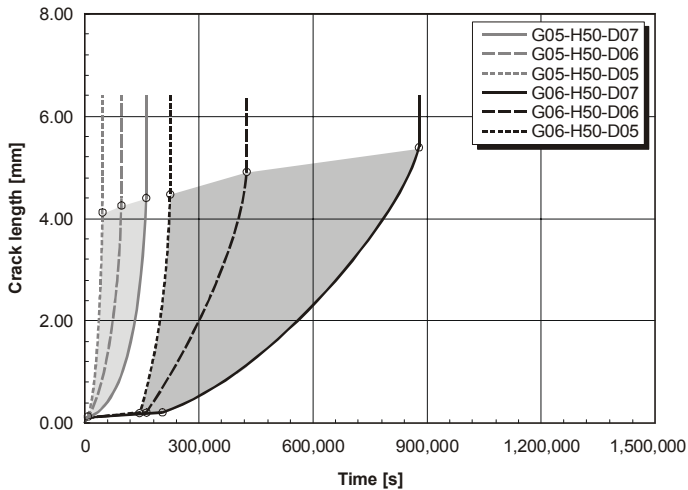


Figure 4-5: Crack length versus time of as-delivered supermartensitic stainless steel with a assumption of higher and lower orders of magnitude for hydrogen diffusion coefficient from the average value (g : global, h : hydrogen subsurface concentration and d : hydrogen diffusion coefficient).

In Figure 4-5, the calculated crack length the as-delivered supermartensitic stainless steel is plotted versus time for a hydrogen subsurface concentration of $50.00 \text{ ml} \cdot (100\text{gFe})^{-1}$. The specimen has been subjected to global strain rates of $1.0\text{E-}06 \text{ s}^{-1}$ and $1.0\text{E-}05 \text{ s}^{-1}$, respectively. It is clearly shown that with a hydrogen diffusion coefficient of $3.7\text{E-}05 \text{ mm}^2 \cdot \text{s}^{-1}$, the local hydrogen concentration increases within relatively short time. The specimen is saturated very rapidly so that rapid rupture is nearly achieved only by hydrogen saturation. This means that the crack propagation caused by hydrogen assisted stress corrosion cracking takes place without requiring much more diffusion time. A time to failure of 223,938 seconds has been obtained at the simulated global strain rate of $1.0\text{E-}06 \text{ s}^{-1}$, and the time to failure of 45,929 seconds at the global strain rate of $1.0 \text{E-}05 \text{ s}^{-1}$, i.e. the difference in the time to failure between the high and the low global strain rate is 178,009 seconds (≈ 50 hours).

In the other case where the hydrogen diffusion coefficient of $3.7\text{E-}07 \text{ mm}^2 \cdot \text{s}^{-1}$ has been used as the material property for numerical modelling, a time to failure of 878,767 seconds has been received using the global stain rate of $1.0\text{E-}06 \text{ s}^{-1}$. With a constant global strain rate of $1.0\text{E-}05 \text{ s}^{-1}$, the time to specimen failure is 162,185 seconds. The difference in the time to failure between high and low global strain rate is 716,582 seconds (≈ 199 hours). The crack propagation behaviour can be influenced by the hydrogen diffusion coefficient. The low global strain rate is required for studying crack propagation behaviour in a range of stable crack growth, in particular. The reason is that hydrogen needs much longer time to diffuse through the supermartensitic stainless steel with an assumption of the low hydrogen diffusion coefficient.

In order to gain an insight into the effects of varying hydrogen diffusion coefficients on the characteristics of hydrogen assisted stress corrosion cracking in the as-delivered material, the diagrams in Figure 4-6 are represented. As expected, changing hydrogen diffusion coefficients influence the characteristics of stable crack growth, which can occur

4. Results and Discussion

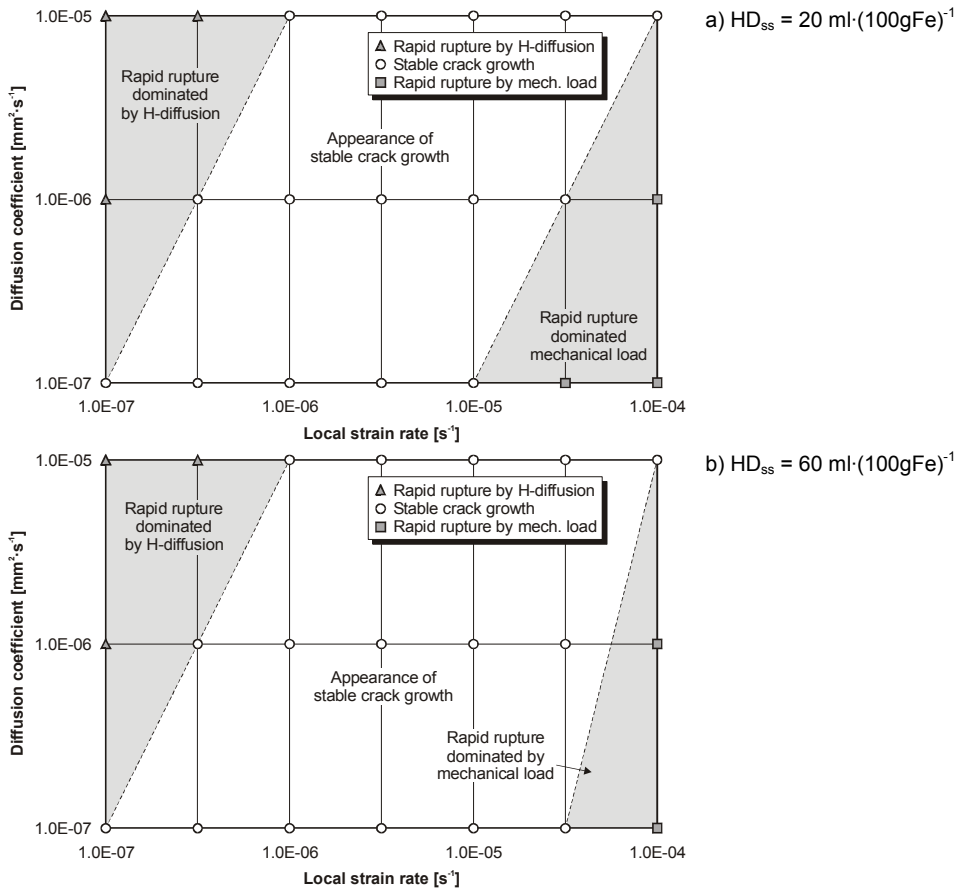


Figure 4-6: Effects of various hydrogen diffusion coefficients with respect to local strain rates on the characteristics of crack propagation: a) $HD_{ss} = 20 \text{ ml} \cdot (100\text{gFe})^{-1}$, b) $HD_{ss} = 60 \text{ ml} \cdot (100\text{gFe})^{-1}$.

when neither high hydrogen diffusion coefficients nor mechanical load dominates the lifetime of the material.

In order to study the effect of the scattered hydrogen diffusion coefficient with respect to hydrogen subsurface concentration, the finite element simulation has been carried out with hydrogen subsurface concentrations of $20.00 \text{ ml} \cdot (100\text{gFe})^{-1}$ and $60.00 \text{ ml} \cdot (100\text{gFe})^{-1}$ at the constant strain rate of $1.0\text{E}-06 \text{ s}^{-1}$. As represented in Figure 4-7, higher hydrogen subsurface concentrations result in shorter times to failure and incubation periods. The hydrogen diffusion coefficient entails greater shortening of the period of stable crack growth than of the incubation period. For example, the numerical finite element simulation with a hydrogen subsurface concentration of $20.00 \text{ ml} \cdot (100\text{gFe})^{-1}$ and the application of a global strain rate of $1.0\text{E}-06 \text{ s}^{-1}$ results in a calculated period of stable crack growth of 758,447 seconds (≈ 211 hours) assuming a hydrogen diffusion coefficient of $3.7\text{E}-07 \text{ mm}^2 \cdot \text{s}^{-1}$ and of 48,963 seconds (≈ 14 hours) assuming a hydrogen diffusion coefficient of $3.7\text{E}-05 \text{ mm}^2 \cdot \text{s}^{-1}$. The difference in the incubation period between the assumed hydrogen diffusion coefficients of $3.7\text{E}-07 \text{ mm}^2 \cdot \text{s}^{-1}$ and $3.7\text{E}-05 \text{ mm}^2 \cdot \text{s}^{-1}$ is about 60,000 seconds (≈ 17 hours).

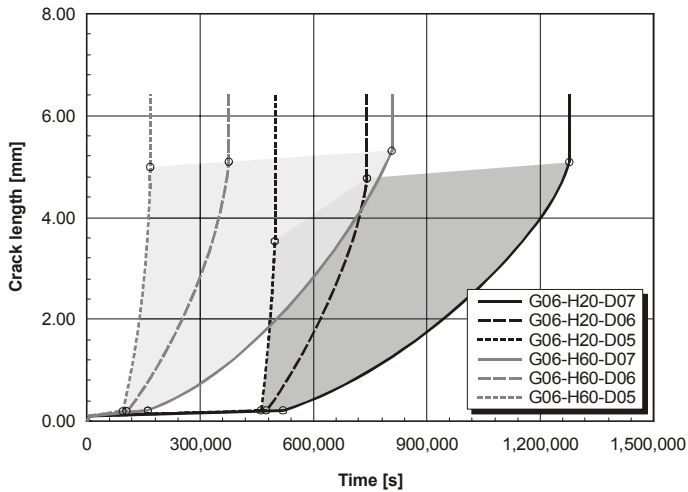


Figure 4-7: Crack length versus time of supermartensitic stainless steel in the as-delivered state taking account of the scatter effect of hydrogen diffusion coefficients at higher and lower orders of magnitude from the average value, $3.7E-06 \text{ mm}^2 \cdot \text{s}^{-1}$, (G: global, H: hydrogen subsurface concentration, D: hydrogen diffusion coefficient).

In the case where the level of global strain rate has been increased from $1.0E-06 \text{ s}^{-1}$ to $1.0E-05 \text{ s}^{-1}$ for a hydrogen subsurface concentration of $60.00 \text{ ml} \cdot (100\text{gFe})^{-1}$, calculated periods of stable crack growth of 648,123 seconds (≈ 180 hours) assuming a hydrogen diffusion coefficient of $3.7E-07 \text{ mm}^2 \cdot \text{s}^{-1}$ and of 52,365 seconds (≈ 15 hours) assuming a hydrogen diffusion coefficient of $3.7E-05 \text{ mm}^2 \cdot \text{s}^{-1}$ have been obtained, while the difference in incubation periods between the assumed hydrogen diffusion coefficients of $3.7E-07 \text{ mm}^2 \cdot \text{s}^{-1}$ and $3.7E-05 \text{ mm}^2 \cdot \text{s}^{-1}$ is about 62,000 seconds (≈ 17 hours).

These results demonstrate the drastic effect of the varied hydrogen diffusion coefficients and global strain rates on the period of stable crack growth. The incubation period is strongly influenced by the global strain rate and the hydrogen subsurface concentration (see Figure 4-5, Figure 4-7). The reason is that the crack tip beneath the global surface for crack incubation, a assumed hydrogen subsurface concentration, can sufficiently provide local hydrogen without a great effect of varied hydrogen diffusion coefficients. During crack propagation, the crack tip is moving far away from the global surface so that the hydrogen transport from the newly cracked surface is significantly controlled by the hydrogen diffusion coefficients and less by the hydrogen subsurface concentration.

The time to failure of supermartensitic stainless steel as a function of the local strain rate with respect to various hydrogen subsurface concentration levels and hydrogen diffusion coefficients is represented in Figure 4-8. It is obvious from these plots that the lifetime of components can be reduced by increasing their material property in terms of a hydrogen diffusion coefficient, but that at local strain rates higher than $5.0E-05 \text{ s}^{-1}$ there is no significant influence of the varied hydrogen diffusion coefficients on the time to specimen failure because this rupture is strongly dominated by the mechanical overload rather than by the hydrogen assisted cracking mechanism.

Likewise, the difference in the time to failure between low and high specific hydrogen subsurface concentrations tends to be more pronounced with decreasing local strain rates,

4. Results and Discussion

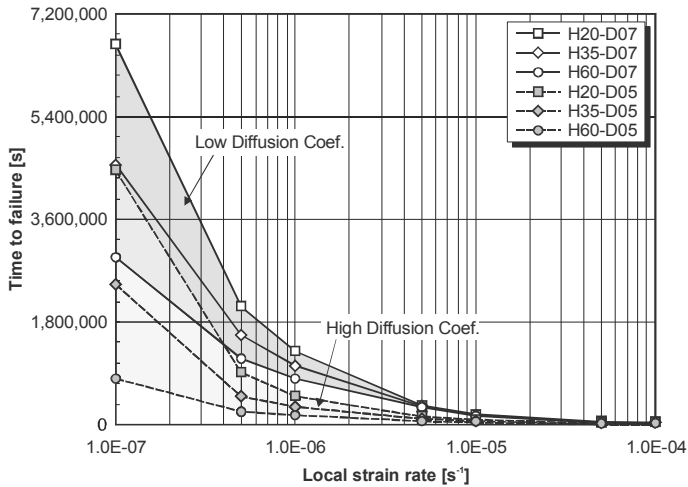


Figure 4-8: Calculated time to failure of as-delivered supermartensitic stainless steel as a function of local strain rates with respect to effects of hydrogen diffusion coefficients and hydrogen subsurface concentrations.

for example, at the local strain rate of $1.0\text{E-}07\text{ s}^{-1}$, the difference in the time to failure between the hydrogen subsurface concentrations of $20.00\text{ ml}\cdot(100\text{gFe})^{-1}$ and $60.00\text{ ml}\cdot(100\text{gFe})^{-1}$ is 3,725,740 seconds (≈ 44 days) simulated with a hydrogen diffusion coefficient of $3.7\text{E-}07\text{ mm}^2\cdot\text{s}^{-1}$, and the same value is obtained with the assumed hydrogen diffusion coefficient of $3.7\text{E-}05\text{ mm}^2\cdot\text{s}^{-1}$. At the local strain rate of $1.0\text{E-}06\text{ s}^{-1}$, the difference in the time to failure between hydrogen subsurface concentrations of $20\text{ ml}\cdot(100\text{gFe})^{-1}$ and $60\text{ ml}\cdot(100\text{gFe})^{-1}$ is 470,436 seconds (≈ 6 days) for a hydrogen diffusion coefficient of $3.7\text{E-}07\text{ mm}^2\cdot\text{s}^{-1}$, and it becomes 332,039 seconds (≈ 4 days) when simulated with a hydrogen diffusion coefficient of $3.7\text{E-}05\text{ mm}^2\cdot\text{s}^{-1}$.

However, in both assumption cases of low and high hydrogen diffusion coefficients for the as-delivered supermartensitic stainless steel there is the same tendency indicating that the curve of time to failure as a function of the local strain rate for low hydrogen subsurface concentrations is steeply inclined in comparison to that of high hydrogen subsurface concentrations.

Thus, it can be summarised that the life time of the specimen may be extended if the hydrogen diffusion coefficient of the material is decreased and the material is subjected to a local strain rate lower than $5.0\text{E-}05\text{ s}^{-1}$. A reduced hydrogen subsurface concentration strongly influences the time to failure, in particular at low hydrogen diffusion coefficients.

4.1.3 Global Strain Rates and Local Strain Factors

Strain is one of significant factors in considering the phenomenon of hydrogen assisted stress corrosion cracking for high-strength steels because they will fail by a loss in their ductility rather than in their strength^{[HAS 86],[HAS 108]}. Therefore, the study on effects of strain rates, i.e. of the global strain rate and the local strain rate, on the crack propagation behaviour is discussed in this section.

Global strain rates in the range of $1.0\text{E-}07\text{ s}^{-1}$ to $1.0\text{E-}04\text{ s}^{-1}$ are appropriate to be used for investigating the susceptibility of materials to hydrogen assisted stress corrosion

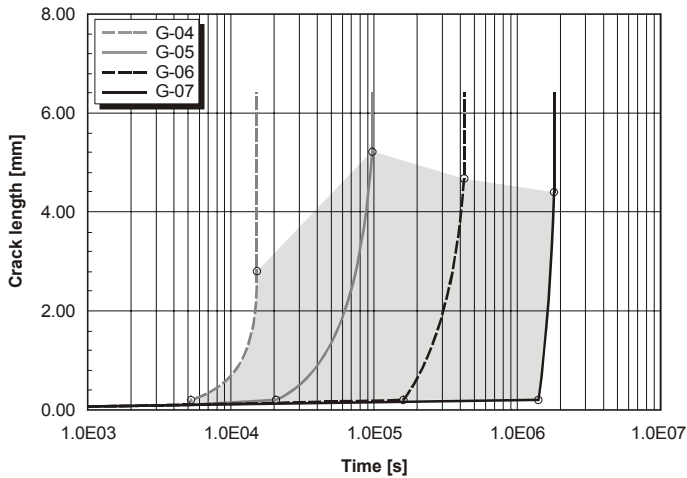


Figure 4-9: Calculated crack length versus time of supermartensitic stainless steel based on the NACE standard test method with various rates of the global strain rate, i.e. $1.0E-04 \text{ s}^{-1}$, $1.0E-05 \text{ s}^{-1}$, $1.0E-06 \text{ s}^{-1}$ and $1.0E-07 \text{ s}^{-1}$, (Assumption: $HD_{ss} = 50 \text{ ml} \cdot (100\text{gFe})^{-1}$, $D = 3.7E-06 \text{ mm}^2 \cdot \text{s}^{-1}$).

cracking. They may also provide distinguishing crack propagation and lifetime characteristics of the materials.

The calculated crack length versus time of supermartensitic stainless steel in the as-delivered state is represented in Figure 4-9 assuming a hydrogen subsurface concentration of $50.00 \text{ ml} \cdot (100\text{gFe})^{-1}$, a hydrogen diffusion coefficient of $3.7E-06 \text{ mm}^2 \cdot \text{s}^{-1}$ and varied levels of the global strain rate. The time to failure and the incubation period are shortened by increasing the global strain rate. A period of stable crack propagation increases with the global strain rates. The crack length versus time curve calculated with a global strain rate of $1.0E-06 \text{ s}^{-1}$ represents a period of stable crack growth almost similar to that calculated with the global strain rate of $1.0E-07 \text{ s}^{-1}$, and they are longer than the others. A shorter crack length, at which unstable fracture occurs, can be explained by the fact that hydrogen can diffuse into the material much deeper from the exposed surface, and thus, the critical hydrogen concentration for rupture of the rest of the specimen is reached earlier. In other words, the local hydrogen concentration reaches the critical value, crack propagation starts without requiring more time for hydrogen diffusion into regions ahead of the crack tip because there is sufficient hydrogen which has already been taken up and transported during extended exposure to the electrolytic solution in the incubation period. Consequently, the time for stable crack growth is reduced. Simulation with a global strain rate of $1.0E-04 \text{ s}^{-1}$ involves a short incubation period due to a high local strain rate, so that the hydrogen subsurface concentration does not have sufficient time to provide the local hydrogen for regions beneath the newly cracked surface.

A long period of stable crack growth enables appropriate interaction between the local hydrogen concentration and the local strain without any extreme effects on either the local hydrogen concentration or the local strain ahead of the crack tip on crack growth behaviour.

The numerical simulation of hydrogen assisted stress corrosion cracking in the present work considers that the local strain is based on Lidbury's relationship (see Equation (2-54)). Effects of the K-factor on the crack propagation behaviour should also be discussed.

4. Results and Discussion

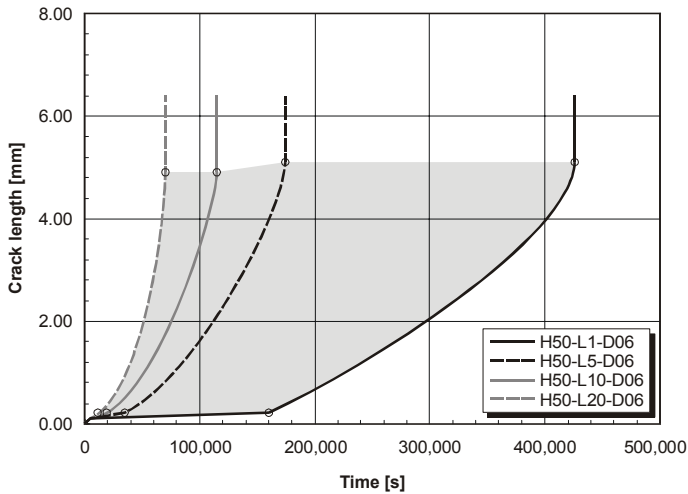


Figure 4-10: Calculated time to failure of as-delivered supermartensitic stainless steel taking account of the effects of K-factor (Assumption: $HD_{ss} = 50 \text{ ml} \cdot (100\text{gFe})^{-1}$, $\varepsilon'_{glob} = 1.0\text{E-}06 \text{ s}^{-1}$, $D = 3.7\text{E-}06 \text{ mm}^2 \cdot \text{s}^{-1}$).

In comparison to Figure 4-9, the crack length versus time of as-delivered supermartensitic stainless steel with taking account of the effect of the K-factor has been calculated under the boundary conditions of a hydrogen subsurface concentration of $50.00 \text{ ml} \cdot (100\text{gFe})^{-1}$, a hydrogen diffusion coefficient of $3.7\text{E-}06 \text{ mm}^2 \cdot \text{s}^{-1}$ and a global strain rate of $1.0\text{E-}06 \text{ s}^{-1}$ as represented in Figure 4-10. A higher K-factor reduces the time to failure and the incubation period. Moreover, the period of stable crack growth can significantly be prolonged when the small K-factor is taken into account for numerical simulation. This means that high K-factors significantly restrict the appropriate interaction between local hydrogen concentration and local strain due to extreme local strain ahead of the crack tip without significant effects on cracking by local hydrogen concentration provided by the hydrogen subsurface concentration.

Thus, it should be noted that a K-factor of 20 generates high local strain rates which usually enhance failure of the material. It is anticipated that such high values are not appropriate for studying on the susceptibility of the material to hydrogen assisted stress corrosion cracking within the specific range of global strain rates of $1.0\text{E-}4 \text{ s}^{-1}$ to $1.0\text{E-}6 \text{ s}^{-1}$. In practice, this means that extreme local strain rates resulting from the sharp crack tip will lead to failure of the material by mechanical overload without hydrogen assisted cracking. This can be characterised by fractured topographies showing micro-void coalescence.

4.1.4 As-Quenched Supermartensitic Stainless Steel

During arc welding fabrication of the as-delivered supermartensitic stainless steel, the material is transformed into the quenched state which causes a different susceptibility to hydrogen assisted stress corrosion cracking in behaviour compared with that of the delivered state. The reason for this is that the quenched state has a higher hydrogen diffusion coefficient, but lower hydrogen subsurface concentration than the delivered state (see Figure 3-13). Additionally, as-quenched supermartensitic stainless steel is more susceptible to cracking caused by hydrogen because of its lower ductility (see Figure 3-14).

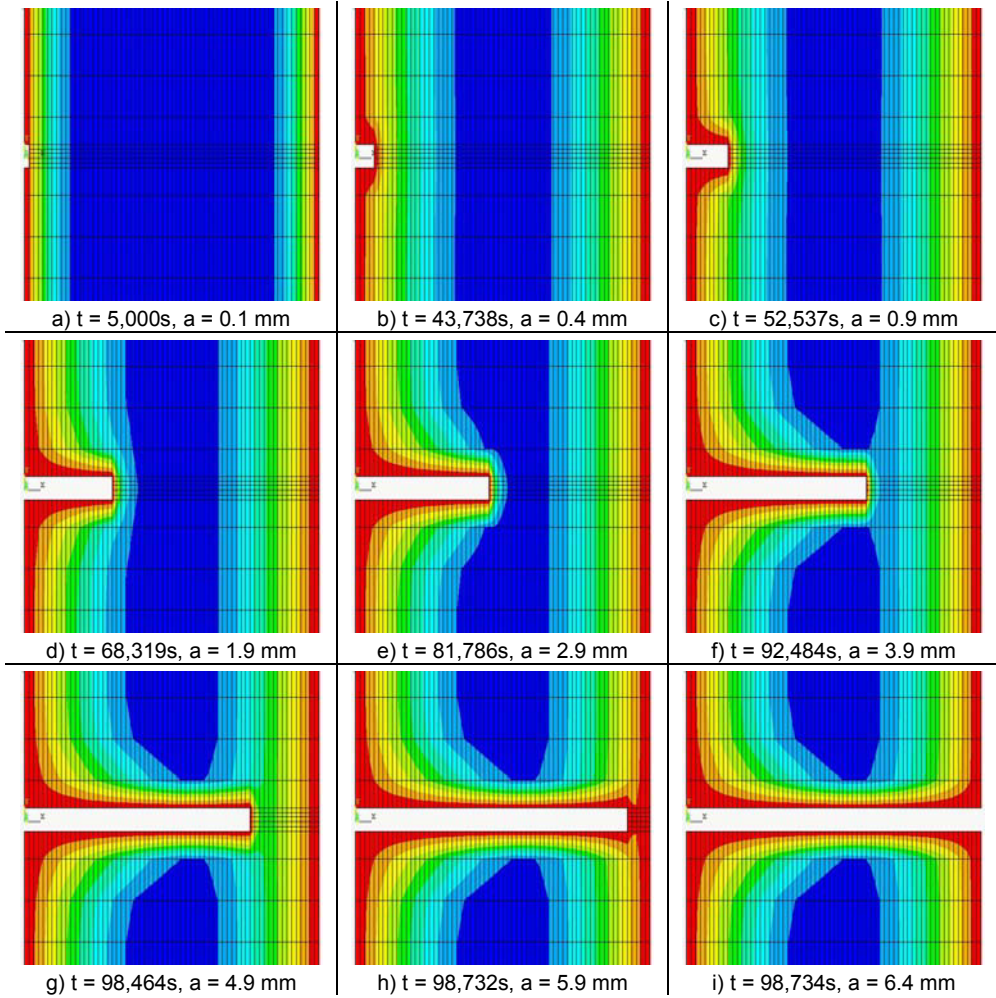


Figure 4-11: Crack propagation and hydrogen distribution profile of hydrogen assisted stress corrosion cracking of supermartensitic stainless steel in the quenched state (Assumption: $\dot{\epsilon}'_{glob} = 1.0E-06$ s⁻¹, $D = 1.8E-05$ mm²·s⁻¹, $HD_{ss} = 6.7$ ml·(100gFe)⁻¹, K-factor = 5).

For the numerical finite element simulation of hydrogen assisted stress corrosion cracking is carried out in this section, a hydrogen diffusion coefficient of $1.8E-05$ mm²·s⁻¹ obtained by experimental determination (see Figure 3-13) has been assumed as the material property for the finite element model. Various boundary conditions, e.g. hydrogen subsurface concentration, global strain rate, etc., have also been studied in order to compare them with the results obtained from the simulation on the material in the delivered state.

The simulation of crack propagation and hydrogen distribution in the as-quenched supermartensitic stainless steel assuming a hydrogen subsurface concentration of 6.7 ml·(100gFe)⁻¹, a global strain rate of $1.0E-06$ s⁻¹ and a K-factor of 5 is represented in Figure 4-11. Exposure of specimen to the NACE solution with 50% H₂S saturation has been

4. Results and Discussion

simulated. After 5,000 seconds, the first series of the finite element is deleted for generating crack incubation. The first period of crack propagation is more time consuming due to a low local hydrogen concentration as well as a low local strain. For example, the time for a crack propagation of 0.9 mm (14 % of the total crack length) is 52,537 seconds (\approx 53.21% of the time to failure).

In comparison with the delivered state (see Figure 4-1), the time to failure of the quenched state (98,734 seconds, \approx 27.43 hours) is shorter than that of the delivered state (173,952 seconds \approx 48.32 hours). This gives some evidence to the anticipation that the quenched state is more susceptible to hydrogen assisted cracking than the delivered state.

Figure 4-12a shows the calculated crack length versus time curve for the quenched supermartensitic stainless steel at a global constant strain rate of $1.0\text{E-}04\text{ s}^{-1}$ and considering a K-factor of 1. There are nearly no effects of varied hydrogen subsurface concentrations on the crack propagation behaviour. In all cases, the specimen is ruptured within about 11,602 seconds (\approx 3.22 hours). For the as-delivered material, a rupture time of 15,300 seconds (\approx 4.25 hours) was calculated at this condition.

Decreasing the global strain rate from $1.0\text{E-}04\text{ s}^{-1}$ to $1.0\text{E-}05\text{ s}^{-1}$ results in a crack propagation behaviour characterised by a prolonged stable crack growth period and the time to failure as represented in Figure 4-12b. The times to failure of 63,306 seconds, 67,028 seconds, 78,704 seconds and 95,337 seconds have been obtained from calculation with hydrogen subsurface concentrations of $7.40\text{ ml}\cdot(100\text{gFe})^{-1}$, $6.70\text{ ml}\cdot(100\text{gFe})^{-1}$, $5.00\text{ ml}\cdot(100\text{gFe})^{-1}$ and $3.20\text{ ml}\cdot(100\text{gFe})^{-1}$, respectively. Additionally, increasing hydrogen subsurface concentrations can shorten the incubation period, but also slightly change the period of stable crack growth. Concerning this phenomenon, it should be mentioned that high hydrogen diffusion coefficients, 5 times greater than the delivered state, and a narrow range of hydrogen subsurface concentration (see Figure 3-13) represent the predominant effects.

For the case where the specimen is subjected to a constant global strain rate of $1.0\text{E-}06\text{ s}^{-1}$, calculated crack length versus time of as-quenched supermartensitic stainless steel is represented in Figure 4-12c. There are no significant effects of varied hydrogen subsurface concentrations as regards a change in the stable crack growth period. The time to failure of the specimen is predominantly related to the incubation period which is increased with decreasing hydrogen subsurface concentration.

The simulation with a constant global strain rate of $1.0\text{E-}07\text{ s}^{-1}$ and different hydrogen subsurface concentrations has demonstrated that the failure of the specimen is controlled by presaturation with hydrogen. There is only a very short period of stable crack growth to be seen in the crack length versus time curve, even though the hydrogen subsurface concentration has been varied as shown in Figure 4-12d. Comparing the results with those of the delivered state (see Figure 4-2d), it becomes obvious that for low hydrogen subsurface concentrations and low local strain rates, the time to failure is controlled by the incubation period with only minor effects of the stable period. Due to a relatively high hydrogen diffusion coefficient for the quenched state, hydrogen at the subsurface is thus transported deeper into the material compared to the delivered state. Therefore, crack critical hydrogen concentrations can appear far away from the crack front. As a consequence, crack propagation can take place shortly after the incubation period.

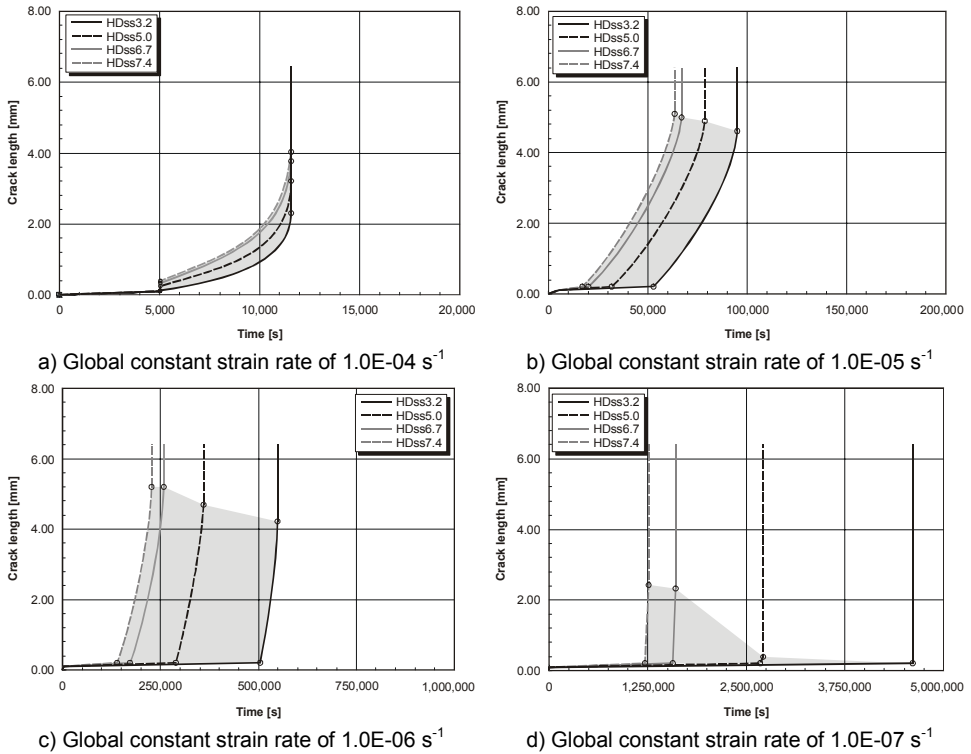


Figure 4-12: Calculated crack length versus time of supermartensitic stainless steel in the as-quenched state subjected to various global constant strain rates with respect to different levels of hydrogen subsurface concentration at a constant K -factor of 1.

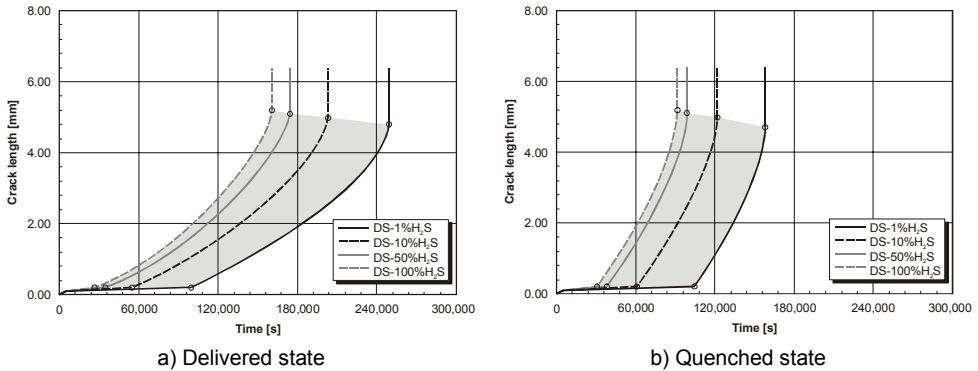


Figure 4-13: Calculated crack length versus time of supermartensitic stainless steel in the as-delivered state and the as-quenched state exposed to various levels of H_2S -saturation in the NACE electrolytic solution (Assumption: $\epsilon'_{\text{glob}} = 1.0E-06 \text{ s}^{-1}$, K -factor = 5).

4. Results and Discussion

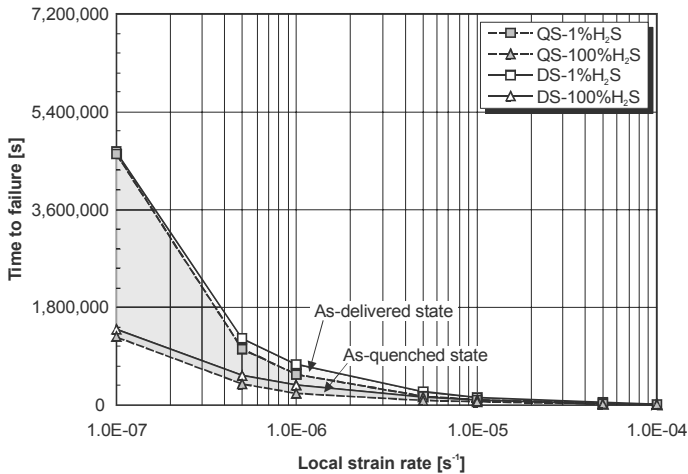


Figure 4-14: Influence of different states of supermartensitic stainless steel on the time to failure of the standard test specimen subjected to local strain rates and exposed to the NACE solution with H₂S saturations in the range of 1 to 100 %.

Figure 4-13a and Figure 4-13b represent calculated crack lengths versus time of supermartensitic stainless steel in the delivered state and quenched state, respectively. The calculation has been carried out with the assumption of a global strain rate of $1.0\text{E-}06\text{ s}^{-1}$, a K-factor of 5, and various H₂S concentrations of 1%, 10%, 50% and 100% in the NACE test solution. The material conditions can influence the crack propagation characteristic and the time to failure due to the difference in hydrogen diffusion behaviour as well as to the true strain-dependent failure criterion.

The time to failure as a function of local strain rate of supermartensitic stainless steel in the delivered state and quenched state exposed to the NACE solution with 1% and 100% H₂S saturation is represented in Figure 4-14.

The time to failure for the quenched state is always lower than that for the delivered state. This indicates that the quenched state might be more susceptible to hydrogen assisted stress corrosion cracking than the delivered state. Additionally, the range of the time to failure between 1% and 100% H₂S saturation appears to be dependent on the local strain rate, and it increases with decreasing the local strain rate. The effect of the local strain rate on the time to failure at low H₂S saturation can be more significant than at high H₂S saturation.

4.1.5 Crack Tip Angle

It is well known that the total area of the newly cracked surface at the crack front exposed to the electrolytic solution can play an important role in changing crack propagation behaviour induced by a hydrogen assisted cracking mechanisms, because the amount of hydrogen ahead of the crack tip can particularly be affected by the surface at the crack front exposed to the environment. This means that the kinetics of crack propagation can be enhanced if the newly cracked surface at the crack front becomes larger.

The effects of a sharp crack tip (74°) on the crack propagation and the time to failure are thus highlighted in this section by the numerical finite element simulation based on the

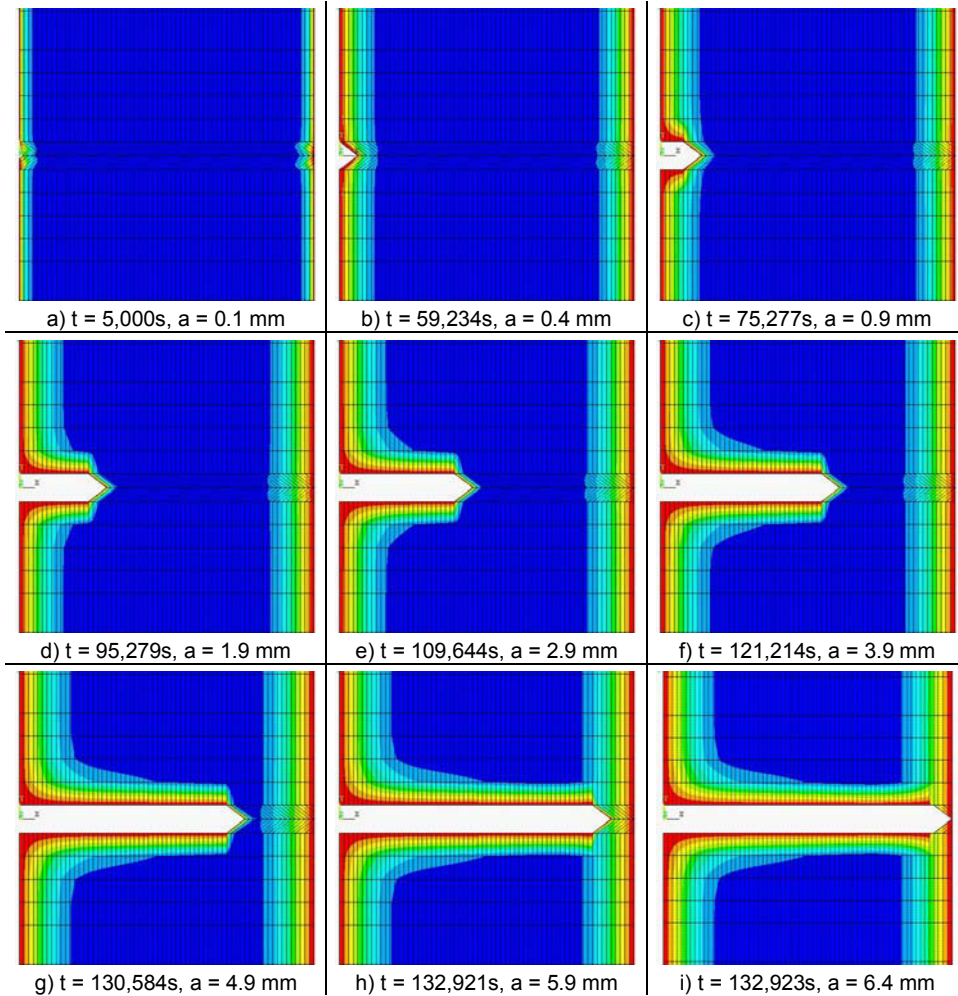


Figure 4-15: Crack propagation and hydrogen distribution profile for hydrogen assisted stress corrosion cracking of supermartensitic stainless steel in the delivered state (Assumption: $\dot{\epsilon}_{glob} = 1.0E-06 \text{ s}^{-1}$, $D = 3.7E-06 \text{ mm}^2 \cdot \text{s}^{-1}$, $HD_{ss} = 50 \text{ ml} \cdot (100\text{gFe})^{-1}$, $K\text{-factor} = 5$, crack angle = 74°).

NACE standard test method in order to compare them with those of a blunt crack tip. In order to evaluate such geometric solely, no increase in stress intensity due to the crack tip geometry has been assumed^[HAS 92].

The finite element model has been created with a predefined cracking path transverse to the direction of externally applied load. A crack tip angle of 74° has constantly been assumed to appear at the crack front.

As demonstrated in Figure 4-15, the simulation of hydrogen assisted stress corrosion cracking on the standard tensile specimen of as-delivered supermartensitic stainless steel with an assumed crack tip of 74° has been carried out considering a global strain rate of $1.0E-06 \text{ s}^{-1}$, a hydrogen diffusion coefficient of $3.7E-06 \text{ mm}^2 \cdot \text{s}^{-1}$, a K-factor of 5 and a hydrogen subsurface concentration of $50.00 \text{ ml} \cdot (100\text{gFe})^{-1}$. By this procedure, the time to

4. Results and Discussion

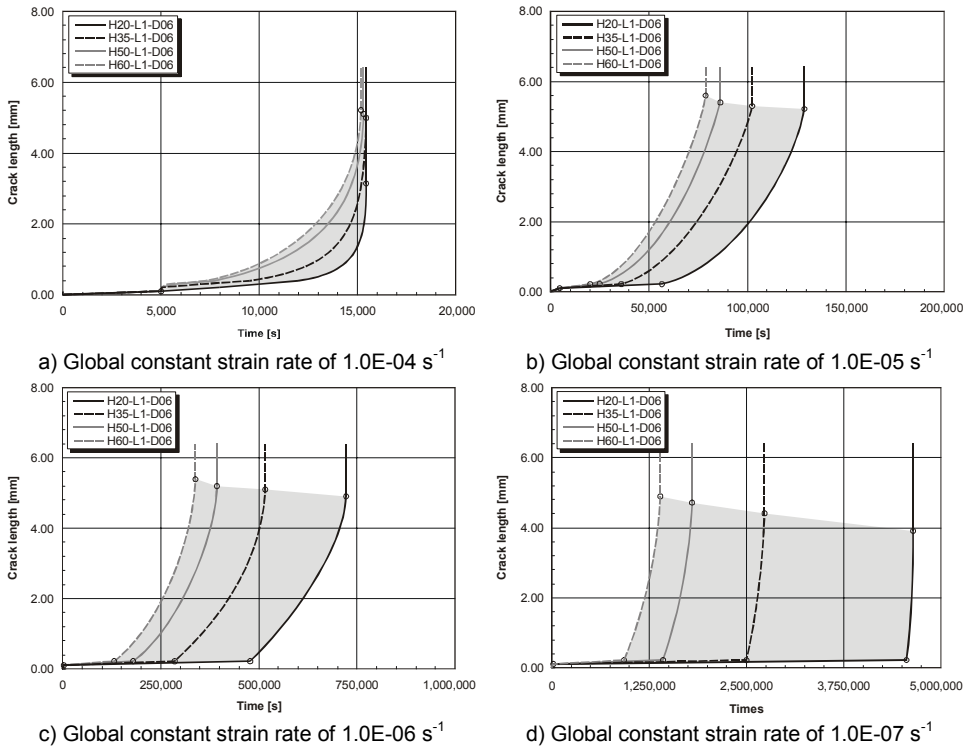


Figure 4-16: Crack length versus time of supermartensitic stainless steel in the as-delivered state subjected to global constant strain rates in the range of $1.0E-04$ to $1.0E-07$ s^{-1} with respect to different levels of hydrogen subsurface concentrations based on the NACE standard test method with assumption of a crack tip angle of 74° .

failure of 132,923 seconds (≈ 36.9 hrs.) has been obtained. It should be noted that the phenomenon of hydrogen assisted stress corrosion cracking in the first period needs more time for increasing the local hydrogen concentration and the local strain.

For example, a crack with a length of 0.9 mm ($\approx 14\%$ of the total crack length) has required 75,277 seconds (56.63% of the time to failure). In order to get a better understanding of the effects of the sharp crack angle on the crack propagation behaviour and on the time to specimen failure, the boundary conditions have been varied similar to previous studies.

Figure 4-16a represents the crack length versus time of supermartensitic stainless steel in the delivered state with an assumed crack angle of 74° . No significant influences of hydrogen subsurface concentration have been found on the time to failure of the specimen subjected to a global strain rate of $1.0E-04$ s^{-1} . The kinetics of the stable crack growth have been enhanced with increasing hydrogen subsurface concentration. A comparison with the blunt crack tip (see Figure 4-2a) reveals that the time to failure of the specimen with the sharp crack tip is not reduced as compared to that of the blunt crack tip. However, at a global strain rate of $1.0E-04$ s^{-1} , hydrogen subsurface concentration seems to have a minor effect as compared to the crack tip angle.

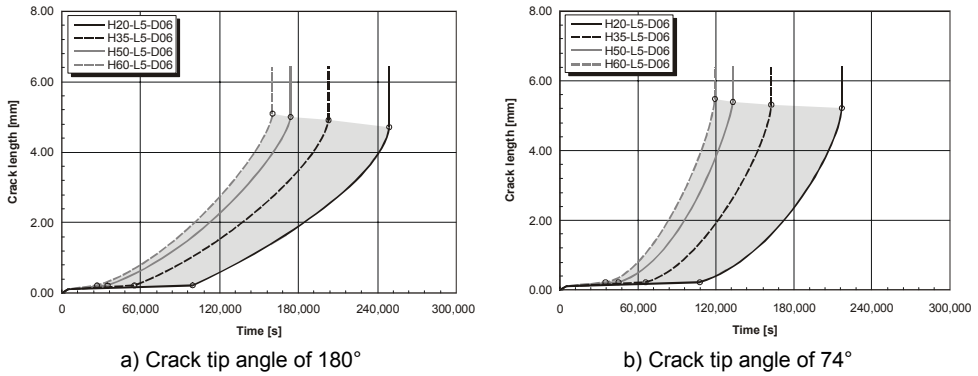


Figure 4-17: Crack length versus time of supermartensitic stainless steel in the delivered state in comparison between crack tip angles of 180° and 74° with respect to different levels of hydrogen subsurface concentration (Assumption: $\dot{\epsilon}'_{glob} = 1.0E-06 \text{ s}^{-1}$, K -factor = 5).

The simulations with a global strain rate of $1.0E-05 \text{ s}^{-1}$ and varied hydrogen subsurface concentrations (Figure 4-16b) showed a large effect of increasing the hydrogen subsurface concentration in terms of reducing the incubation period and increasing the stable crack growth period. In contrast to the higher strain rates investigated before, the time to failure calculated with 74° specimen is obviously reduced. A time to failure of 78,611 seconds (≈ 21.84 hours) has been obtained with the assumption of a hydrogen subsurface concentration of $60.00 \text{ ml} \cdot (100\text{gFe})^{-1}$, whereas the time to failure has been increased to 129,083 seconds (≈ 35.86 hours) with decreasing the hydrogen subsurface concentration to $20.00 \text{ ml} \cdot (100\text{gFe})^{-1}$.

Figure 4-16c represents the crack length versus time simulated with a global constant strain rate of $1.0E-06 \text{ s}^{-1}$ and for the same hydrogen subsurface concentrations. Increased hydrogen subsurface concentration can shorten the period of stable crack growth with respect to the time to failure, e.g. a stable crack growth period of 205,963 seconds (61% of the time to failure) has been obtained by calculation with a hydrogen subsurface concentration of $60.00 \text{ ml} \cdot (100\text{gFe})^{-1}$, whereas a time to failure of 242,391 seconds (33.6% of the total time to failure) has been obtained by decreasing the hydrogen subsurface concentration from $60.00 \text{ ml} \cdot (100\text{gFe})^{-1}$ to $20.00 \text{ ml} \cdot (100\text{gFe})^{-1}$.

As to expected the calculation with a global constant strain rate of $1.0E-07 \text{ s}^{-1}$ and varied hydrogen subsurface concentrations as shown in Figure 4-16d.

As an example to compare the effects of the crack angle between the blunt crack and the sharp crack on the crack propagation behaviour and on the time to failure, the crack length versus time of the blunt crack and of the sharp crack is shown in Figure 4-17, for a global strain rate of $1.0E-06 \text{ s}^{-1}$ and a K -factor of 5. It is clearly shown that the sharp crack tip can reduce the time to specimen failure due to an increase in the kinetics of crack propagation with decreasing stable crack growth period. Considering the simulation with a hydrogen subsurface concentration of $20.00 \text{ ml} \cdot (100\text{gFe})^{-1}$, the times to failure of 249,618 seconds (≈ 69.4 hours) and of 217,442 seconds (≈ 60.4 hours) have been obtained for the blunt crack tip and the sharp crack tip, respectively. In the other case where the simulation with a hydrogen subsurface concentration of $60.00 \text{ ml} \cdot (100\text{gFe})^{-1}$ has been carried out, the

4. Results and Discussion

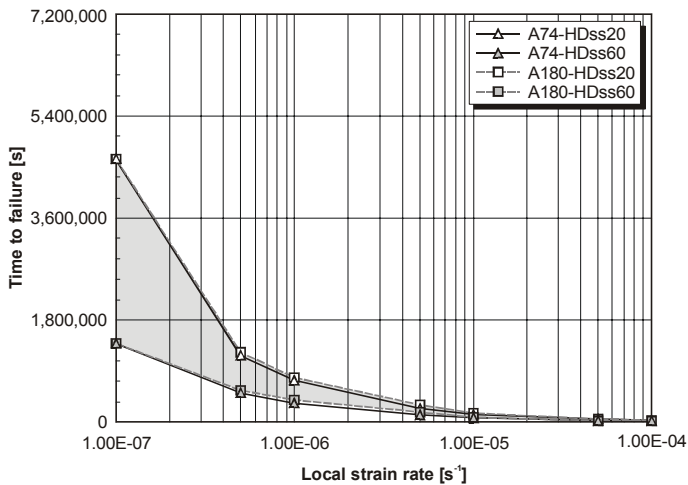


Figure 4-18: Comparison between calculated time to failure dependent on local strain rates of the blunt crack tip (180°) and that of the sharp crack tip (74°) taking account of various levels of hydrogen subsurface concentrations.

time to failures of 160,424 seconds (≈ 44.56 hours) and of 119,083 seconds (≈ 33.08 hours) have been obtained for the blunt crack tip and the sharp crack tip, respectively.

Furthermore, a comparison between the blunt crack tip and the sharp crack is represented in Figure 4-18 with respect to the calculated time to failure as a function of the local strain rate taking account of different hydrogen subsurface concentration levels. There are no significant effects of crack tip geometry on the time to failure for local strain rates higher than $5.0\text{E-}04 \text{ s}^{-1}$.

To summarise above study, sharp crack tips increasingly control the kinetics of crack propagation for hydrogen assisted stress corrosion cracking, if the local strain rate is sufficiently low to allow crack growth by the interaction between hydrogen diffusion and mechanical load.

4.2 Modelling of HASCC in Girth Welds of Pipelines

In order to show the modelling procedure can be transfer to real welded components and respective lifetime assessment, numerical finite element modelling of girth welded supermartensitic stainless steel pipes has been carried out. A constant strain rate was first assumed for gaining a basic understanding of the process of hydrogen assisted stress corrosion cracking. Subsequently, modelling has been performed with load histories corresponding to large scale tests.

4.2.1 Series of Constant Strain Rate

As described above, the global constant strain rates of $1.0\text{E-}07 \text{ s}^{-1}$, $1.0\text{E-}06 \text{ s}^{-1}$ and $1.0\text{E-}05 \text{ s}^{-1}$ in the longitudinal direction represent the appropriate mechanical loads for investigating the effects of hydrogen environments on steel rupture without mechanical overload^[HAS 87].

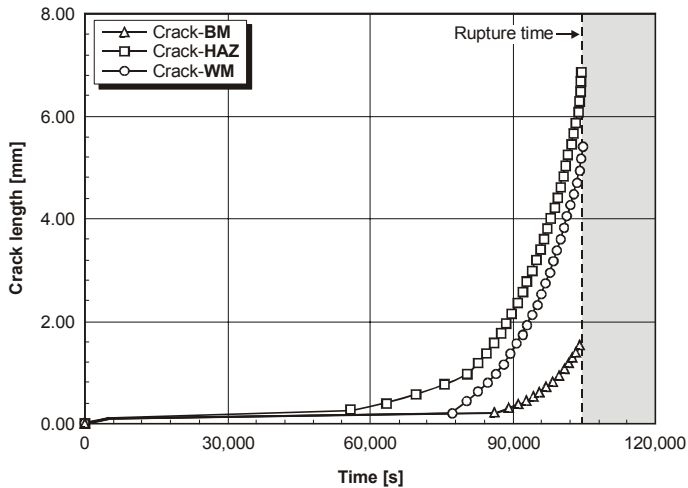


Figure 4-19: Calculated crack length versus time for three significant different zones in orbitally welded supermartensitic stainless steel pipelines exposed to NACE electrolytic solution with 1% H_2S saturation at a constant global strain rate of $1.0E-06 s^{-1}$.

Finite element modelling of the three significant welded joint zones, i.e. the base metal, heat affected zone and weld metal, has been carried out assuming that the interior of the pipeline has been exposed to the NACE electrolytic solution with various H_2S saturations, which directly affects the amount of hydrogen uptake at the surface.

Figure 4-19 shows the calculated crack length versus time curves for the three significant zones in the orbitally welded pipe exposed to the 1% H_2S saturation in the electrolytic solution at a global strain rate of $1.0E-06 s^{-1}$. For the same test conditions the hydrogen concentration profiles for the different stages of cracking in the finite element welded pipe model are illustrated in Figure 4-20.

At this H_2S saturation level, the experimentally investigated supermartensitic stainless steel will take up a hydrogen subsurface concentration of $20.12 ml \cdot (100gFe)^{-1}$ in the as-delivered state and of $3.15 ml \cdot (100gFe)^{-1}$ in the as-quenched state, respectively. Consequently, the hydrogen distribution profiles in Figure 4-20 exhibit significantly higher hydrogen concentrations in the base metal than in the heat affected zone and the weld metal. But, as also represented by Figure 4-19 and illustrated by Figure 4-20, the crack propagation takes place much faster in the heat affected zone than in the base metal and weld metal.

This result is consistent with all component weld tests performed up to the present in which crack initiation always occurred and in most cases the components also completely failed in the heat affected zone. The numerical results clearly show that the base metal generally dissolves more hydrogen than the quenched steel. Consequently, hydrogen follows such concentration gradients and diffuses from the base metal right ahead of the crack tip into the quenched martensite of the heat affected zone which, however, cracks already at lower hydrogen levels. Attraction of hydrogen by the heat affected zone is additionally accelerated by a five times higher diffusion coefficient as compared to the base metal (see Figure 3-13).

4. Results and Discussion

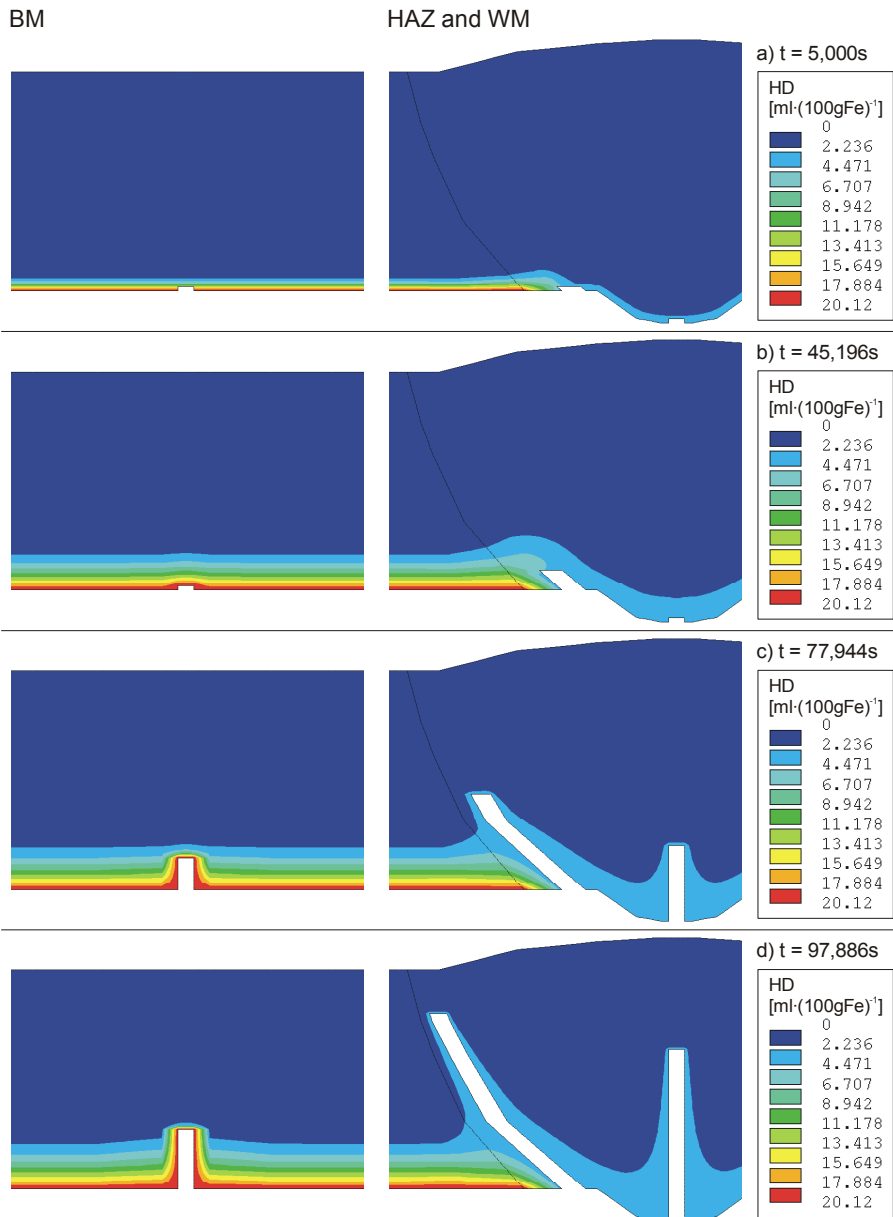
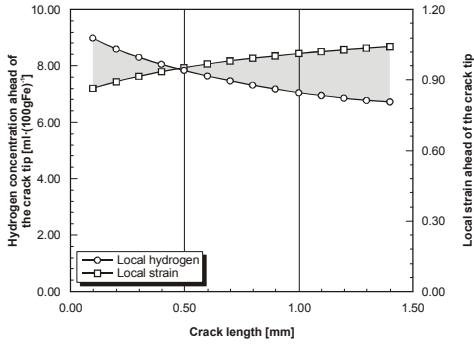
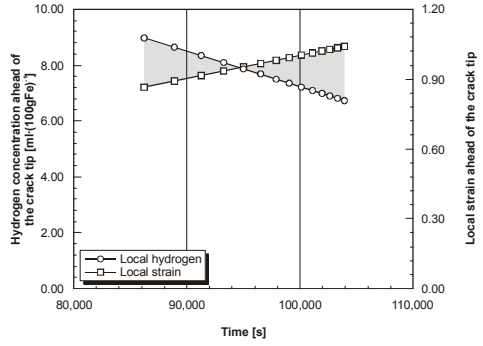


Figure 4-20: Simulated crack propagation in the base metal, heat affected zone and weld metal of orbitally welded pipelines during exposure to NACE standard solution with 1% H_2S saturation at a constant global strain rate of $1.0E-06 \text{ s}^{-1}$.

4. Results and Discussion

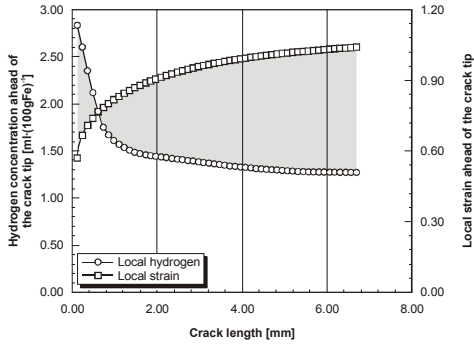


a) Dependent on crack length.

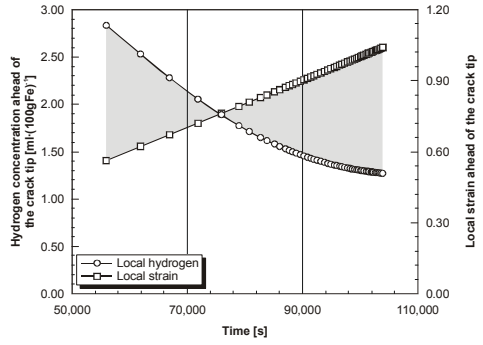


b) Dependent on time.

Figure 4-21: Local hydrogen concentration and local strain distribution at the crack tip in the base metal obtained from the simulated orbital component weld test.

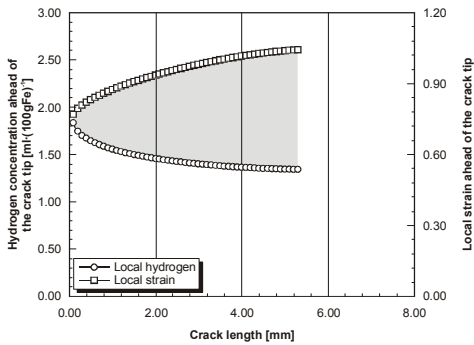


a) Dependent on crack length

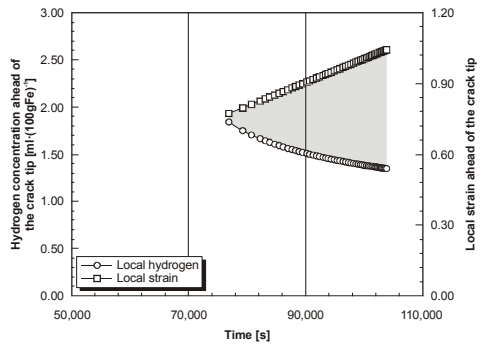


b) Dependent on time

Figure 4-22: Local hydrogen concentration and local strain distribution at the crack tip in the affected zone obtained from the simulated orbital component weld test.



a) Dependent on crack length



b) Dependent on time

Figure 4-23: Local hydrogen concentration and local strain distribution ahead of the crack tip in the weld metal obtained from the simulated orbital component weld test.

4. Results and Discussion

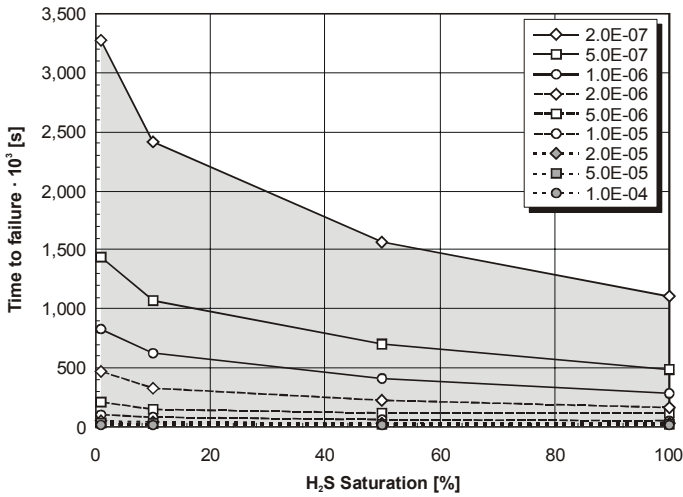


Figure 4-24: Calculated time to failure dependent on the H₂S saturation of the orbitally welded supermartensitic stainless steel pipe exposed to NACE electrolytic solution.

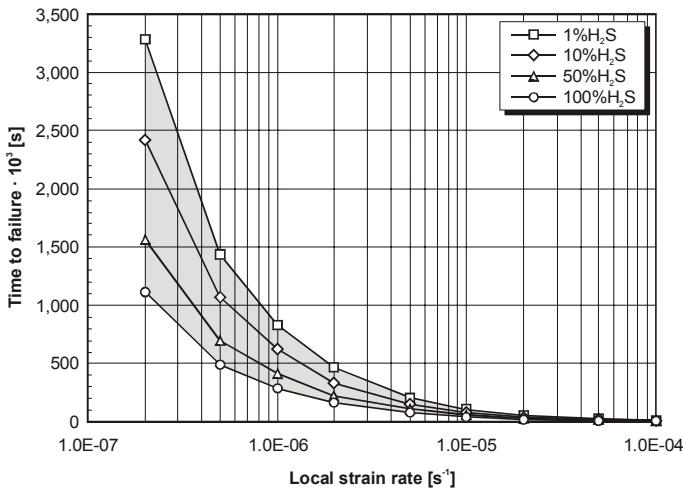


Figure 4-25: Calculated time to failure dependent on the local strain rate of the orbitally welded supermartensitic stainless steel pipe exposed to NACE electrolytic solution.

The different crack propagation characteristics of the welded pipes in different predefined crack path zones can clearly be attributed to the relationship between local hydrogen concentration and local strain levels ahead of the crack tip as function of crack length and time, which is shown in Figure 4-21 for the base metal, in Figure 4-22 for the heat affected zone, and in Figure 4-23 for the weld metal.

The amount of H₂S saturation in the electrolytic solution affects hydrogen assisted cracking mainly by the levels of hydrogen concentration entering the material. In order to quantify this effect with respect to crack propagation in the welded supermartensitic stainless steel pipe, different hydrogen subsurface concentrations produced by 1%, 10%,

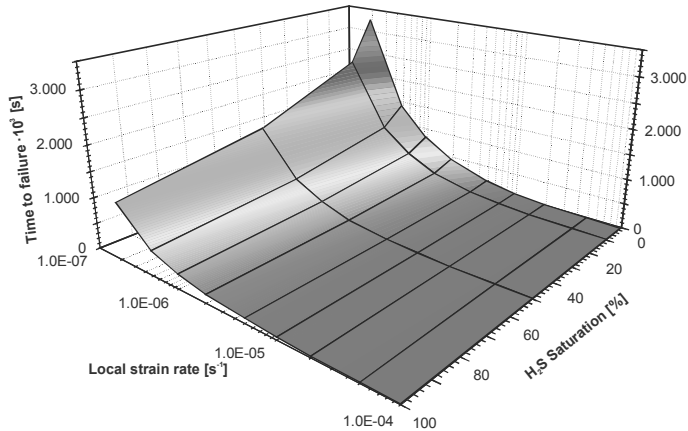


Figure 4-26: Calculated time to failure of the orbitally welded pipe with respect to local strain rates and H₂S saturations in the NACE standard solution.

50% and 100% H₂S saturation in the NACE electrolytic solution have been applied to the surface nodes of the finite element model subjected to the series of global strain rates.

The curves in Figure 4-24 demonstrate how the time to failure of the orbitally welded pipe is significantly shortened by increasing H₂S levels in the electrolytic solution producing higher subsurface concentration at the internal pipeline wall and the tip of the propagating crack concentrations diffusing through the matrix material into the region susceptible to hydrogen assisted stress corrosion cracking at the crack tip. This is additionally indicated by the ranges of the time to failure between low and high strain rate levels, gradually narrowing with increasing hydrogen sulfide levels in the NACE electrolytic solution.

As to be expected from the results obtained from the simulation of the standard specimen, such effects are less pronounced at a higher local strain rate of 1.0E-04 s⁻¹ as compared to a slower local strain rate of 2.0E-06 s⁻¹ and, in particular, of 2.0E-07 s⁻¹ as shown in Figure 4-24. Again, less time is provided for hydrogen transport towards the crack tip, and thus the ductility of the material at the crack tip is less fast reduced at higher strain rates. It can thus be concluded that the rupture of the welded pipe at slower local strain rates resulting from decreasing global strain rates is dominated by stronger mechanisms of hydrogen degrading the material properties than at higher local strain rates. In order to highlight such effects, the time to failure has been plotted versus the local strain rate for different levels of H₂S saturation in the NACE electrolytic solution in Figure 4-25.

As to be expected, increasing local strain rates reduce the time to specimen failure and similarly to the strain rates above 1.0E-05 s⁻¹ are not suitable to show hydrogen effects related to failure of such components effectively, due to rapid ductile rupture of the specimens with too short hydrogen exposure and diffusion times. The fact is that high hydrogen concentrations provided by respective H₂S saturation levels of the environment are particularly crack relevant at slow strain rates. This is implicitly shown in Figure 4-25 by the ranges of the time to failure for different H₂S saturation levels between 1% and 100% which are wider at lower than at higher local strain rates. Again, Figure 4-26 shows the effects of the local strain rates and H₂S saturations in the NACE standard solution on the time to failure of the supermartensitic stainless steel pipe.

4. Results and Discussion

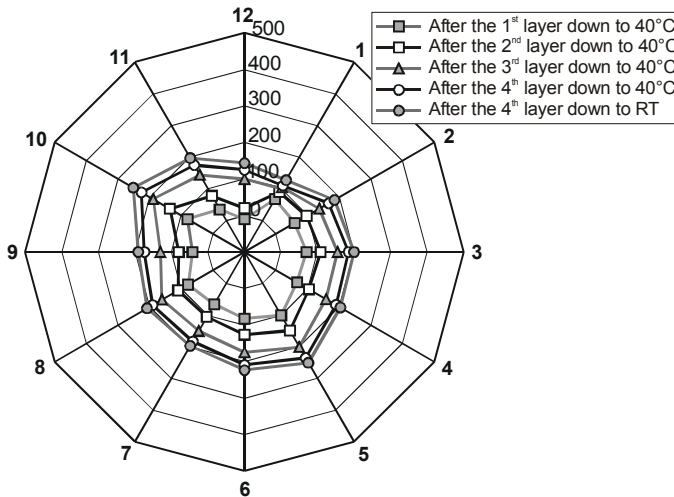


Figure 4-27: Circumferential stress distribution measured by strain gages in the near field at a restraint intensity of $0.45 \text{ kN} \cdot (\text{mm} \cdot \text{mm})^{-1}$ [SPM 56].

4.2.2 Crack propagation in BM, HAZ and WM under the Realistic Test Condition

After these basic considerations, consistent with the component test, constant global straining of the pipe at $\epsilon = 0.1\%$ has been assumed, corresponding to the stress distribution of around 250 MPa introduced during welding and cooling of the pipe at realistic low shrinkage restraints as shown in Figure 4-27.

For three weeks, the pipe has internally been exposed to this stress-strain level and to a realistic sour service condition. After that period, the welded component was stepwise strained each day at rates of around $1.0\text{E-}05 \text{ s}^{-1}$ to 70% and 100% of the weld metal yield strength, corresponding to a simulated global strain of $\epsilon = 0.3\%$ and $\epsilon = 0.5\%$, respectively.

Subsequently, straining of the weld metal up to $\epsilon = 3\%$ and finally to $\epsilon = 5\%$ has been performed in the experiments and has been numerically modelled, respectively.

Due to a lack of realistic data as a worst case scenario, exposure of the welded components to sour service conditions has been simulated in the numerical model by application of the subsurface concentration to the nodes at the internal surface which corresponds to a exposure of the weld metal, the heat affected zone and the base metal to the NACE electrolytic solution with 1% H_2S saturation.

Figure 4-28 shows the hydrogen concentration profile at various stages of crack growth along the three different weld zones for the load history of the component weld test. Corresponding to this simulation, the crack length versus time of three significant cracking zones is shown in Figure 4-29.

Similar to the pre-study at constant strain rates, cracking occurs faster in the heat affected zone than in the base metal and in the weld metal. This result particularly coincides with the component test also exhibiting failure of the welded pipe component in the heat affected zone.

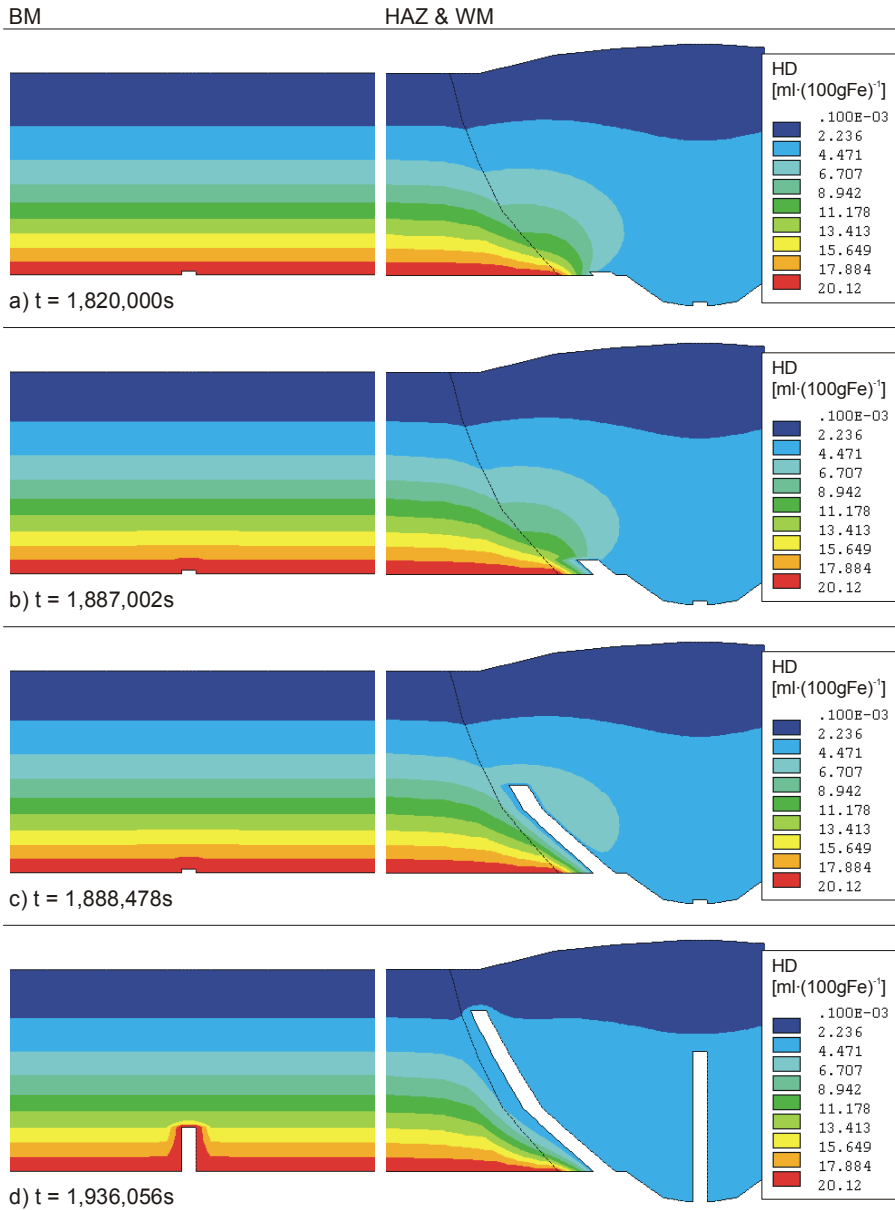


Figure 4-28: Simulated crack propagation in the base metal, heat affected zone and weld metal of orbitally welded supermartensitic stainless steel pipeline exposed to 1% H_2S saturated NACE electrolytic solution at the load history applied to the component weld test.

4. Results and Discussion

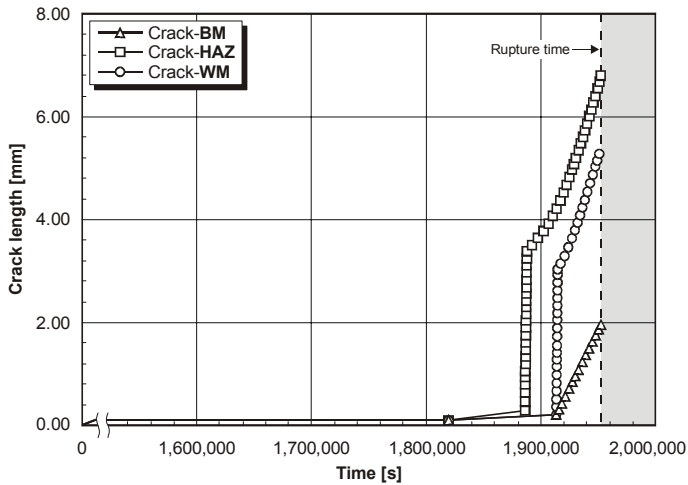


Figure 4-29: Crack length versus time of three significant different cracks in orbitally welded supermartensitic stainless steel pipeline at the load history of the component weld test.

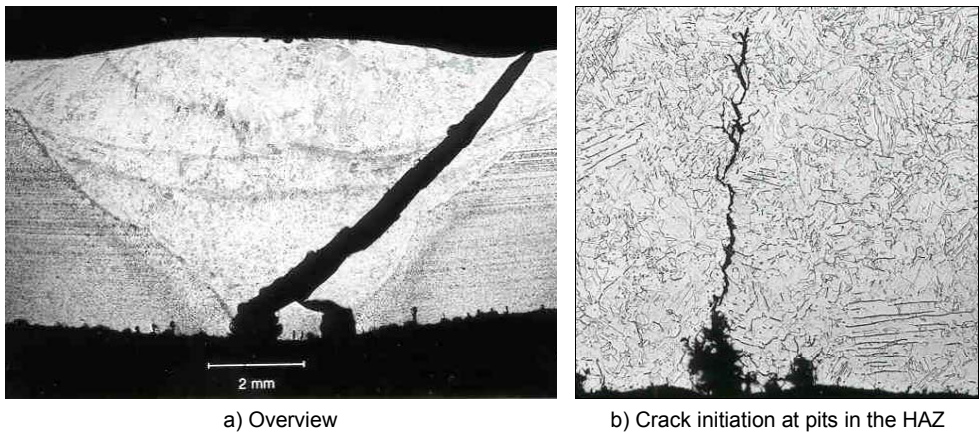


Figure 4-30: Cracked features taking place in the welded pipe during HASCC testing.

Similar to respective slow strain rate tests, the fracture topography exhibited intergranular cracking alongside the former austenite grains, followed by transgranular cleavage-like cracking and finally by more ductile micro-void coalescence. This also indicates that the formation water composition used in the test corresponds to the hydrogen concentration data of the NACE electrolytic solution simulated in the numerical analyses. Future permeation tests and numerical simulation will have to show how much hydrogen is really taken up from the environments used in the experiments and how this will influence crack propagation.

A study of the failure sequences and fracture modes of supermartensitic stainless steels in sour environments showed that intergranular cracking has to be attributed to high hydrogen concentrations under relatively low mechanical loads. By the hydrogen distributions represented in Figure 4-28, it is clearly demonstrated that such high levels are

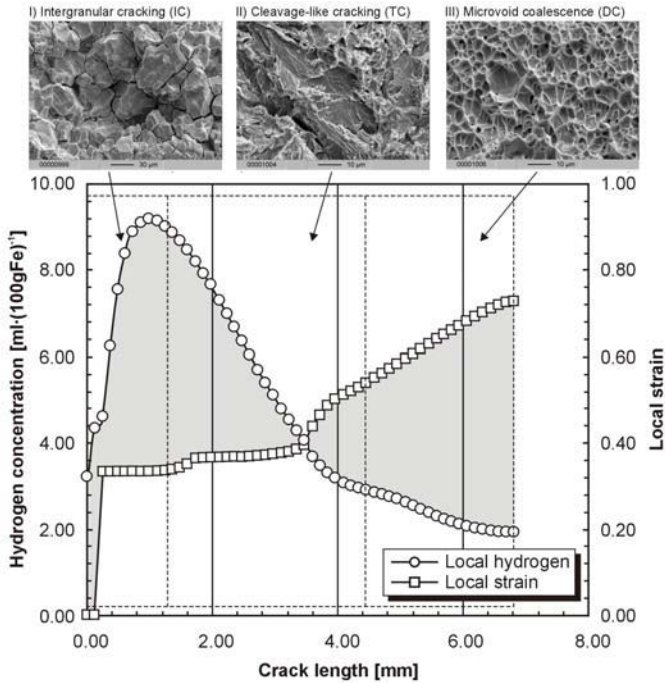


Figure 4-31: Local hydrogen concentration and local strain distribution at the crack tip in the heat affected zone obtained from the numerical modelling with the adopted condition of load history.

provided by hydrogen diffusion from the base metal into the heat affected zone, due to respective concentration gradients. Figure 4-30a and b show an overview and a crack initiation site of the failed supermartensitic stainless steel pipe caused by hydrogen assisted stress corrosion cracking, respectively.

The plots of the actual hydrogen concentration and of the strain at the crack tip versus crack length (Figure 4-31) clearly demonstrate that high hydrogen concentrations relevant for intergranular cracking are particularly piled up in the heat affected zone during the long period of three weeks at a considerably low strains of $\epsilon = 0.1\%$. This is in contrast to the above discussed results for immediate straining of the pipe at a constant strain rate. Due to assumption of a standard test solution in the numerical simulations performed up to the present, the depth of the experimentally determined fracture modes can neither be related to the calculated crack tip positions nor to the local hydrogen concentrations and strains. This has to be left to further research work if subsurface concentrations are applied to the model which have been determined by respective permeation experiments for real formation water compositions.

4.3 Modelling of HACC in Girth Welds of Supermartensitic Stainless Steel Pipelines

Hydrogen introduced into the weld metal during fabrication welding of components can lead to rupture of the welded component when the local hydrogen concentration in a sensitive area reaches the specific critical value dependent on the type of microstructure

4. Results and Discussion

and on the stress-strain levels during cooling to ambient temperature^[GEN 17]. In the present study, welding with matching filler material has been simulated for orbital four-layer TIG welding of supermartensitic stainless steel pipeline. An interpass temperature of 40°C has practically been employed in order to minimise retained austenite in the weld metal and its neighbouring zones, which will promote hydrogen assisted cold cracking by transforming into the martensite with relatively low hydrogen solubility and high hydrogen diffusivity during service^[HAC 39].

Boundary conditions from experimental welding of supermartensitic stainless pipeline have been transferred to numerical finite element modelling for simulating hydrogen assisted cold cracking.

4.3.1 Thermal Analysis

Corresponding to four-layer orbital welding of the supermartensitic stainless steel pipe with matching filler wires (see Figure 4-30a), the numerical modelling of temperature distribution with the same sequences of welding and cooling is simulated. Given the fact that temperature distribution during welding can cause stress-strain build-up due to thermal contraction, and a change in hydrogen diffusion behaviour due to dependence of hydrogen diffusion coefficients on temperature, the first step in the numerical finite element simulation of hydrogen assisted cold cracking has to be the calculation of temperature distribution.

The simulation of temperature distribution during welding of each layer is illustrated in Figure 4-32. The calculation has begun with applying a temperature just above the melting point of supermartensitic stainless steel, i.e. 1540 °C, at weld metal nodes of the first layer for 2 seconds, followed by cooling until the temperature of the welded component reaches the specific interpass temperature. This duration for load application has been assumed according to the welding speed of around 1 mm·s⁻¹ used for orbital welding of the pipe. In order to avoid more complicated phenomena which are recently unclear parameters for calculation of temperature distribution in the weld pool, the constant temperature of 1540°C can appropriately be assumed as the average temperature level in the entire weld pool during TIG welding at the respective welding speed as shown in Christensen's diagram^[GEN 33].

Subsequently, the same welding and cooling conditions as the first layer have been simulated for the next three layers, but cooling of the welded pipeline has been allowed to reach room temperature after completely welding the last layer.

Figure 4-33 represents the temperature distribution at a distance of 25 mm from the weld bead on the exterior surface of the pipeline during welding and subsequent cooling of the four layers. There is a good consistency between the experimental investigation and the finite element simulation. During welding of the first layer, the temperature level of the captured point rises to around 250°C within short time and then practical cooling takes place by heat transfer into the solid material based on Fourier's relationship (see Equation(2-67)) and by heat convection on the surface based on Newton's law (see Equation (2-70)). It should be noted that the cooling rate at temperatures below 100°C becomes much slower with more than 70% of the total cooling time due to the smaller temperature gradient. A peak temperature between 300°C and 350°C is represented for the

4. Results and Discussion

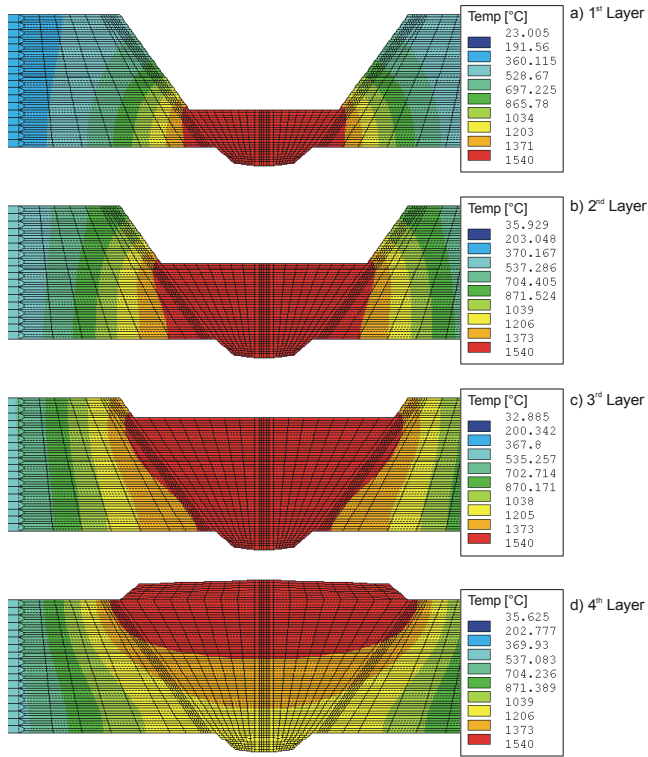


Figure 4-32: Simulation of temperature distribution during orbital welding of supermartensitic stainless steel pipeline with four layers of matching filler material.

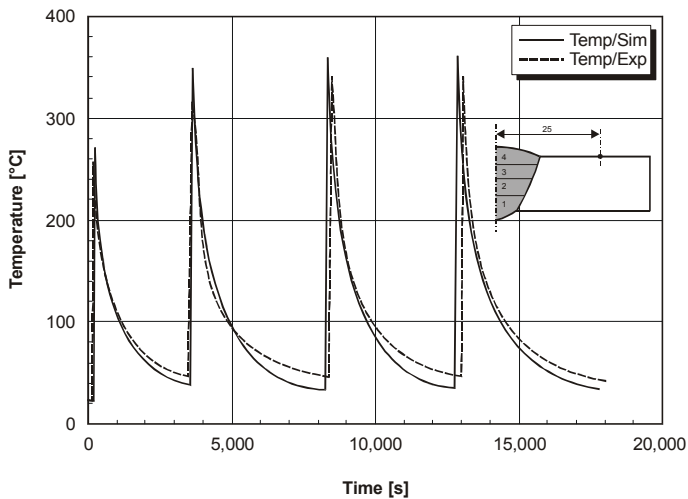


Figure 4-33: Calculated temperature distribution at a distance of 25 mm from the weld bead centerline of supermartensitic stainless steel orbitally welded with four layers in comparison with the measured values.

4. Results and Discussion

next welding layers due to a reduction of the effective distance between the heat source and the detected point.

Until recently, weld pool temperature distribution dependent on time has been impossible to be monitored by usual methods, such as thermocouple, thermo-video camera, etc., because of the high temperature ranging above melting point of the material during welding. But, it can easily be calculated by the finite element simulation. The temperature distribution dependent on time at the middle point in each layer is represented in Figure 4-34a, b, c, and d for the first layer, the second layer, the third layer, and the last layer, respectively.

During welding of the first layer, the temperature at the captured point reaches the specific level for melting the material and the other points do not indicate any temperature distribution. Following the cooling of the first layer to the specific interpass temperature, the specific point in the second layer shows an ascent of temperature up to the specific melting temperature during welding, while the specific point in the first layer indicates a peak temperature level lower than the melting point. The peak temperature distributions at the captured points in the third layer and the last layer are similar to those in the previous layers during welding. But, it must be pronounced that there is difference in the temperature level for each layer. For instance, the peak temperature at the captured point in the first layer is about 1210 °C during welding the last layer (see Figure 4-34a). This means that the previous layers are definitively reaustenised by welding of the further layers (see Figure 2-3a).

Since the specific region of the heat affected zone has previously to be defined in the finite element model with its proper material properties for stress-strain distribution analysis and hydrogen diffusion analysis, the width of the heat affected zone with martensite formation due to thermal effects should be confirmed for the finite element model.

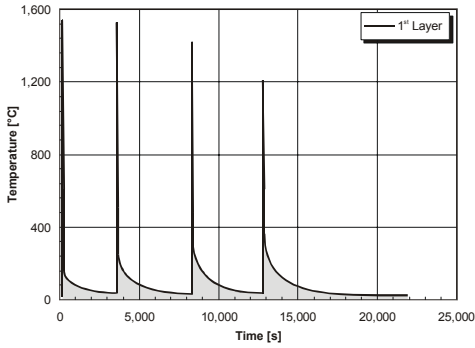
The temperature distribution on the border line between the heat affected zone and the base metal has been calculated by the finite element simulation. The calculated temperature distribution dependent on time at the inside surface of the pipeline is represented in Figure 4-35a. A peak temperature of around 1270 °C during welding the first layer has been obtained, while the peak temperature at the outside surface of the pipeline is about 630 °C as represented in Figure 4-35b. The peak temperature at the captured point of the inside pipeline indicates a tendency towards decreasing its level due to the upward movement of the heat source upwards from the detected point for welding the next layer. In turn, the outside surface of the pipeline shows the opposite tendency for the peak temperature compared to the inside.

Therefore, assuming complete martensite formation for the predefined weld metal and heat affected zone is in good agreement with experimental investigation of the orbitally welded pipeline. This means that further numerical simulation, i.e. structural analysis and diffusion analysis, should take account of individual material properties for the base metal, heat affected zone and weld metal.

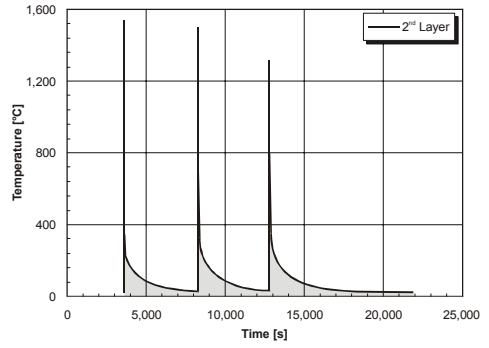
4.3.2 Structural Analysis

Stress-strain distribution that develops in the welded component may result from self-restraint or external restraint, or from a combination of both^[GEN 16]. The thermal contraction

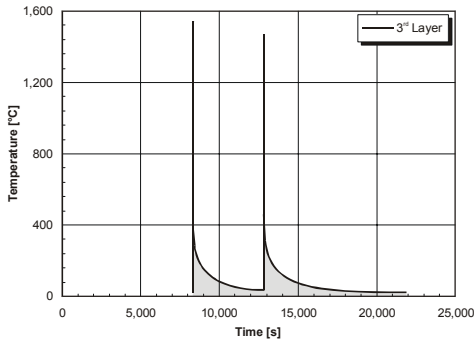
4. Results and Discussion



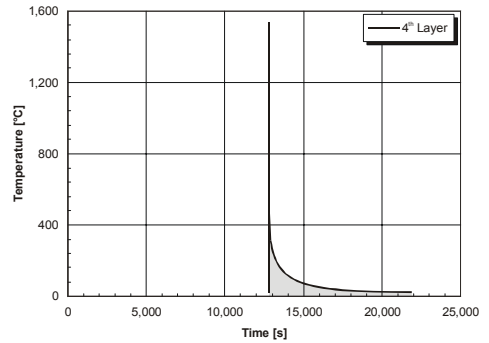
a) First layer



b) Second layer

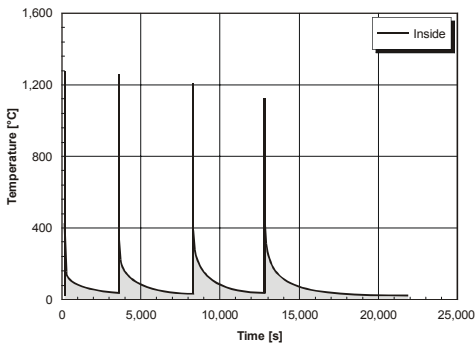


c) Third layer

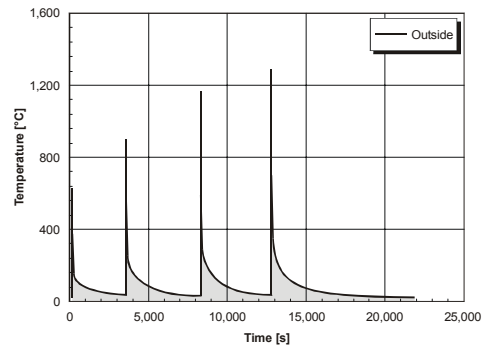


d) Last layer

Figure 4-34: Calculated temperature distribution dependent on time captured from the middle point of each layer in the weld metal during welding and subsequent cooling.



a) Inside of the pipeline



b) Outside of the pipeline

Figure 4-35: Calculated temperature distribution captured at the specific points on the interface between the heat affected zone and base metal: a) Inside of the pipeline, b) Outside of the pipeline.

4. Results and Discussion

and the temperature gradient in the solid material during welding and subsequent cooling significantly change the stress-strain distribution in welded components. The finite element simulation based on structural analysis it is therefore essential to take account of the temperature distribution dependent on time and boundary conditions such as restraint for calculating the actual stress-strain distribution in orbital welding of supermartensitic stainless steel pipeline.

Under the considerable condition of low shrinkage restraints, the both ends of the finite element model have been restrained. The calculation of stress-strain distribution in the first layer is carried out by regarding the temperature from the thermal analysis as a body load for structural analysis.

The calculated equivalent strain in the welded component at the end of cooling process corresponding to the specific temperature conditions in each layer is illustrated in Figure 4-36.

For the same condition, the calculated equivalent strain distribution at the specific point in the weld metal of each layer dependent on the running time is represented in Figure 4-37. At the remote point in the base metal 25 mm away from the weld centreline, the calculated equivalent strain represents the relatively low level of around 0.25% after completed welding for the last layer with subsequent cooling to room temperature. The previously remained equivalent strain level is depressed to be nearly zero during welding the recent layer, but it increases again during the cooling process. The reason is that the total strain in the area of the base metal away from the weld can be built up by the tension force caused by the shrinkage reaction that is present only in the elastic range of the material. Therefore, the compressive force resulting from the expansion of the material during welding can interact with the previous tension force to reduce the total strain level. Moreover, the calculated equivalent strain at the remote point in the base metal seems to be monotonic increased with increasing the number of welding layers because the cross-sectional area of the weld bead subjected to the reaction force has been increased due to multi-run welding. However, it can be pronounced that the remote zone from the weld will not be susceptible to hydrogen assisted cold cracking due to lower strain levels compared with the weld metal and its neighbouring zones.

It is generally accepted that hydrogen assisted cold cracking takes place in the weld metal or the heat affected zone due to increasing weld metal strength. Hydrogen assisted cold cracking is shifted from the heat affected zone into the weld metal. This is assisted by higher hydrogen concentration in the weld metal^{[HAC 23],[HAC 49]}. This makes it necessary to discuss the equivalent strain distribution in the weld.

For each weld metal layer, there is individually a distinct aspect of the calculated equivalent strain distribution at the specific point. For instance, in the finished state of pipeline welding, i.e. after completed welding of the last layer and subsequent cooling to ambient temperature, the calculated equivalent strain in the first layer of the weld indicates the highest level say 4.5%, while a tendency towards reduced calculated equivalent strain level is obviously represented for the specific point in the second layer, the third layer, and the last layer, respectively.

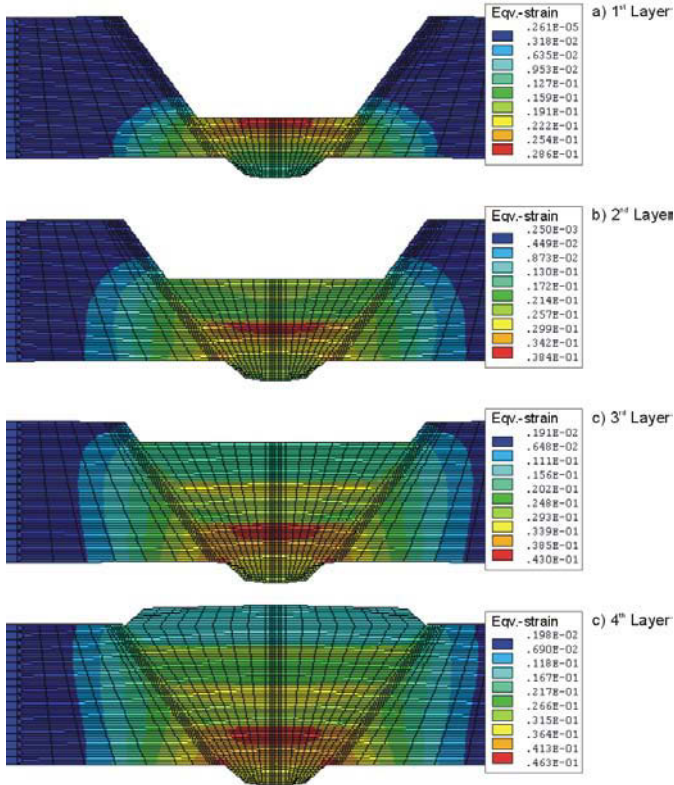


Figure 4-36: Simulation of equivalent strain distribution at the specific interpass temperature of each layer of the four-layer orbitally welded supermartensitic stainless steel pipeline.

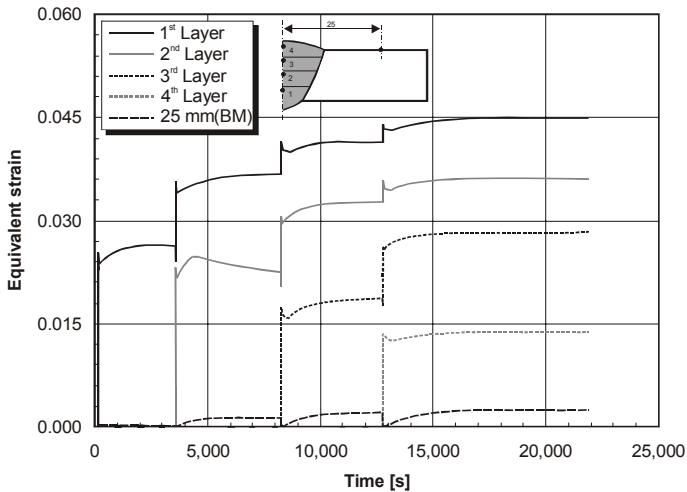


Figure 4-37: Calculated equivalent strain distribution dependent on the running time of supermartensitic stainless steel orbitally joined by four layers of matching filler wires.

4. Results and Discussion

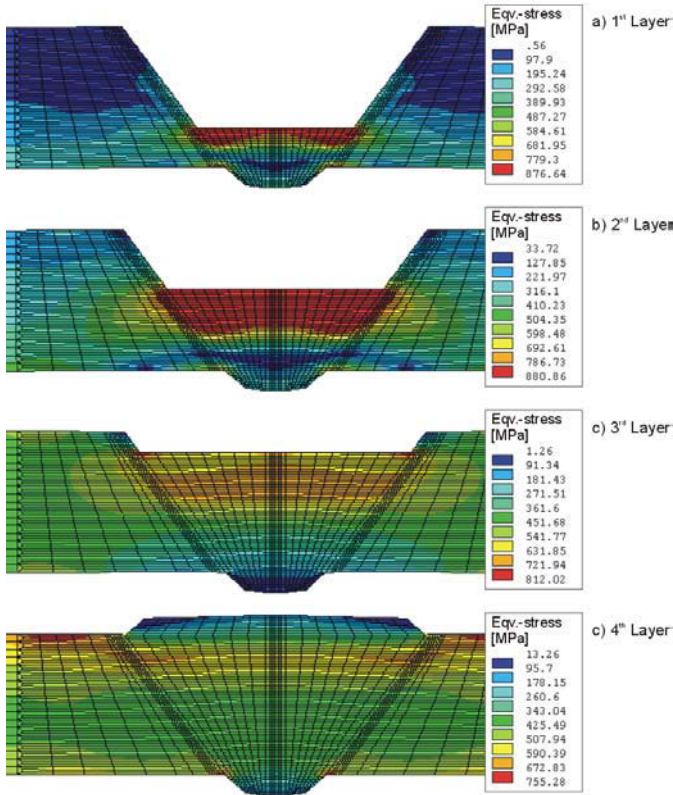


Figure 4-38: Simulation of equivalent stress distribution at the specific interpass temperature of each layer of the orbitally four-layer welded supermartensitic stainless steel pipeline.

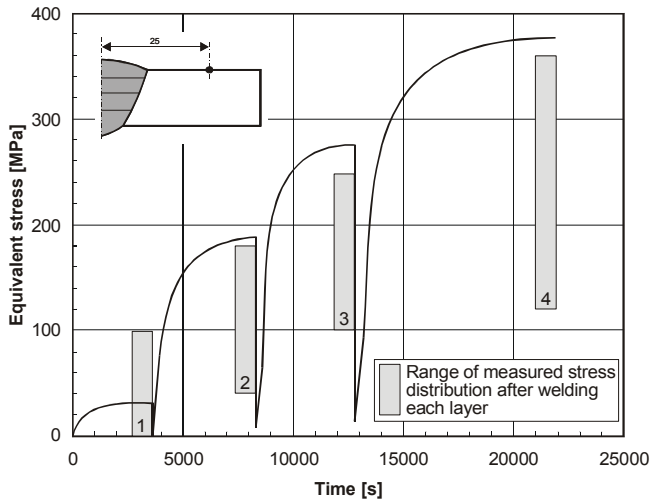


Figure 4-39: Calculated equivalent stress distribution dependent on the running time of supermartensitic stainless steel pipelines orbitally joined by four layers of matching filler wires.

Focusing on the specific point in first weld metal layer, the equivalent strain ascends up to the level of 2.5% during welding the first layer. Subsequently, it continuously increases up to 2.63% during the cooling to the specific interpass temperature for the welded first layer. This equivalent strain is depressed again to 2.45% in the short period during the temperature rise to the melting point, and the calculated equivalent strain becomes 3.52% after completed welding of the second layer. During cooling, the calculated equivalent strain rises monotonically up to 3.38% when the specific interpass temperature has been reached. This sequence can also be used to describe the progression of the curve dependent on the running time for the specific points within the second, third and layers, but only scalar values of each curve are remarkably different (see Figure 4-37).

As a specific item, the equivalent strain in the weld metal cannot be depressed to zero as in the remote area in the base metal (at a distance of 25 mm) during welding the upper layers because the strain in the weld metal ranges in the plastic region.

Figure 4-38 illustrates the equivalent stress distribution after cooling to the specific temperature condition for each layer in the four-layer orbitally welded supermartensitic stainless steel pipeline with application of matching filler material. It indicates a relatively high level of remaining equivalent stress distribution in the weld metal and its neighbouring zones, particularly in the preceding layers. The stress remaining in the welded component is decreased by welding of the next layer. However, the calculated stress distribution can more effectively be shown by creating the equivalent stress versus time diagram for the specific point in the base metal compared with the results from the experimental investigation as represented in Figure 4-39. This indicates that increasing the number of welded layers causes an increase of stress levels determined from the specific point in the base metal. The calculated stress levels are slightly higher the stress ranges measured in different circumferential positions during cooling to the specific interpass temperatures of each layer. The maximum stress ranging between 360 and 380 MPa has been obtained after completed welding and subsequent cooling of the last layer. However, from these results it can be said that there is a good agreement between the experimental investigation and numerical calculation.

4.3.3 Hydrogen Diffusion Analysis

The study of the hydrogen distribution behaviour in the weld metal and its neighbour zone during welding and cooling by numerical simulation is highlighted in this section.

4.3.3.1 Effects of Initial Hydrogen Concentration on Local Hydrogen Distribution

Due to specific hydrogen concentration values dependent on the partial pressure in the shielding gas or dependent on the moisture available for supermartensitic stainless steel welds (see Figure 2-20 and Figure 2-23), specific initial hydrogen concentrations, i.e. 2.50, 5.00, 7.50, 10.00, 15.00, and 20.00 ml·(100gFe)⁻¹ have been applied to the finite element model during welding the first layer. The effects of hydrogen diffusion in the solid material and hydrogen effusion at the material surface have been taken into account in examining the hydrogen escape from the initial hydrogen source during cooling to the specific thermal condition. The hydrogen concentration identical to the first layer has also been applied to finite elements in each layer during welding until the last layer. However, after complete welding of each layer, hydrogen concentration is consequently reduced by hydrogen

4. Results and Discussion

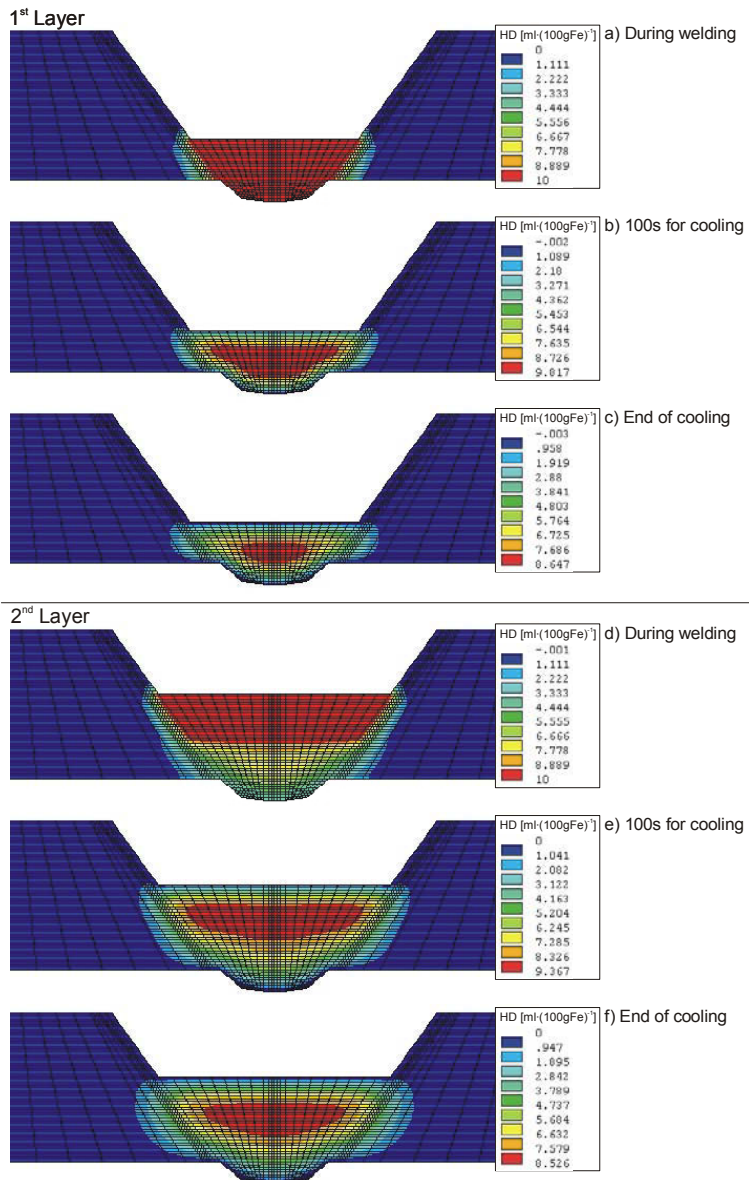


Figure 4-40: Hydrogen distribution in girth welds of supermartensitic stainless steel during welding and subsequent cooling with four layers of matching filler wires (Assumption: $HD = 10.00 \text{ ml} \cdot (100\text{gFe})^{-1}$ picked up during welding).

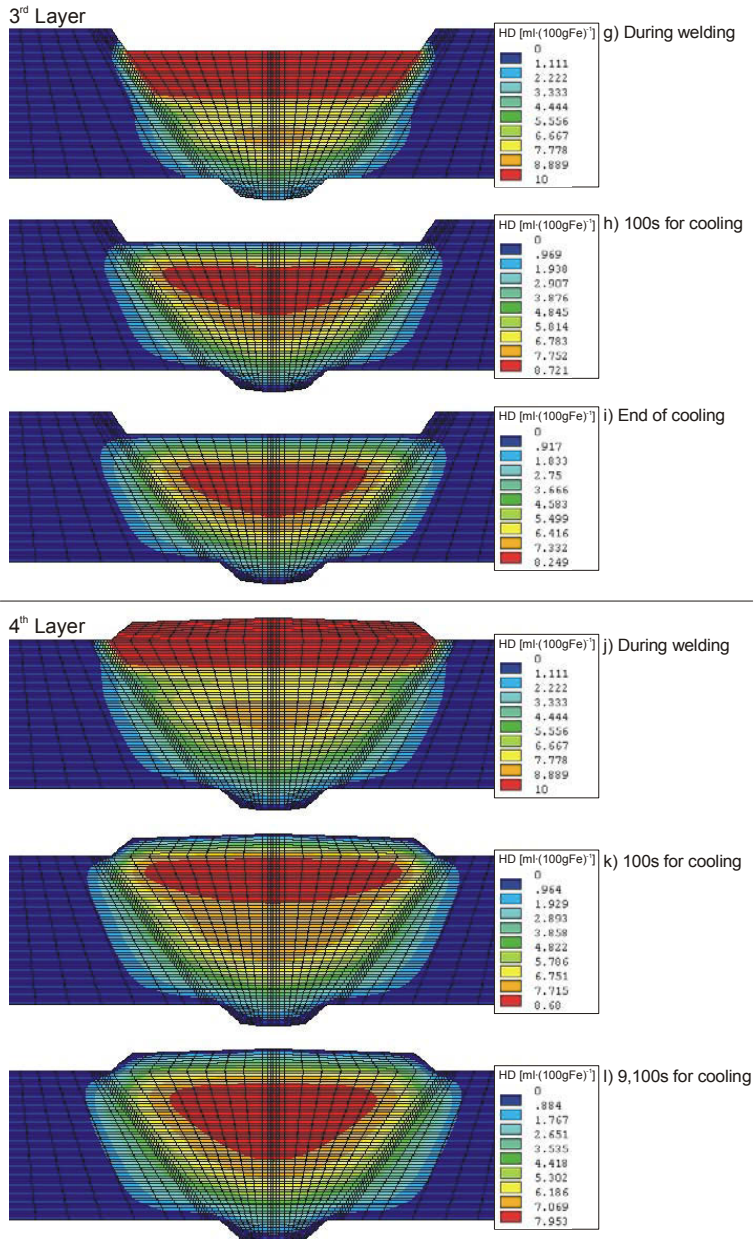


Figure 4-40(continued): Hydrogen distribution in girth welds of supermartensitic stainless steel during welding and subsequent cooling with four layers of matching filler wires (Assumption: $HD = 10.00 \text{ ml} \cdot (100\text{gFe})^{-1}$ picked up during welding).

4. Results and Discussion

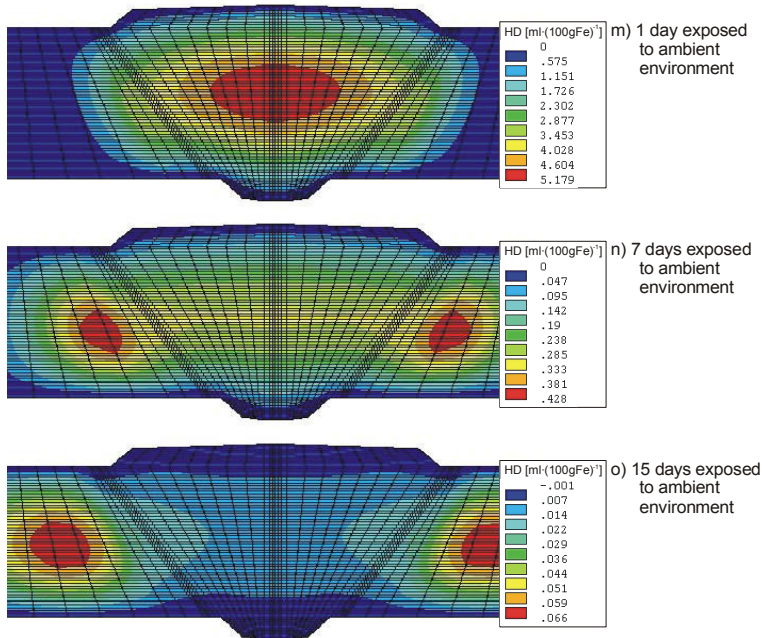


Figure 4-40(continued): Hydrogen distribution in girth welds of supermartensitic stainless steel during welding and subsequent cooling with four layers of matching filler wires (Assumption: $HD = 10.00 \text{ ml} \cdot (100\text{gFe})^{-1}$ picked up during welding).

diffusion and effusion reactions during cooling of the welded component to the specific temperature throughout fabrication as previously described (Chapter 3).

Figure 4-40 shows the simulation of hydrogen distribution in the weld metal and its neighbouring zone of the previously described girth weld of supermartensitic stainless steel pipeline assuming an initial hydrogen concentration of $10.00 \text{ ml} \cdot (100\text{gFe})^{-1}$. It can be seen that high temperatures in early periods of cooling can enhance the distribution of initial hydrogen into the weld metal and its adjacent zones due to higher hydrogen diffusion coefficients than those of the last cooling period. At the same time hydrogen escapes at the surface and the weld root.

For example, after welding of a first layer, a ratio of the maximum local hydrogen concentration to the specific initial hydrogen concentration of 98.17% has been obtained for 100 seconds of cooling, and a cooling time of the order of 3,400 seconds can reduce this ratio to 86.47%. Figure 4-41 shows the respective hydrogen concentration-time diagram for the previously described specific points in the centreline of the weld metal.

Moreover, it has been found that the maximum local hydrogen concentration in the weld metal after welding and subsequent cooling to the specific temperature of each welded layer tends to be decreased with increasing the number of deposited layers for girth welds of pipelines. For example, maximum local hydrogen concentrations of $8.647 \text{ ml} \cdot (100\text{gFe})^{-1}$, $8.526 \text{ ml} \cdot (100\text{gFe})^{-1}$, $8.249 \text{ ml} \cdot (100\text{gFe})^{-1}$ and $7.953 \text{ ml} \cdot (100\text{gFe})^{-1}$ occurring in the welded metal have been obtained after complete welding and subsequent cooling to the specific temperature of the first layer, the second layer, the third layer and the last layer,

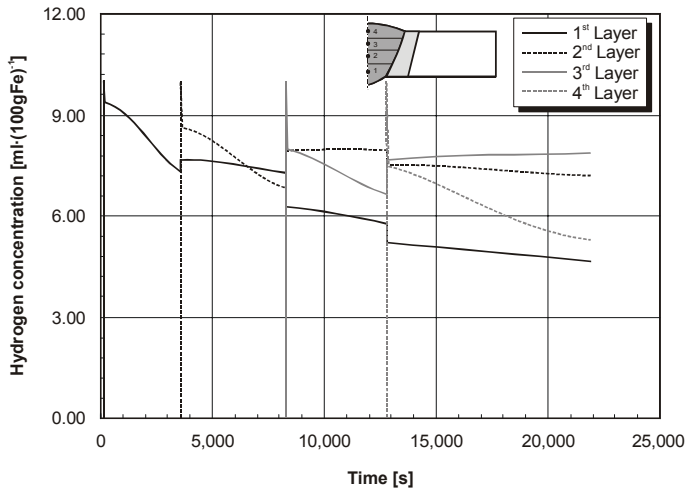


Figure 4-41: Calculated local hydrogen distribution dependent on time at the specific point in each welded layer during welding and subsequent cooling to conform to the specific thermal conditions for the pipeline girth welds (Assumption: $HD = 10.00 \text{ ml} \cdot (100\text{gFe})^{-1}$ picked up during welding).

respectively. One explanation is that the surface for hydrogen effusion increases with each layer. As another explanation, the amount of heat input increases with each layer, and causes a further diffusion into the adjacent zones by higher temperature dependent diffusion coefficient.

However, it might be remarkable that the local maximum hydrogen concentration in the weld metal can be reduced within quite reasonable exposure time. For instance, an exposure time of around 1 day after complete welding and subsequent cooling to ambient temperature can reduce the local maximum hydrogen concentration by nearly 50% with respect to the initial hydrogen uptake in the weld metal, and the local maximum hydrogen concentration can be reduced by more than 95% with respect to the initial hydrogen concentration when the exposure time is extended to 1 week after the welded component has already reached room temperature. As compared to other steel welds, such rapid reduction of the hydrogen concentration is quite remarkable and has also to be attributed to the high diffusivity in the heat affected zone. However, within the first three days after welding, hydrogen concentrations at crack relevant levels are maintained. Moreover, it should be noted that the local hydrogen concentration dependent on time of each specific point after cooling to its specific temperature without depositing the further layer indicates the different hydrogen concentration due to an increase in the contact area of the hydrogen source to ambient environments as well as to the base metal.

Figure 4-41 represents the calculated local hydrogen concentration dependent on time at the specific point in each welded layer for the girth welded supermartensitic stainless steel pipeline produced with four layers of matching filler material. During welding, an amount of hydrogen uptake of $10.00 \text{ ml} \cdot (100\text{gFe})^{-1}$ in the weld metal has initially been assumed, and this local hydrogen is subsequently reduced during the cooling process of the welded component. All curves feature the same characteristic that the reduction rate of local hydrogen concentration is much faster in early periods of the cooling process due to

4. Results and Discussion

high hydrogen diffusion coefficients, and that becomes slower when the temperature of the welded pipeline reaches to the austenite temperature range.

As another important item, the hydrogen concentration of $7.381 \text{ ml}\cdot(100\text{gFe})^{-1}$ obtained at the end of cooling process in the centre the first layer is increased to be around $7.66 \text{ ml}\cdot(100\text{gFe})^{-1}$ by diffusion of hydrogen from the newly welded second layer within about 300 seconds of cooling time (at approximately $180 \text{ }^\circ\text{C}$). After that, the local hydrogen concentration continuously decreases to $7.31 \text{ ml}\cdot(100\text{gFe})^{-1}$. In contrast, welding of the third layer significantly reduces the local hydrogen concentration in the first layer, particularly, during welding and subsequent cooling to about 500°C (30 seconds of cooling).

Similar sequences for the hydrogen concentration changing are observed in the specific points of the second layer, the third layer and the last layer, as well. Each specific point exhibits its individual characteristics, such as hydrogen concentration dependent on time.

However, during welding of the last layer and subsequent cooling to ambient temperature, a local hydrogen concentration of $7.86 \text{ ml}\cdot(100\text{gFe})^{-1}$ at the specific point in the third layer is obtained as the highest level compared with the other specific points, whereas the specific point in the first layer indicates the lowest level of hydrogen concentration ($4.68 \text{ ml}\cdot(100\text{gFe})^{-1}$). The local hydrogen concentrations at the specific points in the second and third layers are higher than those in the first and last layers. It can therefore be pronounced that the high local hydrogen concentration remains in the upper range of weld metal which may be a region susceptible to hydrogen assisted cracking.

Since hydrogen assisted cold cracking may occur in the heat affected zone as well as in the weld metal, hydrogen distribution in the heat affected zone has to be studied, too. The calculated hydrogen concentration dependent on time at the specific points in the heat affected zone corresponding to the respective welding layers is represented in Figure 4-42. The local hydrogen concentration at those specific points is found to be lower than at the specific points in the weld metal. For example, at the end of the pipeline welding, a maximum local hydrogen concentration of $4.82 \text{ ml}\cdot(100\text{gFe})^{-1}$ is obtained for the specific point, which is closest to the third welded layer, in the heat affected zone. It has thus to be anticipated that the local hydrogen concentration in the weld metal, rather than that in the heat affected zone, significantly contributes to hydrogen assisted cold cracking in girth welds of supermartensitic stainless steel pipeline, in particular in combination with a relatively high local strain distribution in the weld metal.

As described above, an extended time of exposure to ambient environment decreases the maximum local hydrogen concentration in the weld metal and its neighbouring zone. The local hydrogen concentration dependent on time at the middle point of the weld metal after welding of the last layer with respect to various amounts of initial hydrogen picked up by the weld metal is represented in Figure 4-43. The remaining local hydrogen concentration in the weld metal is dependent on the initial hydrogen uptake in the weld pool during welding. But, a sufficient time of exposure to ambient environments decreases the predominant effect of the initial hydrogen concentration on the remained hydrogen concentration. For example, local hydrogen concentrations of $1.46 \text{ ml}\cdot(100\text{gFe})^{-1}$ and $0.36 \text{ ml}\cdot(100\text{gFe})^{-1}$ are obtained for 300,000 seconds (≈ 3.5 days) of exposure time from the amounts of initial hydrogen, taken up by the weld metal during welding, of $10.00 \text{ ml}\cdot(100\text{gFe})^{-1}$ and $2.50 \text{ ml}\cdot(100\text{gFe})^{-1}$, respectively.

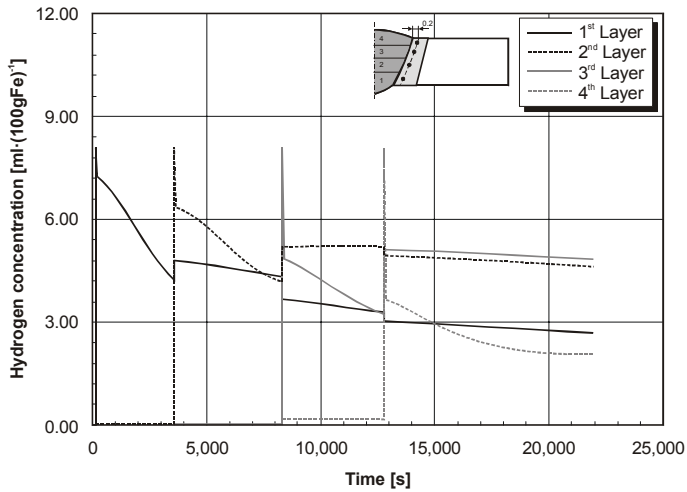


Figure 4-42: Calculated local hydrogen concentration in the heat affected zone, 0.2 mm away from the fusion line, for each welding layer (Assumption: $HD = 10.00 \text{ ml} \cdot (100\text{gFe})^{-1}$ picked up during welding).

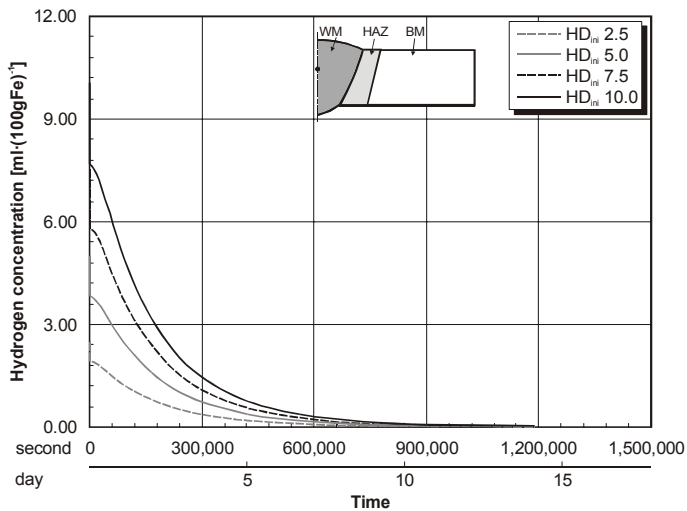


Figure 4-43: Reduction of the maximum hydrogen concentration, dependent on initial hydrogen concentration picked up during welding, in the upper third of the weld with increasing exposure time to ambient environments after completion of welding and cooling to room temperature of the last layer.

However, in practical pipeline fabrication, the exposure time to ambient environment is limited due to the time pressure for field applications. Thus, the various initial hydrogen concentrations may be a main reason for an occurrence of failure caused by hydrogen assisted cold cracking.

4.3.3.2 HACC Initiation and Propagation

The present results show that for numerical finite element simulation of hydrogen assisted cold cracking it can be assumed that the crack occurs at nearly ambient temperature. One reason for this is that low γ - M_s transformation temperatures in this

4. Results and Discussion

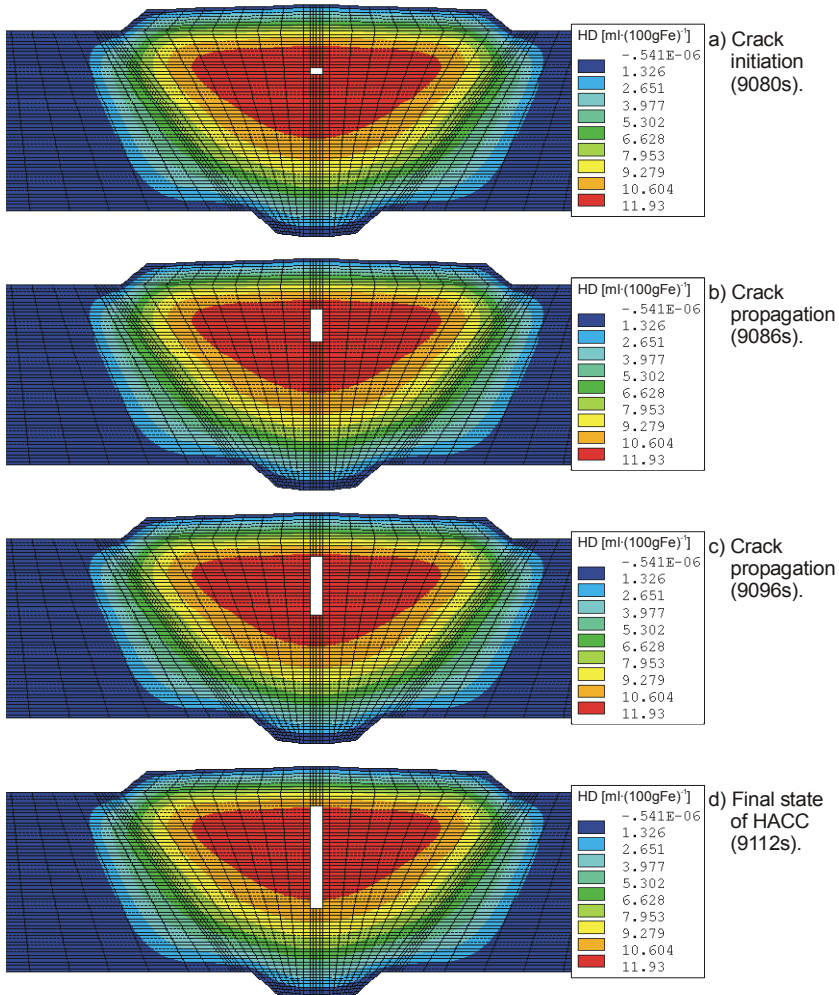


Figure 4-44: Simulation of hydrogen concentration profile and crack propagation for hydrogen assisted cold cracking in the weld metal of orbitally welded pipeline during cooling to room temperature (Assumption: $HD = 15.00 \text{ ml} \cdot (100\text{gFe})^{-1}$ picked up during welding).

context. Another prominent reason is attributed to the capability of the material to carry full load at the γ - M_s transformation temperature. From these reasons, modelling of the cold cracking process has been started at a temperature of 40 °C during cooling after welding.

Following the previous simulation of strain distribution in pipeline girth welds (see Section 4.3.2), the maximum local hydrogen concentration higher than $10 \text{ ml} \cdot (100\text{gFe})^{-1}$ is required for inducing crack propagation caused by hydrogen assisted cold cracking. Accordingly, the finite element simulation of hydrogen distribution analysis is carried out with the assumption of $15.00 \text{ ml} \cdot (100\text{gFe})^{-1}$ for an initial hydrogen concentration picked up by the weld metal during welding.

As represented in Figure 4-44, there is a maximum local hydrogen concentration of $11.93 \text{ ml} \cdot (100\text{gFe})^{-1}$ in the weld metal after completion of the last welded layer and cooling to ambient temperature. In order to identify exactly the location of crack initiation, the numerical simulation first searches the critical node, whose maximum local hydrogen concentration reaches the critical value, on the predefined cracking path in both the weld metal and the heat affected zone. Crack initiation is then simulated by deleting the first element in upward and downward direction adjacent to the critical node. It turned out within in this procedure that crack initiation takes place only in the weld metal due to a relatively high local hydrogen concentration and a relatively high local strain distribution.

An initiated crack may propagate either in upward direction or in downward direction, or both, dependent on the local hydrogen concentration and its critical value. Thus, crack propagation is defined by comparing the local hydrogen concentration at a specific node in downward direction to that in upward direction ahead of both crack tips. As shown by the plots in Figure 4-44, crack propagation first takes place in both directions, particularly into the zone with the relatively high hydrogen concentration. After that, the crack propagates only in downward direction. This is particularly caused by the high strain level resulting in a decrease of the critical hydrogen concentration. Therefore, the crack propagates preferentially in downward direction rather than upwards even though the local hydrogen concentrations in upward direction are higher than those in downward direction.

The crack propagation stops when the local hydrogen concentration at the specific node becomes lower than the critical value.

In order to gain a understanding of the significant interaction between the local hydrogen concentration and strain level affected by temperature distribution during welding and subsequent cooling for the crack initiation, a diagram of temperature–equivalent local strain – local hydrogen concentration dependent on time is represented in Figure 4-45.

Two specific points in the first layer and the third layer have been selected as the interesting comparable locations for study on characteristics of the crack initiation and propagation. The temperature, after complete welding of the last layer, of the second point is higher than that of the first point (1220°C), but during cooling there are no obvious differences between the first and second point.

According to the finite element simulation as represented in Figure 4-44, the second point is defined as the position for crack initiation due to the higher local hydrogen concentration compared with the first point, even though the local strain level at the first point is higher than at the second point. Rupture takes thus place in the susceptible high hydrogen containing region at the relatively low strain levels.

To summarise these findings, two facts can thus be stated:

- 1) Hydrogen assisted cold cracking is initiated at the region of the highest hydrogen concentration with the comparable low strain levels.
- 2) Crack propagation takes first places in both directions, but then preferentially towards the weld root, i.e. into regions of higher strain levels.

4. Results and Discussion

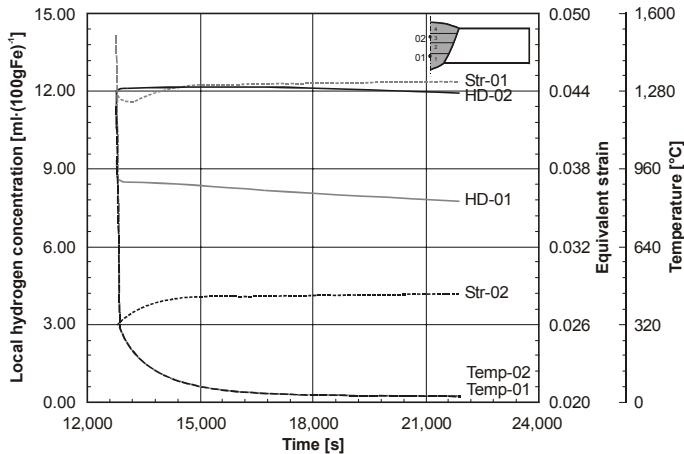


Figure 4-45: Calculated hydrogen distribution, strain distribution and temperature distribution dependent on time at the specific points in the first layer and the third layer during the cooling process after orbital welding of the last layer of pipeline.

As a further point for avoidance of hydrogen assisted cold cracking in orbitally welded supermartensitic stainless pipeline in practice, the hydrogen concentration in the weld pool should always be lower than $10 \text{ ml} \cdot (100\text{gFe})^{-1}$.

4.3.4 Effects of PWHT on Local Hydrogen Concentration in the Welded Component

Post-weld heat treatment (PWHT) is conventionally employed to improve the toughness of welded components by reducing the amount of martensitic microstructure in the matrix material and/or by lowering the residual stress-strain distribution resulting from thermal cycle effects. But for girth welding of supermartensitic stainless steel pipeline deposited with using matching filler material, strength reduction of the welded component has to be avoided to ensure high resistance against anodic stress corrosion cracking during field application in offshore technology.

As suggested by Gooch et al.^[SPM 27] the temperature of post weld heat treatment depends on the A_{C1} -temperature. Nevertheless, it should be recognised that carbide formation, such as $M_{23}C_6$, M_7C_3 , etc., can occur in the matrix material of supermartensitic stainless steel when post weld heat treatment is carried out above 500°C with extension of the tempering duration. Post weld heat treatment for hydrogen removal from crack susceptible weld areas with less changes in the microstructure and strength reductions.

Therefore, two categories of post weld heat treatment, i.e. short-term tempering and long-term tempering, are compared by using finite element simulation.

For both procedures, after welding the last layer and subsequent cooling to the complete martensite transformation temperature, beneath M_f -temperature, the orbitally welded pipeline has been subjected to an additional heat source with the specific temperature level as represented in Figure 4-46. The reason for cooling the orbitally welded supermartensitic stainless steel pipeline to M_f -temperature before applying external heat to it is that at temperatures above the austenite-martensite transformation temperature, the post weld heat treatment cannot effectively reduce the local hydrogen concentration in the

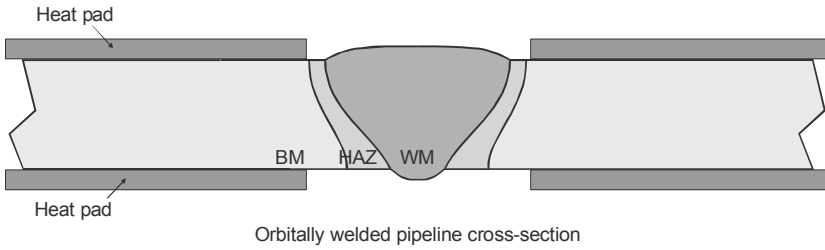


Figure 4-46: Schematic illustration of additionally applied heat on the surface of the orbitally welded supermartensitic stainless steel pipeline for post weld heat treatment.

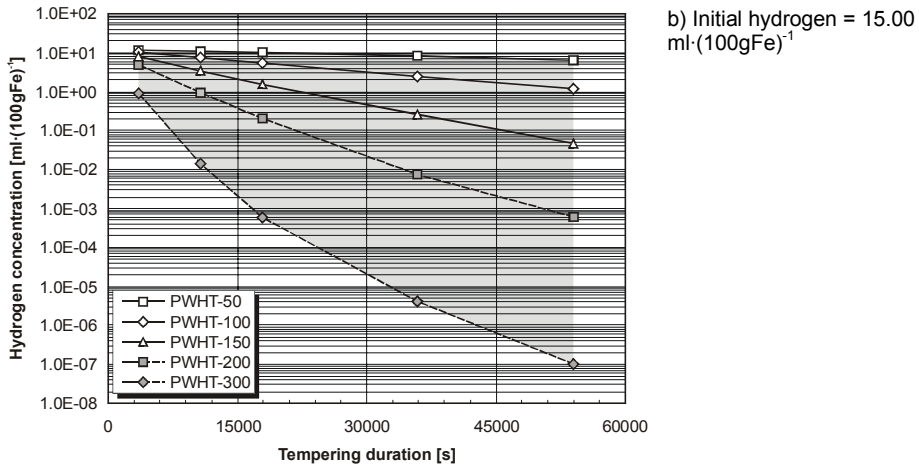
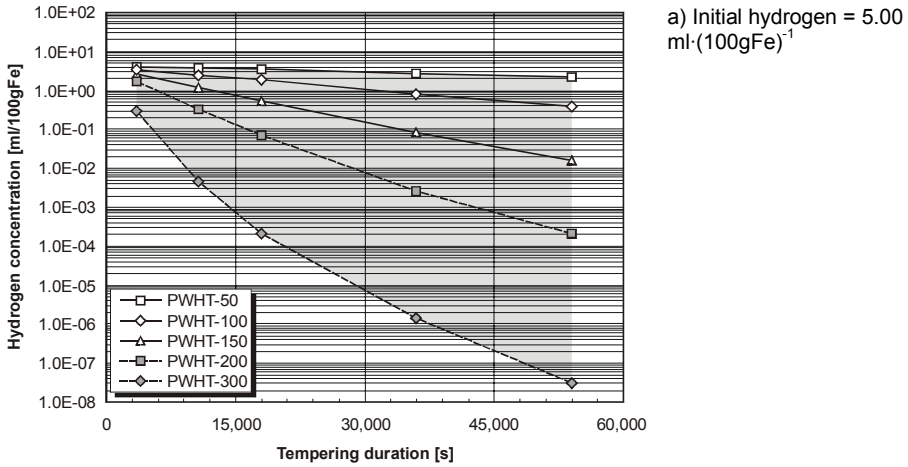


Figure 4-47: Reduction of hydrogen concentration in the weld metal dependent on the tempering duration by long-term approach taking account of the effects of hydrogen concentration picked up during welding.

4. Results and Discussion

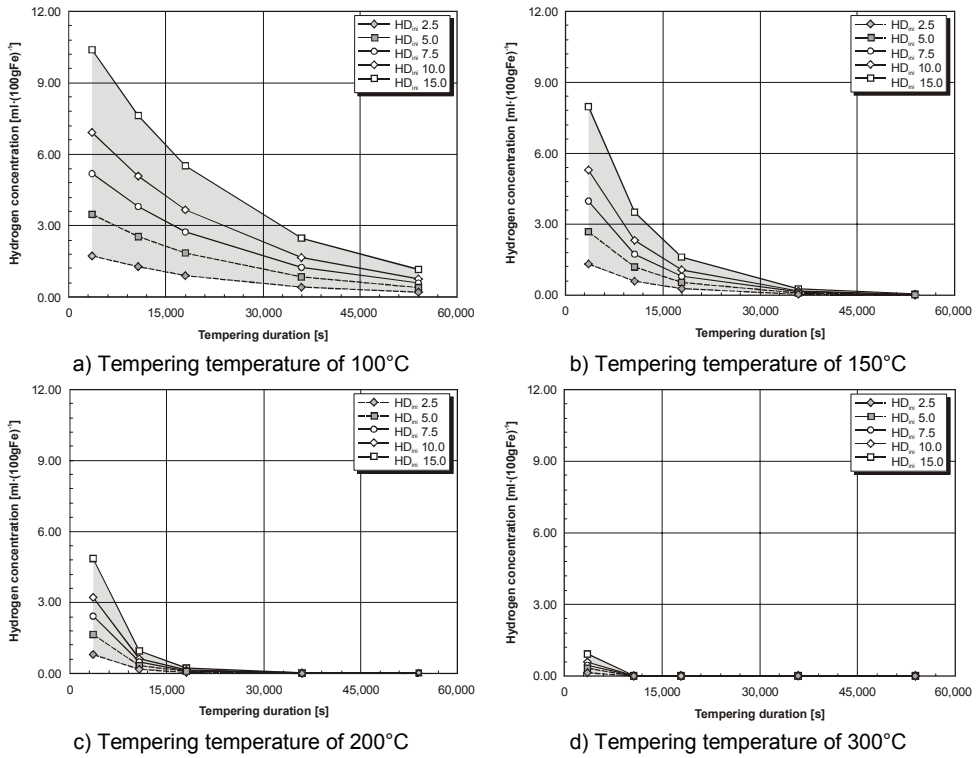


Figure 4-48: Effects of the tempering duration in the long-term approach on the reduction of weld metal hydrogen concentration with respect to various levels of hydrogen concentration picked up during welding.

weld metal and the neighbouring zone due to relatively high hydrogen solubility and relatively low hydrogen diffusion coefficient of the austenitic structure.

A heating rate of about $4\text{ }^{\circ}\text{C}\cdot\text{s}^{-1}$ is used to heat the welded pipeline component up to the various specific tempering temperature of which the holding time is varied. After removing the heat pad, the temperature of the welded component is decreased by exposure to an ambient environment. The first procedure represented a typical long-term hydrogen removal heat treatment. Various levels of relatively low temperatures, i.e. 50°C , 100°C , 150°C , 200°C , and 300°C , have been simulated for different times of up to 900 minutes. The second procedure represented a short-term post weld heat treatment at various levels of high temperatures, i.e. 500°C , 550°C , 600°C , 650°C and 700°C .

The effects of tempering temperature on the maximum local hydrogen concentration as a function of the tempering duration are represented in Figure 4-47a and Figure 4-47b for the different amounts of initial hydrogen, picked up by the weld pool during welding, of $5.00\text{ ml}\cdot(100\text{gFe})^{-1}$ and $15.00\text{ ml}\cdot(100\text{gFe})^{-1}$, respectively. It is clearly indicated that the local hydrogen concentration decreases drastically with increasing duration, if tempering at 300°C is applied. Tempering at 50°C only marginally reduces the local hydrogen concentration even with extended tempering duration. The amount of local hydrogen concentration in the welded component after tempering is obviously dependent on the initial

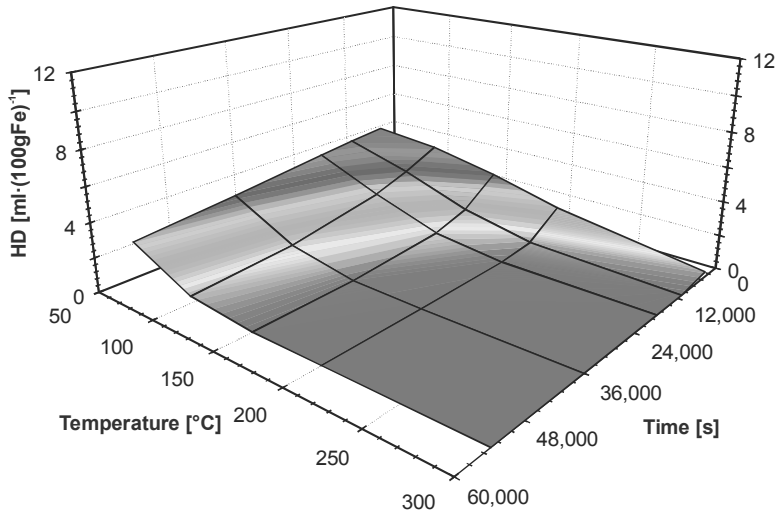
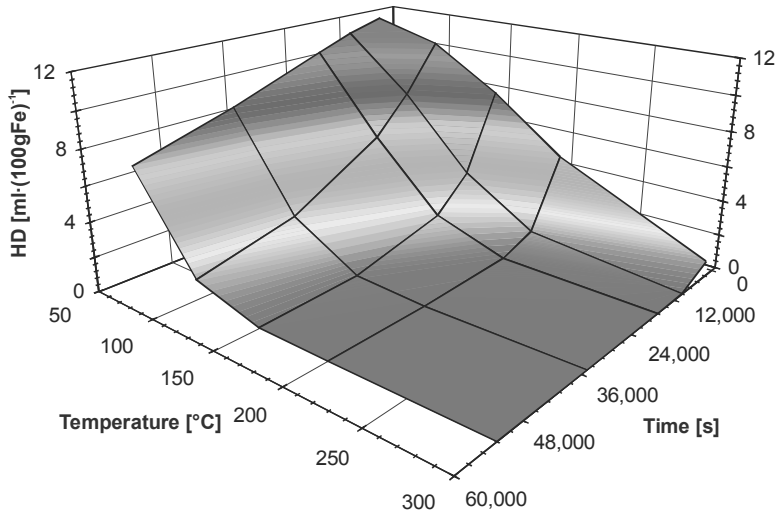
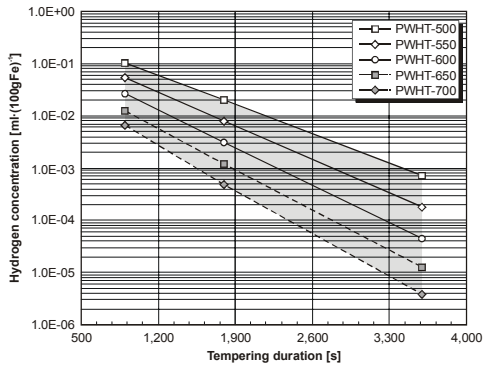
a) Initial hydrogen concentration of $5.00 \text{ ml} \cdot (100\text{gFe})^{-1}$ b) Initial hydrogen concentration of $15.0 \text{ ml} \cdot (100\text{gFe})^{-1}$.

Figure 4-49: Calculated local hydrogen concentration dependent on two major factors of post weld heat treatment by an assumption of different hydrogen concentration picked up by the weld metal during welding: a) $HD_{ini} = 5.00 \text{ ml} \cdot (100\text{gFe})^{-1}$, b) $HD_{ini} = 15.00 \text{ ml} \cdot (100\text{gFe})^{-1}$.

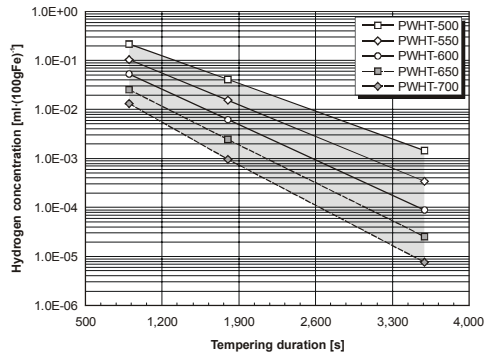
hydrogen concentration in the weld metal. Post-weld heat treatment at temperatures above 150°C applied longer than 30,000 seconds (≈ 8.4 hrs.) reduces the concentration below $1.00 \text{ ml} \cdot (100\text{gFe})^{-1}$ at initial hydrogen concentration of $15.00 \text{ ml} \cdot (100\text{gFe})^{-1}$ as represented in Figure 4-48. This means 8.4 hour is required to achieve less crack critical concentration.

However, at higher temperatures of 300°C , the local hydrogen concentration can significantly be reduced within a short tempering period. For example, after 1 hour, the local hydrogen concentration is $0.89 \text{ ml} \cdot (100\text{gFe})^{-1}$ at the initial hydrogen concentration of $15.00 \text{ ml} \cdot (100\text{gFe})^{-1}$ (Figure 4-48d). The reason for this is a significant high diffusion coefficients at temperatures above 200° .

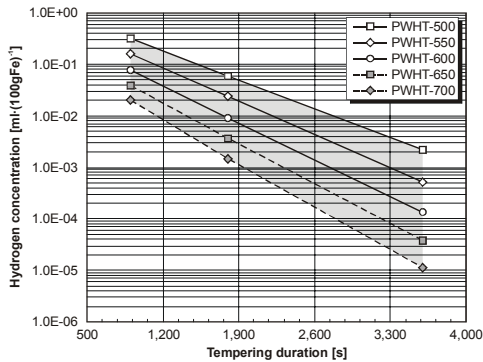
4. Results and Discussion



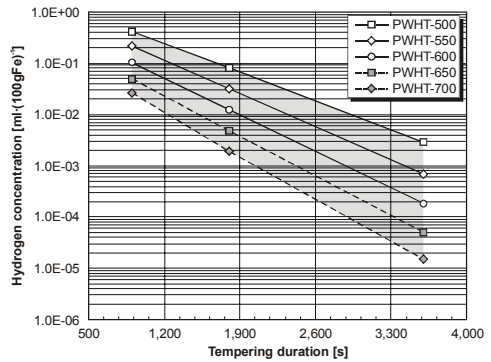
a) Initial hydrogen = 2.5 ml·(100gFe)⁻¹



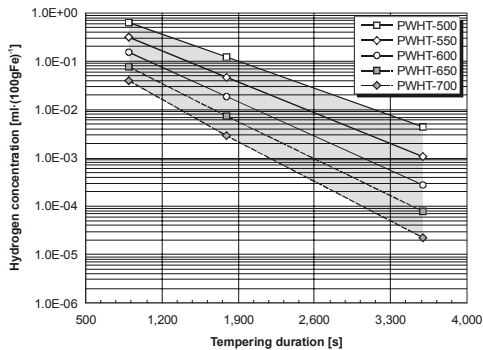
b) Initial hydrogen = 5.0 ml·(100gFe)⁻¹



c) Initial hydrogen = 7.5 ml·(100gFe)⁻¹



d) Initial hydrogen = 10.0 ml·(100gFe)⁻¹



e) Initial hydrogen = 15.0 ml·(100gFe)⁻¹

Figure 4-50: Calculated local hydrogen concentration as a function of the tempering duration for various temperature levels.

Figure 4-49a represents the heat treatment effects considering two major factors, i.e. the tempering duration and the tempering temperature, on the remaining hydrogen concentration in a 3-D diagram with the assumption of 5.00 ml·(100gFe)⁻¹ for the initial hydrogen uptake in the weld metal during welding, which is compared to Figure 4-49b with the assumption of 15.00 ml·(100gFe)⁻¹ for the initial hydrogen uptake. It is clearly shown that the reduction of the local hydrogen concentration is influenced not only by the tempering temperature and tempering duration, but also by the amount of initial hydrogen

uptake. Since the concept of fitness for purpose involving technical-economical challenges is presently taken into account, particularly in offshore technology for improving the reliability of welded pipelines with a reasonable budget, heat treatment should be performed using appropriate tempering temperature and duration based on the amount of initial hydrogen uptake. For example, a post weld heat treatment at 200°C with a tempering duration of 18,000 seconds can suitably be carried out on a welded pipeline with 15.00 ml·(100gFe)⁻¹ of hydrogen concentration picked up by the weld metal during welding, but this seems to be an exaggerated operation of heat treatment for the welded pipeline with an initial hydrogen concentration of 5.00 ml·(100gFe)⁻¹ picked by the weld metal during welding.

As proposed in previous contributions^{[SPM 27],[SPM 37],[SPM 53]}, post weld heat treatment is advantageous for hardness reduction without losing strength in supermartensitic stainless steel welds. For this, it should be carried out at elevated temperatures below the A_{C1}-temperature for supermartensitic stainless steel at a limited time in order to avoid precipitation of chromium carbide which will degrade the mechanical properties as well as the corrosion resistance of material. Therefore, the effects of significant parameters of short-term heat treatment on the remaining local hydrogen concentration have been studied by simulation with the assumption of 500°C, 550°C, 600°C, 650°C and 700°C for the tempering temperatures.

Figure 4-50 represents the calculated local hydrogen concentration as a function of the tempering duration at the end of the heat treatment process with respect to various temperatures. Increased tempering temperatures can result in a steeper slope of hydrogen concentration versus the tempering duration curve, in log-scale.

Since an increase of tempering temperatures might obviously affect the reduction of local hydrogen concentration in welds, the normalised concentration versus tempering temperature dependent on the initial hydrogen concentration is shown in Figure 4-51. This diagram is very useful to estimate local hydrogen concentrations in welds from the initial hydrogen concentration with respect to tempering temperature and duration.

The effects of the specific tempering temperature on the remaining local hydrogen concentration depending on the tempering duration for various amounts of initial hydrogen concentration picked up by the weld metal during welding are represented in Figure 4-52. Similar to the previous investigations at lower concentrations, these diagram show that the slope of the curves becomes much gentler when the initial hydrogen uptake during welding decreases and when a higher tempering temperature is applied during a longer tempering duration. This phenomenon is confirmed by Figure 4-53, which represents the calculated local hydrogen concentration remaining in the welded component as a function of the tempering temperature with consideration of different amounts of initial hydrogen concentration.

From the results of the numerical simulation, it can be proposed that a short-term post weld heat treatment of 900 seconds (15 minutes) at any temperature between 500°C and 700°C is sufficient for reducing the local hydrogen concentration remaining in sensitive regions of orbitally welded supermartensitic stainless steel pipeline to be lower than 1.00 ml·(100gFe)⁻¹. Corresponding to the practice fabrication welding, tempering at temperature of a temperature of 650°C is evidently appropriate so that the duration of 15 minutes is

4. Results and Discussion

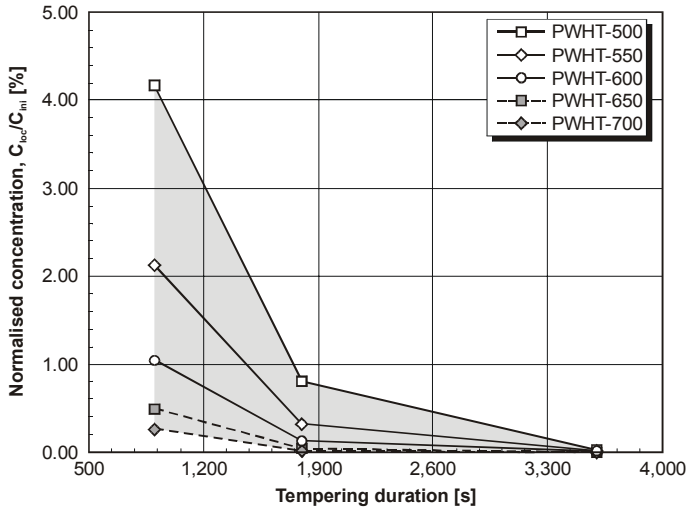


Figure 4-51: Calculation of normalised hydrogen concentrations as a function of tempering duration at various temperatures.

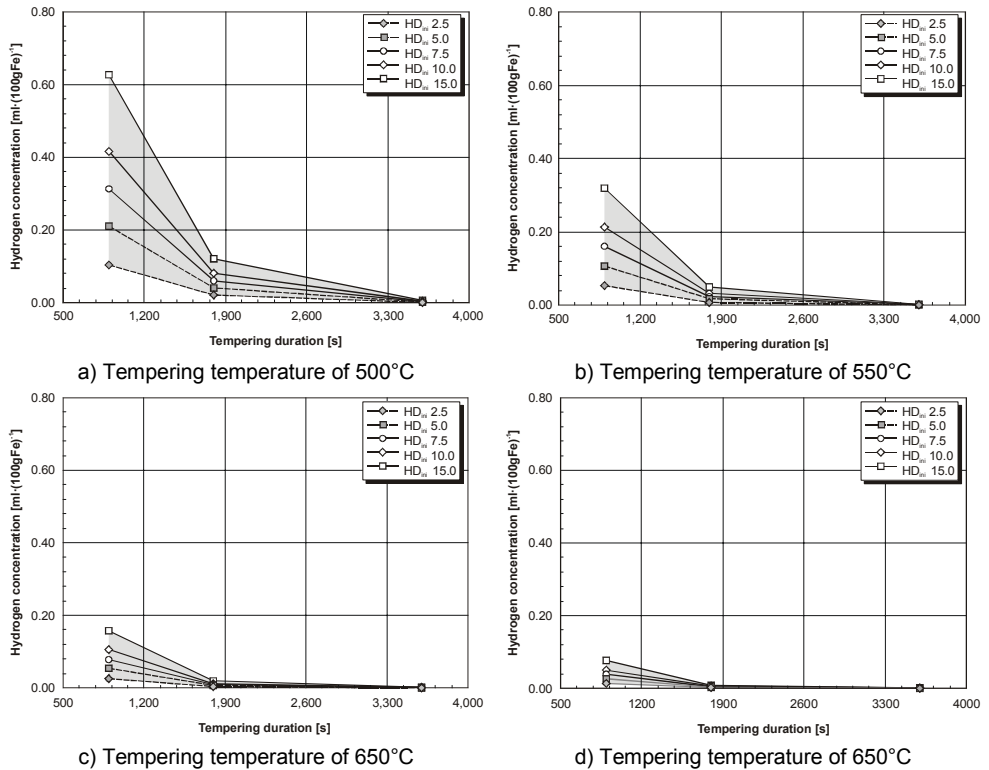


Figure 4-52: Calculated remaining hydrogen concentration at different temperature levels dependent on the tempering duration with respect to different levels of initial hydrogen concentration picked up by the weld metal during welding.

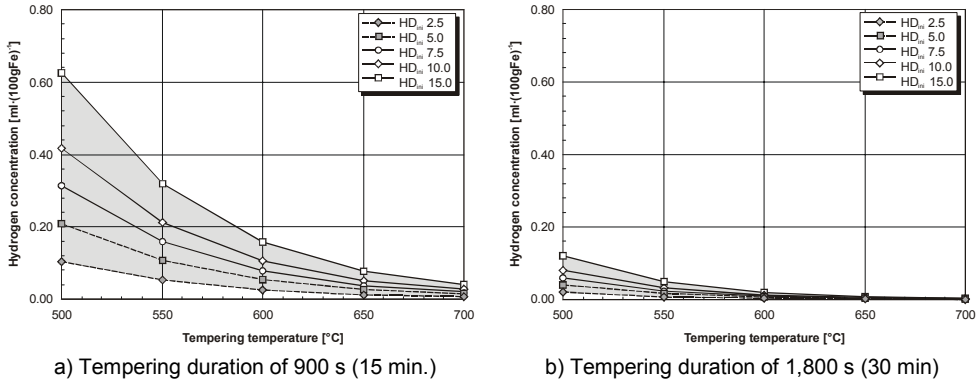


Figure 4-53: Effects of the tempering temperature for different tempering durations on the reduction of the local hydrogen concentration in the weld metal with respect to various levels of initial hydrogen concentration.

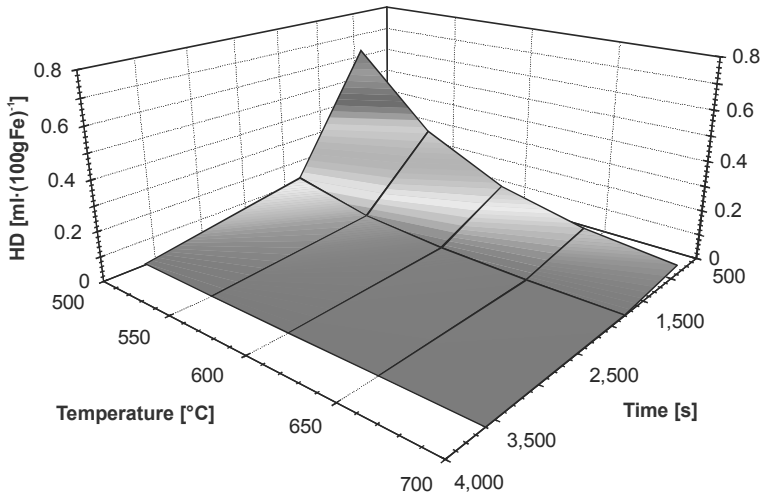


Figure 4-54: Calculation of local hydrogen concentration in the weld metal dependent on two major factors of short-term post weld heat treatment (Assumption: $HD = 15.00 \text{ ml} \cdot (100\text{gFe})^{-1}$ picked up during welding).

recommended for avoidance of hydrogen assisted cracking in the supermartensitic stainless steel pipeline.

Figure 4-54 shows the decrease of the local hydrogen concentration in the weld metal of the orbitally welded pipeline dependent on two significant parameters of short-term post heat treatment with both the tempering duration and the tempering temperature. This is in good correlation with practical supermartensitic stainless steel flowline manufacturing processes in which the short-term heat treatment, i.e. tempering temperatures in the range of 600 to 650°C (below A_{c1} -temperature) and tempering durations in the range of 5 to 20 minutes^{[SPM 53]-[SPM 55]}, is used to improve the resistance of welded components against hydrogen assisted cold cracking by focusing on a decrease of remaining local hydrogen concentration in sensitive regions without losses in material strength.

4. Results and Discussion

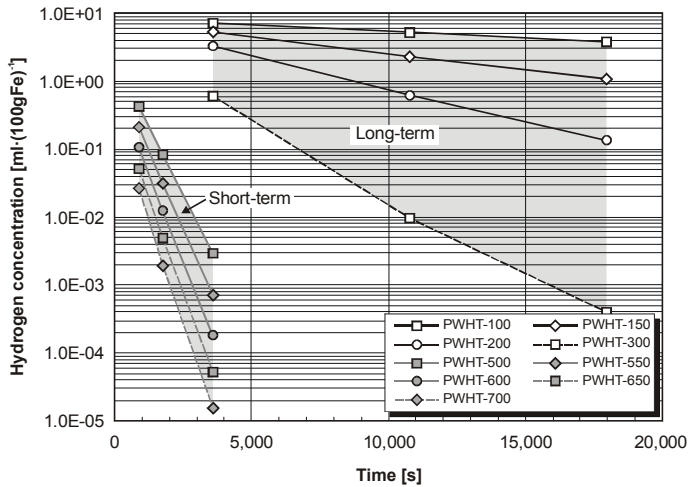


Figure 4-55: Effects of the long-term approach on the reduction of local hydrogen concentration in comparison with the short-term approach (Assumption: hydrogen concentration of $10 \text{ ml} \cdot (100\text{gFe})^{-1}$ picked up by the weld metal during welding).

In the face of today's economical-technical challenges, the short-term heat treatment should be considered as an alternative way to avoid serious failure of assembled flowlines during reeling/pipelaying process.

From the comparison shown in Figure 4-55, it can be suggested that the short-term approach is more appropriate for removing the local hydrogen concentration from zones susceptible to hydrogen assisted cold cracking than long-term soaking procedures. This means that much operation time for the post-weld heat treatment can be saved by the short-term approach. Additionally, the metallurgical behaviour of the welded pipeline is not affected by the short-term approach. This, for instance, can also not be assured for the long-term application due to the high nickel content of supermartensitic stainless steel.

However, further experimental research is still required to verify the metallurgical behaviour of the new generation of supermartensitic stainless steel experiencing specific welding fabrication and subsequent post-weld heat treatment.

4.4 Modelling of HASCC in the Welded Component Having a Pre-Crack Caused by HACC

Orbitally welded pipelines are generally installed within a several hours after complete welding fabrication as subsea flowlines transporting oil and gas products. Hence, interactions between the local hydrogen concentration, remaining in the weld metal and its neighbouring zones, and possible further hydrogen introduced at the interior surface of welded pipeline during exposure to electrolytic solution in sour service have to be investigated to avoid cracking of such welded components. The study of the cracking process involving the two different hydrogen sources can be carried out by adopting and connecting above described finite element simulations.

In the simulation illustrated in Figure 4-56, an pipeline orbitally welded with the assumption of $10.00 \text{ ml} \cdot (100\text{gFe})^{-1}$ for the initial hydrogen uptake during welding has been

4. Results and Discussion

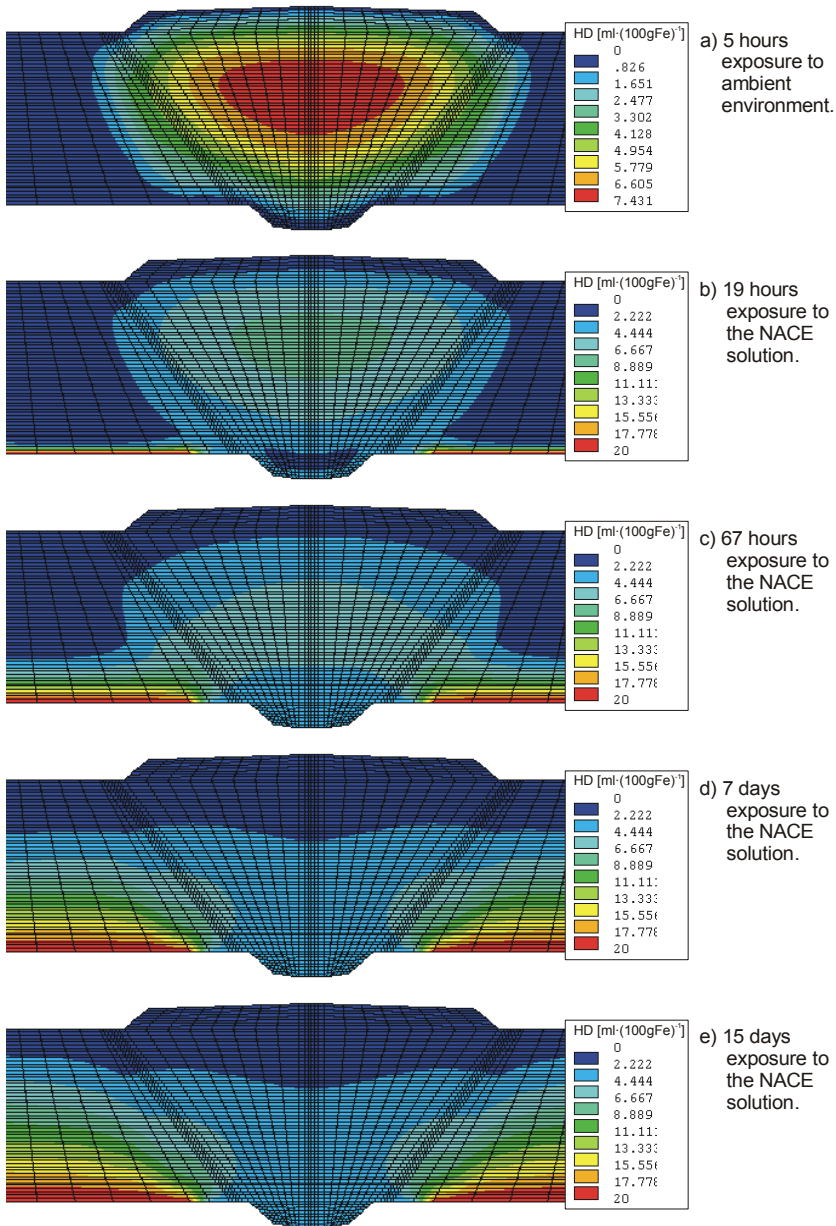


Figure 4-56: Simulation of hydrogen distribution in the orbitally welded supermartensitic stainless steel pipeline exposed to NACE electrolytic solution with 1% H₂S saturation after complete welding and subsequent cooling to room temperature with additionally extended time of 5 hours in ambient environments (Assumption: HD = 10.00 ml·(100gFe)⁻¹ picked up during welding).

4. Results and Discussion

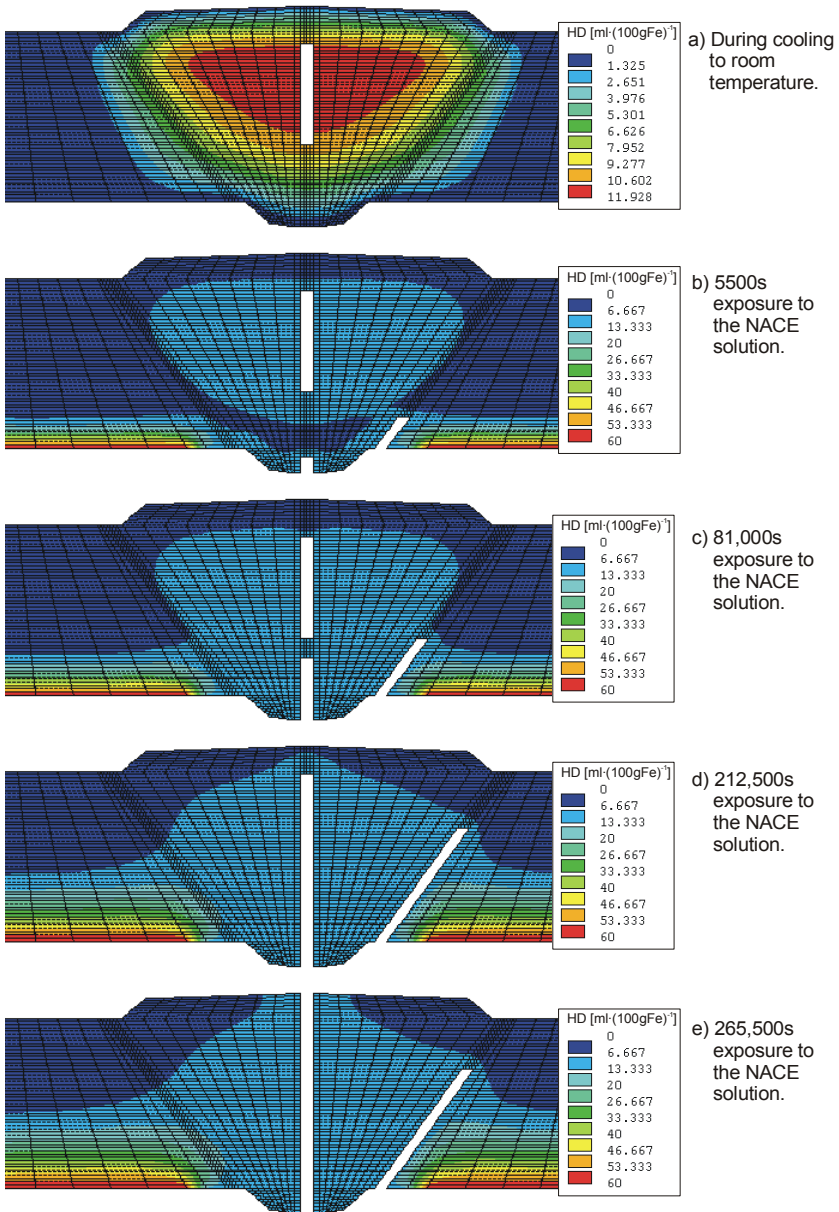


Figure 4-57: Simulation of the influence of hydrogen assisted cold cracking on the lifetime of orbitally welded supermartensitic stainless steel pipeline during exposure to NACE standard solution with 100% H_2S saturation for hydrogen assisted stress corrosion cracking.

exposed to ambient environments for 5 hours prior to the application of hydrogen subsurface concentrations of $20.00 \text{ ml}\cdot(100\text{gFe})^{-1}$ for the base metal and of $3.15 \text{ ml}\cdot(100\text{gFe})^{-1}$ for the heat affected zone and the weld metal at the interior surface of the welded pipeline simulating an exposure to the NACE electrolytic solution with 1% H_2S saturation. At the same time, hydrogen is assumed to be completely desorbed at the exterior surface of the welded pipeline, i.e. a hydrogen subsurface concentration of $0 \text{ ml}\cdot(100\text{gFe})^{-1}$ has been applied to the nodes at that surface.

With increasing time during such process, the remaining local hydrogen concentration from fabrication welding decreases by the effusion reaction at the exterior surface, even though the hydrogen subsurface concentration at the interior surface concurrently diffuses through the material. This means that newly entering hydrogen from the interior surface does not interact with the remaining local hydrogen concentration too much. For example, a maximum hydrogen concentration of $7.43 \text{ ml}\cdot(100\text{gFe})^{-1}$ remaining in the weld metal of the welded component before being exposed to the NACE electrolytic solution decreases to $6.66 \text{ ml}\cdot(100\text{gFe})^{-1}$ within 67 hours. With further exposure for 15 days, the effect of weld metal hydrogen diminishes, for example. It can also be stated that depending on the subsurface concentration, the hydrogen introduced by the electrolytic solution can exert a stronger influence on hydrogen assisted stress corrosion cracking in the orbitally welded pipeline than the hydrogen taken up during welding.

Considering the application case, the welded pipeline will be subjected to additional slow strain rates during service. This means that at the same time, the welded pipeline is continuously displaced, which usually causes a higher increase in stress-strain intensity in the heat affected zone due to the smaller cross-sectional area than in the weld metal. Therefore, the theory can be proposed that hydrogen assisted stress corrosion cracking favourably takes place in the heat affected zone so that the life time of the welded pipeline is dependent on the kinetics of crack propagation in the heat affected zone. However, in the case where hydrogen assisted cold cracking previously occurred in the weld metal, the life time of the weld pipeline controlled by the kinetics of crack propagation in the heat affected zone might be changed to be controlled by that of the weld metal. In order to investigate such interactions of HASCC and HACC, finite element simulations had been carried out at additional straining.

Figure 4-57 shows the respective hydrogen concentration profile and the crack propagation for such a component precracked by hydrogen assisted cold cracking due to a initial hydrogen concentration of $15 \text{ ml}\cdot(100\text{gFe})^{-1}$ in the weld metal and subsequently exposed to a totally H_2S saturated NACE solution. Globally applied loads are not taken into account for this numerical simulation. This implies that only the residual strain introduced during welding fabrication is first the kinetics of crack propagation takes account for only the residual strain for the mechanical factor.

During the exposure to the NACE electrolytic solution, crack propagation takes place on the predefined cracking paths in both sensitive regions, i.e. in the weld metal and the heat affected zone, due to high hydrogen concentration provided by the electrolytic solution as well as to high strain resulting from thermal cycle effects. As can be seen from Figure 4-57, during the first period, the crack progresses in the heat affected zone at a faster rate than in the weld metal because the higher base metal hydrogen subsurface concentration provides

4. Results and Discussion

more hydrogen to the region ahead of the crack tip in the heat affected zone which reaches the critical value within less time than the weld metal. The higher hydrogen concentration from the base metal will reduce its influence on increasing the crack propagation rate in the heat affected zone when the crack length becomes sufficiently long. Crack propagation in the weld metal increases after the crack front reaches into regions with relatively high strain and hydrogen concentration due to welding, which cause to decrease the critical hydrogen concentration required for the crack propagation. But, it has to be considered that the local hydrogen concentration ahead of the crack tip in the weld metal is still more strongly provided by hydrogen taken up from the NACE electrolytic solution than by the remaining local hydrogen concentration picked up by the weld metal during fabrication welding.

However from carefully studying the concentration profiles decreasing with time, it can be seen that this process takes 83,500 seconds (23.2 hours) after the orbitally welded pipeline is exposed to the electrolytic solution. The new entry hydrogen interacts with the remaining local hydrogen concentration. Since the remaining local hydrogen concentration does not have a large influence compared with hydrogen coming from the subsurface inside the propagation crack, it takes a while until the two cracks in the weld metal are conjuncted (110,000 seconds).

Finally, the crack propagating in the weld metal passes through the cross-section causing the rupture of the orbitally welded pipeline, and a time to failure of 265,500 seconds (\approx 74 hours) is obtained.

However, two characteristic features can be drawn from such simulations:

- 1) The weld metal hydrogen concentration does not much contribute to the cracking velocity within the first period.
- 2) Hydrogen assisted stress corrosion cracking in the heat affected zone is shifted towards the weld metal by precracking as a consequence of hydrogen assisted cold cracking.

5 CONCLUSIONS AND PERSPECTIVES

5.1 Conclusions

The present thesis deals with the development of numerical finite element simulation based on the available commercial finite element program for a better understanding of the phenomenon of hydrogen assisted cracking (HAC) in terms of hydrogen assisted stress corrosion cracking (HASCC) and hydrogen assisted cold cracking (HACC) focusing on girth welds of supermartensitic stainless steel pipeline. Firstly, the prediction of the time to failure has been calculated for hydrogen assisted stress corrosion cracking in a standard test specimen based on the NACE-0177-96 standard approach in order to provide basic knowledge for the advanced step. Secondly, a basic numerical approach from the standard test specimen has been developed for predicting the time to failure in the orbitally welded pipeline exposed to the NACE electrolytic solution with various levels of H₂S saturation. Two kinds of the global loading conditions, i.e. a series of constant strain rate tests and load histories of the large scale test, have been taken account for the numerical simulation. Thirdly, hydrogen assisted cold cracking in the supermartensitic stainless steel pipeline orbitally welded with using four layers of matching filler material has been simulated considering three significant analyses: I) the thermal analysis, II) the structural analysis and III) the hydrogen distribution analysis. Finally, the simulation of hydrogen assisted stress corrosion cracking in the orbitally weld pipeline has been carried out with introduction of residual strain distributions and the presence of a weld metal crack, resulting from hydrogen assisted cold cracking, in order to describe the influence of the dominant crack propagation, shifting from the heat affected zone to the weld metal, on the time to failure of the orbitally welded supermartensitic stainless steel pipeline exposed to the NACE electrolytic solution derived from sour service in offshore technology.

Thus, significant conclusions from numerical simulation in the present thesis can be drawn as follows:

- **Hydrogen assisted stress corrosion cracking based on the NACE-TM 0177-96 standard test**
 - I) The time to failure of the standard test specimen is decreased with increasing hydrogen subsurface concentration, global strain rate and local strain rate, but this can only be achieved when the specimen does not fail by mechanical overload.
 - II) Stable crack propagation caused by hydrogen assisted stress corrosion cracking plays a significant role in controlling the time to failure of as-delivered material when appropriate interaction between local hydrogen concentration and local strain takes place. In this period, effects of various hydrogen subsurface concentrations on the time to specimen failure are obviously remarkable.
 - III) The incubation period will dominate the time to failure of the material instead of the period of stable crack propagation if the local strain rate in the specific zone ahead of the crack tip becomes lower than $1.0E-07 \text{ s}^{-1}$. Consequently, crack propagation is characterised by saturated hydrogen assisted stress corrosion cracking due to

5. Conclusions and Perspectives

longer times for depth hydrogen transport from the subsurface to regions in the matrix material.

- IV) Based on the broad scatterband of the hydrogen diffusion coefficients, various hydrogen diffusion coefficients markedly affect the time to failure of the material. This results from a change in the period of stable crack propagation rather than from the incubation period. But, at specific local strain rates above $1.0E-04 \text{ s}^{-1}$, the various hydrogen diffusion coefficients cannot clearly influence the time to failure and the crack propagation behaviour.
 - V) The crack growth rate of the as-quenched supermartensitic stainless steel is higher than the as-delivered one because of differences in hydrogen diffusion behaviour and failure criteria. But, at relatively high levels of local strain rate such as above $5.0E-04 \text{ s}^{-1}$, there is a small difference in the time to failure and the crack propagation behaviour between the delivered state and the quenched state due to the predominant effect of mechanical overload.
 - VI) The sharp crack angle, 74° , can significantly reduce the time to failure of the material if the period of the stable crack propagation controls the time to specimen failure.
 - VII) Increasing newly cracked area, directly exposed to the NACE solution, in front of the crack, for example a crack tip angle of 74° , allows more hydrogen diffusing in the susceptible zone ahead of the crack tip in comparison with a crack tip angle of 180° .
- **Hydrogen assisted stress corrosion cracking in the orbitally welded supermartensitic stainless steel pipe**
- VIII) The results of respective component tests have shown that the heat affected zone represents the most crack-susceptible region in supermartensitic stainless steel pipeline orbitally welded with matching filler material. Moreover, it has clearly been demonstrated that high hydrogen concentrations diffusing from the base metal into the heat affected zone are the reason for preferential cracking in such regions.
 - IX) Increasing H_2S saturation of the environment significantly reduces the time to failure of welded supermartensitic stainless steel pipes by higher hydrogen subsurface concentrations, and consequently by reaching more rapidly critical limits for crack initiation and propagation in the heat affected zone.
 - X) The numerical simulations of a welded pipe component confirmed the results of respective experiments. Modelling of small scale specimens using constant strain rates above $1.0E-05 \text{ s}^{-1}$ are not recommendable for detecting any hydrogen effects in supermartensitic stainless steels. Slower strain rates provide times of exposure to sour environments, and consequently the ductility of the weld microstructures is decreased by respective hydrogen uptake and diffusion into crack critical regions. Again, only strain rates of and below $1.0E-06 \text{ s}^{-1}$ will show the total degradation of material by hydrogen.
 - XI) As confirmed by numerical modelling, the fracture mode in the heat affected zone is significantly dependent on the local hydrogen concentration. Intergranular cracking

occurs at high hydrogen concentrations, which are particularly provided at the beginning of cracking by long-term exposure to sour environments. With decreasing hydrogen concentration, the fracture mode transforms into transgranular cleavage-like cracking and finally to micro-void coalescence at very low hydrogen levels, respectively.

- **Hydrogen assisted cold cracking in the orbitally welded supermartensitic stainless steel pipeline**
- XII) Temperature distribution analysis is the first significant task involved in numerical modelling of hydrogen assisted cold cracking, of which the results are used as reference values for further simulations in the structural analysis and the hydrogen distribution analysis. There is evidently good agreement between experimental investigation and numerical modelling for the temperature distribution.
- XIII) Relatively high levels of stress-strain distribution are always present in the weld metal and the heat affected zone due to extreme temperature gradients during welding and subsequent cooling. Moreover, thermal cycle effects resulting from multi-run welding significantly influence the behaviour of stress-strain distribution in orbitally welded pipelines, as well.
- XIV) Diffusion and effusion reactions play a significant role in reducing the local hydrogen concentration in the weld metal, but they are dependent on the hydrogen concentration gradient and on the hydrogen diffusion coefficients. Hence, a reduction of the local hydrogen concentration indicates a steep incline in the early period of cooling due to increased diffusion coefficients with temperatures.
- XV) During welding the further pass, local hydrogen concentrations in the previously welded layer can be either decreased or increased dependent on the distance from the recent hydrogen source. This means that the local hydrogen concentration at the specific point in a previously welded layer nearly the upper welding layer can be increased by the recent hydrogen uptake, whereas the hydrogen concentration at a specific point far away from the upper layer hydrogen concentration is decreased due to more hydrogen loss, caused by relatively high hydrogen diffusion coefficients during welding and cooling, and insufficient hydrogen diffusing from a new source.
- XVI) In girth welds of supermartensitic stainless steel pipeline, cracks resulting from hydrogen degrading material properties can be avoided by controlling the hydrogen uptake during welding to be lower than $10.00 \text{ ml} \cdot (100\text{gFe})^{-1}$. In the case that a hydrogen concentration of around $15.00 \text{ ml} \cdot (100\text{gFe})^{-1}$ is taken up by the weld metal during welding, a crack initiated in the weld metal during cooling down to ambient temperature at a maximum remaining local hydrogen concentration of $11.93 \text{ ml} \cdot (100\text{gFe})^{-1}$. This crack initiation appears at a position with a relatively high hydrogen concentration even at relatively low strain levels.
- XVII) In order to avoid hydrogen assisted cold cracking, post weld heat treatment can be applied to lower the local hydrogen concentration remaining in susceptible regions, but this might also result in a reduction of mechanical strength which would

5. Conclusions and Perspectives

counteract the deliberate use of matching filler material for orbital welding of supermartensitic stainless steel pipeline. Therefore, the short-term approach of post-weld heat treatment, i.e. the temperature range between 600°C and 650°C with a tempering duration of 5 to minutes, is regarded as sufficient to reduce the local hydrogen concentration according to the fitness for purpose concept.

XVIII) The significant factor to control the lifetime of the welded pipe, as concerns hydrogen assisted stress corrosion cracking, under exposure to the NACE electrolytic solution with H₂S saturation is the kinetics of crack propagation in the heat affected zone due to a higher subsurface concentration of hydrogen diffusing from the base metal to the susceptible region ahead of the crack tip in the heat affected zone. But, crack propagation in the weld metal can dominate the time to failure of the welded pipe over that in the heat affected zone by the presence of a precrack in the weld metal caused by hydrogen assisted cold cracking during fabrication welding.

The present research demonstrates that the numerical modelling is a most helpful tool for providing a better understanding of the failure sequences of hydrogen assisted cracking and for verifying the component lifetime affected by both hydrogen assisted stress corrosion cracking and hydrogen assisted cold cracking. However, further development of numerical modelling for studying the crack propagation behaviour taking account of the stagnant state of the electrolytic solution in the crack and without using predefined cracking paths is recently required. For hydrogen assisted cold cracking, experimental investigation of the effects of duplex microstructure in the weld metal and heat affected zone of supermartensitic stainless steel should be carried out in order to receive precise data for numerical modelling, since retained austenite can cause hydrogen assisted cold cracking if it transforms into martensite with low hydrogen solubility during the spooling/pipelaying process of orbitally welded supermartensitic stainless steel pipeline.

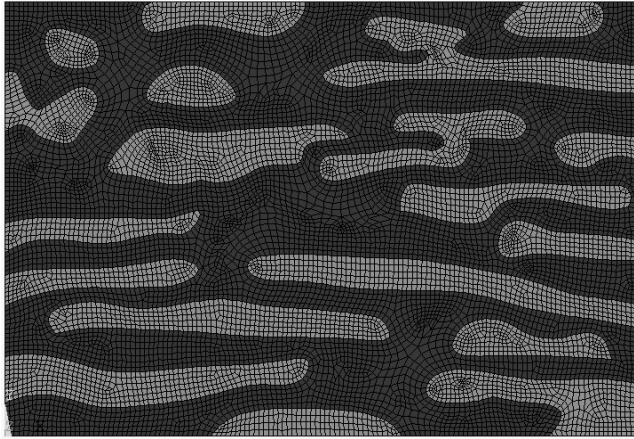
5.2 Perspectives

Since lean duplex stainless steel has been developed as a new alternative to the supermartensitic stainless steel for oil and gas applications to meet economical-technical challenges, more investigations on material corrosion resistance, particularly on hydrogen assisted stress corrosion cracking, must be carried out to get a better understanding of cracking characteristics and to subsequently avoid catastrophic failure of components during service^[GEN 38]. Table 5-1 lists the chemical compositions of three significant duplex stainless steels.

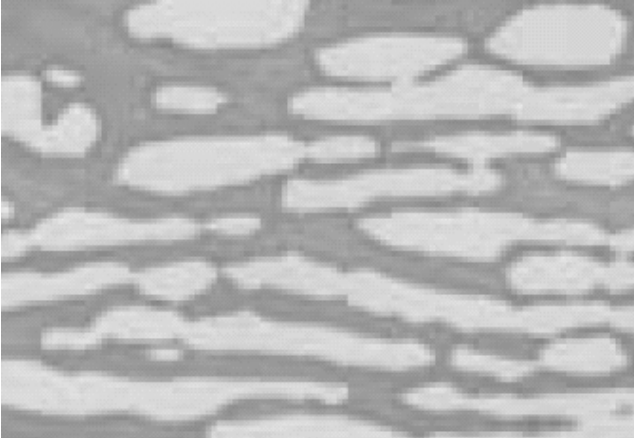
In fact, local phenomena of crack initiation and propagation in duplex stainless steels caused by hydrogen are still difficult to be observed in conventional experiments. Therefore, finite element simulations taking account of basically necessary data obtained from the experimental investigations can conveniently be used to gain an insight into such local phenomena. Figure 5-1a shows a finite element model having austenitic and ferritic microstructures in consistence with the microstructure of duplex stainless steel (Figure 5-1b). Adaptive meshing techniques are adopted in such a model for obtaining more real hydrogen assisted crack growth simulation, which can be oriented in any directions dependent on local interactions.

Table 5-1: Chemical composition of duplex stainless steels.

AISI Designation	Composition [wt.-%]								
	C	Cr	Ni	Mn	Mo	Si	Cu	N	P+S
S32304 Lean	0.03	21.40 - 24.50	3.00 - 5.50	2.50	0.05	1.00	0.05 - 0.60	0.05- 0.20	0.07
S32205 Conventional	0.03	22.00 - 23.00	4.50 - 6.50	2.00	3.00 - 3.50	1.00	-	0.14- 0.20	0.06
S32750 Super	0.03	24.00 - 26.00	6.00 - 8.00	1.20	3.00 - 5.00	0.80	0.50	0.24- 0.32	0.06



a) FE Model



b) Duplex microstructure

Figure 5-1: Development of a FE model for modelling hydrogen assisted cracking in a latest generation of duplex stainless steels.

5. Conclusions and Perspectives

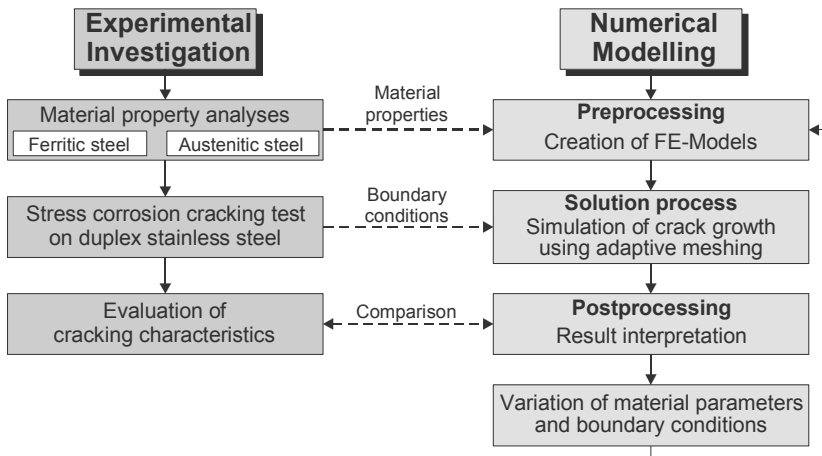


Figure 5-2: Sequences of numerical modelling of hydrogen assisted cracking in duplex stainless steel compared with experimental investigation.

The flowchart of numerical modelling of hydrogen assisted cracking in duplex stainless steel compared with experimental investigation is represented in Figure 5-2. Since the duplex stainless steel is composed of austenite and ferrite, material property analyses, including hydrogen diffusion behaviour and mechanical properties, on ferritic and austenitic steels must be performed in order to provide necessary material data for the finite element model in preprocessing. In the solution process, the simulation of crack growth using adaptive meshing is carried out based on boundary conditions of experimental investigation. Subsequently, calculated results of numerical modelling have to be interpreted and compared with those obtained from experimental investigation. Due to the fact that the finite element method is a more economic approach than the experimental investigation, the variation of material parameters and boundary conditions can be studied more conveniently with numerical modelling in order to gain an insight into the crack growth mechanisms in duplex stainless steel.

REFERENCES

I. General (GEN)

- [GEN 1] F.Häfner, D.Sames and H.-D.Voigt: "*Wärme-und Stofftransport*", Springer-Lehrbuch, ISBN 3-540-54665-0, Ed. 1, Berlin, 1992.
- [GEN 2] A.R.Mitchell and R.Wait: "*The Finite Element Method in Partial Differential Equations*", John Wiley & Sons, ISBN 0-471-99405-7, Ed. 2, London, 1977.
- [GEN 3] C.A.Wert and R.M.Thomson: "*Physics of Solids*", McGraw-Hill Book Company, Ed. 2, New York, 1970.
- [GEN 4] D.Radaj: "*Eigenspannungen und Verzug beim Schweißen*", DVS-Verlag, ISBN 3-87155-194-5, Ed. 1, Düsseldorf, 2002.
- [GEN 5] A.R.Troiano: "*Hydrogen Embrittlement and Stress Corrosion Cracking*", American Society for Metals, ISBN 0-87170-185-5, Ed. 5, 1995.
- [GEN 6] D.Kuron: "*Wasserstoff und Korrosion*", Verlag Irene Kuron, ISBN 3-923623-03-8, Ed. 1, Bonn, 1986.
- [GEN 7] L.Collatz: "*The Numerical Treatment of Differential Equations*", Springer-Verlag, Ed. 3, Berlin, 1966.
- [GEN 8] D.McLean: "*Grain Boundaries in Metals*", Oxford University Press, Ed.1, Glasgow, 1957.
- [GEN 9] J.W.Harris and H.Stocker: "*Handbook of Mathematics and Computational Science*", Springer-Verlag, ISBN 0-387-94746-9, Ed. 1, Berlin, 1998.
- [GEN 10] P.Lacombe, B.Baroux and G.Beranger: "*Stainless Steels*", Les Editions de Physique, ISBN 2-86883-189-3, Ed.1, Les Ulis Cedex, 1993.
- [GEN 11] W.D.Robertson: "*Stress Corrosion Cracking and Embrittlement*", John Wiley & Sons, Inc., ISBN 56-12579, Ed.1, New York, 1956.
- [GEN 12] J.H.G.Monypenny: "*Stainless Iron and Steel*", Chapman & Hall Ltd. Ed.3, London, 1954.
- [GEN 13] J.R.Davis: "*ASM Speciality Handbook-Stainless Steels*", ASM International, ISBN 0-87170-503-6, Ed. 2, 1996.
- [GEN 14] G.-E.Dieter: "*Mechanical Metallurgy*", McGraw-Hill, ISBN 0-07-084187-X, SI-Unit Ed.1, London, 1988.
- [GEN 15] M.-G.Fontana: "*Corrosion Engineering*", McGraw-Hill, ISBN 0-07-021463-8, International Ed.3, New York, 1986.
- [GEN 16] J.F.Lancaster: "*Metallurgy of Welding*", Chapman & Hall, ISBN 0-412-47810-2, Ed.5, London, 1993.
- [GEN 17] F.R.Coe: "*Welding Steels without Hydrogen Cracking*", The Welding Institute, Cambridge, 1973.
- [GEN 18] Th.Boellinghaus: "*Zur Bestimmung risskritischer Schrumpfbinderungen und Wasserstoffverteilungen in Schweissverbindungen durch numerische Simulation*", Dissertation, Hamburg, 1995.

References

- [GEN 19] Th.Boellinghaus: *“Wasserstoffunterstützte Schäden in metallischen Strukturwerkstoffen”*, Habilitation, Hamburg, 1999.
- [GEN 20] Th.Kannengießer: *“Untersuchungen zur Entstehung schweißbedingter Spannungen und Verformungen bei variablen Einspannbedingungen im Bauteilschweißversuch”*, ISBN 3-8265-8008-7, Shaker Verlag, Aachen, 2000.
- [GEN 21] D.Broek: *“Elementary Engineering Fracture Mechanics”*, Martinus Nijhoff Publishers, ISBN 90-247-2580-1, Ed.3, Dordrecht, 1984.
- [GEN 22] A.H.Cottrell: *“Dislocations and Plastic Flow in Crystals”*, Oxford University Press, Oxford, 1953.
- [GEN 23] J.Crank: *“The Mathematics of Diffusion”*, Oxford University Press, ISBN 0-19-853344-6, Oxford, 1975.
- [GEN 24] E.Folkhard: *“Metallurgie der Schweißung nichtrostender Stähle”*, Springer-Verlag, ISBN 3-211-81803-0, Wien, 1984.
- [GEN 25] I.M.Bernstein: *“Handbook of Stainless Steels”*, McGraw-Hill, ISBN 0-07-049147-x, New York,
- [GEN 26] H.S.Carlsaw and J.C.Jaeger: *“Conduction of Heat in Solids”*, Oxford University Press, Ed.2, Oxford, 1959.
- [GEN 27] D.N.Croft: *“Heat Treatment of Welded Steel Structures”*, Abington Publishing, ISBN 1-85573-016-2, Cambridge, 1996.
- [GEN 28] M.Smialowski: *“Hydrogen in Steel”*, Pergamon Press, Oxford, 1962.
- [GEN 29] P.G.Shewmon: *“Diffusion in Solids”*, McGraw-Hill, New York, 1963.
- [GEN 30] A.S.Tetelman and A.J.McEvily: *“Bruchverhalten technischer Werkstoffe“*, Verlag Stahleisen, Düsseldorf, 1971.
- [GEN 31] F.Richter: *“Die wichtigsten physikalischen Eigenschaften von 52 Eisenwerkstoffen“*, Heft 8, Verlag Stahleisen M. B. H., Düsseldorf, 1973.
- [GEN 32] H.W.King: *“Structure of the Pure Metals”*, Physical Metallurgy, R.W.Cahn (Ed.), North-Holland Publishing Company, Amsterdam, 1965.
- [GEN 33] J.F.Lancaster: *“The Physics of Welding”*, Pergamon Press, ISBN 0-08-030555-5, Oxford, 1984.
- [GEN 34] Ansys User’s Manual, Theory Reference for Ansys 6.0.
- [GEN 35] NACE Standard TM0177-96: Laboratory Testing of Material for Resistance to Sulfide Stress Cracking in H₂S Environments.
- [GEN 36] EN ISO 17642-2:2000: Destructives Tests on Welds in Metallic Materials-Cold Cracking Tests for Weldments – Part 2: Self-Restraint Tests.
- [GEN 37] EN ISO 17642-3:2000. Destructives Tests on Welds in Metallic Materials-Cold Cracking Tests for Weldments – Part 2: Externally Loaded Tests.
- [GEN 38] L.Coudreuse, V.Ligier, J.P.Audouard and P.Soullignac: *Lean Duplex Stainless Steel for Oil and Gas Applications“*,Corrosion2003, Paper No.03529, (Houston, TX: NACE International, 2003).
- [GEN 39] ISO 3690:2000: Welding and Allied Process – Determination of Hydrogen Content in Ferrite Arc Weld Metal

- [GEN 40] Verein Deutscher Eisenhüttenleute: "Werkstoffkunde Stahl; Band1", Springer-Verlag, Berlin, ISBN 3-540-12619-8, 1984.

II. Literature for hydrogen assisted stress corrosion cracking (HAS)

- [HAS 1] G.E.Kerns, M.T.Wang and R.W.Staehle: "Stress Corrosion Cracking and Hydrogen Embrittlement in High Strength Steels", ASM-Corrosion, pp.700-735.
- [HAS 2] R.P.Weil and G.W.Simmons: "Environment Enhanced Fatigue Crack Growth in High-Strength Steels", ASM-Corrosion, pp.751-765.
- [HAS 3] R.A.Oriani: "A Decohesion Theory for Hydrogen-Induced Crack Propagation", ASM-Corrosion, pp.351-358.
- [HAS 4] W.A.Tiller: "Thermodynamic-Kinetic Model of Stress Corrosion Cracking", ASM-Corrosion, pp.332-350.
- [HAS 5] J.J.Gilman: "The Role of Surface Hydrides in Stress-Corrosion Cracking", ASM-Corrosion, pp.326-331.
- [HAS 6] A.P.Miodownik: "The Interaction of Hydrogen with Dislocations, Stacking Faults, and Other Interfaces", ASM-Corrosion, pp.272-285.
- [HAS 7] E.N.Pugh: "A Post Conference Evaluation of Our Understanding of The Failure Mechanism", ASM-Corrosion, pp.37-51.
- [HAS 8] P.Sofronis and H.K.Birnbaum: "Mechanics of The Hydrogen Dislocation Impurity Interactions-I. Increasing Shear Modulus", J. Mech. Phys. Solids, Vol.43, No.1, 1995, pp.49-90.
- [HAS 9] P.Sofronis: "The Influence of Mobility of Dissolved Hydrogen on The Elastic Response of A Metal", J. Mech. Phys. Solids, Vol.43, No.9, 1995, pp.1385-1407.
- [HAS 10] R.P.Gangloff and A.Turnbull: "Crack Electrochemistry Modelling and Fracture Mechanics Measurement of The Hydrogen Embrittlement Threshold", Modelling Environmental Effects on Crack Initiation and Propagation, R.H.Jones and W.W.Gerberich (ed.), AIME, 1986, pp.55-81.
- [HAS 11] A.Turnbull: "Modelling of Crack Chemistry in Sensitised Stainless Steel in Boiling Water Reactor Environments", Corrosion Science, Vol.39, No.4, 1997, pp.789-805.
- [HAS 12] J.Toribio: "Fracture Mechanics Approach to Hydrogen-Assisted Microdamage in Eutectoid Steel", Metall. Trans., Vol.28A, 1997, pp.191-197.
- [HAS 13] W.W.Gerberich: "Effect of Hydrogen on High-Strength and Martensitic Steels", Proc. 1st Intern. Conf. on Current Solution to Hydrogen Problems in Steels, C.G.Interrante and G.M.Pressouryre (ed.), ASM, 1982, pp.115-147.
- [HAS 14] Th.Boellinghaus, E.Viyanit and H.Hoffmeister: "Numerical Modelling of Hydrogen Assisted Cracking", Corrosion 2001, Paper No.01226, (Houston, TX: NACE International, 2001).
- [HAS 15] J.Toribio: "The Role of Crack Tip Strain Rate in Hydrogen Assisted Cracking", Corrosion Science, Vol.39, No.9, 1997, pp.1687-1697.

References

- [HAS 16] A. Turnbull: "Comparison of Hydrogen Charging of Structural Steel by Crack Tip Processes and by Bulk Reaction in the Cathodic Protection of Corrosion Fatigue Cracks", *Scripta Metallurgica*, Vol.20, 1986, pp.365-369.
- [HAS 17] H.J.Maier, W.Popp and H.Kaesche: "A Method to Evaluate the Critical Hydrogen Concentration for Hydrogen-Induced Crack Propagation", *Acta metall.*, Vol.35, No.4, 1987, pp.875-880.
- [HAS 18] A.R.Troiano: "The Role of Hydrogen and other Interstitials in the Mechanical Behavior of Metals", *Trans. of The ASM*, Vol.52, 1960, pp.54-80.
- [HAS 19] H.Kurahashi, T.Kurusu, Y.Sone, K.Wada and Y.Nakai: "Stress Corrosion Cracking of 13 Cr Steels in CO₂-H₂S-Cl-Environments", *Corrosion*, Vol.41, No.4, 1985, pp.211-219.
- [HAS 20] L.J.Qiao, J.L.Luo and X.Mao: "Hydrogen Evolution and Enrichment Around Stress Corrosion Crack Tips of Pipeline Steels in Dilute Bicarbonate Solution", *Corrosion*, Vol.54, No.2, 1998, pp.115-120.
- [HAS 21] A.Turnbull: "Modelling of Environment Assisted Cracking", *Corrosion Science*, Vol.34, No.6, 1993, pp.921-960.
- [HAS 22] H.P.V.Leeuwen: "The Kinetics of Hydrogen Embrittlement: A Quantitative Diffusion Model", *Engineering Fracture Mechanics*, Vol.6, 1974, pp.141-161.
- [HAS 23] R.A.Oriani: "A Mechanistic Theory of Hydrogen Embrittlement of Steels", *Berichte der Bunsengesellschaft*, Vol.76, 1972, pp.848-857.
- [HAS 24] S.X.Mao and M.Li: "Mechanics and Thermodynamics on the Stress and Hydrogen Interaction in Crack Tip Stress Corrosion: Experiment and Theory", *J. Mech, Phys, Solids*, Vol.46, No.6, 1998, pp.1125-1137.
- [HAS 25] C.D.Beachem: "A New Model for Hydrogen-Assisted Cracking (Hydrogen Embrittlement)", *Metallurgical Transactions*, Vol.3, 1972, pp.437-451.
- [HAS 26] P.M.Moran and C.F.Shih: "Crack Growth and Cleavage in Mismatched Welds: A Micromechanics Study Using a Cell Model", *International Journal of Fracture*, Vol.92, 1998, pp.153-174.
- [HAS 27] J.Toribio and V.Kharin: "The Effect of History on Hydrogen Assisted Cracking: 2. A Revision of K-dominance", *International Journal of Fracture*, Vol.88, 1997, pp.247-258.
- [HAS 28] J.Toribio and V.Kharin: "The Effect of History on Hydrogen Assisted Cracking: 1.Coupling of Hydrogenation and Crack Growth", *International Journal of Fracture*, Vol.88, 1997, pp.233-245.
- [HAS 29] R.Thomson: "Brittle Fracture in a Ductile Material with Application to Hydrogen Embrittlement", *J. of Materials Science*, Vol.13, 1978, pp.128-142.
- [HAS 30] E.Lunarska and A.Zielinski: "An Application of the Schoeck's Model to the Cold Work Internal Friction Peak in The Hydrogen-Iron System", *Scripta Metallurgica*, Vol.12, 1978, pp.721-725.
- [HAS 31] J.P.Ford: "Quantitative Prediction of Environmentally Assisted Cracking", *Corrosion*, Vol.52, No.5, 1996, pp.375-395.
- [HAS 32] A.Turnbull, M.S.de S.Maria: "Predicting the Kinetics of Hydrogen Generation at the Tips of Corrosion Fatigue Cracks", *Metallurgical Transaction A*, Vol.19A, 1988, pp.1795-1806.

- [HAS 33] B.Strnadel: "Hydrogen Assisted Micro Cracking in Pressure Vessel Steels", Intern. J. of Fracture, Vol.89, 1998, pp.L45-L50.
- [HAS 34] M.Iino: "The Extension of Hydrogen Blister-Crack Array in Linepipe Steels", Metallurgical Transactions A, Vol.9A, 1978, pp.1581-1590.
- [HAS 35] H.C.Chu and R.P.Wei: "Stress Corrosion Cracking of High-Strength Steels in Aqueous Environments", Corrosion, Vol.46, No.6, 1990, pp.468-476.
- [HAS 36] J.D.Atkison, S.T.Cole and J.E.Forrest: "Corrosion Fatigue Mechanisms in Ferritic Pressure Vessel Steels Exposed to Simulated PWR Environments", Presented at an I.A.E.A. Meeting "Sub-Critical Crack Growth", Freiburg, Germany, 1981, pp.173-197.
- [HAS 37] A.S.Tetelman: "Recent Developments in Classical Hydrogen Embrittlement", Proc. of the Intern. Conf. on Hydrogen in Metals, 1973, pp.17-34.
- [HAS 38] P.M.Scott and A.E.Truswell: "Corrosion Fatigue Crack Growth in Reactor Pressure Vessel Steels—Measurement and Application", Structural Integrity of Light Water Reactor Components, L.E.Steele et al.(ed.), Applied Science Publishers, London, 1982, pp.287-309.
- [HAS 39] H.K.Birnbaum, I.M.Robertson, P.Sofronis and D.Teter: "Mechanisms of Hydrogen Related Fracture—A Review", pp.172-195.
- [HAS 40] C.A.Zapffe and C.E.Sims: "Hydrogen Embrittlement, Internal Stress and Defects in Steel", American Institute of Mining and Metallurgical Engineers, No.1307, 1941, pp.1-37.
- [HAS 41] S.P.Lynch: "Mechanisms of Hydrogen Assisted Cracking", Metals Forum, Vol.2, No.3, 1979, pp.189-200.
- [HAS 42] L.J.Qiao, W.Chu and X.Mao: "Critical Hydrogen Concentration for Hydrogen Induced Cracking of Type 321 Stainless Steel Corrosion", Vol.52, No.4, 1996, pp.275-279.
- [HAS 43] B.G.Ateya and H.W.Pickering: "Conditions for which Iron Dissolution Occurs in Cracking Hydrogen Charging of Steel", ASTM-Corrosion, pp.1183-1188.
- [HAS 44] S.K.Yen and H.C.Shih: "Determination of the Critical Hydrogen Concentration for Brittle Fracture of a High Chromium Ferritic Steel", J. Electrochem. Soc., Vol.137, No.7, 1990, pp.2028-2031.
- [HAS 45] A.A.El-Yazgi and D.Hardie: "The Embrittlement of a Duplex Stainless Steel by Hydrogen in a Variety of Environments", Corrosion Science, Vol.38, No.5, 1996, pp.735-744.
- [HAS 46] M.R.Louthan, Jr., G.R.Caskey, Jr., J.A.Donovan and D.E.Rawl, Jr.: "Hydrogen Embrittlement of Metals", Material Science and Engineering, Vol.10, 1972, pp.357-368.
- [HAS 47] H.S.Kwon: "Propagation of Stress Corrosion Cracks of 26Cr-1Mo Ferritic Stainless Steels in a Hot Chloride Solution", Scripta Metallurgica, Vol.27, 1992, pp.341-346.
- [HAS 48] H.H.Johnson: "On Hydrogen Brittleness in High Strength Steels", ASTM-Corrosion, pp. 439-445.
- [HAS 49] A.S.Tetelman: "The Mechanism of Hydrogen Embrittlement in Steel", ASTM-Corrosion, pp.446-464.

References

- [HAS 50] E.H.Phelps: "A Review of the Stress Corrosion Behaviour of Steel with High Yield Strength", ASTM-Corrosion, pp.398-409.
- [HAS 51] H.P.Leckie: "Effect of Environment on Stress Induced Failure of High Strength Maraging Steels" ASTM-Corrosion, pp.411-419.
- [HAS 52] T.Hara and H.Asahi: "Conditions under which Cracks Occur in Modified 13% Chromium Steel in Wet Hydrogen Sulfide Environments, Corrosion, Vol.56, No.5, 2000, pp.533-542.
- [HAS 53] A.W.Thomson: "Current Status of the Role of Hydrogen in Stress Corrosion Cracking", Materials Science and Engineering, Vol.43, 1980, pp.41-46.
- [HAS 54] Y.A.Marichev and I.L.Rosenfeld: "Investigation of the Mechanism of Stress Corrosion Cracking in High Strength Steels", Corrosion, Vol.32, No.11, 1976, pp.423-429.
- [HAS 55] Y.-B.Wang, W.-Y.Chu and C.-M.Hsiao: "Hydrogen Induced Slow Crack Growth in Mild Steel and Pure Iron", Corrosion, Vol.41, No.7, 1985, pp.427-429.
- [HAS 56] Y.Hirose and T.Mura: "Crack Nucleation and Propagation of Corrosion Fatigue in High-Strength Steel", Eng. Fracture Mechanics, Vol.22, No.5, 1985, pp.859-870.
- [HAS 57] P.Neumann: "New Experiments Concerning the Slip Processes at Propagating Fatigue Cracks-I", Acta Metallurgica, Vol.22, 1974, pp.1155-1165.
- [HAS 58] Q.-X.Bai, W.-Y.Chu and C.-M.Hsiao: "Partial Molar Strain Field of Hydrogen in α -Fe", Scripta Metallurgica, Vol.21, 1987, pp.613-618.
- [HAS 59] A.Miyasaka, T.Kanamaru and H.Ogawa: "Critical Stress for Stress Corrosion Cracking of Duplex Strainless Steel in Sour Service", Corrosion, Vol.52, No.8, 1996, pp.592-599.
- [HAS 60] E.A.Steigerwald, F.W. Schaller and A.R.Toriano: "Discontinuous Crack Growth in Hydrogenated Steel", Trans. of the Metallurgical Society of AIME, Vol.125, 1959, pp.1048-1052.
- [HAS 61] M.Lu, P.S.Pao, T.W.Weir, G.W.Simmons and R.P.Wei: "Rate Controlling Processes for Crack Growth in Hydrogen Sulfide for AISI 4340 Steel", Metall. Trans., Vol.12A, 1981, pp.805-811.
- [HAS 62] H.H.Uhlig: "An Evaluation of Stress Corrosion Cracking Mechanisms", ASTM-Corrosion, pp.86-97.
- [HAS 63] A.J.Forty: "The Metal Physics of Stress Corrosion", ASTM-Corrosion, pp.64 – 71.
- [HAS 64] E.Lunarska: "Role of Hydrogen and Stresses in the Failure of Heat Exchanger Pipes", Corrosion, Vol.52, No.2, 1996, pp.143-153.
- [HAS 65] D.A.Jones: "Localized Surface Plasticity During Stress Corrosion Cracking", Corrosion, Vol.52, No.5, 1996, pp.356-362.
- [HAS 66] R.N.Parkins: "Mechanistic Aspects of Intergranular Stress Corrosion Cracking of Ferritic Steels", Corrosion, Vol.52, No.5, 1996, pp.363-374.
- [HAS 67] K.Lian and E.I.Meletis: "Environment Induced Deformation Localization During Transgranular Stress Corrosion Cracking", Corrosion, Vol.52, No.5, 1996, pp.347-355.

- [HAS 68] M.A.Abdelhadi, L.Hyspecka and J.Galland: "Delayed Fracture and Premature Fracture in the Presence of Hydrogen in Martensitic Fe-Ni-C Alloys", NACE 5: Stress Corrosion Cracking and Hydrogen Embrittlement of Iron Base Alloys, R.W.Staehle et al.(ed.), 1977, pp.816-821.
- [HAS 69] G.J.Theus and R.W.Staehle: "Review of Stress Corrosion Cracking and Hydrogen Embrittlement in the Austenitic Fe-Cr-Ni Alloys", NACE 5: Stress Corrosion Cracking and Hydrogen Embrittlement of Iron Base Alloys, R.W.Staehle et al.(ed.), 1977, pp.845-892.
- [HAS 70] S.Shimodaira, M.Takano, Y.Takizawa and H.Kamide: "Mechanisms of Transgranular Stress Corrosion Cracking of Duplex and Ferritic Stainless Steels", NACE 5: Stress Corrosion Cracking and Hydrogen Embrittlement of Iron Base Alloys, R.W.Staehle et al.(ed.), 1977, pp.1003-1015.
- [HAS 71] R.L.Cowan and G.M.Gordon: "Intergranular Stress Corrosion Cracking and Grain Boundary Composition of Fe-Ni-Cr Alloys", NACE 5: Stress Corrosion Cracking and Hydrogen Embrittlement of Iron Base Alloys, R.W.Staehle et al.(ed.), 1977, pp.1023-1070.
- [HAS 72] Q.Yang and J.L.Luo: "Martensite Transformation and Surface Cracking of Hydrogen Charged and Outgassed Type 304 Stainless Steel", Materials Science and Engineering, A288, 2000, pp.75-83.
- [HAS 73] R.Oltra, C.Bouillot and T.Magnin: "Localized Hydrogen Cracking in the Austenitic Phase of a Duplex Stainless Steel", Scripta Materialia, Vol.35, No.9, 1996, pp. 1101-1105.
- [HAS 74] W.Zheng and D.Hardie: "Effect of Structural Orientation on the Susceptibility of Commercial Duplex Stainless Steels to Hydrogen Embrittlement", Corrosion, Vol.47, No.10, 1991, pp.792-799.
- [HAS 75] E.A.Steigerwald and W.D.Benjamin: "Effect of Composition on the Environmentally Induced Delayed Failure of Pre-cracked High-Strength Steel", Metallurgical Transactions, Vol.2, 1971, pp.606-608.
- [HAS 76] T.-Y.Zhang, F.-X.Jiang, W.-Y.Chu and C.-M.Hsiao : "Effect of Hydrogen on the Young's Modulus of Iron", Metallurgical Transactions A, Vol. 16A, 1985, pp.1655-1662.
- [HAS 77] C.Andreone and A.Murut: "Influence of the Austenite Retained in the Hydrogen Embrittlement in AISI 4340", Scripta Metallurgica, Vol.24, 1990, pp.1453-1458.
- [HAS 78] T.Fujita and Y.Yamada: "Physical Metallurgy and SCC in High Strength Steels" NACE 5: Stress Corrosion Cracking and Hydrogen Embrittlement of Iron Base Alloys, R.W.Staehle et al.(ed.), 1977, pp.736-746.
- [HAS 79] M.Prazak and M.Holinka: "The Behavior of Passive Films on Tensile Stressed Steels", NACE 5: Stress Corrosion Cracking and Hydrogen Embrittlement of Iron Base Alloys, R.W.Staehle et al.(ed.),1977, pp.1020-1022.
- [HAS 80] T.P.Hoar: "The Role of Oxide Films in the Stress Corrosion Cracking of Austenitic Stainless Steels in Hot Chloride Solutions", NACE 5: Stress Corrosion Cracking and Hydrogen Embrittlement of Iron Base Alloys, R.W.Staehle et al.(ed.), 1977, pp.1016-1019.
- [HAS 81] D.A.Vermilyea: "A Flim Rupture Model for Stress Corrosion Cracking", NACE 5: Stress Corrosion Cracking and Hydrogen Embrittlement of Iron Base Alloys, R.W.Staehle et al.(ed.), 1977, pp.208-217.

References

- [HAS 82] J.P.Hirth: "SCC and HE from the Viewpoint of the Defect Solid State", NACE 5: Stress Corrosion Cracking and Hydrogen Embrittlement of Iron Base Alloys, R.W.Staehle et al.(ed.), 1977, pp.1-10.
- [HAS 83] D.A.Vermilyea: "Reaction Films, Metal Dissolution and Stress Corrosion Cracking", NACE 5: Stress Corrosion Cracking and Hydrogen Embrittlement of Iron Base Alloys, R.W.Staehle et al.(ed.), 1977, pp.15-31.
- [HAS 84] D.A.Meyn, T.W.Webb, and E.C.Aifantis: "Hydrogen-Assisted Cracking Studies of 4340 Steel by Using The Optical Method of Caustics", Engineering Fracture Mechanics, Vol.33, No.6, 1989, pp.913-925.
- [HAS 85] K.N.Akhurst and T.J.Baker: "The Threshold Stress Intensity for Hydrogen Induced Crack Growth", Metallurgical Transactions A, Vol.12A, 1981, pp.1059-1981.
- [HAS 86] H.G.Nelson: "Hydrogen Embrittlement ", Treatise on Materials Science and Technology, Vol.25, 1983, pp.275-359.
- [HAS 87] R.D.Parkins: "Slow Strain Rate Testing—25 Years Experience", Slow Strain Rate Testing for the Evaluation of Environmentally Induced Cracking: Research and Engineering Applications, R.D.Kane (ed.), ASTM, 1993, pp.7-21.
- [HAS 88] J.A.Beavers and G.H.Koch: "Limitations of the Slow Strain Rate Test Technique", Slow Strain Rate Testing for the Evaluation of Environmentally Induced Cracking: Research and Engineering Applications, R.D.Kane (ed.), ASTM, 1993, pp.22-39.
- [HAS 89] R.D.Kane and S.M.Wilhelm: "Status of Standardization Activities on Slow Strain Rate Testing Techniques", Slow Strain Rate Testing for the Evaluation of Environmentally Induced Cracking: Research and Engineering Applications, R.D.Kane (ed.), ASTM, 1993, pp.40-47.
- [HAS 90] M.E.Indig: "SSRT for Hydrogen Water Chemistry Verification in BWRs", Slow Strain Rate Testing for the Evaluation of Environmentally Induced Cracking: Research and Engineering Applications, R.D.Kane (ed.), ASTM, 1993, pp.51-64.
- [HAS 91] M.T.Miglin and B.P.Miglin: "Application of Slow Strain Rate Testing in the Nuclear Power Industry", Slow Strain Rate Testing for the Evaluation of Environmentally Induced Cracking: Research and Engineering Applications, R.D.Kane (ed.), ASTM, 1993, pp.65-82.
- [HAS 92] J.Toribio: "The Use of Precracked and Notched Slow Strain Rate Specimens", Slow Strain Rate Testing for the Evaluation of Environmentally Induced Cracking: Research and Engineering Applications, R.D.Kane (ed.), ASTM, 1993, pp.105-122.
- [HAS 93] W.Dietzel and K.H.Schwalbe: "Application of the Rising Displacement Test to SCC Investigations", Slow Strain Rate Testing for the Evaluation of Environmentally Induced Cracking: Research and Engineering Applications, R.D.Kane (ed.), ASTM, 1993, pp.134-148.
- [HAS 94] D.T.Nguyen, D.E.Nichols and R.D.Daniels: "Slow Strain Rate Fracture of High-Strength Steel at Controlled Electrochemical Potentials in Ammonium Chloride, Potassium Chloride, and Ammonium Nitrate Solutions", Slow Strain Rate Testing for the Evaluation of Environmentally Induced Cracking: Research and Engineering Applications, R.D.Kane (ed.), ASTM, 1993, pp.149-157.

- [HAS 95] P.A.Klein, R.A.Hays, P.J.Morgan and J.R.Scully: "Hydrogen Cracking Initiation of a High-Strength Steel Weldment", *Slow Strain Rate Testing for the Evaluation of Environmentally Induced Cracking: Research and Engineering Applications*, R.D.Kane (ed.), ASTM, 1993, pp.202-222.
- [HAS 96] H.S.Ahluwalia: "Problems Associated with Slow Strain Rate Quality Assurance Testing of Nickel-Base Corrosion Resistant Alloy Tubulars in Hydrogen Sulfide Environments", *Slow Strain Rate Testing for the Evaluation of Environmentally Induced Cracking: Research and Engineering Applications*, R.D.Kane (ed.), ASTM, 1993, pp.225-239.
- [HAS 97] A.Ikeda, M.Ueda and H.Okamoto: "The Role of Slow Strain Rate Testing on Evaluation of Corrosion Resistant Alloys for Hostile Hot Sour Gas Production", *Slow Strain Rate Testing for the Evaluation of Environmentally Induced Cracking: Research and Engineering Applications*, R.D.Kane (ed.), ASTM, 1993, pp.240-262.
- [HAS 98] S.M.Wilhelm and D. M.Currie: "Relationship of Localized Corrosion and SCC in Oil and Gas Production Environments", *Slow Strain Rate Testing for the Evaluation of Environmentally Induced Cracking: Research and Engineering Applications*, R.D.Kane (ed.), ASTM, 1993, pp.263-289.
- [HAS 99] J.P.Hirth: "Theories of Hydrogen Induced Cracking of Steels", *Hydrogen Embrittlement and Stress Corrosion Cracking*, R.Gibala and R.F.Hehemann (ed.), ASM, 1995, pp.29-41.
- [HAS 100] R.A.Oriani: "Hydrogen Embrittlement of Steels", *Hydrogen Embrittlement and Stress Corrosion Cracking*, R.Gibala and R.F.Hehemann (ed.), ASM, 1995, pp.43-59.
- [HAS 101] R.Gibala and A.J.Kumnick: "Hydrogen Trapping in Iron and Steels", *Hydrogen Embrittlement and Stress Corrosion Cracking*, R.Gibala and R.F.Hehemann (ed.), ASM, 1995, pp.61-77.
- [HAS 102] P.Lacombe, M.Gibala and R.F.Hehemann (ed.), ASM, 1995, pp.79-102.
- [HAS 103] R.P.Weil, K.Klier, G.W. Simmons and Y.T.Chou: "Fracture Mechanics and Surface Chemistry Investigations of Environment-Assisted Crack Growth", *Hydrogen Embrittlement and Stress Corrosion Cracking*, R.Gibala and R.F.Hehemann (ed.), ASM, 1995, pp.103-133.
- [HAS 104] I.M.Bernstein and A.W.Thompson: "The Role of Microstructure in Hydrogen Embrittlement", *Hydrogen Embrittlement and Stress Corrosion Cracking*, R.Gibala and R.F.Hehemann (ed.), ASM, 1995, pp.135-152.
- [HAS 105] H.K.Birnbaum: "Hydrogen Related Second Phase Embrittlement of Solids", *Hydrogen Embrittlement and Stress Corrosion Cracking*, R.Gibala and R.F.Hehemann (ed.), ASM, 1995, pp.153-177.
- [HAS 106] A.R.Troiano and R.F.Hehemann: "Stress Corrosion Cracking of Ferritic and Austenitic Stainless Steels", *Hydrogen Embrittlement and Stress Corrosion Cracking*, R.Gibala and R.F.Hehemann (ed.), ASM, 1995, pp.231-248.
- [HAS 107] R.M.Latanision, C.R.Compeau and M.Kurkela: "Hydrogen Permeation and Embrittlement Studies on Metallic Glasses", *Hydrogen Embrittlement and Stress Corrosion Cracking*, R.Gibala and R.F.Hehemann (ed.), ASM, 1995, pp.297-312.

References

- [HAS 108] Th.Boellinghaus and H.Hoffmeister: "A Numerical Model for Hydrogen Assisted Cracking", *Corrosion*, Vol.56, No.6, 2000, pp.611-622.
- [HAS 109] E.Wendler-Kalsch: "Grundlage und Mechanismen der H-induzierten Korrosion metallischer Werkstoffe", *Wasserstoff und Korrosion*, D.Kuron(ed.), Verlag Irene Kuron, ISBN 3-923623-03-8, Ed.1, Bonn, 1986, pp.8-47.
- [HAS 110] J.K.Tien, A.W.Thomson, I.M.Bernstein and R.J.Richards: "Hydrogen Transport by Dislocation", *Metallurgical Transactions A*, Vol.7A, 1976, pp.821-829.
- [HAS 111] J.R.Galvele: "A Stress Corrosion Cracking Mechanism Based on Surface Mobility", *Corrosion Science*, Vol.27, 1987, pp.1-33.
- [HAS 112] Y.Katz, N.Tymiak and W.W.Gerberich: "Nanomechanical Probes as New Approaches to Hydrogen/Deformation Interaction Studies", *Engineering Fracture Mechanics*, 68, 2001, pp.619-646.
- [HAS 113] D.P.G.Lidbury: "The Estimation of Crack Tip Strain Rate Parameters Characterizing Environment Assisted Crack Growth Data", *Embrittlement by the Localized Crack Environment*, R.P.Gangloff (Ed.), AIME, New York, 1983, pp.149-172.
- [HAS 114] K.L.Baumert and W.R.Watkins, Jr.: "Case Histories Using the Slow Strain Rate Test", *Slow Strain Rate Testing for the Evaluation of Environmentally Induced Cracking: Research and Engineering Applications*, R.D.Kane (ed.), ASTM, 1993, pp.173-180.

III. Literature for hydrogen permeation and diffusion (HPD)

- [HPD 1] A.Turnbull and R.B.Hutchings: "Analysis of Hydrogen Atom Transport in a Two-Phase Alloy", *Materials Science and Engineering*, A177, 1994, pp.161-171.
- [HPD 2] R.H.Hutchings, A.Turnbull and A.T.May: "Measurement of Hydrogen Transport in a Duplex Stainless Steel", *Scripta Metallurgica*, Vol.25, 1991, pp.2657-2662.
- [HPD 3] S.Asano, M.Shibata and T.Tsunoda: "Internal Friction due to Hydrogen in Austenitic Stainless Steels", *Scripta Metallurgica*, Vol.14, 1980, pp.377-382.
- [HPD 4] C.-L.Yu and T.-P.Perng: "Surface Effects on Electrochemical Hydrogen Diffusion in Stainless Steels", *Acta Metall.*, Vol.39, No.6, 1991, pp.1091-1099.
- [HPD 5] T.-P.Perng and C.J.Altstetter: "Effects of Water Vapor and Hydrogen Sulfide on Hydrogen Permeation in Stainless Steel", *Acta Metall.*, Vol.36, No.5, 1998, pp.1251-1260.
- [HPD 6] T.-P.Perng and C.J.Altstetter: "Effects of Deformation on Hydrogen Permeation in Austenitic Stainless Steel", *Acta Metall.*, Vol.34, No.9, 1986, pp.1771-1781.
- [HPD 7] Y.-P.Zheng and T.-Y.Zhang: "Effects of Absorption and Desorption on Hydrogen Permeation-II. Experimental Measurements of Activation Energies", *Acta Mater.*, Vol.14, No.14, 1998, pp.5035-5043.
- [HPD 8] R.C.Brouwer: "Hydrogen Diffusion and Solubility in Vanadium Modified Pressure Vessel Steels", *Scripta Metallurgica*, Vol.27, 1992, pp.353-358.

- [HPD 9] T.P.Perng and C.J.Altstetter: "Hydrogen Permeation and Diffusion in Cryoformed AISI 301 Stainless Steel", *Scripta Metallurgica*, Vol.18, 1984, pp.67-70.
- [HPD 10] X.J.Li, M.H.Wang, C.M.Hsiao, Z.Z.Tien and X.R.Chang: "Effect of Second Phase on Hydrogen Diffusivity in α -Fe", *Scripta Metallurgica*, Vol.22, 1988, pp.815-820.
- [HPD 11] D.L.Johnson and D.A.Davis: "Effect of Sensitization on Hydrogen Transport in Austenitic Stainless Steel", *Scripta Metallurgica*, Vol.23, 1989, pp.321-326.
- [HPD 12] Th.Boellinghaus, H.Hoffmeister and C.Middel: "Scatterbands for Hydrogen Diffusion Coefficients in Steels Having a Ferritic Microstructure and Steels Having an Austenitic Microstructure at Room Temperature", *Welding in the World*, Vol.37, No.1, 1996, pp.16-23.
- [HPD 13] Th.Boellinghaus, H.Hoffmeister and A.Dangeleit: "A Scatterband for Hydrogen Diffusion Coefficients in Micro-Alloyed and Low Carbon Structural Steels", *Welding in the World*, Vol.35, No.2, 1995, pp.83-96.
- [HPD 14] W.C.Luu, H.S.Kuo and J.K.Wu: "Hydrogen Permeation Through Nickel-Plated Steels", *Corrosion Science*, Vol.39, No.6, 1997, pp.1051-1059.
- [HPD 15] B.Ladna and H.K.Birnbaum: "A Study of Hydrogen Transport During Plastic Deformation", *Acta Metallurgica*, Vol.35, No.7, 1987, pp.1775-1778.
- [HPD 16] M.Koiwa: "Trapping Effect in Diffusion of Interstitial Impurity Atoms in B.C.C. Lattices", *Acta Metallurgica*, Vol.22, 1974, pp.1259-1974.
- [HPD 17] J.A.King: "On The Possibility of Path Restricted Diffusion of Hydrogen in BCC Iron", *Scripta Metallurgica*, Vol.22, No.11, 1988, pp.1703-1708.
- [HPD 18] R.A.ORIANI: "The Diffusion and Trapping of Hydrogen in Steel", *Acta Metallurgica*, Vol.18, 1970, pp.147-157.
- [HPD 19] T.-Y.Zhang and Y.-P.Zheng: "Effects of Absorption and Desorption on Hydrogen Permeation-I. Theoretical Modelling and Room Temperature Verification", *Acta Mater.*, Vol.46, No.14, 1998, pp.5023-5033.
- [HPD 20] T.Zakroczymski: "The Effect of Straining on the Transport of Hydrogen in Iron, Nickel, and Stainless Steel", *Corrosion*, Vol.41, No.8, 1985, pp.485-489.
- [HPD 21] Th.Boellinghaus, H.Hoffmeister, J.Klemme and H.Alzer: "Hydrogen Permeation in a Low Carbon Martensitic Stainless Steel Exposed to H₂S Containing Brines at Free Corrosion", *Corrosion99*, Paper No.609, (Houston, TX: NACE International, 1999).
- [HPD 22] Th.Boellinghaus and H.Hoffmeister: "Hydrogen Permeation in Supermartensitic Stainless Steels Dependent on Heat Treatment and Chemical Composition", *Corrosion2000*, Paper No.00141, (Houston, TX: NACE International, 2000).
- [HPD 23] J.B.Lablond and D.Dubois: "General Mathematical Description of Hydrogen Diffusion in Steels-II. Numerical Study of Permeation and Determination of Trapping Parameters", *Acta Metall.*, Vol.31, No.10, 1983, pp.1471-1478.
- [HPD 24] A.J.Griffiths and A.Turnbull: "Hydrogen Uptake and Cracking in 22% Cr Duplex Stainless Steel Under Galvanic Coupling Conditions", *Corrosion*, Vol.53, No.9, 1997, pp.700-704.

References

- [HPD 25] R.A.Oriani: "Hydrogen in Metals", NACE 5: Stress Corrosion Cracking and Hydrogen Embrittlement of Iron Base Alloys, R.W.Staehle et al.(ed.), 1977, pp.32-50.
- [HPD 26] R.N.Parkins, A.J.Markworth, J.H.Holbrook and R.R.Fessler: "Hydrogen Gas Evolution from Cathodically Protected Surfaces", Corrosion, Vol.41, No.7, 1985, pp.389-397.
- [HPD 27] L.J.Qiao and J.L.Luo: "Hydrogen-Facilitated Anodic Dissolution of Austenitic Stainless Steels", Corrosion, Vol.54, No.4, 1998, pp.281-288.
- [HPD 28] M.F.Stevens and I.M.Bernstein: "Microstructural Trapping Effects on Hydrogen Induced Cracking of a Microalloyed Steel", Metallurgical Transactions A, Vol.20A, 1989, pp.909-919.
- [HPD 29] H.M.Lee: "The Solubility of Hydrogen in Transition Metals", Metallurgical Transactions A, Vol.7A, 1976, pp.431-433.
- [HPD 30] N.Eliaz, D.Elizer and D.L.Olson: "Hydrogen-Assisted Processing of Materials", Material Science and Engineering, A289, 2000, pp.41-53.
- [HPD 31] J.P.Hirth: "Effects of Hydrogen on the Properties of Iron and Steel", Metallurgical Transactions A, Vol.11A, 1980, pp.861-890.
- [HPD 32] K.Kiuchi, R.B.McLellan: "The Solubility and Diffusivity of Hydrogen in Well-Annealed and Deformed Iron", Acta Metall., Vol.31, No.7, 1983, pp.961-984.
- [HPD 33] J.B.Lebond and D.Dubois: "A General Mathematical Description of Hydrogen Diffusion in Steels-I. Derivation of Diffusion Equation From Boltzmann-Type Transport Equations", Acta Metall, Vol.31, No.10, 1983, pp.1459-1469.
- [HPD 34] F.C.Larche and J.W.Cahn: "The Effect of Self Stress on Diffusion in Solids", Acta Metall., Vol.30, 1982, pp.1835-1845.
- [HPD 35] T.-Y.Zhang, W.-Y.Chu and C.I-M.Hsiao: "Tetragonal Distortion Field of Hydrogen Atoms in Iron", Metallurgical Transactions A, Vol.16A, 1985, pp.1649-1653.
- [HPD 36] D.L.Cummings and D.A.Blackburn: "The Effect of Pressure Modulation on the Flow of Gas Through a Solid Membrane: Surface Inhibition and Internal Traps", Metallurgical Transactions A, Vol.16A, 1985, pp.1013-1985.
- [HPD 37] J.K.Tien, A.W.Thompson, I.M.Bernstein and R.J.Richards:"Hydrogen Transport by Dislocations", Metallurgical Transactions A, Vol.7A, 1976, pp.821-829.
- [HPD 38] G.M.Pressouyre and I.M.Bernstein: "A Quantitative Analysis of Hydrogen Trapping", Metallurgical Transactions A, Vol.9A, 1978, pp.1571-1579.
- [HPD 39] G.M.Pressouyre and I.M.Bernstein: "A Kinetic Trapping Model for Hydrogen-Induced Cracking", Acta Metallurgica, Vol.27, 1979, pp.89-100.
- [HPD 40] M.Uhlemann and B.G.Pound: "Diffusivity, Solubility and Trapping Behaviour of Hydrogen in Alloys 600, 690tt and 800", Corrosion Science, Vol.40, No.4/5, 1998, pp.645-662.
- [HPD 41] P.Sofronis and R.M.McMeeking: "Numerical Analysis of Hydrogen Transport near a Blunting Crack Tip", J. Mech. Phys. Solids, Vol.37, No.3, 1989, pp.317-350.

- [HPD 42] A.Turnbull and J.G.N.Thomas: "A Model of Crack Electrochemistry for Steels in the Active State Based on Mass Transport by Diffusion and Ion Migration", J. Electrochemical Soc., Vol.129, No.7, 1982, pp.1412-1422.
- [HPD 43] J.O'M.Bockris, J.McBreen and L.Nanis: "The Hydrogen Evolution Kinetics and Hydrogen Entry into α -Iron", J. Electrochem. Soc., Vol.112, No.10, 1965, pp.1025-1031.
- [HPD 44] R.N.Iyer, H.W.Pickering and M.Zamanzadeh: "Analysis of Hydrogen Evaluation and Entry into Metals for the Discharge-Combination Process", J. Electrochem. Soc., Vol.136, No.9, 1989, pp.2463-2470.
- [HPD 45] R.N.Iyer and H.W.Pickering: "A Mechanistic Analysis of Hydrogen Entry into Metals during Cathodic Hydrogen Charging", Scripta Metallurgica, Vol.22, 1988, pp.911-916.
- [HPD 46] D.P.Yao, W.X.Chen, X.K.Sun and J.Xu: "The Permeability of Hydrogen in 18Ni Maraging Steel, Scripta Metallurgica, Vol.22, 1988, pp.611-615.
- [HPD 47] S.L.Amey, G.M.Michal and J.H.Payer: "Modelling Hydrogen Entry and Exit in Metals Exposed to Multiple Charging Processes", Metallurgical Transactions A, Vol.25A, 1994, pp.723-732.
- [HPD 48] M.A.V.Devanathan and Z.Stachurski: "A Technique for the Evaluation of Hydrogen Embrittlement Characteristics of Electroplating Baths", J. Electrochem. Soc., Vol.110, No.8, 1963, pp.886-890.
- [HPD 49] C.D.Kim and B.E.Wilde: "The Kinetics of Hydrogen Absorption into Iron during Cathodic Hydrogen Evolution", J. Electrochem. Soc., Vol.118, No.2, 1971, pp.202-206.
- [HPD 50] B.E.Wilde and C.D.Kim: "Hydrogen Adsorption on Steels Undergoing Corrosion with Hydrogen Evolution", Corrosion, Vol.42, No.4, 1996, pp.243-245.
- [HPD 51] M.M.Makhlof and R.D.Sisson,Jr.: "Modeling Surface Effects on Hydrogen Permeation in Metals", Metallurgical Transactions A, Vol.22A, 1991, pp.1001-1006.
- [HPD 52] R.N.Iyer, I.Takeuchi, M.Zamanzadeh and H.W.Pickering: "Hydrogen Sulfide Effect on Hydrogen Entry into Iron – A Mechanistic Study", Corrosion, Vol.46, No.6, 1990, pp.460-467.
- [HPD 53] J.O'M.Bockris: "On Hydrogen Damage and the Electrical Properties of Interfaces", NACE 5: Stress Corrosion Cracking and Hydrogen Embrittlement of Iron Base Alloys, R.W.Staehle et al.(ed.), 1977, pp.286-305.
- [HPD 54] R.D.McCright: "Effects of Environmental Species and Metallurgical Structure on the Hydrogen Entry into Steel", NACE 5: Stress Corrosion Cracking and Hydrogen Embrittlement of Iron Base Alloys, R.W.Staehle et al.(ed.), 1977, pp. 306-325.
- [HPD 55] P.Azou: "Summary of the Interaction Congress on Hydrogen in Metals", NACE 5: Stress Corrosion Cracking and Hydrogen Embrittlement of Iron Base Alloys, R.W.Staehle et al.(ed.), 1977, pp.836-840.
- [HPD 56] R.Gibala: "Hydrogen-Defect Interactions in Iron-Base Alloys", NACE 5: Stress Corrosion Cracking and Hydrogen Embrittlement of Iron Base Alloys, R.W.Staehle et al.(ed.), 1977, pp.244-271.

References

- [HPD 57] R.Speiser: "Hydrogen in Metals" NACE 5: Stress Corrosion Cracking and Hydrogen Embrittlement of Iron Base Alloys, R.W.Staehle et al.(ed.), 1977, pp. 226-243.
- [HPD 58] G.R.Holcomb: "Countercurrent Gaseous Diffusion Model of Oxidation Through a Porous Coating", Corrosion, Vol.52, No.7, 1996, pp.531-539.
- [HPD 59] J.Voelkl and G.Alefeld: "Diffusion of Hydrogen in Metals", Diffusion in Solids, A.S.Nowick and J.J.Burton (ed.), 1975, pp.321-348.
- [HPD 60] J.Xu, X.K.Sun, W.X.Chen and Y.Y.Li: "Hydrogen Permeation and Diffusion in Iron-Base Superalloys", Acta Metall.Mater., Vol.41, No.5, 1993, pp.1455-1459.
- [HPD 61] E.Owczarek and T.Zakroczymski: "Hydrogen Transport in a Duplex Stainless Steel", Acta Materialia, Vol.48, 2000, pp.3059-3070.
- [HPD 62] I.W.Kang, S.I.Pyun and K.T.Kim: "The Effects of Dislocations on the Trapping and Transport of Hydrogen in 3.3Ni-1.6Cr Steel During Plastic Deformation", Scripta Metallurgica, Vol.23, 1989, pp.223-226.
- [HPD 63] H.W.Jeng, L.H.Chiu, D.L.Johnson and J.K.Wu: "Effect of Pearlite Morphology on Hydrogen Permeation, Diffusion, and Solubility in Carbon Steels", Metallurgical Transactions A, Vol.21A, 1990, pp.3257-3259.
- [HPD 64] K.-K.Baek, S.-I.Pyun and J.-S.Kim: "Wear Enhanced Hydrogen Evolution from Mild Steel", Metallurgical Transactions A, Vol.19A, 1998, pp.1721-1726.
- [HPD 65] E.Conofagos, J.Plusquellec, L.Hyspecka, P.Azou and P.Bastien: "Interactions Between Hydrogen and Structural Defects in Fe-Ni and Fe-Ni-C Alloys", NACE 5: Stress Corrosion Cracking and Hydrogen Embrittlement of Iron Base Alloys, R.W.Staehle et al.(ed.), 1977, pp.831-835.
- [HPD 66] W.Dresler und M.G.Frohberg: "Über ein vereinfachtes Verfahren zur Bestimmung des Diffusionskoeffizienten von Wasserstoff in festen Metallen", Heft 4, 1972, S.204-209.
- [HPD 67] M.A.V.Devanathan and Z.Stachurski: "The Adsorption and Diffusion of Electrolytic Hydrogen in Palladium", pp.90-102.
- [HPD 68] Th.Boellinghaus and E.Viyanit: "Revised Scatterbands for Hydrogen Diffusion Coefficients of Micro Alloy and Low Carbon Steels", IIW-
- [HPD 69] D.M. Seeger: „Wasserstoffaufnahme und -diffusion in Schweißnahtgefügen hochfester Stähle“, Dissertation, Berlin, 2004.

IV. Literature for fracture mechanics (FRM)

- [FRM 1] P.C.Lu: "The FEM Based Calculation of Crack-Tip Strain Rate for Determining the Crack Growth Rate of 304 Stainless Steel in BWR Environments ", Nuclear Engineering and Design, Vol.205, 2001, pp.227-240.
- [FRM 2] S.E.Alexandrov and R.V.Goldstein : "Distributions of Stress and Plastic Strain in Notched Tensile Bars", International Journal of Fracture, Vol.91, 1998, pp.1-11.
- [FRM 3] U.Zerbst und P.Langenberg: "Die industrielle Anwendung Bruchmechanischer Konzepte vor dem Hintergrund Internationaler Bewertungsvorschriften und Regelwerke, ein Bericht von GKSS, 38, 2000, S.1-42.

- [FRM 4] G.T.Hahn and A.R.Rosenfield: "Local Yielding and Extension of a Crack Under Plane Stress", *Aata Metallurgica*, Vol.13, 1965, pp.293-306.
- [FRM 5] S.Jiangbo, S.Jun, D.Zengjie and Z.Huijue: "The Finite Element Analysis of Deformation and Stress Triaxiality of a Mixed I+II Mode Elastic-Plastic Crack Tip", *International Journal of Fracture*, Vol.87, 1997, pp.47-58.
- [FRM 6] E.Pan: "A General Boundary Element Analysis of 2-D Linear Elastic Fracture Mechanics", *International Journal of Fracture*, Vol.88, 1997, pp.41-59.
- [FRM 7] P.R.Onck and E.V.D.Giessen: "Microstructural Modelling of Creep Crack Growth from a Blunted Crack", *International Journal of Fracture*, Vol.92, 1998, pp.373-399.
- [FRM 8] C.Yan and Y.W.Mai: "Numerical Investigation on Stable Crack Growth in Plane Stress", *International Journal of Fracture*, Vol.91, 1998, pp.117-130.
- [FRM 9] J.Xie and Z.W.Shi: "Effect of Yield Stress and Specimen Size on the Position of Fracture Toughness Peak (FTP) in J/W Curves", *Engineering Fracture Mechanics*, Vol.33, No.6, 1989, pp.907-912.
- [FRM 10] L.M.Young, P.L.Andresen and T.M.Angeliu: "Crack Tip Strain Rate: Estimates Based on Continuum Theory and Experimental Measurement", *Corrosion2001*, Paper No.01131, (Houston, TX: NACE International, 2001).
- [FRM 11] U.Zerbst, M.Kocak und P.Hübner: "Bruchmechanische Bewertung von Schweißverbindungen", *MP Materialprüfung*, Jahrg.44, Heft 9, 2002, pp.333-357.
- [FRM 12] J.C.Amazigo and J.W.Hutchinson: "Crack-Tip Fields in Steady Crack-Growth with Linear Strain-Hardening", *J. Mech. Phys. Solids*, Vol.25, 1977, pp.81-97.
- [FRM 13] W.W.Gerberich, D.L.Davidson and M.Kaczorowski: "Experimental and Theoretical Strain Distributions for Stationary and Growing Cracks", *J. Mech. Phys. Solids*, Vol.38, 1990, pp.87-113.
- [FRM 14] R.M.Rieck, A.Atrens and I.O.Smith "The Role of Crack Tip Strain Rate in the Stress Corrosion Cracking of High Strength Steels in Water", *Metallurgical Transactions A*, Vol.20A, 1989, pp.889-895.
- [FRM 15] R.N.Parkins: "Strain Rate Effects in Stress Corrosion Cracking", *Corrosion*, Vol.46, No.3, 1990, pp.178-189.
- [FRM 16] J.Dollhofer: "J-Q Theory for the Fracture of Elastically Mismatched Interfaces", *MP Materialprüfung*, Jahrg. 44, Band 5, 2002, S.167-175.
- [FRM 17] P.Langenberg, G.Sedlacek, W.Dahl und M.Feldmann: "Bruchmechanische Sicherheitskonzepte bei Schweißkonstruktionen", *MP Materialprüfung*, Jahrg. 44, Heft 11-12, 2002, S.442-447.
- [FRM 18] H.J.Schindler: "Berücksichtigung der Constrainteffekte in der technischen Bruchmechanik", *MP Materialprüfung*, Jahrg. 44, Heft 11-12, 2002, S.448-453.
- [FRM 19] S.Rödling, J.Bär und H.J.Gudladt: "Berücksichtigung der Constrainteffekte in der technischen Bruchmechanik", *MP Materialprüfung*, Jahrg. 44, Heft 11-12, 2002, S.454-460.

V. Literature for hydrogen assisted cold cracking (HAC)

- [HAC 1] J.Vulik: "An Update of the State-of-the-Art of Weld Metal Hydrogen Cracking", B.Graville (Original document), Welding in the World, Vol.31, No.5, 1993, pp.308-321.
- [HAC 2] V.Michailov, J.Ruge und K.Thomas: "Berechnung der Wasserstoffverteilung beim Schweißen", Schweißen und Schneiden, Heft11, 43, 1991, S.655-658.
- [HAC 3] V.Michailov, K.Thomas und H.Wohifahrt, "Der Wasserstoff als maßgebliche Einflussgröße für die Kaltrissneigung von Stählen beim Schweißen", DVS-Berichte 176, 1996, S.30-34.
- [HAC 4] P.Adamiec and J.Dziubinski: "Hydrogen Induced Cracking in Welded Steel Tubing", Welding International, 15(6), 2001, pp.431-437.
- [HAC 5] C.Düren und J.Gronsfeld: "Beurteilung der Kaltrissicherheit von Feinkornbaustählen im Implant- und Tekken -Test", DVS-Berichte Band 64, S.80-87.
- [HAC 6] J.Degenkolbe, H.Hoehne und D.Uwer: "Erfahrung mit der Kaltrißprüfung von Baustählen", DVS-Berichte Band 64, S.69-79.
- [HAC 7] A.Bragard und F.Marquet: "Erfahrung des C.R.M. auf dem Gebiet der Bewertung der Kaltrissempfindlichkeit von Stahl", DVS-Berichte Band 64, S.63-68.
- [HAC 8] V.Neumann, W.Florian und W.Schönherr: "Die Bewertung der wasserstoffbeeinflussten Kaltrissneigung mit der Implant-, TRC- und Lehigh-Probe", DVS-Berichte Band 64, S.56-62.
- [HAC 9] F.Erdmann-Jenitzer und M.Jacobi: "Einfluss inhomogener Elementverteilung auf wasserstoffbedingte Rissbildung von Massenbaustahl", DVS-Berichte Band 64, S.45-50.
- [HAC 10] V.Pilous: "Bestimmung der Kaltrissanfälligkeit von Schweißverbindungen und die Möglichkeit ihrer Begrenzung", DVS-Berichte Band 64, S.40-44.
- [HAC 11] K.J.Kipp und H.Hoffmeister: "Zur Prüfung von Schweißverbindungen im instrumentierten Einspannschweißversuch", DVS-Berichte Band 64, S.35-39.
- [HAC 12] H.Kleistner, M.Omar, N.Reuter, W.Schmalenberg und K.Wilken: "Messungen von Schweißeingenspannungen an unterpulvergeschweißten Viellagenschweißnähten", DVS-Berichte Band 64, S.28-34.
- [HAC 13] J.Ruge und G.Schröder: "Einfluss des diffusiblen Wasserstoffgehaltes auf die Querrissbildung eines Feinkornbaustahles", DVS-Berichte Band 64, S.23-27.
- [HAC 14] A.Million: "Stand der Kenntnisse über die Kaltrissbildung und die Beurteilung der Kaltrissanfälligkeit", DVS-Berichte Band 64, S.9-23.
- [HAC 15] T.Kasuya, Y.Hashiba, S.Ohkita and M.Fuji: "Hydrogen Distribution in Multipass Submerged Arc Weld Metals", Science and Technology of Welding and Joining", Vol.6, No.4, 2001, pp.261-266.
- [HAC 16] B.Irving: "Weld Cracking Takes on Some New Twists", Welding Journal, August, 1998, pp.37-40.
- [HAC 17] N.A.: "Weld Cracks", Datasheet219a, Welding Journal, August, 1998, pp.53-54.

- [HAC 18] U.Draugelates, A.Schram und C.C.Kedenburg: "Wasserstoffaufnahme im Tropfenstadium beim Metall-Schutzgasschweißen von niedriglegierten Feinkornbaustählen", Schweissen & Schneiden, Heft 9, 49, 1997, S.693-699.
- [HAC 19] A.Million und G.A.v.Reumont: "Wasserstoffbeeinflusste Querrisse in Schweißen-Verbindungen höherfester, schweißgeeigneter Feinkorn-Baustähle, Erscheinungsformen, Ursachen und Abhilfe, VGB Kraftwerktechnik, Heft 7, 57, 1972, S.490-499.
- [HAC 20] B.Graßhoff und W.Dahl: "Wasserstoffeffusionsverhalten von Schweißgutproben in Abhängigkeit von Temperatur und chemischer Zusammensetzung", Schweissen & Schneiden, Heft 7, 48, 1996, S.544-549.
- [HAC 21] Th.Boellinghaus, H.Hoffmeister, K.Feuerstake, H.Alzer and J.Krewinkel: "Finite Element Calculation of Hydrogen Uptake and Diffusion in Martensitic Stainless Steel Welds", Mathematical Modelling of Weld Phenomena 3, H.Cerjak and H.K.D.H.Badeshia (ed.), The Institute of Materials, London, 1999, pp.355-378.
- [HAC 22] V.D.Makarenko, V.A.Belyaev, V.N.Protosov, S.P.Shatilo and K.K.Gumerski: "Mathematical Model of the Mechanism of Resistance of Welded Joints in Oil and Gas Pipelines to Static Hydrogen Fatigue", Welding International, 14(4), 2000, pp.324-326.
- [HAC 23] Th.Boellinghaus and H.Hoffmeister: "Finite Element Calculations of Pre- and Post-Heating Procedures for Sufficient Hydrogen Removal in Butt Joints", Mathematical Modelling of Weld Phenomena 3, H.Cerjak and H.K.D.H.Badeshia (ed.), The Institute of Materials, London, 1997, pp.726-756.
- [HAC 24] K.Shinozaki, L.Ke and T.H.North: "Hydrogen Cracking in Duplex Stainless Steel Weld Metal", Welding Journal, November, 1992, pp.387s-396s.
- [HAC 25] Y.Komizo, K.Ogawa and S.Azuma: "HAZ Embrittlement in High Cr-Mo Duplex Stainless Steel and the Effects of Ni and N", Welding International, 5(4), 1991, pp.277-282.
- [HAC 26] J.Brozada: "A Comparison between the Levels of Preheat Temperature Necessary to Prevent Cold Cracking during Welding of Low-Alloy High- and Higher-Strength Steels", Welding International, 11(2), 1997, pp.95-102.
- [HAC 27] E.P.Beachum, H.H.Johnson and R.D.Stout: "Hydrogen and Delayed Cracking in Steel Weldments", Welding Journal, April, 1961, pp.155s-159s.
- [HAC 28] J.Mikula: "The Role of Hydrogen in the Initiation of Cold Cracking (Part II)", Welding International, 8(11), 1994, p.851-855.
- [HAC 29] J.Mikula: "The Role of Hydrogen in the Initiation of Cold Cracking (Part I)", Welding International, 8(10), 1994, pp.761-765.
- [HAC 30] K.Masubuchi and D.C.Martin: "Investigation of Residual Stresses by Use of Hydrogen Cracking", Welding Journal, December, 1961, pp.553s-563s.
- [HAC 31] Y.Kikuta and T.Araki: "Microscopic Redistribution Behaviour of Hydrogen and Fracture Morphology of HAZ Cold Cracking in High Strength Steel", IIW Doc.11-927-80, IX-1165-80, 1980, pp.1-11.
- [HAC 32] H.Suzuki, N.Yurioka and M.Okumura: "A New Cracking Parameter for Welded Steels Considering Local Accumulation of Hydrogen", IIW Doc.IX-1195-81, 1981, pp.1-10.

References

- [HAC 33] N.Yurioka, S.Ohshita, H.Nakamura and K.Asano: "An Analysis of Effects of Micro-Structure, Strain and Stress on the Hydrogen Accumulation in the Weld Heat-Affected Zone", IIW Doc.1X-1161-80, 1980, pp.1-19.
- [HAC 34] M.Matsushita and S.Liu: "Hydrogen Control in Steel Weld Metal by Means of Fluoride Additions in Welding Flux", *Welding Journal*, 2000, pp.295s-303s.
- [HAC 35] M.D.Rowe, T.W.Nelson and J.C.Lippold: "Hydrogen-Induced Cracking along the Fusion Boundary of Dissimilar Metal Welds", *Welding Journal*, February, 1999, pp.31s-37s.
- [HAC 36] L.Fletcher and N.Yurioka: "A Holistic Model of Hydrogen Cracking in Pipeline Girth Welding", *Welding in the World*, Vol. 44, No. 2, 2000, pp.29-36.
- [HAC 37] J.Goldak et al.: "Modelling the Slit Test for Assessing Sensitivity to Hydrogen Cracking", pp.161-173.
- [HAC 38] P.Adamied und J.Dziubinski: "Wasserstoffrisse in geschweißten Stahlrohren", 2001, S.1-19.
- [HAC 39] Y.D.Park, I.S.Marouf, A.Landau and D.L.Olson: "Retained Austenite as a Hydrogen Trap in Steel Welds", *Welding Journal*, February, 2002, pp.27s-35s.
- [HAC 40] V.I.Makhnenko, T.V.Korolyova and I.G.Lavrinet: "Effect of Microstructural Transformations on Redistribution of Hydrogen in Fusion Welding of Structural Steels", *The Paton Welding Journal*, Vol.2, 2002, pp.6-13.
- [HAC 41] P.Adamiec und J.Dziubinski: "Wasserstoffrisse in geschweißten Stahlrohren-Teil 1: Entstehung und Kenngrößen", *Schweissen & Schneiden*, Heft 5, 54, 2002, S.240-245.
- [HAC 42] P.Adamied und J.Dziubinski: "Wasserstoffrisse in geschweißten Stahlrohren-Teil 2: Einfluss von Wasserstoff und Zugspannungen auf die mechanischen Eigenschaften", *Schweissen & Schneiden*, Heft 6, 54, 2002, S.315-320.
- [HAC 43] D.J.Kim et al.: "Hydrogen Attack on Simulated Weld Heat Affected Zone of 3Cr-1Mo-0.25V Steel", *Science and Technology of Welding and Joining*, Vol.6, No.6, 1999, pp.402-404.
- [HAC 44] R.D.Smith II, G.P.Landis, I.Marouf, D.L.Olson and T.R.Wildeman: "The Determination of Hydrogen Distribution in High-Strength Steel Weldments Part 1: Laser Ablation Methods", *Welding Journal*, May, 2001, pp.115s-121s.
- [HAC 45] R.D.Smith II, D.K.Benson, I.Marouf, D.L.Olson and T.R.Wildeman: "The Determination of Hydrogen Distribution in High-Strength Steel Weldments Part 2: Opto-Electronic Diffusible Hydrogen Sensor", *Welding Journal*, May, 2001, pp.122s-125s.
- [HAC 46] C.Wildash, R.C.Cochrane and R.Gee: "Simulation of Hydrogen Induced Cold Cracking Using Electrolytic Precharging Procedure", *Science and Technology of Welding and Joining*, Vol.6, No.2, 2001, pp.73-78.
- [HAC 47] H.Hoffmeister: "Concept and Procedure Description of the IRC Test for Assessing Hydrogen Assisted Weld Cracking", IIW Doc.IX-1369-85, *Comp. Steel Research*, Vol.57, No.7, 1986, pp.345-347.
- [HAC 48] H.Hoffmeister: "Effect of Heat Input and Preheating on Hydrogen Assisted Weld Joint Cracking of a 0.13%C, 1.5%Mn, 0.032%Nb High Strength Steel of 50 mm Plate Thickness in the IRC Test", *Steel Research*, Vol.58, No.12, 1987, pp.570-576.

- [HAC 49] H.Hoffmeister: "Effect of Hydrogen, Restraint and Welding Conditions on Weld Metal Cold Cracking of HSLA Steels in the IRC Test", Steel Research, Vol.58, No.3, 1987, pp.142-147.
- [HAC 50] H.Hoffmeister: "Entwicklung und Aussagen eines instrumentierten Einspann-Schweißversuchs", Arch. Eisenhüttenwes., 49, No.3, 1978, pp.151-154.
- [HAC 51] H.Hoffmeister: "Cold Cracking Behaviour of two Medium-Strength Steels StE355 Containing 0.10 and 0.13%C ", Arch. Eisenhüttenwes., 55, No.3, 1984, pp.29-32.
- [HAC 52] H.Hoffmeister: "Investigation of the Conditions for Weld Metal Hydrogen Cracking of Low Carbon Offshore Steels by the IRC Weldability Test", Steel Research, Vol.58, No.3, 1987, pp.134-141.
- [HAC 53] H.Hoffmeister: "Quality Assessment of High Strength Steel Welds by Quantitative Stress and Strain Measurement During Cooling and After Welding", Steel Research, Vol. 58, No.3, 1987, pp.134-141.
- [HAC 54] B.CHEW and R.A.WILLGOSS: "Weld Metal Hydrogen Absorption during TIG-Welding with Argon-Hydrogen Gas Shields", The Welding Institute, Cambridge, Paper 25.
- [HAC 55] N.N: "Investigation of a Failed Supermartensitic Stainless Steel Weld of Tune Pipeline", BAM-Technical Report, No. V.50-23/01, Berlin, 2001.
- [HAC 56] Th.Boellinghaus: Personal communication.
- [HAC 57] P.Zimmer: Personal communication

VI. Literature for supermartensitic stainless steels (SPM)

- [SPM 1] A.Dhooge, E.Deleu and A.Holy: "Weld Simulation Testing of Different Supermartensitic Stainless Steel", IIW Document IXH-533-02.
- [SPM 2] L.Karisson, S.Rigdal, J.Broek, M.Goldschmitz and R.Pederson: "Welding of Supermartensitic Stainless Steels Recent Developments and Application Experience", IXH-532-02 Supermartensitic Stainless Steel World, 2001, pp.1-8.
- [SPM 3] M.Kimura, Y.Miyata and T.Toyooka: "Development of New 13Cr Steel with High Strength and Good Toughness", Corrosion2002, Paper No.02044, (Houston, TX: NACE International,2002).
- [SPM 4] M.Ueda, H.Amaya, K.Kondo, K.Ogawa and T.Mori: "Corrosion Resistance of Weldable Supermartensitic in H₂S Containing CO₂ Environments", Corrosion96, Paper No.58, (Houston, TX: NACE International, 1996).
- [SPM 5] S.Sakamoto, K.Maruyama and H.Kaneta: "Corrosion Property of API and Modified 13Cr Steels in Oil and Gas Environment", Corrosion96, Paper No.77, (Houston, TX: NACE International, 1996).
- [SPM 6] S.Srinivasan and R.D.Kane: "Prediction of Corrosivity of CO₂/H₂S Production Environments", Corrosion96, Paper No.11, (Houston, TX: NACE International, 1996).

References

- [SPM 7] N.N.Bich and K.Goerz: "Caroline Pipeline Failure: Findings on Corrosion Mechanisms in Wet Sour Gas Systems Containing Significant CO₂", Corrosion96, Paper No.26, (Houston, TX: NACE International, 1996).
- [SPM 8] M.Ueda and A.Ikeda: "Effect of Microstructure and Cr Content in Steel on CO₂ Corrosion", Corrosion96, Paper No.13, (Houston, TX: NACE International, 1996).
- [SPM 9] R.D.Kane, G.Farquhar and D.Sanders: "Performance of 12Cr-4 Ni Simulated Moderately Sour Production Environments", Corrosion97, Paper No.29, (Houston, TX: NACE International, 1997).
- [SPM 10] C.P.Linne, F.Blanchard, G.C.Guntz and B.J.Orlans-Joliet: "Corrosion Performances of Modified 13Cr for OCTG in Oil and Gas Environments", Corrosion97, Paper No.28, (Houston, TX: NACE International, 1997).
- [SPM 11] S.Huizinga and W.E.Lick: "Limitations for the Application of 13Cr Steel in Oil and Gas Production Environments", Corrosion97, Paper No.39, (Houston, TX: NACE International, 1997).
- [SPM 12] M.Kimura et al.: "Corrosion Resistance of High Strength Modified 13Cr Steel", Corrosion97, Paper No.22, (Houston, TX: NACE International, 1997).
- [SPM 13] P.J.Cooling, M.B.Kermani, J.W.Martin and P.I.Nice: "The Application Limits of Alloyed 13%Cr Tubular Steels for Downhole Duties", Corrosion98, Paper No.94, (Houston, TX: NACE International, 1998).
- [SPM 14] P.Felton and M.J.Schofield: "Understanding The High Temperature Corrosion Behaviour of Modified 13% Cr Martensitic OCTG", Corrosion98, Paper No.99, (Houston, TX: NACE International, 1998).
- [SPM 15] M.S.Cayard and R.D.Kane: "Serviceability of 13Cr Tubulars in Oil and Gas Production Environments", Corrosion 98, Paper No.112, (Houston, TX: NACE International, 1998).
- [SPM 16] S.Hashizume, Y.Inohara and K.Masamura: "Effects of pH and P_{H₂S} on SSC Resistance of Martensitic Stainless Steels", Corrosion2000, Paper No.00130, (Houston, TX: NACE International, 2000).
- [SPM 17] M.Kimura et al.: "Effect of test Method on SSC Performance of Modified 13Cr Steel", Corrosion 98, Paper No.114, (Houston, TX: NACE International, 1998).
- [SPM 18] H.Amaya, K.Kondo, H.Hirata, M.Ueda and T.Mori: "Effect of Chromium and Molybdenum of Super 13Cr Martensitic Stainless Steel in CO₂ Environment", Corrosion98, Paper No.113, (Houston, TX: NACE International, 1998).
- [SPM 19] S.Olsen, L.Borvik and G.Rorvik: "Corrosion Testing of Supermartensitic Weldments with Matching Consumables", Corrosion2000, Paper No.00129, (Houston, TX: NACE International, 2000).
- [SPM 20] J.L.Crolet and G.Maisonneuve: "Construction of a Universal Scale of Severity for Hydrogen Cracking", Corrosion2000, Paper No.00127, (Houston, TX: NACE International, 2000).
- [SPM 21] T.Rogue, J.M.Drugli, O.O.Knudsen, S.Olsen and J.Enerhaug: "Corrosion Performance of 13Cr Stainless Steels", Corrosion2000, Paper No.00152, (Houston, TX: NACE International, 2000).

- [SPM 22] S.Hashizume, Y.Inohara and K.Masamura: "Effect of Strength on Stress Corrosion Cracking Resistance of Martensitic Stainless Steels", Corrosion 2001, Paper No.01085, (Houston, TX: NACE International, 2001).
- [SPM 23] L.Beres und W.Irmer: "Festlegung einer optimierten Zwischenlagentemperatur beim martensitischen Schweißen", Schweissen und Schneiden, Heft 1, 51, 1999, S.28-31.
- [SPM 24] L.Beres und Z.Beres: "Neue Gleichung zur Berechnung der M_s-Temperatur", Schweissen und Schneiden, Heft 8, 46, 1994, S.372-374.
- [SPM 25] A.Pourbaix: "Cathodic Protection of Supermartensitic 13Cr Stainless Steels without Hydrogen Damage", Supermartensitic Stainless Steels 99:S99-33, 1999, pp.283-290.
- [SPM 26] M.Swidzinski, G.Hutt and C.Fowler: "Mechanical and Corrosion Assessment of Advanced 13%Cr Steel Welds Produced by Radial Friction Welding (RFW)", Supermartensitic Stainless Steels 99:S99-29, 1999, pp.246-254.
- [SPM 27] T.G.Gooch, P.Woollin and A.G.Haynes: "Welding Metallurgy of Low Carbon 13% Chromium Martensitic Steels", Supermartensitic Stainless Steels 99:S99-22, 1999, pp.188-195.
- [SPM 28] M.Turdy et al.: "Effect of Metallurgical Factors on the Toughness and Corrosion Resistance of 16/5Mo and 13/6Mo Steels", Supermartensitic Stainless Steels 99:S99-39, 1999, pp.331-344.
- [SPM 29] M.Ueda et al.: "Corrosion Performance of Supermartensitic Stainless Steel", Supermartensitic Stainless Steels 99:S99-41, 1999, pp.346-352.
- [SPM 30] T.Rogne, J.M.Drugli and M.Bjoldal: "EAC Testing Welded 13% Cr Grades Martensitic Stainless Steels for Sour Service Application", Supermartensitic Stainless Steels 99:S99-38, 1999, pp.323-330.
- [SPM 31] L.Coudreuse, M.Verneau and J.J.Dufrane: "Sulfide Stress Cracking Resistance of Weldable Super-Martensitic Stainless Steel", Supermartensitic Stainless Steels 99:S99-35, 1999, pp.299-306.
- [SPM 32] P.Felton and M.J.Schofield: "Extending the Limits of Corrosion Behaviour of Modified 13%Cr Martensitic OCTG at High Temperature", Supermartensitic Stainless Steels 99:S99-32, 1999, pp.272-282.
- [SPM 33] Th.Boellinghaus, H.Hoffmeister and L.Reuter: "Material Properties of As Delivered and Quenched Modified Martensitic Stainless Steels Dependent on Hydrogen Concentration", Supermartensitic Stainless Steels 99:S99-31, 1999, pp.264-271.
- [SPM 34] J.J.Dufrane: "Metallurgical Basis for The Development of Weldable Martensitic Stainless Steels", Supermartensitic Stainless Steels 99:S99-2, 1999, pp.19-24.
- [SPM 35] K.J.Irvine, D.J.Crowe and F.B.Pickering: "The Physical Metallurgy of 12% Chromium Steels", Journal of The Iron and Steel Institute, August, 1960, pp.386-405.
- [SPM 36] M.C.Balmforth and J.C.Lippold: "A Preliminary Ferritic-Martensitic Stainless Steel Constitution Diagram", Welding Journal, January, 1998, pp.1s-7s.
- [SPM 37] T.G.Gooch: "Heat Treatment of Welded 13%Cr-4%Ni Martensitic Stainless Steels for Sour Service", Welding Journal, July, 1995, pp.213s-223s.

References

- [SPM 38] G.Cumino and R.Spelgatti: "Evaluation of High Steel Grade Linepipes for Sour Service with Special Corrosion Testing", Corrosion98, Paper No.122, (Houston, TX: NACE International, 1998).
- [SPM 39] A.W.Marshall and J.C.M.Farrar: "Welding of Ferritic and Martensitic 11-14% Cr Steels", Welding in the World, Vol.45, 2001, pp.19-42.
- [SPM 40] A.Anderko and R.D.Young: "A Model for Calculating Rates of General Corrosion of Carbon Steel and 13%Cr Stainless Steel in CO₂/H₂S Environments", Corrosion2001, Paper No.01086, (Houston, TX: NACE International, 2001).
- [SPM 41] D.Festy: "Cathodic Protection of Steel in Deep Sea: Hydrogen Embrittlement Risk and Cathodic Protection Criteria", Corrosion2001, Paper No.01011, (Houston, TX: NACE International, 2001).
- [SPM 42] S.Trasatti, L.Scoppio and T.Cheldi: "H₂S and CO₂ of Some 9Cr-1Mo Alloys for Downhole Applications", Corrosion2001, Paper No.01083, (Houston, TX: NACE International, 2001).
- [SPM 43] L.X.Yang, X.Z.Yang and A.Pourbaix: "Potential-pH Diagrams Relevant to 13Cr Stainless Steels in Chloride and Sulfide Containing Solutions, Corrosion2001, Paper No.01084, (Houston, TX: NACE International, 2001).
- [SPM 44] S.Huizinga and R.K.Ohm: "Qualification and Application Limits of Weldable Supermartensitic 13Cr Linepipe Steels", Corrosion2001, Paper No.01093, (Houston, TX: NACE International, 2001).
- [SPM 45] G.Cumino et al.: "Supermartensitic 13%Cr Large Diameter Seamless Pipes : Corrosion Resistance of the Girth Weld", Corrosion2001, Paper No.01095, (Houston, TX: NACE International, 2001).
- [SPM 46] J.C.M.Farrar and A.W.Marshall: "Super Martensitic Stainless Steel Overview and Weldability", Doc: IIW-IX-H-423-98, 1998, pp.1-16.
- [SPM 47] T.Gooch: "Welding of Ferritic and Martensitic 11-14%Cr Steels", Doc: IX-1975-00-IXH-494-2000, 2000, pp.1-38.
- [SPM 48] S.Hashizume, Y.Inohara, Y.Minami and K.Masamura: "Effect of Chemical Composition and Strength on Corrosion Resistance of Martensitic Stainless Steels in CO₂ and H₂S Environments", Supermartensitic Stainless Steels 99:S99-2, 1999, pp.307-314.
- [SPM 49] G.Rabensteiner, E.Pertender und J.Tösch: "Optimierung von weichmartensitischen Chrom-Nickel-Schweißgutlegierungen für den Einsatz im Kernreaktorbau", DVS-Berichte Band 75, S.261-265.
- [SPM 50] E.Delue, A.Dhooge and J.J.Dufrane: "Weldability and Hot Deformability of Different Supermartensitic Stainless Steel Grades by Weld Simulation Testing", Supermartensitic Stainless Steels 99:S99-2, 1999, pp.232-240.
- [SPM 51] K.Kondo et al.: "Alloy Design of Super 13Cr Martensitic Stainless Steel: Development of Super 13Cr Martensitic Stainless Steel for Line Pipe I", Supermartensitic Stainless Steels 99:S99-2, 1999, pp.11-18.
- [SPM 52] A.G.Haynes: "Some Factors Governing the Metallurgy and Weldability of 13%Cr and Newer Cr-Ni Martensitic Stainless Steels", Supermartensitic Stainless Steels 99:S99-2, 1999, pp.25-32.

- [SPM 53] H.Heuser, C.Jochum, E.Perteneder and J.Tösch: “GMAW and SAW Matching Filler Materials for Supermartensitic Stainless Steels”, Supermartensitic Stainless Steels 99:S99-2, 1999, pp.150-159.
- [SPM 54] P.C.Gough, J.C.M.Farrar and Z.Zhang: “Welding Consumables for Supermartensitic Stainless Steels”, Supermartensitic Stainless Steels 99:S99-2, 1999, pp.160-171.
- [SPM 55] L.Karlsson et al.: “Matching Composition Supermartensitic Stainless Steel Welding Consumables”, Supermartensitic Stainless Steels 99:S99-2, 1999, pp.172-179.
- [SPM 56] Th.Boellinghaus, Th.Kannengiesser, C.Jochum and I.Stiebe-Springer: “Effect of Filler Material Selection on Stress Strain Build Up and Stress Corrosion Cracking Resistance of Welded Supermartensitic Stainless Steel Pipes”, Corrosion2002, Paper No.02061, (Houston, TX: NACE International, 2002).
- [SPM 57] M.C.Balmforth, J.C.Lippold: A New Ferritic-Martensitic Stainless Steel Constitution Diagram, IIW-Doc. II-1439-01 (II-C-205-01)

VII. Literature for stress-strain distribution in welding processes (SDW)

- [SDW 1] S.T.Tu and K.B.Yoon: “The Influence of Material Mismatch on the Evaluation of Time-Dependent Fracture Mechanics Parameters”, Engineering Fracture Mechanics, Vol.64, 1999, pp.765-780.
- [SDW 2] K.Satoh and S.Matsui: “Reaction Stress and Weld Cracking under Hindered Contraction”, IX-574-68, 1968, pp.353-375.
- [SDW 3] H.Wenkao, Z.Wenyue and C.Banggu: “Relationship between Restraint Intensity and Restraint Stress in Elastoplastic Range”, China Welding, Vol.2, No.2, 1993, pp.118-124.
- [SDW 4] Y.Dong, J.K.Hong, C.L.Tsai and P.Dong: “Finite Element Modelling of Residual Stresses in Austenitic Stainless Steel Pipe Girth Welds, Welding Journal, October, 1997, pp.442s-449s.
- [SDW 5] W.G.Xu: “Failure Assessment Diagrams in the Presence of Residual Stresses”, Welding in the World, Vol.39, No.6, 1997, pp.314-330.
- [SDW 6] H.Murakawa, Y.Lei, Y.Shi and Y.Ueda: “Dependence of J –Integral and Failure Assessment Diagram on Strength Mismatching and Crack Length for Welded Joint Specimen”, Transaction of JWRI, Vol.26, No.1, 1997, pp.13-22.
- [SDW 7] E.P.Pokataev, Y.P.Trykov and A.S.Kraev: “Calculations and Experimental Determination of Residual Deflections of Bimetallic Components Produced by Explosion Welding”, Welding International, Vol.13, No.6, 1999, pp.9-484.
- [SDW 8] J.Spurrier, P.Hancock and J.P.Chubb: “An Assessment of Weld Mis-Matching”, Engineering Fracture Mechanics, Vol.53, No.4, 1996, pp.581-592.
- [SDW 9] Th.Boellinghaus, H.Hoffmeister and M.Littich: “Application of the IRC-Test for Assessment of Reaction Stresses in Tubular Joints with Respect to Hydrogen Assisted Cracking”, Welding in the World, Vol.43, No.2, 1999, pp.27-35.
- [SDW 10] M.Takanashi, K.Kamata and K.Iida: “Relaxation Behaviour of Welding Residual Stresses by Fatigue Loading in Smooth Longitudinal Butt Welded Joints”, Welding in the World, Vol.44, No.4, 2000, pp.28-34.

References

- [SDW 11] T.Kannengiesser, W.Florian and H.Herold: "Incremental Hole-Drilling Method for the Determination of Residual Stresses on Welds", Schweissen&Schneiden, August, 1999, pp.12-19.
- [SDW 12] W.Tang and Y.W.Shi: "Influence of Strength Matching and Crack Depth on Fracture Toughness of Welded Joints", Engineering Fracture Mechanics, Vol.51, No.4, 1995, pp.649-659.
- [SDW 13] J.-B.Roelens: "Numerical Simulation of some Multipass Submerged Arc Welding-Determination of the Residual Stresses and Comparison with Experimental Measurements", Welding in the World, Vol.35, No.2, 1995, pp.17-24.
- [SDW 14] J.Puchaicela: "Control of Distortion of Welded Steel Structures", Welding Journal, August, 1998, pp.49-52.
- [SDW 15] P.Dong, J.Zhang, J.K.Hong, W.Bell and E.J.McDonald: "Finite Element and Experimental Study of Residual Stresses in a Multi-Pass Repair Weld", Recent Progress in Analysis of Welding Residual Stresses, WRC Bulletin 455, September, 2000, pp.22-28.
- [SDW 16] Z.Cao, P.Dong and F.Brust: "A Fast Thermal Solution Procedure for Analyzing 3D Multi-Pass Welded Structures", Recent Progress in Analysis of Welding Residual Stresses, WRC Bulletin 455, September, 2000, pp.12-21.
- [SDW 17] P.Dong: "Modelling of Weld Residual Stresses and Distortions: Computational Procedures and Applications", Recent Progress in Analysis of Welding Residual Stresses, WRC Bulletin 455, September, 2000 , pp.1-11.
- [SDW 18] K.-H.Schwalbe and M.Kocak: "Fracture Mechanics of Weldments: Properties and Application to Components", Keynote Lecture: 3rd International Conference on Trending in Welding Research, Tennessee, 1992, pp.1-27.
- [SDW 19] Th.Boellinghaus, H.Hoffmeister, I.Stiebe-Springer, W.Florian and Th.Michael: "Component Testing of Welded Supermartensitic Stainless Steel Pipes",
- [SDW 20] Y.Shim ed al.: "Determination of Residual Stresses in Thick-Section Weldments", Welding Journal, September, 1992, pp.305s-312s.
- [SDW 21] L.Jihong, Z.Jianxun and P.Yi: "Study on Fracture Mechanics Parameters of Surface Crack in Overmatched Weldments", China Welding, Vol.8, No.1, 1999, pp.30-36.
- [SDW 22] J.-B.Roelens: "Numerical Simulation of Some Multipass Submerged Arc Welding-Determination of the Residual Stress and Comparison with Experimental Measurements", Welding in the World, Vol.35, No.2, 1995, pp. 110-117.
- [SDW 23] J.B.Roelens, F.Maltrud and J.Lu: "Determination of Residual Stresses in Submerged Arc Multi-Pass Welds by Means of Numerical Simulation and Comparison with Experimental Measurements", Welding in the World, Vol.33, No.3, 1994, pp.152-159.
- [SDW 24] P.Dong and J.K.Hong: "Analysis of IIW X/XV RSDP Phase I Round-Robin Residual Stress Results", Welding in the World, Vol.46, No.5/6, 2002, pp.24-31.

VIII. Literature for temperature distribution in welding process (TDW)

- [TDW 1] P.N.Sabapathy, M.A.Wahab and M.J.Painter: "Numerical Models of In-Service Welding of Gas Pipelines", *Journal of Materials Processing Technology*, No.118, 2001, pp.14-21.
- [TDW 2] N.N.Rykalin and A.V.Nikolaev: "Welding Arc Heat Flow ", *Welding in the World*, Vol.9, No.3, 1971, pp.112-133.
- [TDW 3] K.Mundra, T.Debroy, T.Zacharia and S.A.David: "Role of Thermo-physical Properties in Weld Pool Modelling", *Welding Journal*, September, 1992, pp.313s-320s.
- [TDW 4] N.D.Malmuth, W.F.Hall, B.I.Davis and C.D.Rosen: "Transient Thermal Phenomena and Weld Geometry in GTAW" *Welding Journal*, September, 1974, pp.388s-400s.
- [TDW 5] N.T.Nguyen, Y.W.Mai and A.Ohta: "A New Hybrid Double-Ellipsoidal Heat Source Model for Weld Pool Simulation", *Australasian Welding Journal*, Vol.46, 2001, pp.39-46.
- [TDW 6] T.W.Eagar and N.S.Tsai, "Temperature Fields Produced by Travelling Distributed Heat Sources", *Welding Journal*, December, 1993, pp.346s-355s.
- [TDW 7] S.Murungan, T.P.S.Gill, P.V.Kumar, B.Raj and M.S.C.Bose: "Numerical Modelling of Temperature Distribution During Multipass Welding of Plates", *Science and Technology of Welding and Joining*, Vol.5, No.4, 2000, pp.208-214.
- [TDW 8] D.Rosenthal: "The Theory of Moving Sources of Heat and Its Application to Metal Treatment", *Transactions of the A.S.M.E.*, November, 1946, pp.849-866.
- [TDW 9] N.T.Nguyen, A.Ohta, K.Matsuoka, N.Suzuki and Y.Maeda: "Analytical Solutions for Transient Temperature of Semi-Infinite Body Subjected to 3-D Moving Heat Sources", *Welding Journal*, August, 1999, pp.265s-274s.
- [TDW 10] R.N.Suzuki, R.E.Trevisan and O.V.Trevisan: "Analytical Solutions for Heat Flow in Multiple Pass Welding", *Science and Technology of Welding and Joining*, Vol.5, No.2, 2000, pp.63-70.
- [TDW 11] S.Shibata and T.Watanabe: "The Effect of Grain Growth in a Heat Affectad Zone on the Weld Metal of Austenitic Stainless Steel", *Welding in the World*, No.41, 1998, pp.236-239.
- [TDW 12] T.Kasuya and N.Yurioka: "Prediction of Welding Thermal History by a Comprehensive Solution", *Welding Journal*, March, 1993, pp.107s-115s.
- [TDW 13] R.I.Karlsson and B.L.Josefson: "Three-Dimensional Finite Element Analysis of Temperatures and Stresses in a Single-Pass Butt-Welded Pipe", *Transactions of the ASME*, Vol.112, 1990, pp.76-84.
- [TDW 14] S.Murungan, P.V.Kumar, T.P.S.Gill, B.Raj and M.S.C.Bose: "Numerical Modelling and Experimental Determination of Temperature Distribution during Manual Metal Arc Welding", *Science and Technology of Welding and Joining*, Vol.4, No.6, 1999, pp.357-364.
- [TDW 15] H.Cerjak and B.Buchmayr: "Mathematical Modelling of Weld Phenomena", *Third European Conference on Joining Technology*, 1998, pp.259-266.

References

- [TDW 16] M.J.M.Hermans and G.den Ouden: "Modelling of Heat Transfer in Short Circuiting Gas Metal Arc Welding", Science and Technology of Welding and Joining, Vol.3, No.3, 1998, pp.135-138.
- [TDW 17] K.Kondoh and T.Ohji: "In Process Heat Input Control in Arc Welding", Science and Technology of Welding and Joining, Vol.3, No.6, 1998, pp.295-303.
- [TDW 18] X.K.Zhu and Y.J.Chao: "Effect of Temperature-Dependent Material Properties on Welding Simulation", Computers and Structures, No.80, 2002, pp.967-976.
- [TDW 19] J.Goldak, A.Chakravarti and M.Bibby: "A Double Ellipsoid Finite Element Model for Welding Heat Sources", IIW-Doc.212-603-85.

BIOGRAPHICAL SKETCH

Personal Data:

Name: Ekkarut VIYANIT
Address: Bottroper Weg 14, 13507 Berlin
Date of Birth: 25 October 1972
Place of Birth: Ayutthaya, Thailand
Nationality: Thai
Family Status: Single

Schooling:

05/1980 – 04/1985 Wat Talad (Udomwitthaya) School, Ayutthaya Thailand
05/1985 – 04/1988 Benjamarajanusorn School, Nonthaburi, Thailand
06/1988 – 03/1991 Cert. in Technical Education, King Mongkut's Institute of Technology North Bangkok, Bangkok, Thailand

Education:

06/1992 – 03/1996 Bachelor of Engineering in Production Engineering (B.Eng.), King Mongkut's Institute of Technology North Bangkok, Bangkok, Thailand
05/1996 – 10/1999 Master of Engineering in Metallurgical Engineering (M.Eng.), Chulalongkorn University, Bangkok, Thailand

Occupational Activity:

05/1996 – 12/1998 Teaching Assistant, Physical Metallurgical Lab., Chulalongkorn University, Bangkok, Thailand
10/1999 – 12/1999 Metallurgical Engineer, Thai-German Special Steel Co. Ltd., Samut Prakan, Thailand
05/2000 - present Research Associate, Division V: Safety in Joining Technology, Federal Institute for Materials Research and Testing (BAM)

Berlin, October 2004

Ekkarut Viyanit

